STRUCTURE AND DYNAMICS IN SELF-ASSEMBLED ALKYLTHIOL/GOLD MONOLAYERS

by

Antonella Badia

A thesis submitted to the Faculty of Graduate Studies and Research
in partial fulfillment of the requirements for the degree of
Doctor of Philosophy

Department of Chemistry
McGill University
Montreal, Quebec
Canada

National Library
of Canada

Acquisitions and
Bibliographic Services Branch

395 Wellington Street
Ottawa, Ontario
K1A 0N4

Bibliothèque nationale
du Canada

Direction des acquisitions et
des services bibliographiques

395, rue Wellington
Ottawa (Ontario)
K1A 0N4

Your file Votre référence

Our file Notre référence

ISBN 0-612-19706-9

Canada

ABSTRACT

Self-assembled monolayers (SAMs) of *n*-alkanethiolates on gold, silver, and copper have been intensively studied as model organic surfaces and as modulators of metal surface properties. Sensitivity restrictions imposed by monolayer coverage and the low surface area of planar metal substrates limit the characterization of these films by signal enhancement techniques. As a result, key aspects such as the nature of the metal-sulfur interaction, alkyl chain ordering, and adsorbate phase diagrams remain open and ill-defined. The characterization of the thermotropic properties of SAMs is important not only for the design of stable well-ordered organic superlattices, but also for the fundamental understanding of the factors which drive molecular interactions in two dimensions. The question of phase properties in SAMs has been addressed by using the electron transfer process between a water-soluble redox species and a thiol-derivatized gold electrode as a probe of the monolayer film structure. The redox ion current at RS/Au electrodes (where R = n-$C_{16}H_{33}$ - n-$C_{20}H_{41}$ and $HO(CH_2)_{16}$) exhibits maxima at temperatures defined by the alkyl chain length and the presence of stabilizing endgroup interactions. This behavior closely parallels the enhanced permeability of phospholipid bilayer vesicles to ions at their chain tilt/untilt and gel-to-liquid crystalline phase transition temperatures. The 1:1 correlation between the pre-transition (T_p) and main transition (T_m) temperatures of the RS/Au monolayers studied here and *n*-diacylphosphatidylcholine bilayer membranes suggests that there are similar mechanisms for chain melting and reorientation in these two systems. This correlation arises because the chain packing configuration and density, as established by the Au lattice and phospholipid headgroup, are very similar. The noted parallels with the permeability profile of phospholipid membrane systems indicates that permeation, and not electron tunneling, is the dominant electron transfer process at RS/Au electrodes.

Furthermore, the synthesis of large surface area, thiol-modified gold nanoparticles of *ca*. 20-30 Å diameter has enabled the *quasi*-2D monolayer film structure to be uniquely characterized by transmission FT-IR spectroscopy, NMR spectroscopy, and differential scanning calorimetry (DSC). These studies show that Au-thiolate monolayers do, in fact, undergo order-disorder transitions. FT-IR spectroscopy verifies that the phase transition detected by electrochemistry for planar RS/Au monolayers and by DSC for RS/Au nanoparticles arises from an increased population of *gauche* conformers. ^{2}H NMR and FT-IR studies of perdeuterated and selectively deuterated $C_{18}S$/Au samples establish that melting starts at the chain termini and propagates towards the middle of the chains. *Trans-gauche* bond isomerization and C-C bond axial rotation are the motional processes which accompany the chain order/disorder transition. Chain mobility near the tethered sulfur headgroup is greatly restricted. The physical properties of these alkylated nanoparticles indicate that the RS/Au nanoparticles can serve as a highly dispersed analogue to the much-studied planar SAMs. This paves the way for the application of these readily prepared colloidal systems to a number of biomimetic and optical devices.

RÉSUMÉ

Les monocouches auto-assemblées de *n*-alcanethiols sur des surfaces d'or, d'argent et de cuivre ont été très utilisées pour modeler les surfaces organiques et modifier les propriétés des surfaces métalliques. Cependant, à cause du caractère monomoléculaire du recouvrement et de la petite surface des substrats métalliques, la caractérisation des monocouches auto-assemblées n'est possible que si des techniques amplifiant le signal sont utilisées. Par conséquent, les facteurs-clés tels que la nature de l'intéraction métal-soufre, l'arrangement des chaînes hydrocarbonées et le diagramme de phase des espèces adsorbées sur les surfaces métalliques restent à être définis. La caractérisation des propriétés thermotropiques des monocouches auto-assemblées est très importante non seulement du point de vue de l'élaboration de monocouches organiques stables et bien ordonnées, mais aussi pour la compréhension fondamentale des facteurs qui contrôlent les intéractions moléculaires en deux dimensions. Les différentes phases des monocouches auto-assemblées ont été étudiées en utilisant la technique du transfert électronique entre un couple rédox soluble dans l'eau et une électrode recouverte de molécules d'alcanethiols. Le couple rédox constitue le moyen par lequel la structure de la monocouche organique peut être caractérisée. Le courant du couple rédox à l'interface métal/thiol (RS/Au, où R = n-$C_{16}H_{33}$ à n-$C_{20}H_{41}$ et $HO(CH_2)_{16}$) montre un maximum à des températures précises. Ces températures sont définies par la longeur de la chaîne hydrocarbonée ainsi que par la présence de liaisons hydrogènes à l'interface monocouche organique/eau. Il existe un parallèle entre ces résultats et l'augmentation de la perméabilité des ions dans les vesicules de phospholipides aux températures de transition de phase, ainsi qu'aux températures auxquelles les chaînes engendrent des changements d'inclinaison. En ce qui concerne la température de pré-transition (T_p) et la température de transition principale (T_m), la correspondance exacte entre les monocouches RS/Au etudiées ici et les membranes de *n*-diacylphosphatidylcholines suggère qu'il existe des mécanismes similaires qui régissent la fusion et la réorientation

des chaînes. Ceci s'explique par le fait que l'arrangement et la densité des chaînes sont similaires pour ces deux cas. Le parallèle établi entre les caractéristiques de perméabilité des membranes de phospholipides et celles des monocouches RS/Au démontre que la perméabilité, et non l'effet tunnel, est le processus majeur par lequel le transfert électronique se fait aux électrodes RS/Au.

De plus, la synthèse de nanoparticules à grande surface, modifiées avec des thiols et ayant un diamètre d'environ 20 à 30 Å, a permis de caractériser la structure de la monocouche en utilisant des techniques telles que la spectroscopie de transmission infrarouge, la spectroscopie RMN et la calorimétrie différentielle. Ces études montrent que les monocouches de thiols adsorbées sur des surfaces d'or engendrent en fait des transitions d'un état ordonné à un état désordonné. La spectroscopie d'infrarouge confirme que la transition de phase observée par électrochimie pour les monocouches planes RS/Au et par calorimétrie différentielle pour les nanoparticules RS/Au est causée par une augmentation du nombre de conformères *gauche*. La RMN du deutérium et la spectroscopie d'infrarouge pour des systèmes $C_{18}S/Au$ ayant été prédeutérés ou sélectivement deutérés montrent que la fusion des chaînes commence par l'extrémité de celles-ci et se propage ensuite vers l'intérieur. L'isomérisation ***trans/gauche*** et la rotation axiale C-C sont les phénomènes qui accompagnent les transitions de phase. La mobilité des chaînes à proximité du groupe sulfuré est grandement restreinte. Les propriétés physiques des nanoparticules alkylées montrent que les nanoparticules RS/Au peuvent servir comme système analogue hautement dispersé aux surfaces planes. Ceci ouvre la voie à l'application de ces colloïdes à de nombreux systèmes biologiques et optiques.

FOREWORD

In accordance with guideline 3 of the "Guidelines for Thesis Preparation" (Faculty of Graduate Studies and Research), the following text is cited:

> "Candidates have the option of including, as part of the thesis, the text of a paper(s) submitted or to be submitted for publication, or the clearly-duplicated text of a published paper(s). These texts must be bound as an integral part of the thesis.
>
> If this option is chosen, **connecting texts that provide logical bridges between the different papers are mandatory**. The thesis must be written in such a way that it is more than a mere collection of manuscripts; in other words, results of a series of papers must be integrated.
>
> The thesis must still conform to all other requirements of the "Guidelines for Thesis Preparation". **The thesis must include:** A Table of Contents, an abstract in English and French, an introduction which clearly states the rationale and objectives of the study, a comprehensive review of the literature, a final conclusion and summary, and a thorough bibliography or reference list.
>
> Additional material must be provided where appropriate (e.g. in appendices) and in sufficient detail to allow a clear and precise judgment to be made of the importance and originality of the research reported in the thesis.
>
> In the case of manuscripts co-authored by the candidate and others, **the candidate is required to make an explicit statement in the thesis as to who contributed to such work and to what extent**. Supervisors must attest to the accuracy of such statements at the doctoral oral defense. Since the task of the examiners is made more difficult in these cases, it is in the candidate's interest to make perfectly clear the responsibilities of all the other authors of the co-authored papers. **Under no circumstances can a co-author of any component of such a thesis serve as an examiner for that thesis.**"

Foreword

This dissertation is written in the form of four papers. These papers each comprise one chapter in the main body of the thesis (Chapters 2 to 5), with a general introduction to this work in the first chapter and conclusions in the sixth chapter. Following normal procedure, the papers have either been published or submitted for publication in scientific journals. A list of the papers is given below:

Chapter 2: *Angew. Chem.* **1994**, *106*, 2429-2431 (German version)
Angew. Chem. Int. Ed. Engl. **1994**, *33*, 2332-2335 (English version)
Chapter 3: *Langmuir* (submitted)
Chapter 4: *Chem. Eur. J.* **1996**, *2*, 359-363
Chapter 5: *Journal of the American Chemical Society* (submitted)

All of these papers include the research supervisor, Professor R. Bruce Lennox, as co-author since the work was done under his direction. Chapter 2 includes Dr. Roberta Back as co-author in acknowledgment of the fact that she first observed the phenomenon reported in this paper. This phenomenon was fully characterized by the present author. Chapter 4 includes Ms. Shanti Singh in recognition of her help with the synthesis of the gold nanoparticles used in this study. Mr. Louis Cuccia is a co-author in Chapters 4 and 5 because he acquired all of the solution-state NMR spectra shown in Chapter 4, and he helped the present author acquire the deuterium NMR spectra shown in Chapter 5. Ms. Linette Demers is included as a co-author in Chapters 4 and 5 for her contributions to the synthesis and characterization of the Au nanoparticles. Professor G. Ronald Brown is a co-author in Chapter 4 for having generously placed his laboratory facilities at our disposal and for insightful discussions. Dr. Fred Morin is a co-author in Chapter 5 due to his expertise in solid-state NMR instrumentation. Other than the aforementioned contributions, all of the work presented in this dissertation was initiated and performed by the author.

ACKNOWLEDGMENTS

I wish to thank all of those who helped at various stages in the development of this thesis.

It is with great pleasure that I express my sincere gratitude to my supervisor, Professor R. Bruce Lennox, for his support, advice, and continued devotion to this work. I am especially grateful for his positive encouragement whenever I expressed the eagerness to pursue new ideas.

All the students (past and present) in my lab deserve a very special thanks for helpful discussions and for their friendship. These include Louis Cuccia, Joy Klass, Tara Heitner, Emmanuelle Boubour, Pollyanna Peters, Fuyuan Ma, Zhigang Qi, Roberta Back, Michelle Meszaros, and Bruce Constantine. I am particularly grateful to Louis Cuccia for the particular interest that he has shown in this work, and for the countless help that he has given me during my stay in the lab. The abstract was kindly translated by Emmanuelle Boubour.

I would like to extend a very special thank you to Shanti Singh for her help in the gold nanoparticle synthesis and characterization. I will never forget those gold washing marathons that we ran together.

During my stay in the Chemistry Department at McGill, I was very fortunate to have worked with several fantastic undergraduate students: Linette Demers, Hélène Schmitt, and Karen Sum. These three young ladies taught me more about life than I could ever teach them about chemistry!

I am grateful to Professor Linda Reven, McGill University, for her collaboration in the matter of solid-state ^{13}C NMR, and for numerous discussions on the physical properties of RS/Au nanoparticles.

I would also like to acknowledge Professor Tom Ellis and Farid Bensebaa, Université de Montréal, for the characterization of planar RS/Au monolayers by RAIRS.

I am forever indebted to Professor G. Ronald Brown for allowing me open access to his laboratory facilities. Without the equipment, alot of this work would not have been possible.

Acknowledgments

It has been my good fortune to learn from the advice and wisdom of Dr. Francis Chubb during my term at McGill.

I would like to thank Drs. Fred Morin and Françoise Sauriol for sharing their NMR expertise and for training on the NMR instruments.

I am greatful to the Natural Sciences and Engineering Research Council (Canada) and to the Fonds pour la Formation de Chercheurs et l'Aide à la Recherche (Quebec) for postgraduate fellowships. I would also like to thank SigmaXi - The Scientific Research Society for the award of a personal grant-in-aid of research.

Finally, I acknowledge with heartfelt gratitude the love and support of my parents and my sisters.

TABLE OF CONTENTS

Chapter One

GENERAL INTRODUCTION

Chapter Two

PHASE TRANSITIONS IN SELF-ASSEMBLED MONOLAYERS DETECTED BY ELECTROCHEMISTRY

Chapter Three

ORDER/DISORDER PHASE TRANSITIONS IN SELF-ASSEMBLED MONOLAYERS

Chapter Four

SELF-ASSEMBLED MONOLAYERS ON GOLD NANOPARTICLES

Chapter Five

STRUCTURE AND DYNAMICS IN SAMs: A DSC, IR, AND DEUTERIUM NMR STUDY

Chapter Six

CONCLUSIONS, CONTRIBUTIONS TO ORIGINAL KNOWLEDGE, AND IDEAS FOR CONTINUED RESEARCH

Appendix

LIST OF FREQUENTLY USED SYMBOLS

Å	Angstrom (10^{-10} m)
AFM	atomic force microscopy
β	electron tunneling constant
C_i	capacitance
CI	chemical ionization
CV	cyclic voltammetry
δ	NMR chemical shift in ppm
d^-	antisymmetric stretching vibration
d^+	symmetric stretching vibration
d, D	deuterium
2D	two-dimensional
DSC	differential scanning calorimetry
E	applied potential
E°, $E^{\circ\prime}$	standard potential of a redox couple
EI	electron impact
FAB	fast atom bombardment
FT-IR	Fourier transform infrared
ΔH_{endo}	endothermic change in enthalpy
ΔH_{exo}	exothermic change in enthalpy
hr	hour
i	Faradaic current
IR	infrared
k_{app}	apparent rate constant
LB	Langmuir-Blodgett
µA	10^{-6} amps
µF	10^{-6} farads
MD	molecular dynamics

min	minute
MLV	multilamellar lipid vesicle
mM	10^{-3} mol/L
mp	melting point
MS	mass spectrometry
mV	10^{-3} volt
η	overpotential
nm	nanometer (10^{-9} m)
NMR	nuclear magnetic resonance
PC	phosphatidylcholine lipid
PE	phosphatidylethanolamine lipid
R	alkyl chain length
RAIRS	reflection absorption infrared spectroscopy
RS^-, RS	alkylthiolate
RS/Au	*n*-alkylthiol chemisorbed on gold
RSH	*n*-alkylthiol
RSSR	alkyldisulfide
SAM	self-assembled monolayer
SSV	single lipid bilayer supported on a glass microsphere
STM	scanning tunneling microscopy
T	temperature
T_m, T_m^e	main transition temperature
T_p, T_p^e	pre-transition temperature
TEM	transmission electron microscopy
TLC	thin layer chromatography
UPD	underpotential deposition
V	volt
UHV-STM	ultrahigh-vacuum scanning tunneling microscopy
ν_a	antisymmetric stretching vibration
ν_s	symmetric stretching vibration
XPS	X-ray photoelectron spectroscopy

LIST OF FIGURES

List of Figures

LIST OF TABLES

Chapter One

GENERAL INTRODUCTION

1.1. SAMs: Model Organic Surfaces

The fabrication and characterization of thin film organic surfaces is currently the focus of intensive research effort since the interfacial properties of these composites may provide insights into fundamental aspects of surface chemistry.[1] These problems include thin film adhesion, catalysis, lubrication mechanisms, wetting/dewetting phenomena, corrosion, and interfacial electron transfer. The spontaneous organization or ***self-assembly*** of organic molecules at solid surfaces, due to molecule-substrate interactions and intermolecular forces, provides a rational methodology for the preparation of structurally well-defined, organic thin films.[2,3] Self-assembled monolayers (SAMs) of organosulfur adsorbates, especially alkanethiols, on gold surfaces are the most studied systems to date.[4-10] Their popularity stems from the fact that highly ordered SAMs can be prepared under readily accessible laboratory conditions, and strong coordination of the sulfur to the metal yields a film which is sufficiently stable to desorption. In fact, applications of alkanethiol SAMs as artificial membranes, electrocatalysts, photoresists, biosensors, immunosensors, pH-sensors, and corrosion protectants have already been reported.[7,11]

1.2. Monolayer Film Formation

Self-assembled thiol monolayers are usually prepared by immersing a clean metal substrate into a saturated solution (10^{-3} M) of an *n*-alkanethiol (RSH) or alkyldisulfide (RSSR) in an organic solvent. Although silver, platinum, copper, and mercury surfaces have been used for the self-assembly of thiols, gold remains the most widely used metal due to the fact that it is relatively inert and does not form a stable surface oxide under ambient conditions. Gold substrates include single crystals, polycrystalline bulk electrodes, and evaporated or sputtered thin films. Typical immersion times in solution of several minutes to several hours are used for RSHs, while several days are required for monolayer formation from RSSR.[12-14] The thiol-modified metal substrate is then removed from the incubation solution, rinsed with solvent, and dried briefly under nitrogen or argon. Although solution deposition is the most versatile method, monolayer films have also been prepared by vapor deposition of volatile, short chain RSHs[15,16], by immersion of the metal in neat liquid adsorbates[17], and by electrochemical deposition[18].

The self-assembly of alkanethiols is driven by the strong affinity of the sulfur for the metal, which results in the apparent covalent bonding of the thiol adsorbate to the metal surface. Lateral van der Waals interactions between the tethered alkyl chains, as well as electrostatic and hydrogen bonding interactions between polar terminal groups in ω-substituted alkanethiols, order and orient the chains. (Scheme 1.1).

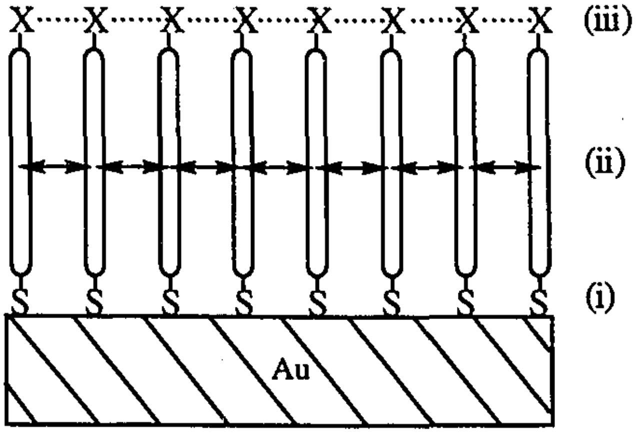

Scheme 1.1. A physical representation of the main interactions responsible for two-dimensional ordering of thiols onto metal substrates: (i) bonding of the sulfur to the metal surface, (ii) interchain van der Waals interactions, and (iii) interaction between the terminal functional groups and the ambient/film interface.

Kinetic studies of the adsorption of long chain alkanethiols onto gold surfaces from solution show two distinct regimes. The initial adsorption of the thiol to the gold surface is very fast (on the order of minutes). Bain *et al.* observed that this rapid first step results in contact angles (wetting) and film thicknesses which are ~ 80-90% of the maximum values.[12] Initial thiol adsorption follows simple diffusion-controlled Langmuir kinetics, and the adsorption time is strongly concentration dependent.[12] While thiol adsorption from a 10^{-3} M solution is essentially complete after ~ 1 min, over 100 min are required if a 10^{-6} M thiol solution is used. The second regime was found to occur over a significantly longer time (hours), at the end of which contact angle and ellipsometric film thickness measurements reached their saturation values.[12] This second step has been postulated to be a slow two-dimensional chain crystallization process, involving additional thiol adsorption and consolidation, thiol-assisted reconstruction of the Au surface lattice, dissolution of Au surface features, displacement of contaminants from the metal surface, expulsion of included solvent from the monolayer, and place-exchange of adsorbates at surface defect sites.[8,12,19,20] The kinetic description of the rapid first step was confirmed by following thiol adsorption from dilute solution (10^{-6} M) in real time, using second-harmonic generation (SHG) in conjunction with ex-situ X-ray photoelectron spectroscopy (XPS) measurements of monolayer coverage.[21] Since SHG probes only the electronic properties of the metal-thiol interface, information on molecular ordering as a function of the adsorption time could not be obtained using this technique. The slow second step in the self-assembly of alkanethiols on gold surfaces was recently examined in terms of the alkyl chain orientation and conformation by near-edge X-ray absorption fine structure spectroscopy (NEXAFS). [22] This study demonstrates that chain ordering during the self-assembly process is analogous to the stretching of grafted "polymer brushes". In fact, the NEXAFS results show that the alkanethiol molecules are initially adsorbed as entangled chains with a high concentration of *gauche* conformers. The disordered chains gradually straighten out so as to adopt an all-*trans*, extended conformation and they orient at an angle of 35° from the surface normal to produce densely packed, highly-ordered films (Scheme 1.2). A similar two-step self-assembly process was recently observed in-situ by following the vapor-deposition of short chain RSH molecules onto a Au (111) surface using a ultrahigh-vacuum scanning tunneling microscope (UHV-STM).[23] This UHV-STM study reveals that low-density striped-phase islands, characterized by head-to-tail and head-to-head alignment of the RSH molecular axes with the surface plane, initially condense on the metal surface. Additional RSH adsorption causes the RSH molecules in this striped phase to undergo a phase transition which tips the RSH tails or chains away from the Au surface to allow for a denser packing of the sulfur headgroups. This two-step self-assembly mechanism is analogous to the lateral surface pressure-induced formation of ordered monolayer films from amphiphile molecules confined to the air-water interface in a Langmuir trough.[23]

An electrochemical quartz crystal microbalance (EQCM) study of the adsorption and desorption behavior of alkylthiols on Au-coated quartz crystals also shows that the preparation protocols can largely influence the quality of the SAM and the self-assembly rate.[24] For instance, the solvent used in the thiol incubation solutions appears to play an important role in the film formation kinetics.[24] For example, exposure of the Au-coated quartz crystal to RSH in acetonitrile initially (in the first few minutes) leads to multilayer deposition which only over several hours evolves to stable monolayer coverage. If, on the other hand, dimethylformamide is used as the solvent, no initial multilayer adsorption is detected. Furthermore, submonolayer deposition of thiols occurs on a time scale of seconds in dimethylformamide, but over a period of minutes in acetonitrile.[24] Thus, the important role that solvent plays on the kinetics of thiol self-assembly may ultimately lead to the preparation of SAMs with different structures, given the various conditions used by different laboratories.

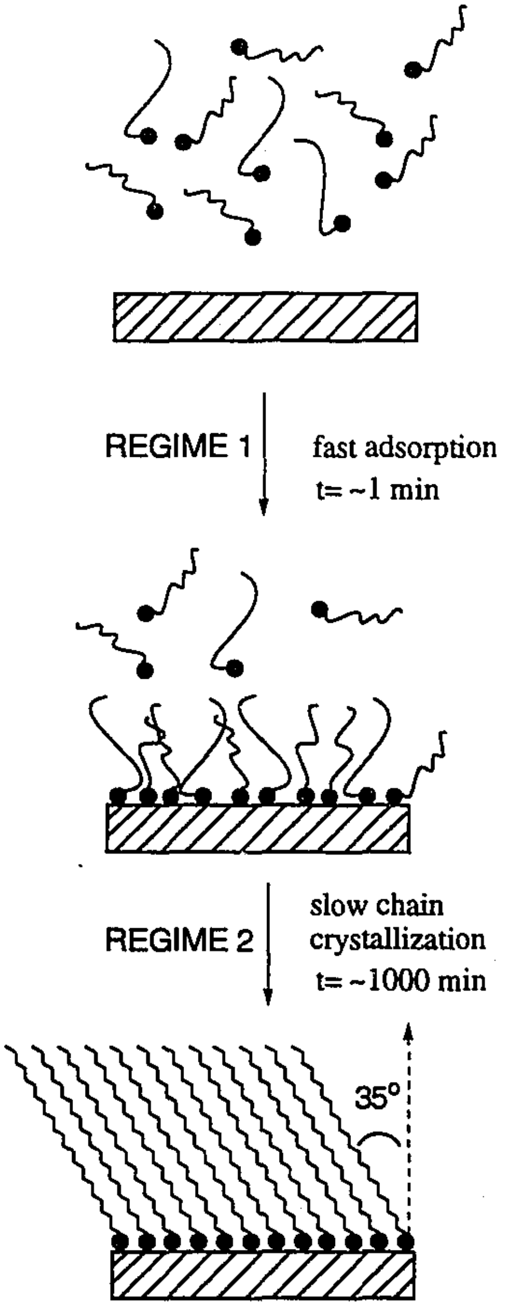

Scheme 1.2. Kinetics of monolayer self-assembly summarized from discussions and data in references 12 and 21-23.

1.3. Film Characterization Techniques

Studies of the physical properties of RSH/Au SAMs have addressed the following structural issues:

(i) thiol-metal epitaxy;
(ii) nature of the Au-S interaction;
(iii) molecular conformation and orientation of the alkyl chains;
(iv) order and orientation of the chain terminal groups at the film/ambient interface;
(v) film integrity and stability;
(vi) film defect sites.

Figure 1.1 summarizes the surface techniques which have been used to probe the film structure of RSH/Au SAMs.

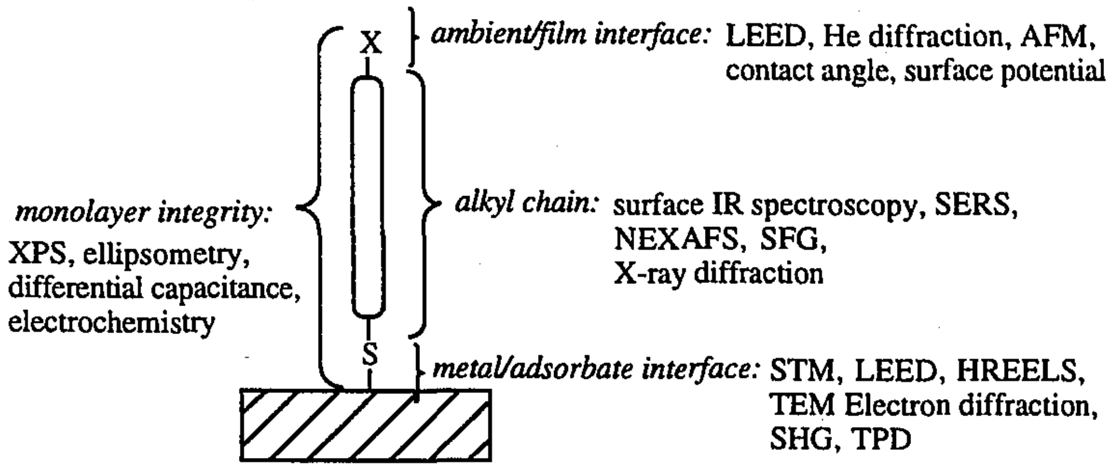

Figure 1.1. Film characterization techniques. LEED (low energy electron diffraction); AFM (atomic force microscopy); SERS (surface enhanced Raman scattering); NEXAFS (near edge X-ray absorption fine structure spectroscopy); SFG (sum-frequency generation); STM (scanning tunneling microscopy); HREELS (high resolution electron energy loss spectroscopy); TEM (transmission electron microscopy); SHG (second harmonic generation); TPD (temperature programmed desorption); XPS (X-ray photoelectron spectroscopy).

Monolayer film coverage (*i.e.* ~ 4.6 x 10^{14} molecules/cm^2 on Au[25]) and the low surface area of planar metal surfaces have largely limited the characterization of these SAMs to techniques amenable to signal enhancement. More importantly, since the adsorbate domain size is typically tens to hundreds of nanometers, the study of molecular ordering in organic thin films often requires techniques capable of sensitively probing surface areas of less than 1 μm^2.[1] Most of the SAM characterization techniques used to date, such as infrared and Raman spectroscopy, contact angle/wetting measurements, ellipsometry, XPS, and X-ray diffraction are signal averaged techniques that report only the "bulk" properties of the film. In this respect, the scanning probe microscopies, particularly atomic force microscopy (AFM) and scanning tunneling microscopy (STM), have played an important role in probing the monolayer structure and morphology, given that they provide information at the molecular level.[16,20,26-42]

1.4. Gold-Sulfur Interaction

Although there is currently no direct supporting evidence, adsorption of alkanethiols and alkyldisulfides to gold surfaces is thought to proceed *via* oxidative addition of the S-H or S-S bond to gold producing a gold(I) thiolate (RS^-) species [6,8]:

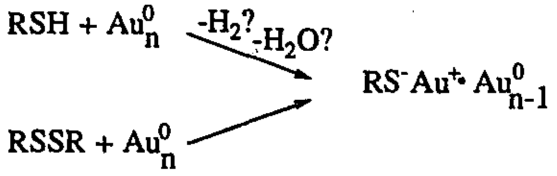

$$RSH + Au^0_n \xrightarrow{-H_2?\ -H_2O?} RS^-Au^{+\cdot}\,Au^0_{n-1} \xleftarrow{} RSSR + Au^0_n \qquad (1).$$

The absence of S-H (~ 2600 cm^{-1}) and S-S (~ 520 cm^{-1}) stretching vibrations in both the infrared[13,43-45] and Raman spectra[46,47] of adsorbed alkanethiols and disulfides, and the *ca.* 20 cm^{-1} shift to lower frequency observed for the *gauche* and *trans* C-S stretching bands[46,47] is commonly offered as evidence for the cleavage of the S-H and S-S bonds. XPS measurements[44,48-50], electrochemical monolayer desorption investigations[51], and laser desorption Fourier transform mass spectrometry studies[52,53] all suggest that the adsorbed organosulfur species is a thiolate (RS^-). The Au-S bond has been described as being largely covalent, but with some ionic character, and the homolytic bond strength has been measured to be 40-50 kcal mol^{-1}. [2,9,43]

The S··S spacing and alkyl chain packing density in RS/Au SAMs is largely dictated by the underlying metal lattice. For example, grazing incidence X-ray diffraction[54], He diffraction[19,55], electron diffraction[56], and STM studies[16,26,29,31-33,35,40,41] of alkanethiolates on Au (111) surfaces show a commensurate hexagonal array with a S··S spacing of 4.99 Å. More specifically, STM studies reveal that the sulfur atoms are bonded to the Au triple hollow sites (Figure 1.2A), leading to a $(\sqrt{3} \times \sqrt{3})R30^\circ$ unit cell.[16,26,29,31-33,35,40,41] Since the spacing between adjacent sulfurs in this RS/Au (111) overlayer is greater than the distance of closest approach of the alkyl chains (4.24 Å), the chains tilt by ~ 30° (from the surface normal) to maximize lateral van der Waals interactions. This results in a chain packing density of 21.7 $Å^2$ per molecule.[19] By comparison, the S··S spacing of thiolates adsorbed on a Au (110) surface is 5.76 Å, with the sulfur atoms bonded to the rectangular hollow sites of the Au (110) surface in a commensurate c(2x2) structure (Figure 1.2B).[19] In the RS/Au (110) configuration, the chain tilt is ~ 40°, and the area occupied per RSH chain is 23.5 $Å^2$,[19] resulting in a surface packing of chains that is ~ 8% less dense than for the RS/Au (111) monolayer. In contrast to the results obtained for RS/Au (111) and RS/Au (110), studies of the structure of alkanethiolates on Au (100) report quite different results. Camillone *et al.* observed a complex He diffraction pattern for the terminal methyl groups of a n-$C_{22}H_{45}S$/Au (100) monolayer.[19] A tentative analysis of the data revealed an incommensurate oblique array with four kinds of equivalent chain domains due to the four fold symmetry of the Au (100) lattice. An area per RSH molecule of 17.8 $Å^2$ was calculated[19], which translates to a 20% tighter chain packing density than for monolayers on Au (111). The results of an earlier transmission electron diffraction study however suggested a c(10x10) overlayer, where the alkyl chains are packed in a square lattice with an interchain spacing of 4.54 Å, a calculated chain tilt of 6-12°, and an area of 20.6 $Å^2$ per molecule.[56] Molecular dynamics calculations do not support this latter bonding configuration on Au (100) because the simulations show that if the sulfurs are restricted to a square lattice with a S··S distance of 4.54 Å, the alkyl chains undergo progressive distortions of the C··C··C bond angles to reduce the free energy of packing of the all-*trans* chains.[57] More specifically, the simulations predict a rearrangement from the square lattice geometry at the thiolate/Au interface to a distorted hexagonal packing towards the tenth methylene of a n-$C_{22}H_{45}SH$ chain.[57] Recently, Scoles *et al.* investigated the possibility of a qualitatively different packing arrangement of the chemisorbed sulfur atoms, the alkyl chains, and the terminal methyl groups in n-$C_{18}H_{37}S$/Au (100) monolayers by using a combination of He diffraction and synchrotron X-ray scattering experiments.[58] Their results show that the structure of the thermally equilibrated RS/Au (100) surface consists of a p(1x4) thiolate/Au interface, and thus a distorted hexagonal alkyl chain array. The result is a chain tilt angle of 33.5±1.0° from the surface normal, and a packing density of 22.19 $Å^2$/chain.[58] The He diffraction data reveal a highly corrugated methyl surface which forms a c(2x8) structure.[58] These results clearly point to the complex interplay which exists between the interchain van der Waals interaction and the sulfur/gold interaction for thiol SAMs on Au (100) surfaces.

Recently, some controversy has arisen over the nature of the adsorbed organosulfur species. Since the 4.99 Å S··S spacing of alkanethiolates on Au (111) is nearly three times the van der Waals diameter of a sulfur atom (*i.e.* 1.85 Å), S-S interactions would seem to be minimal. Contrary to previous X-ray and electron diffraction studies[54,56], an interpretation of the results of a recent grazing angle X-ray diffraction study of *n*-$C_{10}H_{21}SH$ self-assembled on Au (111) concluded that there is a dimerized array of sulfurs on the surface, whose S··S spacing is 2.2 Å.[59] This implies that the adsorbate is equivalent to a disulfide. A *gauche* S-C bond apparently accomodates the well-known hexagonal alkyl chain array in this disulfide bonding scheme.[59] Furthermore, a kinetic analysis of the desorption and place-exchange processes of ^{35}S radiolabeled octadecanethiol from gold suggests desorption as the disulfide, although a spectroscopic characterization of the actual desorption products is required to provide more compelling proof.[25] Nevertheless, these anomalous results challenge the generally accepted metal thiolate bonding structure.

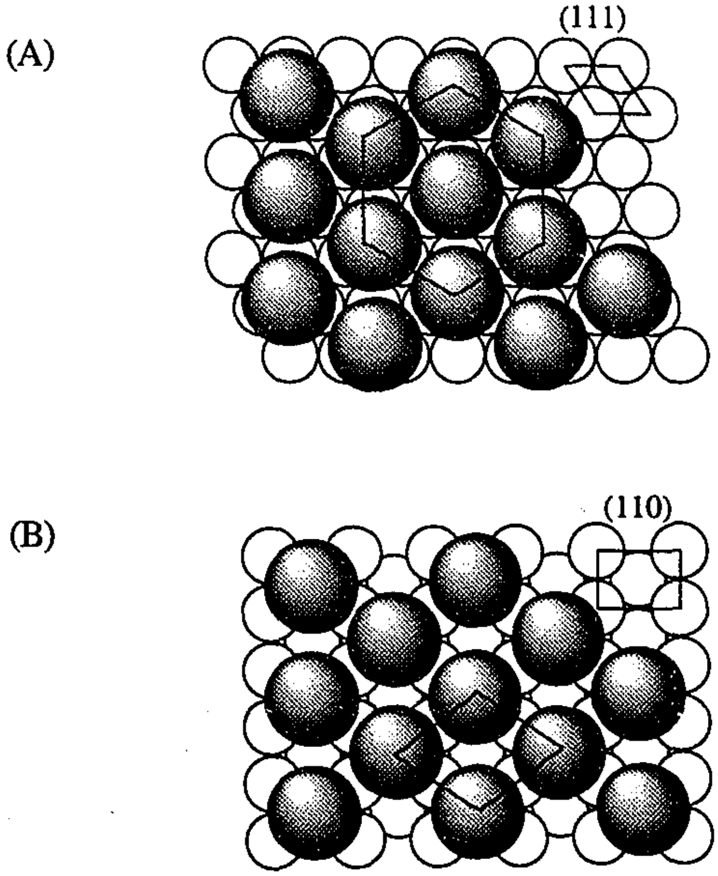

Figure 1.2. A schematic representation of the overlayer structures formed by long chain alkanethiols on Au (111) and (110) surfaces. The open circles denote the Au atoms and the larger shaded circles represent the sulfurs. (A) Commensurate (($\sqrt{3} \times \sqrt{3})R30^\circ$) hexagonal array of sulfur atoms on Au (111) places all the sulfurs at identical threefold hollow sites; (B) Commensurate c(2 x 2) adlayer lattice of sulfurs bonded to the rectangular hollow sites of the Au (110) surface.

1.5. Chain Structure and Dynamics

Surface infrared spectroscopy (*i.e.* polarization reflection-absorption infrared spectroscopy, infrared external reflection spectroscopy, and grazing-angle FT-IR spectroscopy) has been particularly useful in characterizing the conformation and orientation of the alkylthiol chains. IR studies of long chain *n*-alkanes report that both the peak frequency and the peak width of the antisymmetric (υ_a) and symmetric (υ_s) CH_2 stretching vibrations are sensitive markers of *trans* and *gauche* bond populations in the chains.[60,61] For instance, crystalline polymethylene chains exhibit $\upsilon_a(CH_2)$ and $\upsilon_s(CH_2)$ at 2920 cm^{-1} and 2850 cm^{-1}, respectively, whereas the peak positions shift to 2928 cm^{-1} (υ_a) and 2856 cm^{-1} (υ_s) in the liquid state. A similar trend is observed for bulk *n*-alkanethiols where the $\upsilon_a(CH_2)$ and $\upsilon_s(CH_2)$ peak frequencies shift from 2918 cm^{-1} to 2924 cm^{-1} and from 2851 cm^{-1} to 2855 cm^{-1} on going from the crystalline to liquid state.[44] A comparison of the $\upsilon_a(CH_2)$ peak frequencies of RS/Au SAMs for R = C_4-C_{22} shows a trend to lower peak frequencies as R increases. More specifically, the υ_a peak position (*i.e.* 2917 cm^{-1} - 2918 cm^{-1}) indicates that for $C_{16} \leq R \leq C_{22}$, the monolayer exists in a crystalline-like state, whereas for $R \leq C_8$ (*i.e.* 2921 cm^{-1}) the local environment of the alkyl chains approaches that of the bulk disordered or liquid state. A similar, but less pronounced trend is also observed with $\upsilon_s(CH_2)$.[44] Thus, the crystalline-like $\upsilon(CH_2)$ values for long chain RS/Au SAMs suggest that the alkyl chains exist in a fully-extended, all-*trans* conformation.

The ellipsometric film thickness measurements as a function of the alkylthiol chain length show two distinct regions: a linear region between C_{10} and C_{22}, and another non-linear region between C_2 and C_{10}.[44] A comparison of the measured film thicknesses with values calculated assuming close-packed, *trans*-extended alkyl chains which are tilted between 0° and 30° from the surface normal reveals close agreement only for chain lengths between C_{10}-C_{22}.[44] Low energy helium diffraction experiments, which probe the surface structure of RS/Au (111) SAMs, show that as the carbon chain length is shortened from C_{22} to C_6, an abrupt decrease in the diffraction peak intensities is observed for the $C_{10}H_{21}SH$ monolayers and no diffraction is seen with $C_6H_{13}SH$.[62,63] These results, which indicate a transition from a densely packed ordered monolayer, to a less dense more disordered state at about the C_{10} chain length, correlate well with the conclusions of the surface IR spectroscopy studies. Furthermore, a recent UHV-STM study reports that RS/Au (111) monolayers composed of $R \leq C_6$ exist in a two-dimensional (2-D) disordered or liquid phase at room temperature. No such liquid domains were observed for C_8 and C_{10} chain lengths however.[30] The results of these experiments seem to conclude that *n*-RS/Au SAMs with chain lengths longer than C_{10} exist predominantly in an ordered, all-*trans* conformation.

The measured intensities of the $\upsilon(CH_2)$ peaks are used to calculate the molecular orientation of the thiol monolayer using surface selection rules which relate the average tilt between transition dipole moments (*m*) and the surface normal (*z*) according to the equation:

$$\cos^2\theta_{mz} = I_{\mathrm{obs}}/3(I_{\mathrm{calc}}) \qquad (2);$$

where θ_{mz} is the average tilt angle of a vibrational mode with respect to the surface normal, I_{obs} is the experimental peak intensity, and I_{calc} is the peak intensity calculated for a hypothetical isotropic monolayer with the same packing density.[43,44] I_{calc} is usually determined from the transmission FTIR spectra of RSHs in the bulk state.[43,44] The results of this type of calculation yield an average tilt angle, α, of the chain axis from the surface normal of 20°-35° and a twist angle, β, of 50°-55° for long chain alkylthiol monolayers on polycrystalline gold surfaces (Figure 1.3).[43,44] The modulation of the intensities of the CH stretching modes associated with the terminal methyl groups (*i.e.* r^+ and r_a^-) in the surface IR spectra of RS/Au SAMs reveal an odd-even chain length dependent orientation of the methyl group (Figure 1.3), clearly establishing that the Au-S-C bond angle (~ 110°) is conserved. Therefore, in even number chain lengths, the intensities of the r^+ and r_a^- bands are approximately equal, for odd number chain lengths, the r_a^- band intensity is significantly stronger than that of the r^+ band.[43,64]

The structures of a variety of ω-substituted *n*-alkanethiols, $X(CH_2)_{15}SH$ (where X = CH_2OH, CO_2H, CO_2CH_3, and $CONH_2$), adsorbed on polycrystalline gold surfaces have also been characterized by surface IR spectroscopy, XPS, contact angle (wetting) measurements, and ellipsometry.[43] The results of these characterization studies show that these ω-substituted thiols also form densely packed, crystalline-like assemblies with a *trans*-extended alkyl chain conformation, with α ranging from 28°-40°, and β = *ca.* 55°. The terminal CO_2H groups appear to exist in short hydrogen-bonded sequences. The IR spectra also suggest that the terminal functional groups adopt specific orientations at the film/ambient interface which are poorly modeled by the bulk phases.[43] Molecular dynamics (MD) calculations further predict that monolayers formed from alkylthiols with polar terminal groups adopt more rigid structures than their terminal CH_3 counterparts.[65] For X = CH_2OH, MD simulations show that there is hydrogen bonding between the chain ends, but that the surface is largely disordered, with a significant amount of free hydroxyl groups. For X = CN, the terminal groups organize in a ferroelectric configuration which is incommensurate with the underlying sulfur headgroup lattice. The simulated configurations of these polar terminal groups at the film/ambient interface seem to be consistent with their wetting properties.[65]

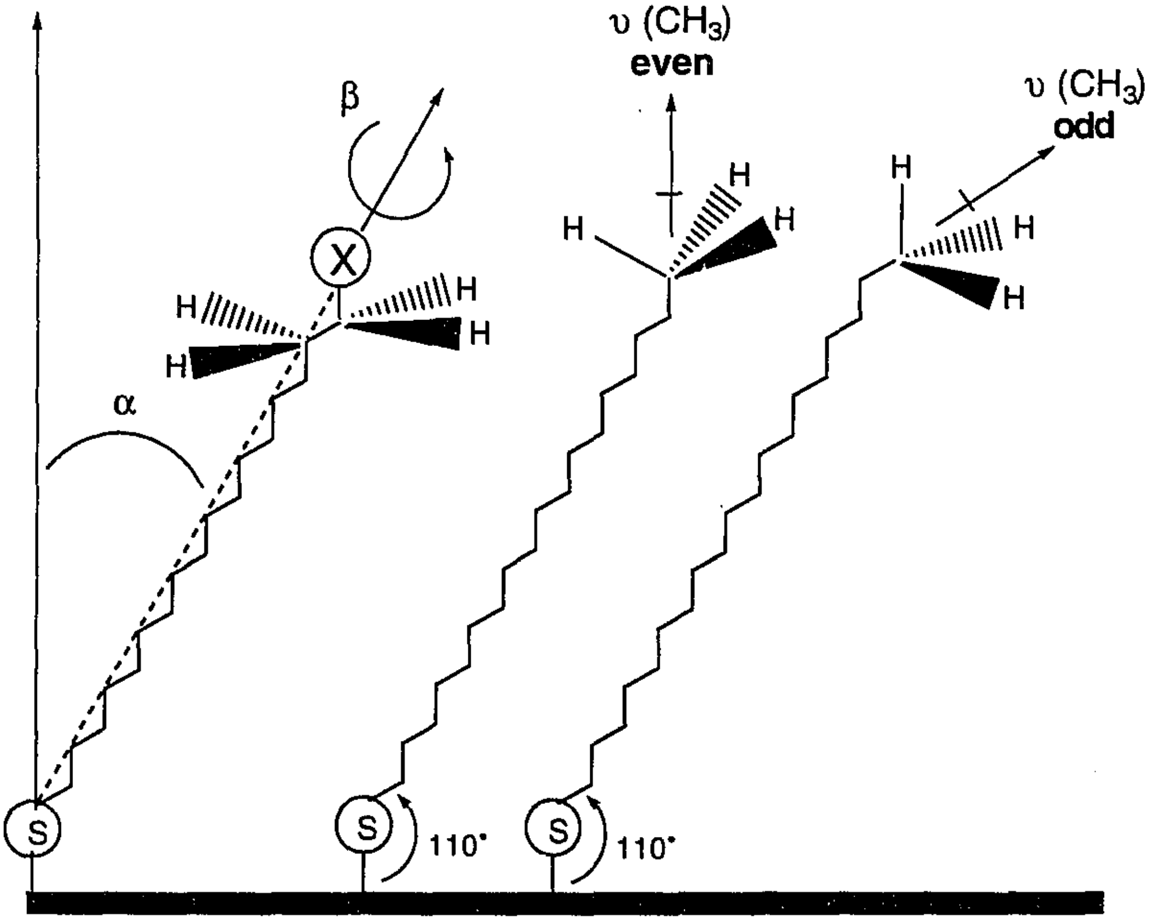

Figure 1.3. A schematic representation of the conformation and orientation of long chain RS/Au SAMs. The angle α represents the tilt of the chain axis away from the surface normal and β is the twist angle of the C-C-C plane about the chain axis. The odd-even (chain length) transition dipole orientations of the terminal CH_3 group are shown.

Scoles and co-workers have used low energy He diffraction experiments to study these systems.[62,63] The He atom penetration depth exclusively probes the ordering and thermal motion of the chain end methyl groups of RS/Au (111) films. These studies report that at temperatures lower than 100 K, the methyls form oriented, hexagonally packed domains with a lattice constant equivalent to the interchain distance of 5.01 Å. However, the increasing thermal motion of the terminal methyl groups with increasing temperature reduces the ordered coherence length, bringing the diffraction intensities to zero at *ca.* 100 K.[62,63] This indicates that even for long chain RSH monolayers that exist in a predominantly all-*trans* conformation at room temperature, the chain ends are disordered. In fact, MD simulations show that at *ca.* room temperature, long methyl-terminated chains are tilted. Moreover, they are rotated about their long axes and there is a significant population of conformational defects located at the chain ends.[65-67] Variable temperature IR studies of RS/Au (111) SAMs further indicate that as the film temperature is lowered below *ca.* 200 K, the CH_2 scissoring vibration splits into a doublet of nearly equal intensity (*i.e.* 1472 cm^{-1} and 1463 cm^{-1}).[64,68] This implies not only that there are at least two chains per surface unit cell, but that the alkyl chains exist in a more ordered environment at lower temperatures. The concomitant decrease in the $\upsilon_a(CH_2)$ frequency (*i.e.* from 2918 cm^{-1} at 300 K to 2916 cm^{-1} at 80 K), the narrowing of all the observed peak linewidths, and the large increase in the peak intensities as the temperature is lowered below 200 K are also consistent with greater chain order due to freezing out of both chain-end and internal conformational defects (*i.e.* *gauche* and kink). A decrease in the thermal motion of the terminal methyl groups also accompanies this freezing out process.[64,68]

Variable temperature surface IR spectroscopy studies show only the gradual appearance of *gauche* conformational chain defects upon heating, instead of the dramatic population increase expected for first-order melting processes.[64,68] MD simulations of the thermal behaviour of *n*-$C_{16}H_{33}S$/Au (111) monolayers predict both gradual orientational and rotational disordering of the tethered alkyl chains with increasing temperature (Figure 1.4).[65-67] A recent grazing incidence X-ray diffraction study of $C_{12}S$/Au (111) and $C_{14}S$/Au (111) monolayers instead reports reversible melting transitions, with the co-existence of both solid and liquid phases.[54] These transitions occur at temperatures that are *ca.* 60 °C above the melting points of the corresponding bulk *n*-alkanes.[54] The thermal stability of RS/Au films has also been investigated using (^{35}S) radiolabelled $C_{18}H_{37}SH$.[25] Under ambient atmosphere, thiolate desorption begins at 100 °C (373 K), with a 50% monolayer loss occurring at ~ 160 °C (433 K). A complete loss of surface sulfur is observed by 210 °C.[25] However, a temperature-programmed desorption study of a $C_{16}H_{33}S$/Au (111) monolayer detected the start of thiolate desorption at *ca.* 225 °C (498 K).[43]

In addition to chain disordering processes, temperature-induced reconstructions of the monolayer/Au interface[54,58], nucleation and growth of ordered domains induced by the partial desorption of surface thiolates[16,26,30], and surface migration of the thiolate-Au species[28,32,34] have also been observed. Furthermore, contact angle measurements show that hydroxyl-terminated SAMs undergo a slow reorganization to bury the polar hydroxyl groups into the hydrocarbon film.[65,69,70] The rate of reorganization of the monolayer was found to be influenced by both the alkyl chain length and the temperature.[65,69,70] Clearly, the dynamics of RS/Au SAMs are complex.

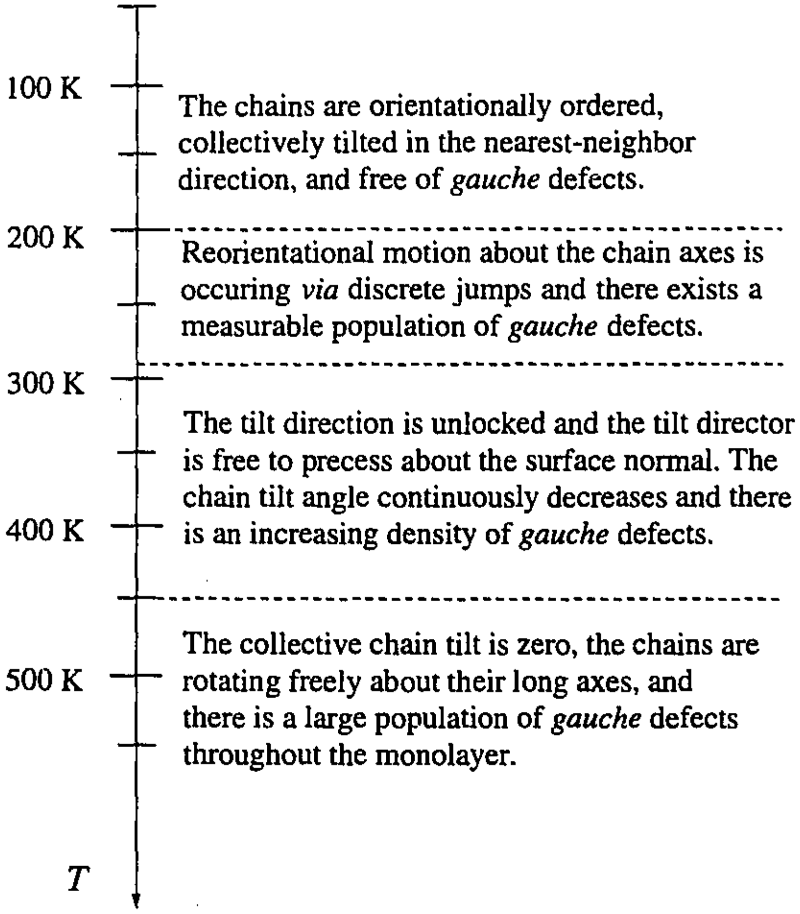

The chains are orientationally ordered, collectively tilted in the nearest-neighbor direction, and free of *gauche* defects.

Reorientational motion about the chain axes is occuring *via* discrete jumps and there exists a measurable population of *gauche* defects.

The tilt direction is unlocked and the tilt director is free to precess about the surface normal. The chain tilt angle continuously decreases and there is an increasing density of *gauche* defects.

The collective chain tilt is zero, the chains are rotating freely about their long axes, and there is a large population of *gauche* defects throughout the monolayer.

Figure 1.4. A summary of the chain dynamics of RS/Au SAMs predicted by MD simulations of the thermal behavior of a $C_{16}S/Au$ (111) system.[65-67] This schematic is modeled after one presented in references 65-67.

1.6. Interfacial Electron Transfer

Electrochemical characterization techniques, such as cyclic voltammetry, a.c. impedance spectroscopy, and differential capacitance, have been used to:

(i) determine the surface thiolate coverage;
(ii) probe the structural integrity of the film in terms of film thickness and defect sites;
(iii) understand the mechanism of interfacial electron transfer.

The surface coverage of RSH-modified Au electrodes has been determined by using the characteristic Au oxide formation (+1.1 to 1.4 V *vs.* S.C.E.) and stripping (+0.9 V *vs.* S.C.E.) peaks in the cyclic voltammograms (CVs) of electrodes immersed in 0.1 M H_2SO_4.[71-74] A comparison of the charge under the Au oxide stripping peaks of bare and thiol-coated electrodes is reported to yield a quantitative measurement of bare metal or "pinhole" sites. This method assumes that areas covered with the densely-packed monolayer are electrochemically inert. Typical fractional thiol coverages of 0.95-0.999 are reported for $C_{18}H_{37}SH$-modified Au electrodes (*i.e.* thin film Au/glass substrates and polycrystalline Au flags) using the Au oxide stripping method.[72] This methodology clearly damages the SAM however[75,76] and is not useful if the SAM is to be used in subsequent studies. Underpotential deposition and stripping of Cu has also been used to image, by STM, the density of surface bare patches as a function of the thiol incubation time.[42]

Studies reported to date on interfacial electron transfer have employed either water-soluble redox couples (*eg*. $Fe(CN)_6^{3-/4-}$, $Ru(NH_3)_6^{2+/3+}$, $Mo(CN)_8^{3-/4-}$, $Fe^{2+/3+}$, and $Fe(bpy)(CN)_4^{1-/2-}$)[17,44,71-74,77-87] or redox couples tethered to the alkylthiol chain end (*eg*. viologens, $pyRu(NH_3)_5^{2+/3+}$, ferrocene)[84,86,88-96]. The general consensus arising from electrochemical studies of RS/Au SAMs and water-soluble redox couples is that these 10-30 Å thick films can be formidable barriers for electron transfer, reducing the heterogeneous electron transfer rates by $10\text{-}10^6$ fold. The result is that the kinetics of otherwise very fast redox couples can be studied. Transmonolayer electron transfer to redox species in solution has been proposed to occur *via* an electron tunneling mechanism[77,79,81-83,88-90], through monolayer defect sites[71-74,87], ion permeation[75,78,80,85] or through redox species mediation[97] (Figure 1.5).

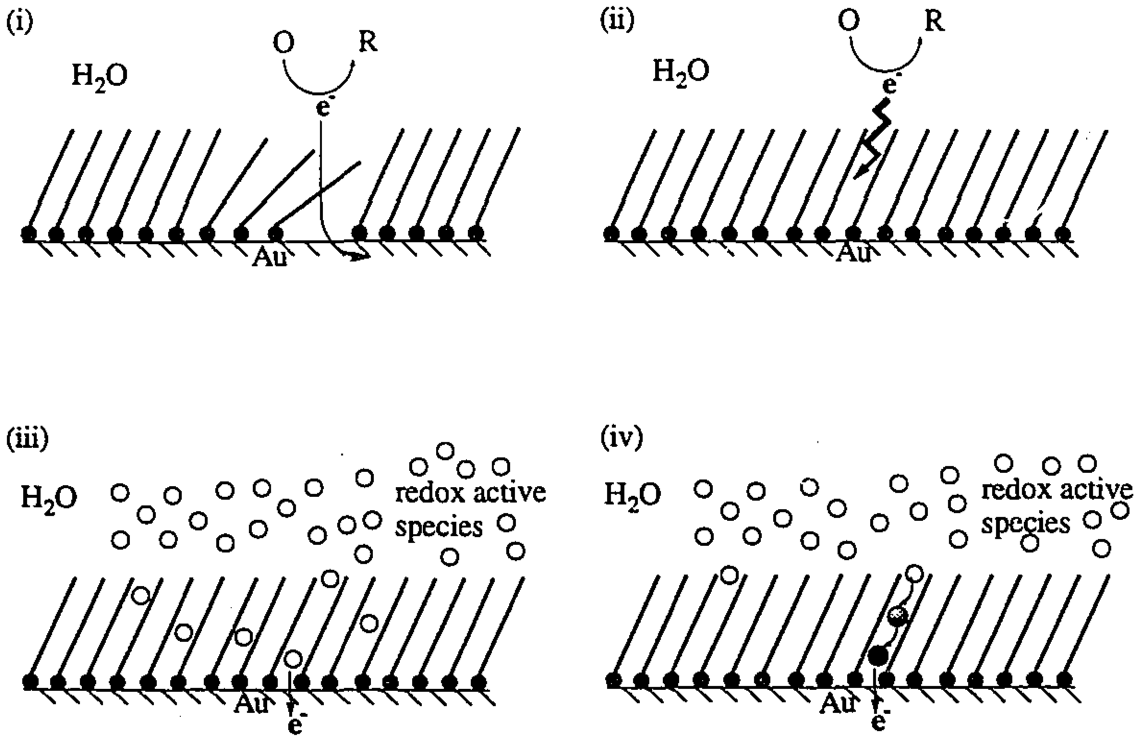

Figure 1.5. Possible mechanisms of electron transfer at RS/Au electrodes: (i) direct electron transfer at pinholes or other film defect sites; (ii) electron tunneling, either through-bond or through-space, across the full width of the film; (iii) permeation of the redox species through the monolayer and reaction at the electrode surface and (iv) redox species mediation wherein the redox couple exists in an number of hydration states that have different $E^{\circ\prime}$ values.

In an early study, Finklea *et al.* investigated the blocking properties of long alkylthiol chains (C_{12}, C_{14}, C_{16}, and C_{18}) self-assembled on gold electrodes (evaporated Au films on glass substrates).[87] They found that the monolayers are stable over a wide potential range in aqueous electrolytes (*i.e.* -0.4 V to +1.4 V *vs.* S.C.E. in 0.5 M H_2SO_4), suppress gold oxidation by 3-5 orders of magnitude, and decrease the electrode/electrolyte capacitance by 20-100 fold. The charging currents of CVs (obtained in 0.5 M H_2SO_4 electrolyte) gave capacitances of 1-5 $\mu F/cm^2$ for the RSH-modified Au electrodes, compared to values greater than 100 $\mu F/cm^2$ for bare Au. If one assumes a parallel-plate capacitor model (*i.e.* an ideal Helmholz model), with the thiol monolayer serving as the dielectric spacer between the metal surface and the electrolyte solution, the capacitance, C_i, is expected to be proportional to the reciprocal of the monolayer thickness[98]:

$$C_i = \varepsilon\varepsilon_0 A/d \qquad (3);$$

where ε is the dielectric constant of the monolayer, ε_0 is the permittivity of free space (8.85×10^{-14} F cm^{-1}), A is the electrode area (cm^2), and d is the monolayer thickness (cm). However, no such correlation was observed between the measured capacitances of C_{12}, C_{14}, C_{16}, and C_{18} thiol-modified Au electrodes and the ellipsometric film thicknesses.[87]

Greatly reduced Faradaic currents were reported for $Fe^{2+/3+}$, $Fe(CN)_6^{3-/4-}$, and $Ru(NH_3)_6^{2+/3+}$ in aqueous electrolyte solution with no visible depletion of the redox species at the electrode surface.[87] More importantly, curved linear free energy relationships or Tafel plots (*i.e.* log of current (log *i*) *vs.* applied potential (*E*)) were observed with a tendency toward lower slopes at larger overpotentials. These curved Tafel plots did not arise from potential-induced changes in the monolayer structure. It is significant that the monolayers did not retain their blocking capacity to ferrocene oxidation/reduction in acetonitrile. CVs of bare and RS/Au electrodes show identical peak currents and potentials in this case. Solvation of the alkyl chains in organic solvent apparently renders the monolayer permeable to ferrocene.[87]

The Tafel plot curvature led Finklea and co-workers to conclude that electron transfer at RSH-coated Au electrodes cannot be described by a single transfer rate coefficient and rate constant.[87] The observed low Tafel slopes and the absence of limiting currents at large overpotentials (η = 0.2V - 0.6 V) in both the anodic (oxidation) and cathodic (reduction) segments are inconsistent with direct electron transfer at pinholes or other defect sites. Non-linear Tafel plots can originate from an electron tunneling formalism. Classic studies of long-range electron transfer between donor/acceptor pairs, separated by rigid hydrocarbon spacers of known length, showed that electrons use the orbitals (π, π^*, σ, σ^* etc.) of the intervening spacer molecule to tunnel or migrate between the donor and acceptor groups (*i.e.* through-bond coupling).[99-105] Furthermore, theories for tunneling at oxide-covered electrodes predict a linear relationship between the tunneling barrier thickness and the log of the kinetic current at a given overpotential.[106-109] However, no such dependence was found between log *i* (at η= +0.5 V) and the measured film thicknesses for the $Fe(CN)_6^{3-/4-}$ and $Fe^{2+/3+}$ redox couples. Thus, the observed Faradaic currents could not be entirely due to electron tunneling across the full monolayer width. Instead, Finklea *et al.* postulated that the Faradaic currents observed at RS/Au electrodes is composed of electron transfer at defect sites at low overpotentials and electron tunneling through thin film patches at large overpotentials.[87]

Sabatini and Rubinstein attempted to model the defect sites present in thiol monolayers as an array of ultramicroelectrodes.[71-74] With fractional thiol surface coverages (θ) close to one, the remaining bare electrode surface can be treated as an array of nanometer-size ultramicroelectrodes. The density, size, and average spacing of the defect sites is calculated using peak current-potential sweep rate data from CVs obtained in aqueous solutions of the redox species according to the Amatore-Saveant-Tessier (A-S-T) theory for ultramicroelectrodes.[110] This approach is limited to monolayer-insoluble redox probes and makes several assumptions about the distribution and shape of the defect sites in the monolayer. For instance, a small number of defects spaced sufficiently far apart are expected to act as individual electrodes resulting in radial diffusion of the redox probe to the defect sites. This results in *i-E* voltammograms which exhibit limiting current plateaus (Figure 1.6B). By contrast, a large number of defects spaced close together act as electroactive sites with overlapping diffusion layers. This results in linear diffusion of the redox probe to monolayer defect sites and a CV which is similar in shape to that obtained with a bare electrode (Figure 1.6C).

When the film coverage is very close to unity, the A-S-T theory[110] predicts a CV shape with a limiting current plateau which does not vary with the scan rate (Figure 1.6B, i). In this case, the plateau current height (i_{lim}) is related to the fractional film coverage (θ) and to the center-to-center inter-microelectrode spacing ($2R_O$) through:

$$2R_0 f(1-\theta) = FAC_0D/i_{\text{lim}} \qquad (4)$$

and $$f(1-\theta) = 0.3/(1-\theta)^{1/2} \qquad \text{(for disk-shaped microelectrodes)} \qquad (5);$$

where D is the redox probe diffusion coefficient, C_0 is the bulk redox probe concentration, F is Faraday's constant, A is the electrode area, and $(1-\theta)$ is the total fractional pinhole area. If the current plateau occurs at an overpotential (Figure 6B, ii), an additional relationship can be derived between the inter-microelectrode spacing ($2R_0$) and the fractional film coverage (θ) from the measurement of the half-wave potential ($E_{1/2}$):

$$2R_0(1-\theta)f(1-\theta) = (D/k_{\text{app}})\exp[(\alpha F/RT)(E_{1/2}-E^{o})] \qquad (6);$$

where the standard rate constant k_{app}, transfer coefficient α, and standard potential E^{o} refer to values at a bare electrode, and T is the absolute temperature. When θ and R_0 are known, the average microelectrode diameter (R_a) can be estimated using:

$$R_a = R_0\,(1-\theta)^{1/2} \qquad \text{(for disk-shaped microelectrodes)} \qquad (7).$$

In the case where the fractional film coverage is not very close to one, the average distance between the pinholes is small compared to the diffusion layer thickness. As mentioned above, this results in a CV shape characteristic of linear diffusion (Fig. 6C). According to the A-S-T theory, one can estimate the microelectrode diameter, R_a, and the average inter-microelectrode spacing, $2R_0$, by increasing the potential sweep rate, v, until a transition from linear diffusion behavior to radial diffusion behavior is observed.[110] The scan rate, v_{max}, corresponding to the transition is then related to R_0 according to the relationship:

$$R_0 \approx (DRT/Fv_{max})/\ 14.8f(1-\theta) \qquad (8).$$

Again, by modeling the monolayer defect sites as disk-shaped microelectrodes, R_a is related to θ and R_0 through equations (5) and (7).[110]

Theoretical analyses of the CV shapes of thiol-modified electrodes with fractional surface coverages of > 0.9 have estimated pinhole diameters of *ca.* 0.2-20 μm and average spacings of 1-100 μm.[44,71,72] Majda and co-workers[111] and Chailapakul and Crooks[112,113] have also used the A-S-T theory to characterize the molecular size defects or pores created by the incorporation of "gating" molecules into the passivating thiol monolayer. They have reported pore radii of 0.5 nm - 0.8 nm and a pore number density of *ca.* 10^6-10^9/cm^2.

Finally, it is appropriate to note that the rate equations derived in the A-S-T theory are formally identical to an entirely different class of mechanism.[110] The authors of this theory point out that both CE (a chemical reaction followed by an electrochemical reaction) and EC (an electrochemical reaction followed by a chemical reaction) electrode mechanisms yield the same form of equations, when surface film coverage terms are replaced by kinetics terms.[110] The implications of this equivalence are important, given that a good fit of *i*/*E* curves to A-S-T theory has been used as evidence for microscopic pore defects or channels in RS/Au SAMs.[41,71,72,111-113] Prior rate limiting chemistry, as in the CE case, must also be considered as being viable unless shown otherwise.

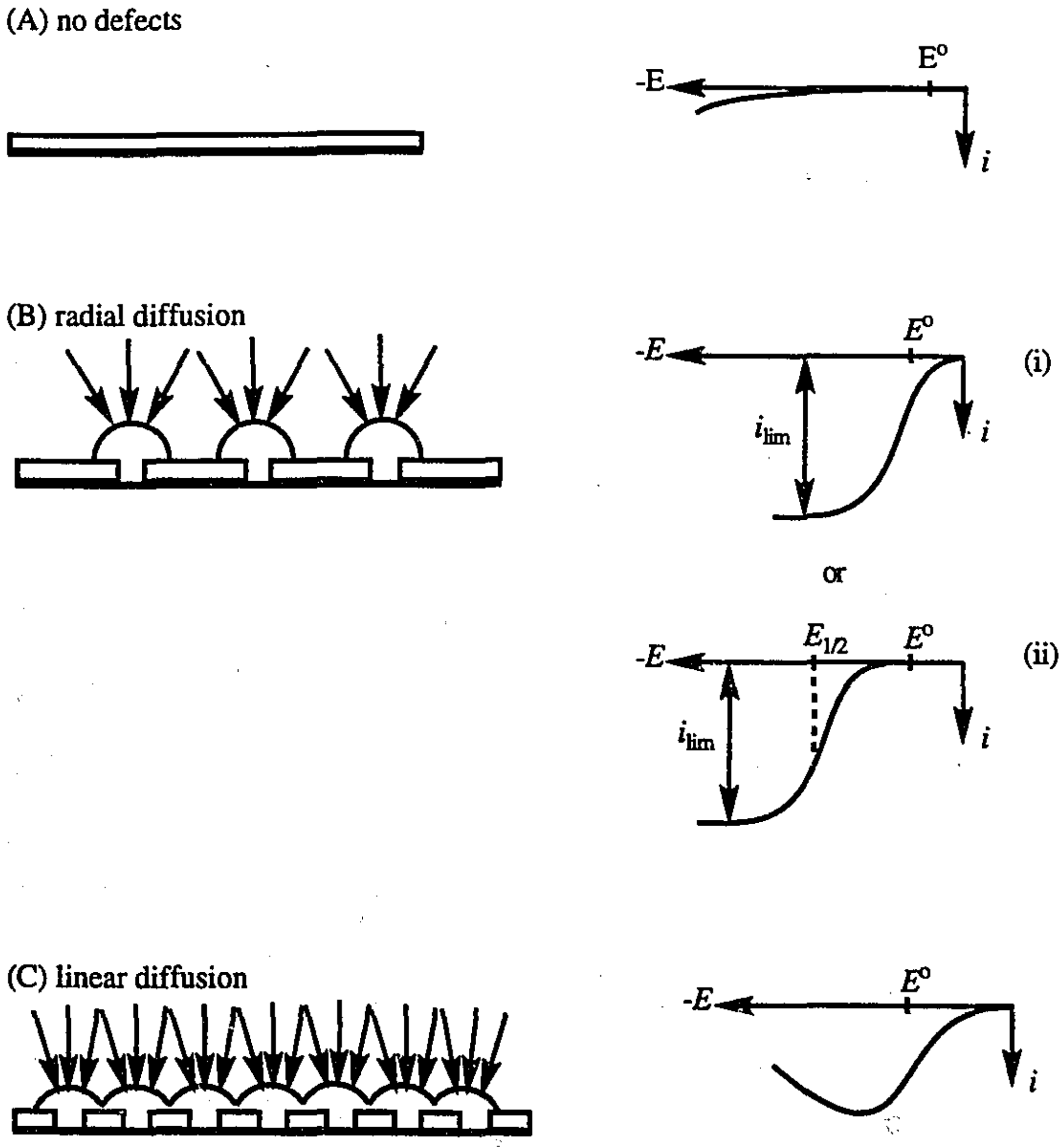

Figure 1.6. Cyclic voltammogram shapes (*i vs. E*) predicted by treating monolayer defect sites as arrays of ultramicroelectrodes according to the Amatore-Saveant-Tessier theory[110]. The schematic is modeled after one presented by Crooks *et al.*[112,113].

Porter and Allara, on the other hand, claim that the long chain alkylthiol monolayers prepared by their group are well ordered and free of measurable pinholes.[44] The capacitive currents for C_{16}, C_{18}, and C_{22} are a factor of 100 less than that at bare Au. A plot of the reciprocal capacitance *vs.* the carbon chain length for C_{10}-C_{22} followed a linear relationship and a dielectric constant of 2.6 (similar to the polyethylene value of 2.3) was calculated from the data. The capacitance data thus suggests that the monolayer behaves as a dielectric medium of a certain thickness. Furthermore, as the chain length increases, the blocking capacity of the monolayer to heterogeneous electron transfer increases. For a $C_{18}S$/Au monolayer, the $Fe(CN_6)^{3-}$ reduction current is reduced by $>10^4$ at the $E^{\circ\prime}$ (*ca.* 0.29 V *vs.* Ag/AgCl) compared to bare Au. More specifically, at the C_{18} chain length, the measured current is largely capacitive, with only a small contribution from Faradaic processes. The data indicate that the $Fe(CN_6)^{3-}$ reduction is kinetically limited. Porter and Allara conclude electron transfer proceeds through thin patches in the monolayer where electron tunneling is more probable.[44] The significant variability observed in the reduction currents from one sample preparation to another did not allow for a more extensive treatment of the data.[44]

Miller *et al.* investigated the heterogeneous electron transfer properties of pinhole-free monolayers of ω-hydroxyl alkylthiols on Au evaporated film electrodes.[81-83] As in the *n*-alkylthiol monolayers studied by Porter and Allara[44], a linear relationship was observed between the reciprocal capacitance and the alkyl chain length for C_2-C_{16}. A dielectric constant of 3.0 was calculated from the slope of the plot of reciprocal capacitance *vs.* monolayer thickness. As reported by Finklea *et al.*[87] curved Tafel plots were observed for the $Fe(CN)_6^{3-/4-}$ and $Fe^{2+/3+}$ redox couples. The rate of electron transfer was found to be the rate-limiting step in the overall electrode reaction. Unlike Finklea[87] however, Miller observed a logarithmic dependence of the heterogeneous electron-transfer rate constants on the monolayer film thickness for the reduction of $Fe(CN)_6^{3-}$ and Fe^{3+}. Miller reasoned that if electron tunneling across the full monolayer width is the dominant electron transfer mechanism, the Faradaic current (i) at a given overpotential should decrease exponentially with the monolayer thickness according to the expression:

$$i = i_0 e^{-\beta d} \qquad (9)$$

$$\ln i = \ln i_0 - \beta d \qquad (10);$$

where i_0 is the current measured at a bare electrode, d is the monolayer film thickness (Å), and β is the electron tunneling constant (Å^{-1}).[81-83] A linear plot of ln i *vs.* d gives a slope whose value is β. If one assumes a rectangular barrier, β gives a measure of the barrier height, V, through the equation[81-83]:

$$\beta = 1.025 V^{1/2} \qquad (11).$$

After correcting the CVs for diffusion limitation, a β of 1.08 ± 0.20 per methylene unit (0.83 ± 0.15 $Å^{-1}$) was calculated which was found to be independent of the redox couple and nearly independent of the electrode potential.[81,83] Following the example of Miller, Xu *et al.* measured an electronic tunneling coefficient of 1.02 ± 0.20 per methylene unit (0.82 ± 0.16 $Å^{-1}$) in long-chain *n*-alkylthiol SAMs with the $Fe(CN)_6^{3-/4-}$ and $Fe^{2+/3+}$ redox couples.[79]

Several electrochemical studies of RS/Au SAMs formed from terminally substituted RSHs (*eg.* -OH, -COOH, $-NH_2$, $-N(CH_3)_3^+$) have, however, definitively shown that the monolayer surface charge and hydrophobicity/hydrophilicity have a dramatic effect on the double layer capacitance [114,115] and the electron transfer rates associated with water-soluble redox couples[75,78,80,85]. For example, the voltammetric response of $Fe(CN)_6^{3-}$ was observed to decrease in the order NH_2 » OH > COOH for C_{11} ω-substituted RS/Au monolayers (Figure 1.7A).[78] By contrast, the $Ru(NH_3)_6^{3+}$ reduction rate increased in the order NH_2 < OH < COOH (Figure 1.7B).[78] Likewise, Doblhofer and co-workers report that $Au/S(CH_2)_{11}N(CH_3)_3^{3+}$ monolayers do not block $Fe(CN)_6^{3-}$ reduction but significantly reduce the $Ru(NH_3)_6^{3+}$ reduction rate.[85] In fact, Miller himself recently stated that although electron transfer proceeds through the entire thickness of the monolayer, the electron transfer rates are largely determined by preconcentration or permeability factors.[80] It is this type of contradiction which requires a more careful evaluation of the mechanism of electron transfer across thin film barriers. The redox species is concentrated (or depleted) at the electrode surface *via* electrostatic interaction between charged ω−substituents and the ionic redox complexes.[78,85] Hydrophobic/hydrophilic interactions between the monolayer surface and the solvated redox species are also affected by the change in the overall dipole moment of the monolayer assembly, even if the ω–substituent is an uncharged species.[80,114,115] These results clearly point to the importance of the redox species' solvation and charge on the permeation and facility of electron transfer at RS/Au monolayers.

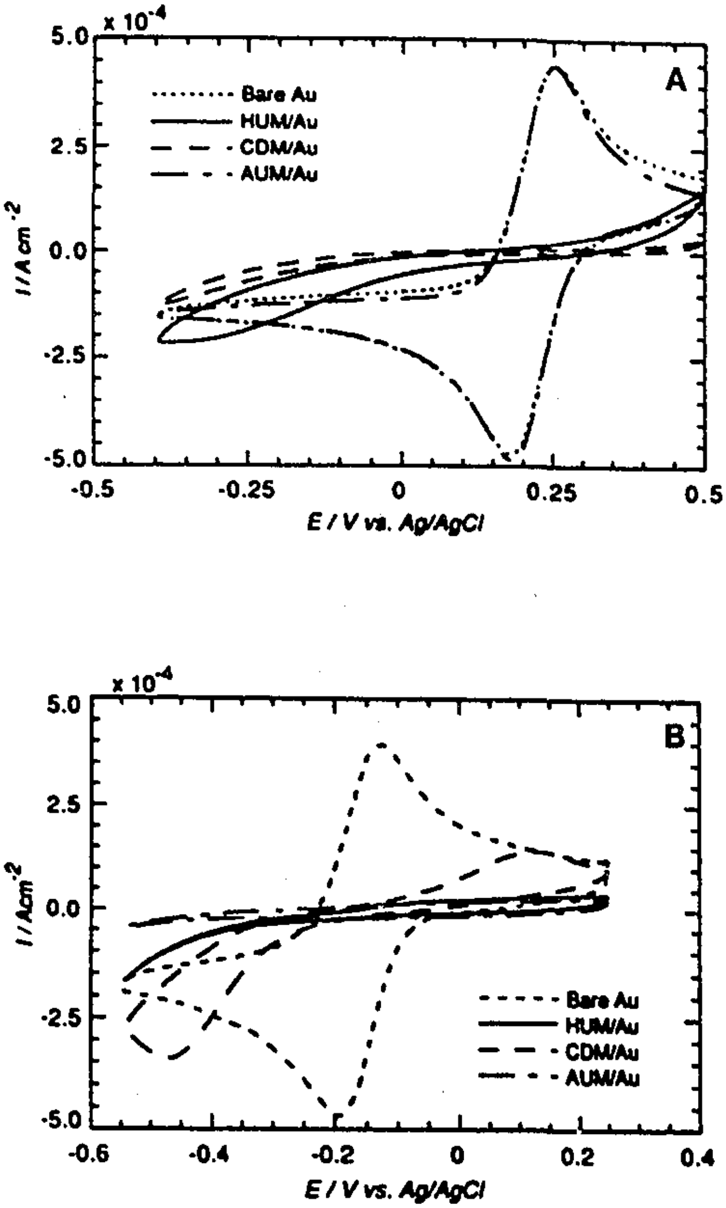

Figure 1.7. Stationary-state CVs obtained with bare Au and **X-(CH_2)$_{10}$SH-modified** Au electrodes where X = CH_2OH for **HUM**, X = COOH for **CDM**, and X = CH_2NH_2 for **AUM**. CVs have been reprinted from reference 78, Copyright (1994) with kind permission from Elsevier Science Ltd., The Boulevard, Langford Lane, Kidlington 0X5 1GB, UK. (A) 2 mM $K_3Fe(CN)_6$, 0.2 M KCl aqueous solution at pH 5.8. Scan rate is 100 mVs^{-1}. (B) 2 mM $Ru(NH_3)_6Cl_3$, 0.2 M KCl aqueous solution at pH 5.2. Scan rate is 100 mVs^{-1}.

1.7. Thiol-Derivatized Gold Nanoparticles

A novel surfactant-mediated synthesis of gold colloids was recently reported by Brust and co-workers.[116] This system is particularly interesting given that the surfactant used, dodecanethiol, is well-known to form SAMs on planar gold surfaces as discussed above. The thiol-coated nanoparticles are synthesized using a two-phase (toluene/water) synthesis and tetraoctylammonium bromide as the phase transfer reagent. Briefly, $Au(III)Cl_4^-$ is transferred to the toluene layer from the water layer, and then reduced by sodium borohydride in the presence of thiol surfactant at the toluene/water interface:

$$AuCl_4^- \text{ (aq)} + (C_8H_{17})_4N^+ \text{ (toluene)} \rightarrow (C_8H_{17})_4N^+AuCl_4^- \text{ (toluene)} \qquad (12)$$

$$x AuCl_4^- \text{ (toluene)} + y C_nH_{2n+1}SH \text{ (toluene)} + 3xe^- \rightarrow (Au_x)(C_nH_{2n+1}SH)_y \text{(toluene)} + 4xCl^- \text{ (aq)} \qquad (13).$$

The thiol surfactant adsorbs onto the growing metallic cluster until complete surface coverage prevents further cluster growth. Leff *et al.* have further demonstrated the control of particle size (from 1.5 nm to 20 nm diameter) by varying the gold-to-thiol ratio and applied a model in which the role of the thiol is analogous to that of the surfactant in water-in-oil microemulsions.[117] These thiol-derivatized Au nanoparticles are air-stable and soluble in chloroform, toluene, hexanes, and other non-polar solvents. The solvent can be evaporated, and the particles can be redissolved in organic solvent without metallization occurring.[116]

The large surface area of these nanoparticles (*i.e. ca.* 100 m^2/g) makes the self-assembled thiol monolayer amenable to structural characterization by techniques conventionally used for bulk materials, such as NMR spectroscopy, transmission FT-IR spectroscopy, and differential scanning calorimetry. All these techniques are particularly powerful in terms of defining the state of chain organization in self-assembled systems such as lipid membranes and micelles.

1.8. The Present Work

Although the structural and barrier properties of alkylthiol monolayers on gold have been intensively studied, a molecular level understanding of the structure/property/activity relationships of these 2D organized assemblies is relatively limited. More importantly, the manner in which temperature affects these relationships remains substantially unresolved.

If RS/Au SAMs are to be ultimately used for novel technological applications, their structural integrity must be thoroughly characterized, in both kinetic and thermodynamic terms. We are particularly concerned with how restricted chain motion, due to strong pinning of the sulfur headgroup to the metal surface, affects long and short-range ordering of the alkyl chains, surface reorganization processes, and order-disorder phase transitions. It is therefore the aim of this thesis to address the phase properties of self-assembled alkylthiol/Au monolayers through (i) the interfacial electron transfer process at classical planar surfaces and (ii) the structure and dynamical behavior of thiol-derivatized Au nanoparticles.

The thesis is divided into six chapters:

Chapter One presents a general introduction to self-assembled alkylthiol monolayers on gold surfaces. The introduction of each subsequent chapter specifically addresses the topics covered in that chapter.

Chapter Two demonstrates the potential of the heterogeneous electron transfer process as a probe of the phase properties of RS/Au SAMs. Preliminary results are presented in the context of gel-to-liquid crystalline phase transitions in organized lipid bilayers.

Chapter Three presents an extensive electrochemical investigation of the thermally-induced changes in RS/Au SAMs. The electron transfer mechanism across the monolayer film is discussed in light of the results.

In Chapter Four, the film structure and thermal properties of RSH-derivatized Au nanoparticles are addressed through ^{1}H and ^{13}C NMR spectroscopy, transmission infrared spectroscopy, transmission electron microscopy, and differential scanning calorimetry. The chain packing structure and thermotropic behavior of these alkylated nanoparticles are compared to those of planar SAMs.

In Chapter Five, the chain order and dynamics of SAMs on Au nanoparticles are examined using solid-state deuterium NMR spectroscopy, transmission infrared spectroscopy, and differential scanning calorimetry. The nanoparticles have been derivatized with perdeuterated and specifically deuterated octadecanethiols.

Chapter Six is an overview of the conclusions which can be drawn from the work presented in the thesis. The present findings are discussed in the context of previous knowledge. The significant contributions made to original research are noted and suggestions for future work are proposed.

Appendix A contains the journal reprints of publications co-authored by the author. The results of these studies are not discussed in the main body of the thesis but provide important insights into the present research and are valuable adjuncts to the work presented in Chapters 2-5. These papers include "***Structure and Chain Dynamics of Alkanethiol-Capped Gold Colloids***", *Langmuir* **1996**, *12*, 1262-1269 and "***Probing the Different Phases of Self-Assembled Monolayers on Metal Surfaces: Temperature Dependence of the C-H Stretching Modes***", *J. Vac. Sci. Technol. A* **1995**, *13*, 1331-1336.

References

(1) Swalen, J. D.; Allara, D. L.; Andrade, J. D.; Chandross, E. A.; Garoff, S.; Israelachvili, J.; McCarthy, T. J.; Murray, R.; Pease, R. F.; Rabolt, J. F.; Wynne, J.; Yu, H. *Langmuir* **1987**, *3*, 932-950.

(2) Ulman, A. *An Introduction to Ultrathin Organic Films From Langmuir-Blodgett to Self-Assembly*; Academic Press, Inc.: San Diego, CA, 1991.

(3) Whitesides, G. M. *Sci. Am.* **9/95**, 146-149.

(4) Bishop, A. R.; Nuzzo, R. G. *Current Opinion in Colloid & Interface Science* **1996**, *1*, 127-136.

(5) Ulman, A. *Chem. Tech.* **3/95**, 22-28.

(6) Ulman, A. *MRS Bulletin* **6/95**, 46-51.

(7) Xu, J.; Li, H. *Journal of Colloid and Interface Science* **1995**, *176*, 138-149.

(8) Dubois, L. H.; Nuzzo, R. G. *Annu. Rev. Phys. Chem.* **1992**, *43*, 437-463.

(9) Whitesides, G. M.; Laibinis, P. E. *Langmuir* **1990**, *6*, 87-96.

(10) Bain, C. D.; Whitesides, G. M. *Angew. Chem. Int. Ed. Engl.* **1989**, *28*, 506-512.

(11) Mandler, D.; Turyan, I. *Electroanalysis* **1996**, *8*, 207-213.

(12) Bain, C. D.; Troughton, E. B.; Tao, Y.-T.; Evall, J.; Whitesides, G. M.; Nuzzo, R. G. *J. Am. Chem. Soc.* **1989**, *111*, 321-335.

(13) Nuzzo, R. G.; Fusco, F. A.; Allara, D. L. *J. Am. Chem. Soc.* **1987**, *109*, 2358-2368.

(14) Nuzzo, R. G.; Allara, D. L. *J. Am. Chem. Soc.* **1983**, *105*, 4481-4483.

(15) Dubois, L. H.; Zegarski, B. R.; Nuzzo, R. G. *J. Chem. Phys.* **1993**, *98*, 678.

(16) Camillone, N.; Eisenberger, P.; Leung, T. Y. B.; Schwartz, P.; Scoles, G.; Poirier, G. E.; Tarlov, M. J. *J. Chem. Phys.* **1994**, *101*, 11031-11036.

(17) Demoz, A.; Harrison, D. J. *Langmuir* **1993**, *9*, 1046-1050.

(18) Weisshaar, D. E.; Lamp, B. D.; Porter, M. D. *J. Am. Chem. Soc.* **1992**, *114*, 5860-5862.

(19) Camillone, N.; Chidsey, C. E. D.; Liu, G.; Scoles, G. *J. Chem. Phys.* **1993**, *98*, 4234-4245.

(20) Edinger, K.; Golzhauser, A.; Demota, K.; Woll, C.; Grunze, M. *Langmuir* **1993**, *9*, 4-8.

(21) Buck, M.; Eisert, F.; Fischer, J.; Grunze, M.; Trager, F. *Appl. Phys. A* **1991**, *53*, 552.

(22) Hahner, G.; Woll, C.; Buck, M.; Grunze, M. *Langmuir* **1993**, *9*, 1955-1958.

(23) Poirier, G. E.; Pylant, E. D. *Science* **1996**, *272*, 1145-1148.

(24) Schneider, T. W.; Buttry, D. A. *J. Am. Chem. Soc.* **1993**, *115*, 12391-12397.

(25) Schlenoff, J. B.; Li, M.; Ly, H. *J. Am. Chem. Soc.* **1995**, *117*, 12528-12536.

(26) Schonenberger, C.; Jorritsma, J.; Sondag-Huethorst, J. A. M.; Fokkink, L. G. J. *J. Phys. Chem.* **1995**, *99*, 3259-3271.

(27) Rohwerder, M.; de Weldige, K.; Vago, E.; Viefhaus, H.; Stratmann, M. *Thin Solid Films* **1995**, *264*, 240-245.

(28) Poirier, G. E.; Tarlov, M. J. *J. Phys. Chem.* **1995**, *99*, 10966-10970.

(29) Poirier, G. E.; Tarlov, M. J. *Langmuir* **1994**, *10*, 2853-2856.

(30) Poirier, G. E.; Tarlov, M. J.; Rushmeier, H. E. *Langmuir* **1994**, *10*, 3383-3386.

(31) Liu, G.-y.; Salmeron, M. B. *Langmuir* **1994**, *10*, 367-370.

(32) Bucher, J. P.; Santesson, L.; Kern, K. *Langmuir* **1994**, *10*, 979-983.

(33) Schonenberger, C.; Sondag-Huethorst, J. A. M.; Jorritsma, J.; Fokkink, L. G. J. *Langmuir* **1994**, *10*, 611-614.

(34) Stranick, S. J.; Parikh, A. N.; Allara, D. L.; Weiss, P. S. *J. Phys. Chem.* **1994**, *98*, 11136-11142.

(35) Delamarche, E.; Michel, B.; Gerber, C.; Anselmetti, D.; Guntherodt, H.-J.; Wolf, H.; Ringsdorf, H. *Langmuir* **1994**, *10*, 2869-2871.

(36) Salmeron, M.; Neubauer, G.; Folch, A.; Tomitori, M.; Ogletree, D. F.; Sautet, P. *Langmuir* **1993**, *9*, 3600-3611.

(37) Alves, C. A.; Porter, M. D. *Langmuir* **1993**, *9*, 3507-3512.

(38) Durig, U.; Zuger, O.; Michel, B.; Haussling, L.; Ringsdorf, H. *Physical Review B* **1993**, *48*, 1711-1717.

(39) Schott, J. H.; White, H. S. *Langmuir* **1993**, *9*, 3471-3477.

(40) Kim, Y.-T.; McCarley, R. L.; Bard, A. J. *J. Phys. Chem.* **1992**, *96*, 7416-7421.

(41) Widrig, C. A.; Alves, C. A.; Porter, M. D. *J. Am. Chem. Soc.* **1991**, *113*, 2805-2810.

(42) Sun, L.; Crooks, R. M. *J. Electrochem. Soc.* **1991**, *138*, L23-L25.

(43) Nuzzo, R. G.; Dubois, L. H.; Allara, D. L. *J. Am. Chem. Soc.* **1990**, *112*, 558-569.

(44) Porter, M. D.; Bright, T. B.; Allara, D. L.; Chidsey, C. E. D. *J. Am. Chem. Soc.* **1987**, *109*, 3559-3568.

(45) Sandroff, C. J.; Herschbach, D. R. *J. Phys. Chem.* **1982**, *86*, 3277-3279.

(46) Garrell, R. L.; Chadwick, J. E.; Severance, D. L.; McDonald, N. A.; Myles, D. C. *J. Am. Chem. Soc.* **1995**, *117*, 11563-11571.

(47) Bryant, M. E.; Pemberton, J. E. *J. Am. Chem. Soc.* **1991**, *113*, 8284-8293.

(48) Laibinis, P. E.; Whitesides, G. M.; Allara, D. L.; Tao, Y.-T.; Parikh, A. N.; Nuzzo, R. G. *J. Am. Chem. Soc.* **1991**, *113*, 7152.

(49) Bain, C. D.; Biebuyck, H. A.; Whitesides, G. M. *Langmuir* **1989**, *5*, 723.

(50) Nuzzo, R. G.; Zegarski, B. R.; Dubois, L. H. *J. Am. Chem. Soc.* **1987**, *109*, 733-740.

(51) Widrig, C. A.; Chung, C.; Porter, M. D. *J. Electroanal. Chem.* **1991**, *310*, 335-359.

(52) Hagenhoff, B.; Benninghoven, A.; Spinke, J.; Liley, M.; Knoll, W. *Langmuir* **1993**, *9*, 1622-1624.

(53) Li, Y.; Huang, J.; McIver Jr., R. T.; Hemminger, J. C. *J. Am. Chem. Soc.* **1992**, *114*, 2428-2432.

(54) Fenter, P.; Eisenberger, P.; Liang, K. S. *Phys. Rev. Lett.* **1993**, *70*, 2447-2450.

(55) Camillone, N.; C.E.D., C.; Liu, G.; Scoles, G. *J. Chem. Phys.* **1993**, *98*, 3503-3511.

(56) Strong, L.; Whitesides, G. M. *Langmuir* **1988**, *4*, 546-558.

(57) Shnidman, Y.; Ulman, A.; Eilers, J. E. *Langmuir* **1993**, *9*, 1071-1081.

(58) Li, J.; Liang, K. S.; Camillone, N.; Leung, T. Y. B.; Scoles, G. *J. Chem. Phys.* **1995**, *102*, 5012-5028.

(59) Fenter, P.; Eberhardt, A.; Eisenberger, P. *Science* **1994**, *266*, 1216-1218.

(60) Synder, R. G.; Maroncelli, M.; Strauss, H. L.; Hallmark, V. M. *J. Phys. Chem.* **1986**, *90*, 5623-5630.

(61) Synder, R. G.; Strauss, H. L.; Elliger, C. A. *J. Phys. Chem.* **1982**, *86*, 5145-5150.

(62) Camillone, N.; Chidsey, C. E. D.; Liu, G.; Putvinski, T. M.; Scoles, G. *J. Chem. Phys.* **1991**, *94*, 8493-8502.

(63) Chidsey, C. E. D.; Liu, G.; Rowntree, P.; Scoles, G. *J. Chem. Phys.* **1989**, *91*, 4421-4423.

(64) Dubois, L. H.; Zegarski, B. R.; Nuzzo, R. G. *J. Electron Spectrosc. Relat. Phenom.* **1990**, *54/55*, 1143.

(65) Hautman, J.; Bareman, J. P.; Mar, W.; Klein, M. L. *J. Chem. Soc. Faraday Trans.* **1991**, *87*, 2031-2037.

(66) Mar, W.; Klein, M. L. *Langmuir* **1994**, *10*, 188-196.

(67) Hautman, J.; Klein, M. L. *J. Chem. Phys.* **1990**, *93*, 7483-7492.

(68) Nuzzo, R. G.; Korenic, E. M.; Dubois, L. H. *J. Chem. Phys.* **1990**, *93*, 767-773.

(69) Evans, S. E.; Sharma, R.; Ulman, A. *Langmuir* **1991**, *7*, 156-161.

(70) Ulman, A. *Adv. Mater.* **1991**, *3*, 298-303.

(71) Finklea, H. O.; Snider, D. A.; Fedyk, J.; Sabatini, E.; Gafni, Y.; Rubinstein, I. *Langmuir* **1993**, *9*, 3660-3667.

(72) Finklea, H. O.; Snider, D. A.; Fedyk, J. *Langmuir* **1990**, *6*, 371-376.

(73) Sabatani, E.; Rubinstein, I.; Maoz, R.; Sagiv, J. *J. Electroanal. Chem.* **1987**, *219*, 365-371.

(74) Sabatani, E.; Rubinstein, I. *J. Phys. Chem.* **1987**, *91*, 6663-6669.

(75) Chidsey, C. E. D.; Loiacono, D. N. *Langmuir* **1990**, *6*, 682-691.

(76) deRege, P., personal communication.

(77) Slowinski, K.; Chamberlain II, R. V.; Bilewicz, R.; Majda, M. *J. Am. Chem. Soc.* **1996**, *118*, 4709-4710.

(78) Takehara, K.; Takemura, H.; Ide, Y. *Electrochimica Acta* **1994**, *39*, 817-822.

(79) Xu, J.; Li, H.; Zhang, Y. *J. Phys. Chem.* **1993**, *97*, 11497-11500.

(80) Becka, A. M.; Miller, C. J. *J. Phys. Chem.* **1993**, *97*, 6233-6239.

(81) Becka, A. M.; Miller, C. J. *J. Phys. Chem.* **1992**, *96*, 2657-2668.

(82) Miller, C.; Gratzel, M. *J. Phys. Chem.* **1991**, *95*, 5225-5233.

(83) Miller, C.; Cuendet, P.; Gratzel, M. *J. Phys. Chem.* **1991**, *95*, 877-886.

(84) Creager, S. E.; Hockett, L. A.; Rowe, G. K. *Langmuir* **1992**, *8*, 854-861.

(85) Doblhofer, J.; Figura, J.; Furhop, J.-H. *Langmuir* **1992**, *8*, 1811-1816.

(86) Chidsey, C. E. D.; Bertozzi, C. R.; Putvinski, T. M.; Mujsce, A. M. *J. Am. Chem. Soc.* **1990**, *112*, 4301-4306.

(87) Finklea, H. O.; Avery, S.; Lynch, M. *Langmuir* **1987**, *3*, 409-413.

(88) Finklea, H. O.; Ravenscroft, M. S.; Snider, D. A. *Langmuir* **1993**, *9*, 223-227.

(89) Finklea, H. O.; Hanshew, D. D. *J. Am. Chem. Soc.* **1992**, *114*, 3173-3181.

(90) Chidsey, C. E. D. *Science* **1991**, *251*, 919-922.

(91) Collard, D. M.; Fox, M. A. *Langmuir* **1991**, *7*, 1192-1197.

(92) Rowe, G. K.; Creager, S. E. *Langmuir* **1991**, *7*, 2307-2312.

(93) Hickman, J. J.; Ofer, D.; Zou, C.; Wrighton, M. S.; Laibinis, P. E.; Whitesides, G. M. *J. Am. Chem. Soc.* **1991**, *113*, 1128-1132.

(94) Katz, E.; Itzhak, N.; Willner, I. *Langmuir* **1993**, *9*, 1392-1396.

(95) Creager, S. E.; Collard, D. M.; Foxe, M. A. *Langmuir* **1990**, *6*, 1617-1620.

(96) Li, T. T.-T.; Weaver, M. *J. Am. Chem. Soc.* **1984**, *106*, 6107-6108.

(97) Noftle, R. E.; Pletcher, D. *J. Electroanal. Chem.* **1990**, *293*, 373.

(98) Bard, A. J.; Faulkner, L. R. *Electrochemical Methods: Fundamentals and Applications*; John Wiley & Sons, Inc.: New York, USA, 1980, pp 488-552.

(99) Paddon-Row, M. *Acc. Chem. Res.* **1994**, *27*, 18-25.

(100) Paddon-Row, M. N.; Oliver, A. M.; Warman, J. M.; Smit, K. J.; deHaas, M. P.; Oevering, H.; Verhoeven, J. W. *J. Phys. Chem.* **1988**, *92*, 6958-6962.

(101) Closs, G. L.; Miller, J. R. *Science* **1988**, *240*, 440.

(102) Closs, G. L.; Calcaterra, L. T.; Green, N. J.; Penfield, K. W.; Miller, J. R. *J. Phys. Chem.* **1986**, *90*, 3673-3683.

(103) Beratan, D. N. *J. Am. Chem. Soc.* **1986**, *108*, 4321-4326.

(104) Oevering, H.; Paddon-Row, M. N.; Heppener, M.; Oliver, A. M.; Cotsaris, E.; Verhoeven, J. W.; Hush, N. S. *J. Am. Chem. Soc.* **1987**, *109*, 3258-3269.

(105) Haran, A.; Waldeck, D. H.; Naaman, R.; Moons, E.; Cahen, D. *Science* **1994**, *263*, 948-950.

(106) Schultze, J. W.; Elfenthal, L. *J. Electroanal. Chem.* **1986**, *204*, 153-171.

(107) Ulstrup, J. *Surf. Sci.* **1980**, *101*, 564-582.

(108) Schmickler, W.; Ulstrup, J. *J. Chem. Phys.* **1977**, *19*, 217-232.

(109) Schmickler, W. *J. Electroanal. Chem.* **1977**, *82*, 65-80.

(110) Amatore, C.; Saveant, J. M.; Tessier, D. *J. Electroanal. Chem.* **1983**, *147*, 39-51.

(111) Bilewicz, R.; Sawaguchi, T.; Chamberlain II, R. V.; Majda, M. *Langmuir* **1995**, *11*, 2256-2266.

(112) Chailapakul, O.; Crooks, R. M. *Langmuir* **1995**, *11*, 1329-1340.

(113) Chailapakul, O.; Crooks, R. M. *Langmuir* **1993**, *9*, 884-888.

(114) Sondag-Huethorst, J. A. M.; Fokkink, L. G. J. *Langmuir* **1995**, *11*, 2237-2241.

(115) Swietlow, A.; Skoog, M.; Johansson, G. *Electroanalysis* **1992**, *4*, 921-928.

(116) Brust, M.; Walker, M.; Bethell, D.; Schiffrin, D. J.; Whyman, R. *J. Chem. Soc., Chem. Commun.* **1994**, 801-802.

(117) Leff, D. V.; Ohara, P. C.; Heath, J. R.; Gelbart, W. M. *J. Phys. Chem.* **1995**, *99*, 7036-7041.

Chapter Two

Phase Transitions in Self-Assembled Monolayers Detected by Electrochemistry*

2.1. Introduction

Self-assembled monolayers (SAMs) of *n*-alkylthiols (RSHs) on metals have been used both as models for organic surfaces and as modulators of metal surface properties.[1] These SAMs are prepared under readily accessible laboratory conditions, and the strong interaction between the metal substrate (Au, Pt, Ag, Cu, Hg etc.) and the sulfur atom provides a monolayer film which is sufficiently stable to desorption to allow spectroscopic, diffraction, and electrochemical experiments to be performed with a minimum of precautions.[1] Grazing-angle FT-IR studies and grazing incidence diffraction experiments[2,3] of a typical $n\text{-}C_{18}H_{37}S$ monolayer on a Au(111) surface show that molecular ordering is present.

One key aspect of SAMs which has so far eluded detailed description concerns the question of film thermodynamics and, more specifically, the nature of film phases. A very recent grazing incidence X-ray diffraction study has shown that 2D structural phase transitions may be observable in SAMs.[4] This reveals that, like Langmuir and Langmuir-Blodgett films,[5] SAMs do indeed have a complex phase behaviour. Contact angle/wetting studies hint at rearrangement processes in RS/Au monolayers,[6] while temperature dependent FT-IR studies reveal only gradual changes,[7] and not the discontinuities expected from first-order processes. We have addressed the important problem of phase properties of SAMs by using the electron transfer process between a water-soluble redox species and

---

* This chapter is almost a *verbatim* copy of the text of the paper *Angew. Chem. Int. Ed. Engl.* **1994**, *33*, 2332-2335. Slight modifications have been made for clarity and continuity.

a RSH-modified Au electrode as a *probe* of the monolayer film structure. We have discovered that phase transitions do, in fact, occur and that film preparation protocols play a crucial role in their formation.

2.2. Experimental Section

2.2.1. Materials: *n*-Octadecanethiol ($C_{18}H_{37}SH$; Aldrich, 98%) was triply recrystallized from ethanol. *n*-Hexadecanethiol ($C_{16}H_{33}SH$), heptadecanethiol ($C_{17}H_{35}SH$), nonadecanethiol ($C_{19}H_{39}SH$), and eicosanethiol ($C_{20}H_{41}SH$) were synthesized using standard procedures. Their purity was monitored by ^1H and ^{13}C NMR spectroscopy, thin layer chromatography, mass spectrometry (NH_3, CI), and melting point determination using differential scanning calorimetry (DSC). The melting point measurements by DSC are particularly useful in detecting the presence of trace amounts of homologous hydrocarbons.

2.2.2. RS/Au Electrode Preparation: Bulk polycrystalline Au electrodes (0.020 cm^2 geometric area; BAS, West Lafayette, IN) were mechanically polished (Buehler, Ecomet II polisher) on microcloth pads with alumina (Buehler) slurries of decreasing particle size (1.0, 0.3, and 0.05 μm). The polished electrodes were sonicated in H_2O to remove any residual polishing alumina from the Au surface. The sonicated Au electrodes were then rinsed copiously with H_2O, followed by absolute ethanol, and were immediately immersed in RSH solutions. The Au substrates were incubated in 5 mL, argon-saturated ethanol solutions of the thiol (2-5 mM RSH) in sealed glass vials at 23±2 °C for days to weeks. The RSH-modified electrodes were rinsed copiously with ethanol, followed by H_2O, immediately prior to the electrochemical experiments.

2.2.3. Electrochemical Experiments: The RS/Au working electrode was introduced into a degassed, thermostated (Haake G circulating bath) 150 mL cell containing 0.1 M KBr (Anachemia) electrolyte and 0.020 M $K_3Fe(CN)_6$ (BDH). Deionized H_2O (18 $M\Omega \cdot cm^{-1}$) was obtained from a Milli-Q water system (Millipore; 3 bed ion-exchange/1 bed organic removal cartridge unit) connected to house distilled H_2O. The counter electrode was a Pt wire (Aldrich), and all potentials refer to a Ag/AgCl reference electrode (3 M NaCl; BAS). Currents were obtained from steady-state cyclic voltammograms (BAS 100B electrochemical analyzer) at 20 $mV \cdot s^{-1}$ between +500 mV and -150 mV. Typical heating rates of 0.2 - 0.3 $°C \cdot min^{-1}$ were used for all experiments. The $Fe(CN)_6^{3-}$ reduction current reported at each temperature was measured from the cathodic segment of the cyclic voltammogram at an overpotential $\eta = -250$ mV for $Fe(CN)_6^{3-/4-}$ at that temperature.

2.3. Results and Discussion

Electrochemical thermograms for RS/Au electrodes (R = n-$C_{16}H_{33}$ - n-$C_{20}H_{41}$) were obtained over an approximate temperature range of 10 - 65 °C. Electrodes which exhibit striking discontinuities in the electrochemical thermograms were prepared using a variation on the conventional preparation protocols.[1,8] Specifically, polycrystalline Au electrodes were incubated in thiol solutions for prolonged periods (days to weeks) at 23 ± 2 °C. Conventional protocols usually employ much shorter incubation times (*i.e.* minutes to hours), a variety of heating/annealing procedures, re-immersion in thiol solution after each experiment, or co-surfactants in the thiol solution.[9] One of the most interesting properties of RS monolayers is their ability to attenuate the rate of electron transfer between a water-soluble redox couple and the underlying metal electrode.[2c, 9a-c, 10] The transmonolayer electron transfer mechanism has been studied with several soluble or monolayer-bound redox couples and a variety of electrochemical techniques.[2c, 9, 10, 11] The electrodes discussed here exhibited the characteristics of being thoroughly blocked: reduced capacitance values, greatly attenuated $Fe(CN)_6^{3-}$ reduction currents *cf.* bare Au electrodes, and the absence of features in cyclic voltammograms which are diagnostic of pinholes or bare patches in the films.

The temperature dependence of the ferricyanide reduction current, observed at constant overpotential, for a representative $C_{18}H_{37}S$/Au electrode is shown in Figure 2.1. The reduction of $Fe(CN)_6^{3-}$ at a clean bare electrode increases monotonically with increasing temperature (Figure 2.1), as is expected for an activated process.[12] For each chain length studied, the modified Au electrode, however, exhibits a pronounced current maximum. In all but the C_{19} case, a distinct shoulder on the low temperature side of the maximum is also observed. Clearly, these substantial current changes reflect temperature-induced modification of the SAM as a barrier to electron transfer. Previous studies suggest that an electron tunneling mechanism is overall rate-limiting in the case of well-blocked RS/Au monolayers,[1d, 9a, b, 10d, e, 11f] although some data is also consistent with a permeation mechanism.[9a, 10a, b, e, g, 13] Current derived exclusively from a through-bond tunneling mechanism, for example, should be either temperature independent or should increase with increasing temperature, depending on whether there is an activation component to the electron transfer.[12a] On the other hand, current derived from permeation of the redox couple into the monolayer would exhibit a complex temperature dependence, as it would depend on the relationship between film structure, the solvent-monolayer partition coefficient, the diffusion coefficient of the redox couple in the monolayer, and interfacial resistances. The data in Figure 2.1 is clearly inconsistent with tunneling, but is qualitatively consistent with a complex permeability-linked process.

Our experiments with SAMs prepared under prolonged incubation conditions exhibit striking parallels to the temperature-dependent permeability profiles of phosphatidylcholine lipid vesicles to Na^+, K^+, H_2O.[14] Bilayer lipid vesicles have been extensively characterized by calorimetric and spectroscopic techniques and are known to undergo a series of phase transitions, the two most prominent being a gel-to-liquid crystalline transition (at $T = T_m$) and an untilting/rippling transition (at $T = T_p$).[15] This untilting transition precedes T_m by 3 - 6 °C, depending on the alkyl chain length. Large anomalous increases in transmembrane permeability are observed at $T_m \pm 5$ °C.[14] These large current fluxes are attributable to transient dislocations or grain boundaries found at the interface between domains of the coexisting gel and liquid crystalline phases. These boundaries provide a low energy barrier to ion and solute diffusion across the membrane. Recent theoretical studies support this experimentally-based description.[16] The current maxima described here are thus believed to arise from regions of facilitated diffusion in the monolayer where there are coexistence boundaries between ordered and disordered alkyl chain domains (Scheme 2.1). It is interesting to note that evidence for electron tunneling in the well-studied lipid vesicle systems is decidedly lacking and that permeation processes are in fact responsible for current generation in these systems.[17]

The temperatures at which the current maxima and shoulders (which we designate as $T_m{}^e$ and $T_p{}^e$, respectively) are observed in the electrochemical thermograms correlate with T_m (1:1) values (measured by calorimetry) of *n*-diacylphosphatidylcholines of equivalent chain length (Figure 2.2A).[15] This correlation arises because the underlying Au substrate dictates that the RS chain packing configuration and density are very similar in the two cases. The underpotential deposition of Pb[10c] establishes our bulk Au electrodes to be 70% Au(110) and 30% Au(111), so that the areas occupied per unit cell (*i.e.* 2 RS chains) are 46.9 $Å^2$ and 43.5 $Å^2$,[3c] respectively. *n*-Diacylphosphatidylcholines, by comparison, occupy 43 - 48 $Å^2$ in their condensed phase.[15] Clearly, the phosphatidylcholine headgroup and the Au lattice serve the same purpose - to enforce a defined packing density on the alkyl chains. The chains in a RS/Au(100) monolayer have an 18% greater surface packing density.[3c] Since phosphatidylethanolamine lipids are packed tighter and have higher T_ms than phosphatidylcholines, we expect a RS/Au(100) monolayer to exhibit higher $T_m{}^e$s than those shown in Figure 2.2.

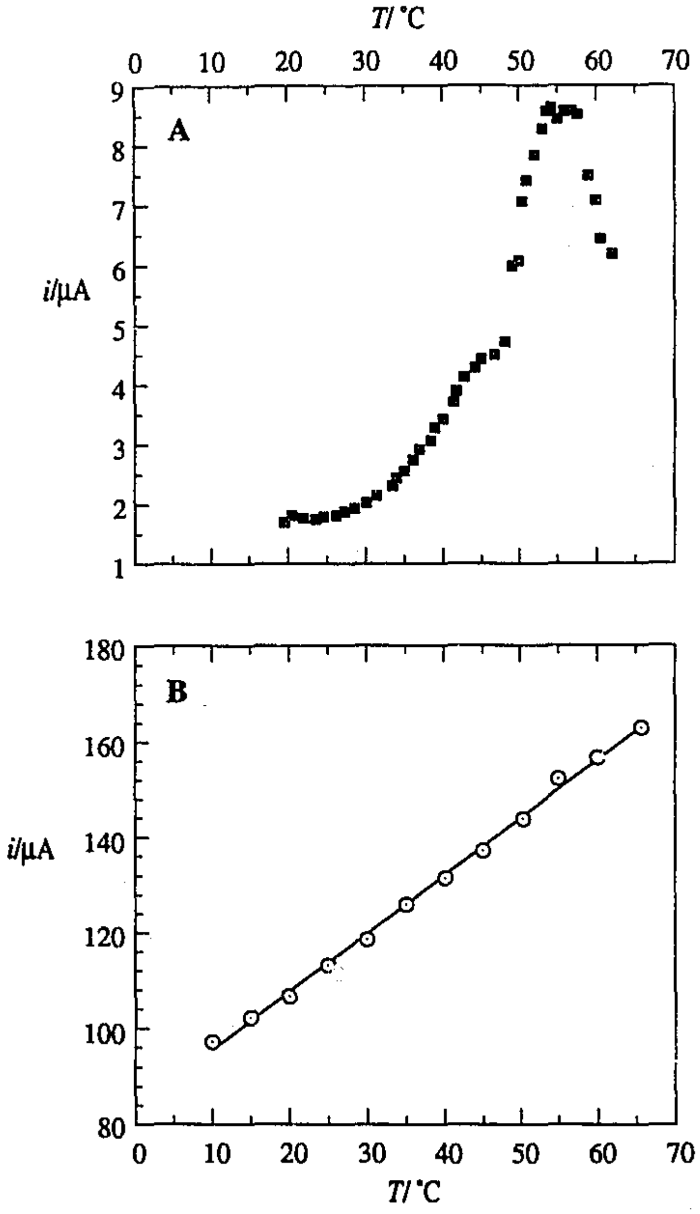

Figure 2.1. Electrochemical thermograms (plot of current *i* *vs*. temperature *T*) for $Fe(CN)_6^{3-}$ reduction at (A) $C_{18}H_{37}S/Au$ and (B) bare Au electrodes obtained by cyclic voltammetry (0.020 M $K_3Fe(CN)_6$, 0.1 M KBr, scan rate $v = 20\ mV{\cdot}s^{-1}$), temperature corrected overpotential $\eta = -250$ mV.

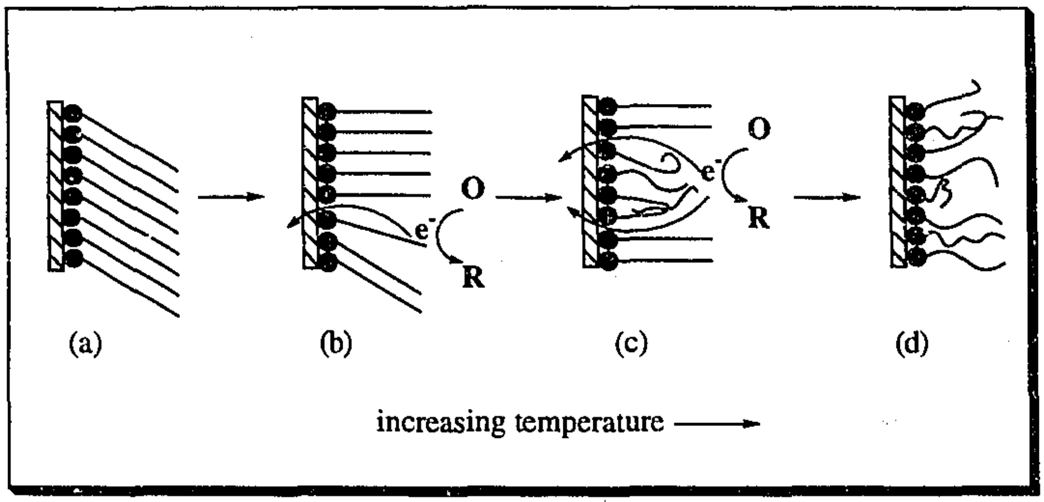

Scheme 2.1. A sketch of the physical representation of phase transitions in SAMs: (a) close-packed monolayer, (b) coexistence of tilted and untilted chains, (c) coexistence of melted and unmelted chains, and (d) melted chains.

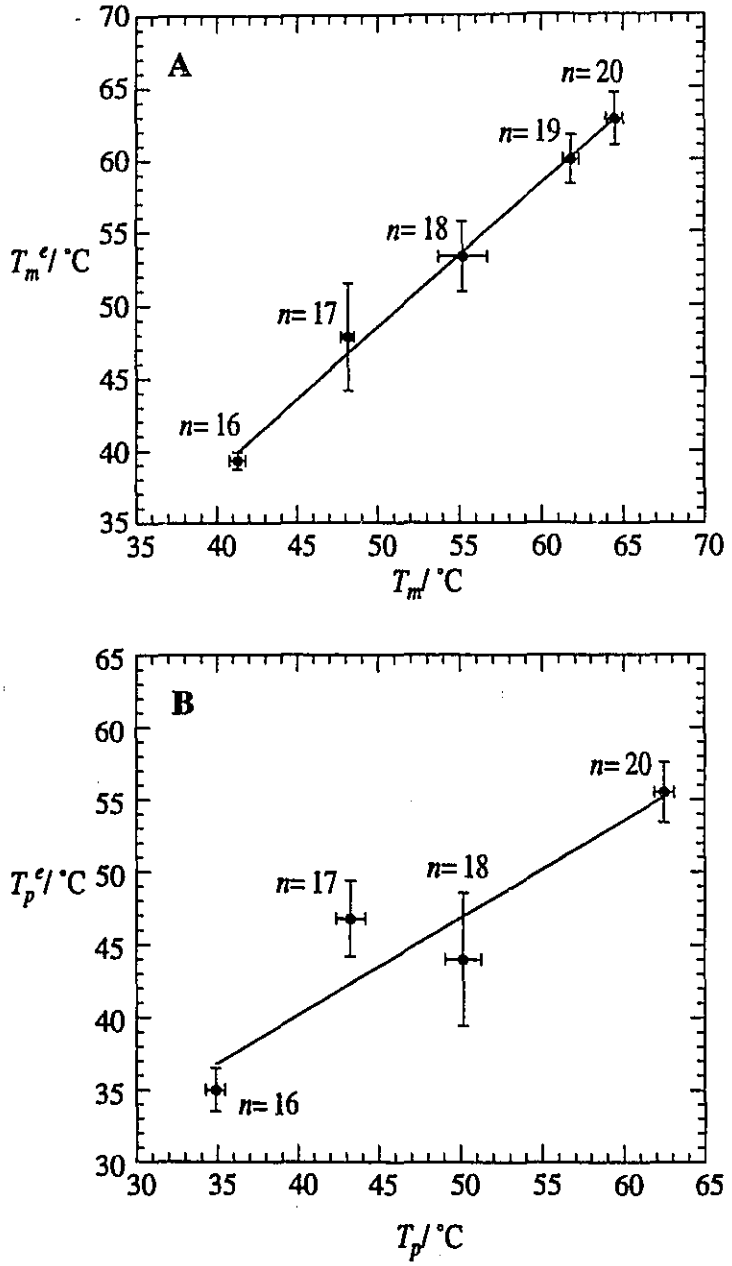

Figure 2.2. (A) Relationship between the electrochemically determined temperature T_m^e for $C_nH_{2n+1}S/Au$ (n = 16 - 20) and T_m of the gel-to-liquid crystalline phase transitions of n-diacylphosphatidylcholines measured by DSC. Error bars represent standard deviations reported here (T_m^e) and in the literature (T_m)[15]. Slope = 1.0, correlation coefficient r = 0.998. (B) Pretransition observed in the electrochemical thermograms of the modified electrode (T_p^e) *vs.* the pretransition of phosphatidylcholines (T_p). Note that a T_p^e has not been observed for $C_{19}H_{39}S/Au$, nor has a T_p been reported for the C_{19} phospholipid[15]. Slope = 0.67, correlation coefficient r = 0.920.

The $T_p{}^e$ for the monolayer also correlates with phosphatidylcholine data, but is attenuated to *ca*. 70% of the lipid T_p value (Figure 2.2B). This may arise because the position of the headgroup is fixed in the SAMs where the Au-S bond eliminates the possibility of vertical motion of the alkyl chains necessary for a periodic rippling of the surface. The current increase at $T_p{}^e$ is caused by enhanced permeability along tilt/untilt boundaries in the monolayer.

The experimental observation of thermally induced changes in RS/Au monolayers is dependent upon two conditions. Firstly, we find that only if prolonged incubation (days to weeks) in monolayer forming solutions is used will the features shown in Figure 2.1 have the opportunity to arise. Chain ordering is apparently a very slow process,[1d, 18] and may also be accompanied by RSH-assisted Au reconstructions. Dissolution of Au surface features or reconstructions of the binding sites of the sulfur on the Au are also possible.[19, 20] Secondly, the thermal history of the electrode is important. The complex behavior does not arise for many as-prepared electrodes, nor for all annealed electrodes. These share another form of temperature dependence, to be described elsewhere in a detailed description of the electrochemistry (Chapter 3)[21]. Preliminary studies show that kinetics are in fact important in these systems. Figure 2.3 shows the behaviour of a $C_{16}H_{33}S$/Au electrode under a heat-cool-reheat cycle. So far as we have observed, these annealed electrodes will not re-exhibit a maximum (as in Figure 2.1) unless subjected to prolonged cooling at 5 °C.

We conclude that SAMs which have been prepared under conventional conditions and/or have been annealed may be viewed as assemblies of conformationally all-*trans* chains (as reported by FT-IR) with short range order. However, the order is insufficient to manifest phase transitions. It is noteworthy that order/disorder transitions are observed in molecular dynamics simulations,[22] and a recent analysis shows that a domain must be a minimum size to manifest a phase coexistence region.[23, 24]

It is important to emphasize that the film discontinuities responsible for the electrochemical thermogram features (Figure 2.1) are intrinsic to SAMs which have been prepared under the experimental conditions described. The film discontinuities reported here are not the ill-defined pathological defects frequently invoked as disclaimers of film imperfection. These latter generic defects are synonymous with thin patches, defect regions commensurate with Au substrate defect structures, or regions where a co-adsorbate is clustered. The sites of enhanced passive diffusion responsible for maxima as in Figures 2.1 and 2.3 are clearly thermodynamically controlled. This is apparent because they exist at defined temperatures and are determined solely by the chain length of the alkylthiol adsorbate. Our studies suggest that order/disorder phase transitions *are* possible in SAMs.

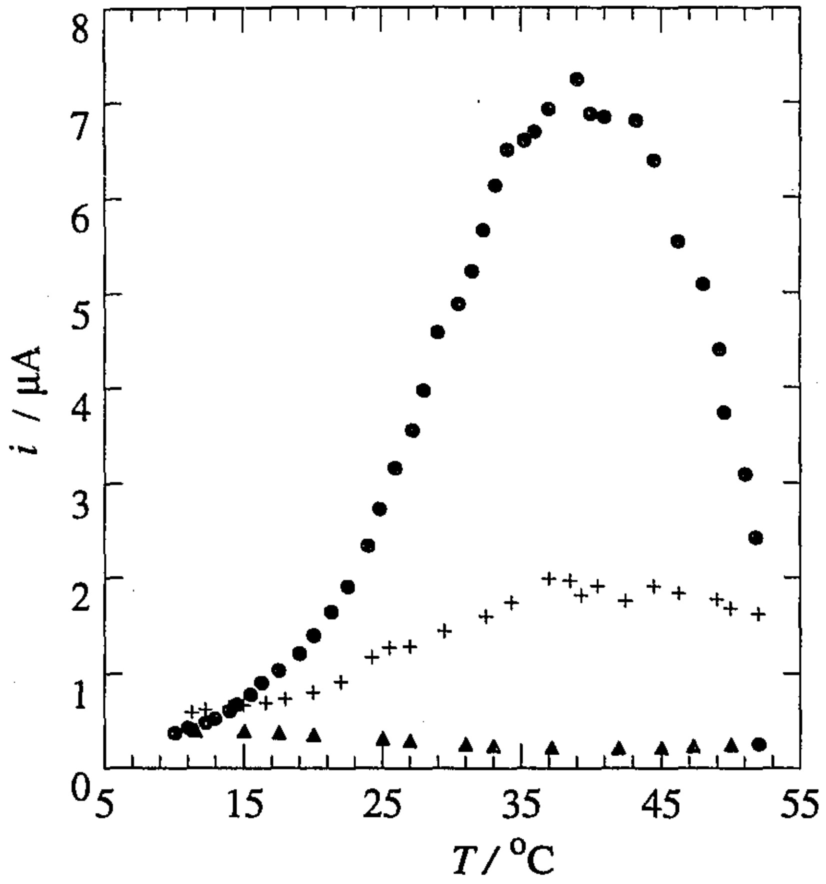

Figure 2.3. Electrochemical thermogram (see Figure 2.1 caption for experimental details) showing a heat-cool-reheat cycle for a $C_{16}H_{33}S$/Au electrode. The $C_{16}S$/Au electrode was cycled as follows: (●) initial heating curve of the $C_{16}S$/Au electrode prepared at 23 ± 2 °C; (▲) $C_{16}S$/Au electrode was cooled to 15 °C, removed from the electrochemical cell, and incubated in air at ~ 5 °C for 18 hr; (+) $C_{16}S$/Au electrode was subjected to a second heating cycle.

2.4. Conclusions

Our electrochemical results show that the electron transfer process between aqueous-based redox species and RS/Au SAMs is a sensitive probe of film structure and dynamics. The transmonolayer redox ion flux goes through maxima at chain length defined temperatures for *n*-RS/Au monolayers. This behavior closely parallels the enhanced permeability of lipid bailer vesicles to ions at their order/disorder phase transition temperatures. The monolayer preparation conditions and thermal history have been found to be important variables in these investigations. This study demonstrates that the chain packing density and configuration imposed by the Au lattice establish RS/Au SAMs as excellent functional models of biological lipid membranes.

References

(1) a) A. Ulman, *An Introduction to Ultrathin Organic Films From Langmuir-Blodgett to Self-Assembly*, Academic Press, Inc., San Diego, CA, **1991**, pp. 237-304; b) C.D. Bain, G.M. Whitesides, *Angew. Chem. Adv. Mater.* **1988**, *101*, 522; *Angew. Chem. Int. Ed. Engl. Adv. Mater.* **1989**, *28*, 506-512; c) G.M. Whitesides, P.E. Laibinis, *Langmuir* **1990**, *6*, 87-96; d) L.H. Dubois, R.G. Nuzzo, *Annu. Rev. Phys. Chem.* **1992**, *43*, 437-463, and references therein.

(2) a) R.G. Nuzzo, L.H. Dubois, D.L. Allara, *J. Am. Chem. Soc.* **1990**, *112*, 558-569; b) P.E. Laibinis, G.M. Whitesides, D.L. Allara, Y-T. Tao, A.N. Parikh, R.G. Nuzzo, *ibid.* **1991**, *113*, 7167-7177; c) M.D. Porter, T.B. Bright, D.L. Allara, C.E.D. Chidsey, *ibid.* **1987**, *109*, 3559-3568.

(3) a) L. Strong, G.M. Whitesides, *Langmuir* **1988**, *4*, 546-558; b) N. Camillone, C.E.D. Chidsey, G. Liu, T.M. Putvinski, G. Scoles, *J. Chem. Phys.* **1991**, *94*, 8493-8502; c) N. Camillone, C.E.D. Chidsey, G. Liu, G. Scoles, *ibid.* **1993**, *98*, 4234-4245; d) N. Camillone, C.E.D. Chidsey, G. Liu, G. Scoles, *ibid.* **1993**, *98*, 3503-3511; e) C.E.D. Chidsey, G. Liu, P. Rowntree, G. Scoles, *ibid.* **1989**, *91*, 4421-4423.

(4) P. Fenter, P. Eisenberger, K.S. Liang, *Phys. Rev. Lett.* **1993**, *70*, 2447-2450.

(5) a) S.W. Barton, B.N. Thomas, E.B. Flom, S.A. Rice, B. Lin, J.B. Peng, J.B. Ketterson, P. Dutta, *J. Chem. Phys.* **1988**, *89*, 2257; b) K. Kjaer, J. Als-Nielsen, C.A. Helm, P. Tippmann-Krayer, H. Mohwald, *Thin Solid Films* **1988**, *159*, 17.

(6) a) A. Ulman, *Adv. Mater.* **1991**, *3*, 298-303; b) S.E. Evans, R. Sharma, A. Ulman, *Langmuir* **1991**, *7*, 156-161.

(7) a) R.G. Nuzzo, E.M. Korenic, L.H. Dubois, *J. Chem. Phys.* **1990**, *93*, 767-773; b) L.H. Dubois, B.R. Zegarski, R.G. Nuzzo, *J. Electron Spectrosc. Rel. Phen.* **1990**, *54/55*, 1143.

(8) a) C.D. Bain, E.B. Troughton, Y-T. Tao, J. Evall, G.M. Whitesides, R.G. Nuzzo, *J. Am. Chem. Soc.* **1989**, *111*, 321-335; b) R.G. Nuzzo, D.L. Allara, *ibid.* **1983**, *105*, 4481-4483.

(9) a) C. Miller, P. Cuendet, M. Gratzel, *J. Phys. Chem.* **1991**, *95*, 877-886; b) C. Miller, M. Gratzel, *ibid.* **1991**, *95*, 5225-5233; c) M.A. Fox, D.M. Collard, S.E. Creager, *Langmuir* **1990**, *6*, 1617-1620; d) H.O. Finklea, D.D. Hanshew, *J. Electroanal. Chem.* **1993**, *347*, 327-340; e) H.O. Finklea, M.S. Ravenscroft, D.A. Snider, *Langmuir* **1993**, *9*, 223-227.

(10) a) H.O. Finklea, S. Avery, M. Lynch, T. Furtsch, *Langmuir* **1987**, *3*, 409-413; b) C.E.D. Chidsey, D.N. Loiacono, *ibid.* **1990**, *6*, 682-691; c) S.E. Creager, L.A. Hockett, G.K. Rowe, *ibid.* **1992**, *8*, 854-861; d) A.M. Becka, C.J. Miller, *J. Phys. Chem.* **1992**, *96*, 2657-2668; e) A.M. Becka , C.J. Miller, *ibid.* **1993**, *97*, 6233-6239; f) H.O. Finklea, D.A. Snider, J. Fedyk, E. Sabatini, Y. Gafni, I. Rubinstein, *Langmuir* **1993**, *9*, 3660-3667; g) K. Doblhofer, J. Figura, J-H. Fuhrhop, *ibid.* **1992**, *8*, 1811-1816.

(11) a) C.E.D. Chidsey, *Science* **1991**, *251*, 919-922; b) C.E.D. Chidsey, C.R. Bertozzi, T.M. Putvinski, A.M. Mujsce, *J. Am. Chem. Soc.* **1990**, *112*, 4301-4306; c) D.M. Collard, M.A. Fox, *Langmuir* **1991**, *7*, 1192-1197; d) G.K. Rowe, S.E. Creager, *ibid.* **1991**, *7*, 2307-2312; e) J.J. Hickman, D. Ofer, C. Zou, M.S. Wrighton, P.E. Laibinis, G.M. Whitesides, *J. Am. Chem. Soc.* **1991**, *113*, 1128-1132; f) H.O. Finklea, D.D. Hanshew, *ibid.* **1992**, *114*, 3173-3181; g) E. Katz, N. Itzhak, I. Willner, *Langmuir* **1993**, *9*, 1392-1396; h) A.J. Black, T.T. Wooster, W.E. Geiger, M.N. Paddon-Row, *J. Am. Chem. Soc.* **1993**, *115*, 7924-7925.

(12) a) R.A. Marcus, N. Sutin, *Biophys. Acta.* **1985**, *811*, 265; b) F. Mollers, R. Memming, *Ber. Bunsen-Ges. Phys. Chem.* **1972**, *76*, 475; c) V. Marecek, Z. Samec, J. Weber, *J. Electroanal. Chem.* **1978**, *94*, 169.

(13) A. Swietlow, M. Skoog, G. Johansson, *Electroanalysis* **1992**, *4*, 921-928.

(14) a) D. Papahadjopoulous, K. Jacobson, S. Nir, T. Isac, *Biochim. Biophys. Acta.* **1973**, *311*, 33; b) E. Corvera, O.G. Mouritsen, M.A. Singer, M.J. Zuckerman, *ibid.* **1992**, *1107*, 261.

(15) D. Marsh, *Handbook of Lipid Bilayer Membranes*, CRC Press, Boca Raton, **1991**, pp. 135-150.

(16) L. Cruzeiro-Hansson, O.G. Mouritsen, *Biochim. Biophys. Acta.* **1988**, *944*, 63.

(17) a) J.N. Robinson , P.J. Cole-Hamilton, *Chem. Soc. Rev.* **1991**, *20*, 49-94;
b) S.V. Lymar, J.K. Hurst, *J. Phys. Chem.* **1994**, *98*, 989, and references therein;
c) L. Hammarström, H. Berglund, M. Almgren, *J. Phys. Chem.* **1994**, *98*, 9588-9593.

(18) a) G. Hahner, Ch. Woll, M. Buck, M. Grunze, *Langmuir* **1993**, *9*, 1955-1958;
b) C.D. Bain, E.B. Troughton, Y.T. Tao, J. Evall, G.M. Whitesides, R.G. Nuzzo, *J. Am. Chem. Soc.* **1989**, *111*, 321.

(19) K. Edinger, A. Golzhauser, K. Demota, Ch. Woll, M. Grunze, *Langmuir* **1993**, *9*, 4-8.

(20) H. Sellers, A. Ulman, Y. Shnidman, J.E. Eilers, *J. Am. Chem. Soc.* **1993**, *115*, 9389-9401.

(21) A. Badia, R.B. Lennox, manuscript submitted to *Langmuir*.

(22) a) J. Hautman, M.L. Klein, *J. Chem. Phys.* **1990**, *93*, 7483-7492; b) W. Mar, M.L. Klein, *Langmuir* **1994**, *10*, 188-196.

(23) J.I. Siepmann, I.R. McDonald, *Langmuir* **1993**, *9*, 2351-2355.

(24) At the present time, we do not understand why ordering is apparently induced by annealing (reference 4), except to say that the observation conditions in that study and the present study (UHV *vs*. aqueous electrolyte) are quite different.

Chapter Three

ORDER/DISORDER PHASE TRANSITIONS IN SELF-ASSEMBLED MONOLAYERS*

3.1. Introduction

Self-assembled monolayers (SAMs) of organosulfur adsorbates on metal and semiconductor substrates are of great interest both for novel technological applications and for an understanding of fundamental aspects of surface chemistry.[1-10] Many studies have reported applications of SAMs to the modeling of reactivity problems, especially those associated with corrosion[11-13] and electron transfer[14-27]. As a means of deliberately modifying a metal surface, SAMs based on alkanethiols (RSHs) offer ready access to a broad variety of spectroscopic, electrochemical, and reactivity experiments.[3,5,7,8,28] Because RS/metal SAMs are obtainable in close to complete surface coverage using simple conditions, one can probe the chemistry of films with thicknesses of 10-30 Å. Such thin films, when strongly associated with a metal surface, would be expected to modulate both the properties of the metal and the elements of the solution or atmosphere in which it is immersed.

One common perception is that RS/metal SAMs (and related Langmuir-Blodgett films of long chain surfactant molecules deposited on solid supports) may be viewed as organized two-dimensional (2D) arrays of molecules. A detailed understanding of monolayer film organization and chain thermodynamics will help to place SAMs in the context of their more thoroughly understood relatives, lipid bilayer membranes. A recent grazing incidence X-ray diffraction study reported a striking difference in the high temperature phase behavior of long ($R \geq C_{14}$) and short ($R \leq C_{12}$) chain length RSHs on Au (111).[29] More specifically, an hysteretic reconstruction of the $C_{14}S/Au$ monolayer was observed above 60 °C from an hexagonal commensurate structure to a non-hexagonal

---

* Manuscript submitted to *Langmuir*, June 1996.

incommensurate one. However, no such change in the epitaxial film structure was observed for RSH chain lengths ≤ 12 carbons. Upon further heating, both the $C_{12}S/Au$ and $C_{14}S/Au$ monolayers showed reversible melting transitions, with the coexistence of both solid and liquid phases, at temperatures that are ~ 60 °C above the melting points of the corresponding bulk *n*-alkanes.[29] A quartz crystal microbalance/transverse shear mode study of $C_{18}SH$ self-assembled onto a gold-coated piezoelectric crystal showed discontinuities in the conductance, resonance frequency, and impedance of the SAM at 18-20 °C, which were attributed to an increase in the film viscosity.[28] On the other hand, variable temperature reflection absorption infrared spectroscopy (RAIRS) studies[30-32] show only the gradual appearance of *gauche* conformational chain defects upon heating, instead of the dramatic population increase expected for first-order melting processes. Molecular dynamic simulations have been used to study the effect of temperature on long chain RSH molecules chemisorbed on a Au (111) surface.[33-35] These simulations predict both orientational and rotational disordering of the tethered alkyl chains. Contact angle (wetting) measurements show that hydroxyl-terminated SAMs undergo a slow reorganization so as to bury the polar hydroxyl groups into the hydrocarbon film.[33,36,37] The rate of reorganization of the hydrophilic monolayer was found to be influenced by both the alkyl chain length and the temperature. Clearly, the dynamics of RS/Au SAMs are complex. The manner in which temperature affects the structure/property/activity relationships of these 2D organized monolayer assemblies remains substantially unresolved. We are particularly concerned with how restricted chain motion, due to the strong pinning of the sulfur headgroup to the metal surface, affects long and short-range ordering of the alkyl chains, surface reorganization processes, and order-disorder phase transitions.

Our approach has been to use the electron transfer process across self-assembled RS/Au monolayers to probe thermally-induced changes in film phases between organizational states.[38] The electron transfer kinetics of solution-based redox couples (*eg.* $Fe(CN)_6^{3-/4-}$, $Ru(NH_3)_6^{2+/3+}$, $Fe^{2+/3+}$)[14-19,21-24,39-46] and of monolayer-associated redox active surfactants (*eg.* viologens, pyRu $(NH_3)_5^{2+/3+}$, ferrocene)[25-27,44,47-53] have been the subject of considerable interest over the last decade. Viewed as an ultrathin hydrocarbon layer on a metal surface, RS/Au SAMs, where $R = C_{12}H_{25}$-$C_{20}H_{41}$, offer the possibility of retarding heterogeneous electron transfer rates by 10-10^6 fold. These studies usually employ the SAM as a spacer between the redox couple and the electrode, where the spacer is well-defined in terms of composition and distance. Following on the classic studies of Miller and Closs[54,55] and Paddon-Row[56], where donor/acceptor pairs are separated by rigid hydrocarbon spacers of known length, several groups have studied the relationship between SAM film thickness and electron transfer rate[14,16,25,26,43]. In the following we show that the SAM/electrochemical experiment can be viewed as a *probe* of film structure and thermodynamics and that its use as a probe of the electron transfer mechanism in SAMs is perhaps problematic given the complex nature of the film structure.

3.2. Experimental Section

3.2.1. Materials: Octadecanethiol ($C_{18}SH$), received from Aldrich (98%), was triply recrystallized from ethanol. Tetradecanethiol ($C_{14}SH$) was obtained from Fluka (purum) and used without further purification. Hexadecanethiol ($C_{16}SH$) was synthesized by refluxing bromohexadecane (Aldrich, 98%), dissolved in 95% ethanol, with one equivalent of thiourea for 6-8 hr. The resulting thiourium salt was hydrolyzed to the alkanethiol by refluxing with a three-fold excess of sodium hydroxide (2 N aqueous solution) for 3 hr under nitrogen.[57] The cooled mixture was diluted with equal volumes of water and diethyl ether. The aqueous phase was first acidified to pH 2 with 2 N HCl and the organic layer was then separated from the aqueous layer. The aqueous phase was further extracted with diethyl ether and the combined ether extracts were washed with water before drying over anhydrous sodium sulfate. Evaporation of the ether yielded the crude alkylthiol which was purified by recrystallization from ethanol. Heptadecanethiol ($C_{17}SH$), nonadecanethiol ($C_{19}SH$), and eicosanethiol ($C_{20}SH$) were synthesized by conversion of the corresponding aliphatic alcohol (Fluka, purum) to the alkylbromide by refluxing with 48% HBr, prior to reaction with thiourea.[57] 16-Mercaptohexadecanol ($HOC_{16}SH$) was synthesized from 1,16-hexadecanediol (Fluka, purum) following the procedure reported by Becka and Miller.[16]

$CH_3(CH_2)_nSH$ (for n = 15-19): TLC (silica gel, n-hexane): $R_f = 0.7$; ^1H NMR (500 MHz, $CDCl_3$): δ 2.52 (q, 2H, $C\mathit{H}_2SH$), 1.58 (m, 2H, $C\mathit{H}_2CH_2SH$), 1.40 (m, 2H, $C\mathit{H}_2CH_2CH_2SH$), 1.31 (t, 1H, $CH_2S\mathit{H}$), 1.24 (s, $2(n\text{-}3)$H, $(CH_2)_{n-3}$), 0.87 (t, 3H, CH_3). The DSC measured melting points and the mass spectral results are the following: $CH_3(CH_2)_{15}SH$: mp 19.5-21 °C; MS (CI, NH_3): m/z 257 $[M\text{-}H]^+$, m/z 224 $[M\text{-}SH]^+$; $CH_3(CH_2)_{16}SH$: mp 31-32 °C; MS (CI, NH_3): m/z 271 $[M\text{-}H]^+$, m/z 238 $[M\text{-}SH]^+$; $CH_3(CH_2)_{17}SH$: mp 28.5-30 °C; MS (CI, NH_3): m/z 285 $[M\text{-}H]^+$, m/z 252 $[M\text{-}SH]^+$; $CH_3(CH_2)_{18}SH$: mp 39-40 °C; MS (CI, NH_3): m/z 299 $[M\text{-}H]^+$, m/z 266 $[M\text{-}SH]^+$; $CH_3(CH_2)_{19}SH$: mp 37-38 °C; MS (CI, NH_3): m/z 313 $[M\text{-}H]^+$, m/z 280 $[M\text{-}SH]^+$.

$HO(CH_2)_{16}SH$: mp 52.5-54 °C; TLC (silica gel, 12:88 (w/w) ethyl acetate: chloroform): $R_f = 0.5$; ^1H NMR (500 MHz, $CDCl_3$): δ 3.62 (t, 2H, $HOC\mathit{H}_2$), 2.56 (q, 2H,

CH_2SH), 1.55 (m, 4H, CH_2CH_2SH, $HOCH_2CH_2$), 1.31 (t, 1H, CH_2SH), 1.28 (s, 24H, $(CH_2)_{12}$); MS (FAB$^+$, NBA): m/z 275 [MH]$^+$, m/z 257 [M-OH]$^+$.

$K_3Fe(CN)_6$ (BDH), $K_4Fe(CN)_6$ (BDH), and KBr (Anachemia) were of the highest available grade. Distilled/deionized water (18 MΩ·cm) was obtained from a Milli-Q water system (3 bed ion-exchange/1 bed organic removal cartridge unit) connected to house distilled water.

3.2.2. Monolayer preparation: Bulk polycrystalline gold electrodes (0.020 cm^2 geometric area; BAS, West Lafayette, IN.) were mechanically polished (Buehler, Ecomet II polisher) on microcloth pads (Buehler) with alumina slurries of decreasing particle diameter: 1.0 μm, 0.3 μm, and 0.05 μm alumina (Buehler). The polished electrodes were sonicated in water to remove residual polishing alumina adhered to the gold surface. The chemically etched gold electrodes were prepared by immersion of the polished gold electrodes in dilute aqua regia (3:1:6 $HCl:HNO_3:H_2O$) at room temperature for 5 min.[44]

Immediately after the polishing or etching procedure, the gold electrodes were thoroughly rinsed with water, then by absolute ethanol, and immersed in an argon-saturated absolute ethanol solution of the alkanethiol (2-5 mM RSH). The electrodes were incubated in the RSH coating solution in sealed glass vials at 23 ± 2 °C for 3-16 days. Ellipsometry gave film thicknesses which are consistent with monolayer coverage, so that prolonged incubation does not cause multilayer formation[58]. Mixed RSH monolayers were prepared by incubation of polished Au electrodes in 1:1 molar ethanol solutions of $C_{14}SH$ and $C_{18}SH$ or $C_{16}SH$ and $C_{18}SH$ (2 mM total thiol concentration) at 23 ± 2 °C for periods ranging from several days to one month. Modified electrodes were removed from solution, copiously rinsed with fresh ethanol followed by water, and were then immediately introduced into the electrochemical cell.

3.2.3. Electrochemical measurements: The RS/Au working electrode was introduced into a degassed, thermostated (Haake G circulating bath) 150 mL cell containing 0.1 M KBr electrolyte and 0.020 M $K_3Fe(CN)_6$. The counter electrode was a Pt wire (Aldrich) and all potentials refer to a Ag/AgCl reference electrode (3 M NaCl; BAS). Currents were obtained from steady-state cyclic voltammograms (BAS 100B electrochemical analyzer) run at 20 mVs^{-1} between +500 mV to -150 mV. Typical heating and cooling rates of 0.2-0.3 °C/min were used for all experiments.

The temperature dependence of $Fe(CN)_6^{3-}$ reduction at a bare gold electrode was determined so as to quantify the exact shift of the $E^{\circ\prime}$ for the $Fe(CN)_6^{3-/4-}$ couple as a function of temperature. The $E^{\circ\prime}$ was found to change linearly by -1.55 mV/°C with increasing temperature in the range of 5 - 65 °C.[38] Thus, temperature dependent cathodic currents are reported for the RSH-modified electrodes at an overpotential of -250 mV from the $E^{\circ\prime}$ of $Fe(CN)_6^{3-/4-}$ at each given temperature.

Variable-temperature underpotential deposition (UPD) of Cu on RS/Au electrodes was performed as a single potential, time base experiment at $E = 0.0$ V in a 2 mM $CuSO_4$/ 1 M KCl/ 0.1 M Na_2SO_4 solution.

The bare Au surface roughness and the thiol monolayer film coverage were determined by stripping off underpotential-deposited Cu. Cu UPD was carried out by holding the bare Au and RS/Au electrodes at $E = +100$ mV for 60 s in a stirred 5 mM $CuSO_4$, 0.1 M Na_2SO_4 solution. The deposited Cu was then stripped off by potential cycling from +100 mV to +600 mV at 20 mV/s. The amount of Cu deposited was determined from the area (*i.e.* charge) under the background corrected (*i.e.* 0.1 M Na_2SO_4) stripping peaks. A value of 2.2×10^{-9} mol/cm^2 was used for the Cu coverage on polycrystalline Au.[59]

The surface crystallography of the bulk Au electrodes was determined from the stripping voltammograms of underpotential-deposited Pb.[44] Pb UPD was first carried out at -440 mV for 60 s in a 1 mM PbO, 0.1 M $HClO_4$ solution. The deposited Pb monolayer was then stripped off by potential cycling from -440 mV to +600 mV at 5 mV/s.

The capacitance of the RSH-modified gold electrodes was determined in 0.1 M KBr from cyclic voltammograms run between +500 mV to -100 mV at scan rates of 100, 200, 300, 400, and 500 mVs^{-1}. The average of the cathodic and anodic charging currents at -75 mV[14,20-22,60] was plotted *vs.* the scan rate. A linear relationship was obtained and the slope was taken as the differential capacitance.

3.3. Results

3.3.1. Current *vs.* Temperature Heating Curves: An RSH-modified Au electrode (R = $C_{16}SH$-$C_{20}SH$) prepared under conditions of controlled temperature, and often prolonged immersion times, exhibits one of 3 types of current variation (*i.e.* $Fe(CN)_6^{3-}$ reduction) as the temperature is slowly increased. These different behaviors are illustrated by typical examples of $C_{18}S$/Au monolayers in Figure 3.1. Of immediate note is that all 3 types of current (*i*) *vs.* temperature (*T*) curves have features indicating that complex interactions between the redox couple and the monolayer are occurring. An activated process, such as the reduction of $Fe(CN)_6^{3-}$ at $\eta = -250$ mV, exhibits monotonically increasing rates (*i.e.* current) over the temperature range studied here.[38]

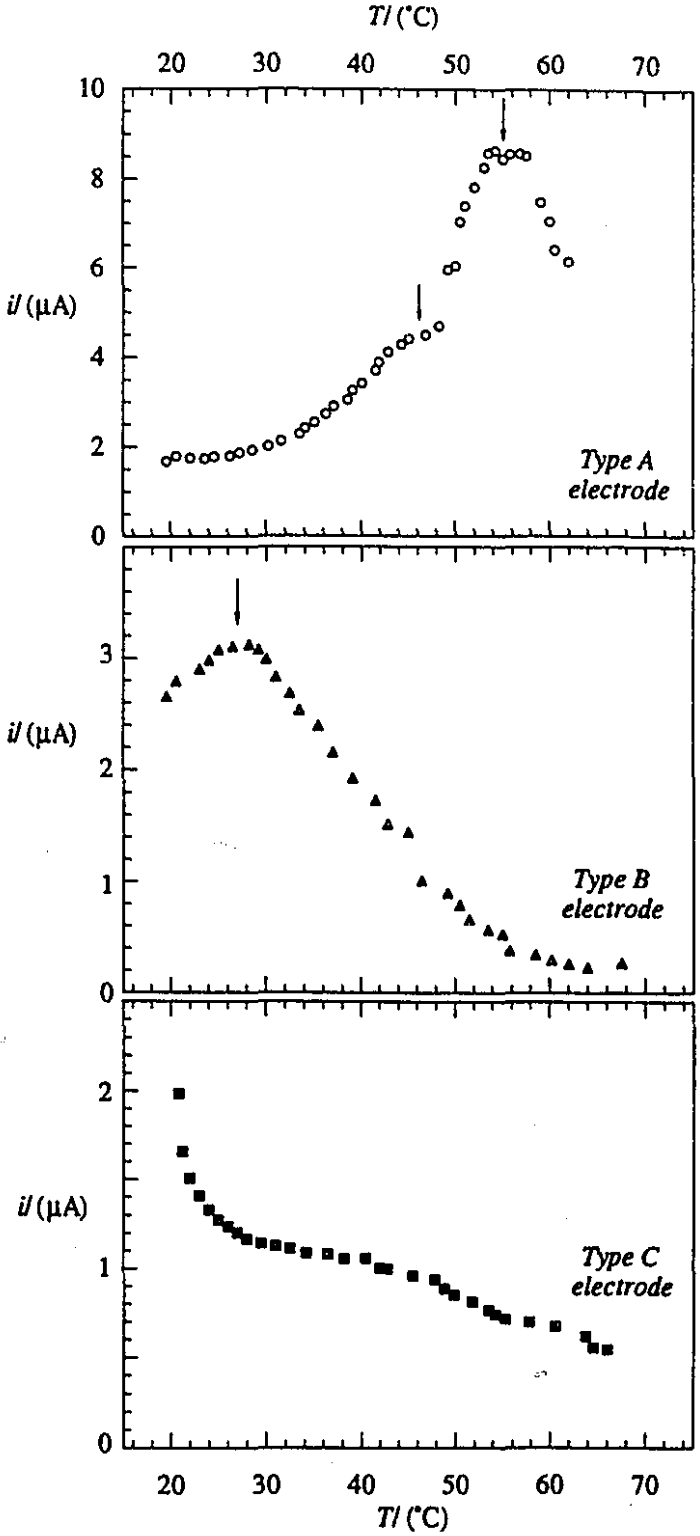

Figure 3.1. The 3 types of *i/T* behavior observed for the reduction of $Fe(CN)_6^{3-}$ (η= -250 mV) at $C_{18}S$/Au electrodes.

Instead, Types A and B RSH-modified Au electrodes (Figure 3.1) have distinct maxima and Type C electrodes exhibit *di /dT* values which are < 0 over the temperature range studied.

(a) *Type A electrodes:* Gold electrodes exposed to prolonged incubation in RSH solutions will frequently exhibit maxima in the *i/T* curves (Figure 3.1). These maxima follow a distinct pattern which is dependent upon the length of the alkyl RSH chain (Figure 3.2). The first, smaller maximum occurs at a temperature designated $T_p{}^e$. $T_p{}^e$ occurs ~ 5-10 °C lower than the much larger maximum, designated $T_m{}^e$. The smaller maximum frequently appears as a shoulder on the larger current maximum and is observed for all chain lengths except C_{19}. The $T_m{}^e$ values range from 40 °C ($C_{16}S/Au$) to 62 °C ($C_{20}S/Au$) and correspond to current increases of some 3-12 fold over currents at $T_m{}^e$ - 25 °C. $T_m{}^e$ and $T_p{}^e$ values are quite reproducible, where for example, in the $C_{18}S/Au$ case, $T_p{}^e = 48 \pm 2$ °C and $T_m{}^e = 54 \pm 1$ °C (for measurements made on 5 electrodes). Interestingly, the $T_m{}^e$ for the $HOC_{16}SH$-modified Au electrodes (Figure 3.3) was found to occur some 30 degrees higher ($T_m{}^e = 70 \pm 1$ °C; n= 3 electrodes) than the corresponding $C_{16}S/Au$ ($T_m{}^e = 39 \pm 1$ °C; n= 2 electrodes). This increase in the $T_m{}^e$ of hydroxyl-terminated RSHs compared with methyl-terminated RSHs is thought to arise from hydrogen bonding between the terminal OH groups of neighboring chains which would provide added thermal stability to the alkyl chain ordering. Molecular dynamics simulations of hydroxyl-terminated RSH SAMs on Au actually predict structures which are more rigid that their methyl-terminated counterparts, and which contain both free and hydrogen bonded hydroxyl groups.[33]

Type A *i/T* curves are observed with polished electrodes, but have been observed with only one of 20 chemically etched Au electrodes (*i.e.* $C_{16}S/Au$) studied. Distinct maxima are readily apparent for well-blocked electrodes (distinguished by very low currents at 25 °C), but can even be discerned as discontinuities on the *i/T* curves associated with poorly blocking electrodes. Poorly blocking electrodes are made up of two film structures- defect laden and well-blocked.

The substantial current changes observed for the RS/Au SAMs reflect temperature-induced modification of the SAM as a barrier to electron transfer. This is clearly shown in Figure 3.4, where current changes for the $C_{18}S/Au$ electrode as a function of temperature only appear at potentials close to or more negative than where ferricyanide reduction actually occurs on a bare Au electrode. More importantly, the $T_p{}^e$ and $T_m{}^e$ features are identical at all these potentials, indicating that the observed current changes detected in RS/Au SAMs are not due to a potential-induced reorganization of the film.

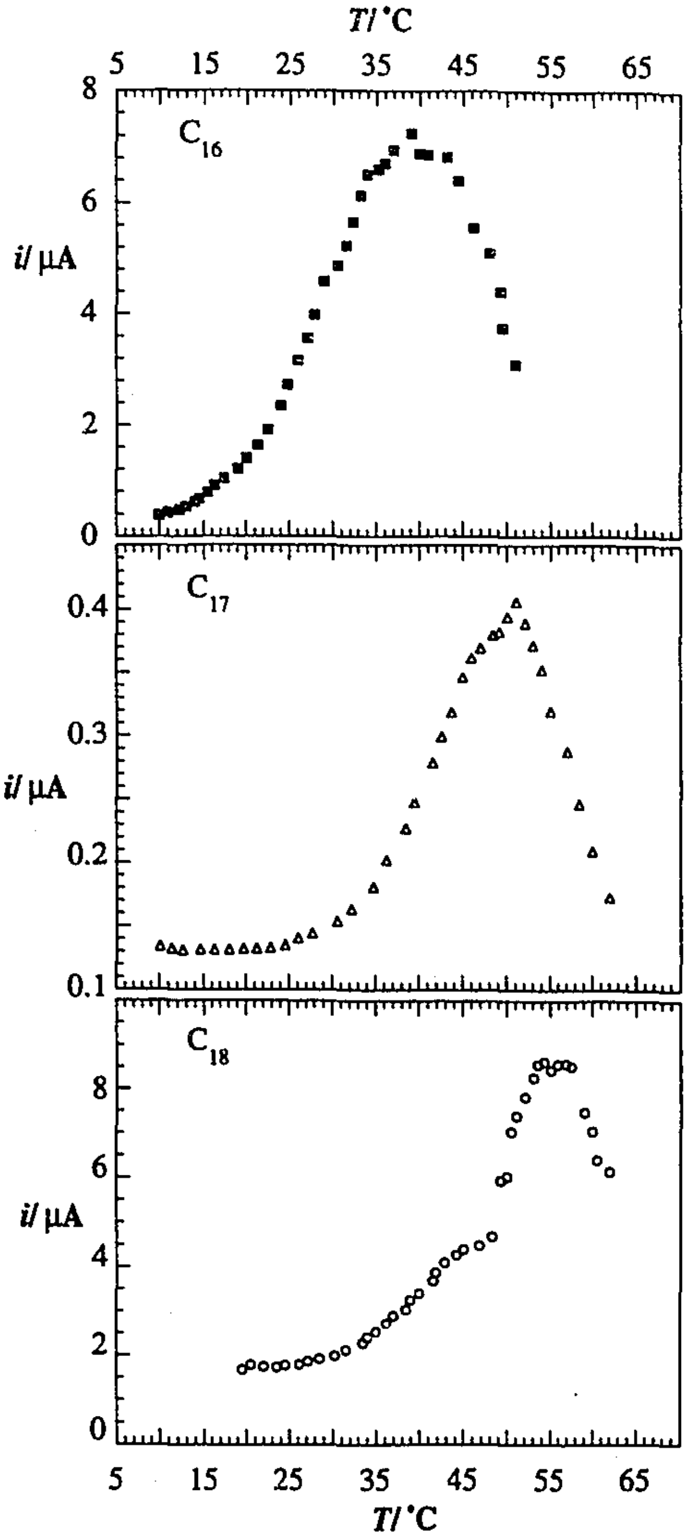

Figure 3.2. Electrochemical thermograms (*i*/*T* plots) for Type A RS/Au electrodes, where R= $C_{16}H_{33}$, $C_{17}H_{35}$, $C_{18}H_{37}$, $C_{19}H_{39}$, and $C_{20}H_{41}$.

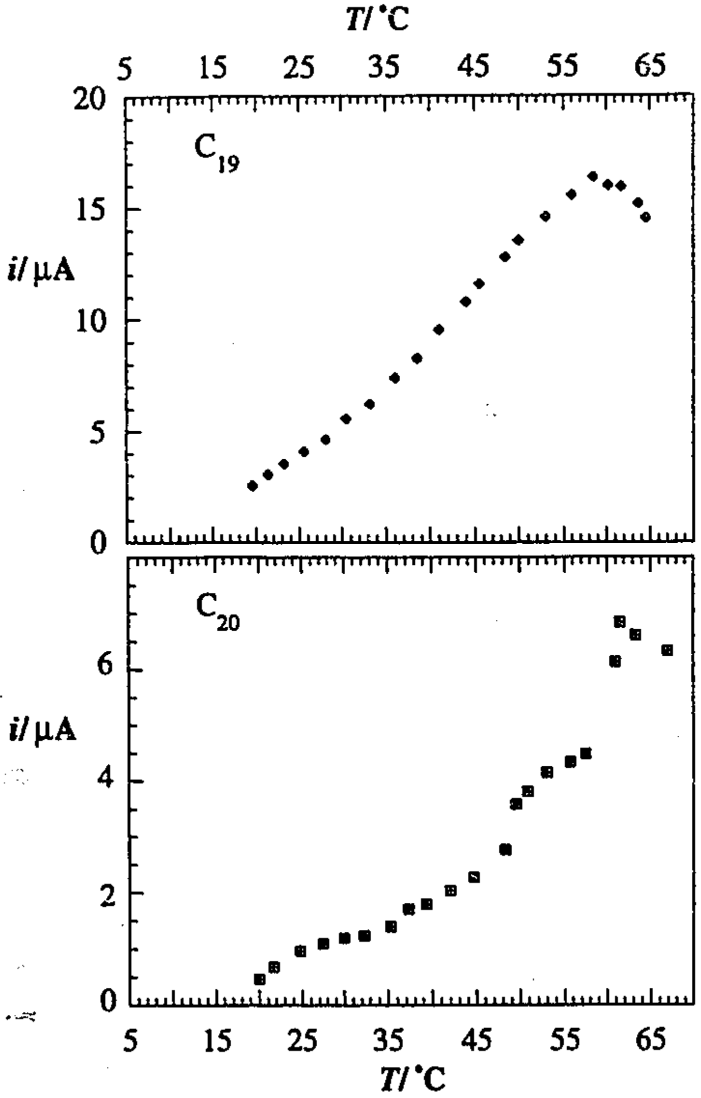

Figure 3.2. (cont'd) Electrochemical thermograms for Type A RS/Au electrodes.

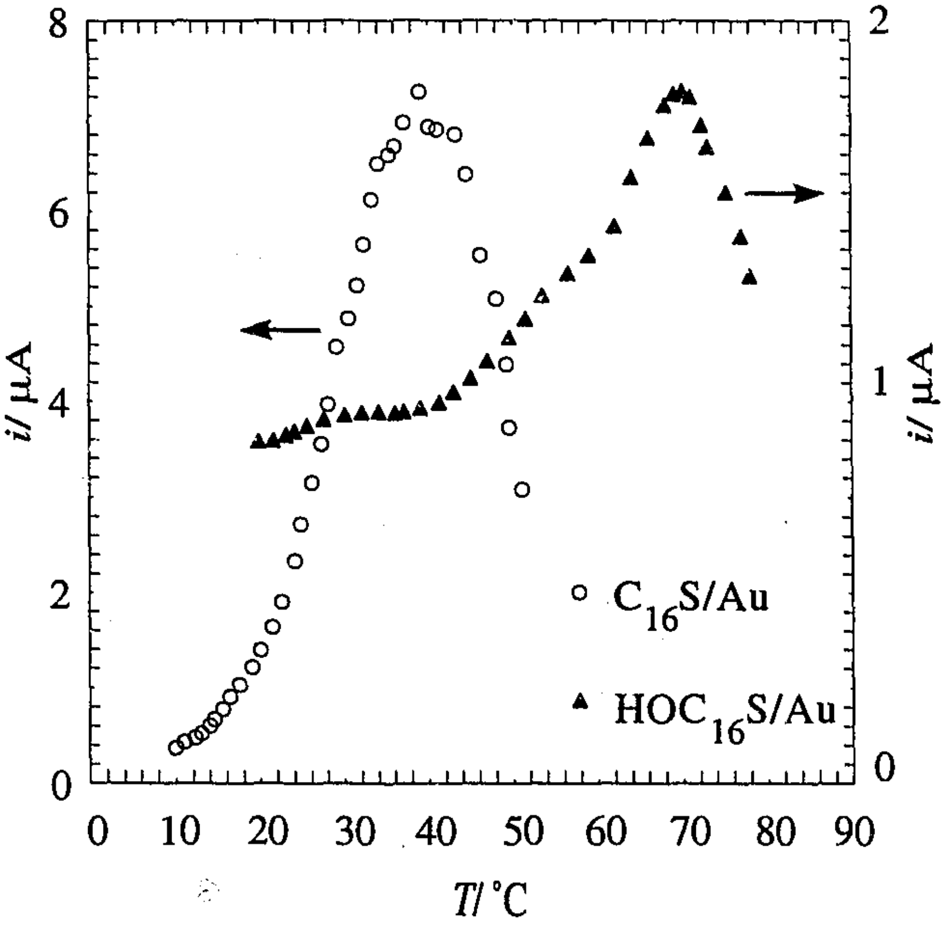

Figure 3.3. A comparison of the i/T plots for $C_{16}H_{33}S/Au$ ($T_m^e = 39 \pm 1$ °C) and $HO(CH_2)_{16}S/Au$ ($T_m^e = 70 \pm 1$ °C) electrodes.

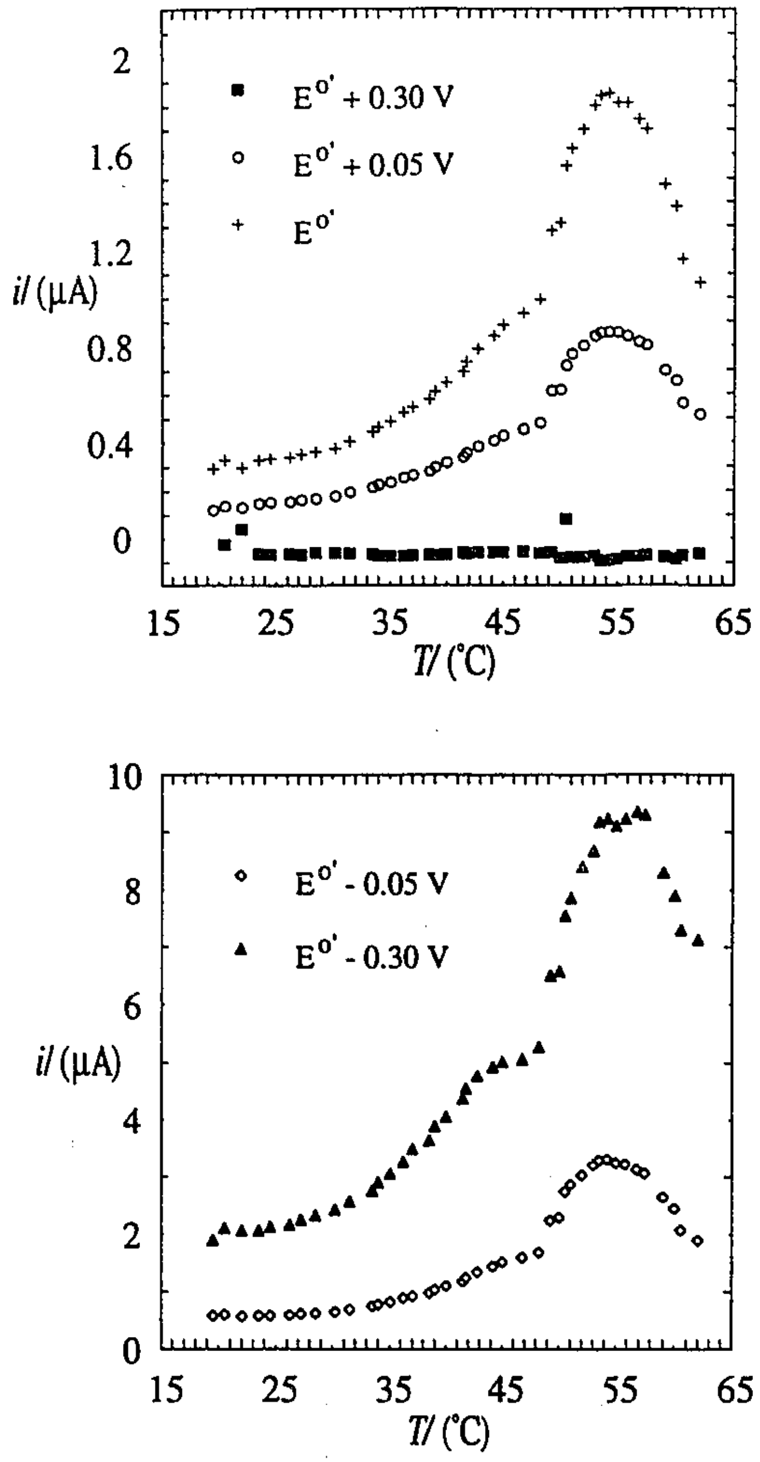

Figure 3.4. i/T plots for $Fe(CN)_6^{3-}$ reduction at a $C_{18}S$/Au electrode as a function of the electrode potential. i is reported at potentials equivalent to $E^{o'}$ + 0.30 V, $E^{o'}$ + 0.05 V, $E^{o'}$, $E^{o'}$ - 0.05 V, and $E^{o'}$ - 0.30 V.

Single potential (-50 mV *vs.* Ag/AgCl), time base experiments yield similar results and establish that continuous potential cycling of the RS/Au-$Fe(CN)_6^{3-}$ interface is not the cause of these current changes.

Variable-temperature (25 - 60 °C) Cu UPD on well-blocked $C_{18}S/Au$ electrodes exhibits an increasing current value with temperature up to ~ 55 °C, after which the current reaches a steady value. The transition temperature in this experiment (55 °C) corresponds closely to the T_m^e of $C_{18}S/Au$ electrodes determined using $Fe(CN)_6^{3-/4-}$.

(b) *Type B electrodes:* Not all electrodes prepared as per above exhibit Type A *i/T* traces. In some cases, the Faradaic current gradually rises until a well defined temperature is reached, and it then drops quite sharply (Figure 3.1). This maximum temperature is designated $T_m^{e'}$. $T_m^{e'}$ is alkyl chain dependent and never exceeds the T_m^e value observed for that particular RSH chain in Type A modified electrodes. In many cases, $T_m^{e'}$ is 10-30 °C less than T_m^e. No inflection suggestive of a T_p^e process is observed for these electrodes. Type B behavior occurs with polished electrodes, but has not been observed with chemically etched electrodes.

(c) *Type C electrodes:* The third *i/T* pattern involves a monotonically decreasing current with increasing *T* (Figure 3.1). The decrease in *i* can be up to seven-fold for a 30 °C change. This pattern occurs with both chemically etched Au electrodes and with Type A electrodes which have been incubated in RSH-coating solutions at $T > T_m^e$. Type C clearly does not reflect simple activated-process kinetics, but is obviously distinct from Type A behavior. No reproducible features or discontinuities on the *i/T* curves are discernible.

The data in Figures 3.1 - 3.4 foretell a rich phase behavior in the RS/Au monolayer systems which has not been previously described.

3.3.2. Capacitance: The *i/T* curves ($Fe(CN)_6^{3-}$ reduction) are not corrected for capacitance, C_i. It has been noted that RS/Au monolayers lead to a substantial reduction in the capacitance compared to a bare Au electrode.[20-22,60,61] This diminution in C_i is observed for both polished and chemically etched RS/Au electrodes in this work. Although not studied in detail here, Figure 3.5 provides an illustrative example of C_i/T properties. In this case, the capacitance exhibits the same maximum as the Faradaic current (Type A electrode) does. The maximum in the C_i/T curves for the $C_{16}S/Au$ monolayer arises at a temperature equivalent to the T_m^e value for that chain length. These data establish that electron transfer is not a necessary condition for current maxima to occur. Clearly these current maxima are related to processes occurring in the monolayer film. Finklea *et al.* also reported an increase in the interfacial capacitance upon heating mixed

$HS(CH_2)_{15}CONHCH_2pyRu(NH_3)_5^{2+}$/ $HS(CH_2)_{15}COOH$ monolayers from 25 °C to 55 °C.[27] This increase in C_i with temperature was postulated to be due to an increased permeability of the monolayer to ions, without reference being made to the mechanism of this increased permeability.

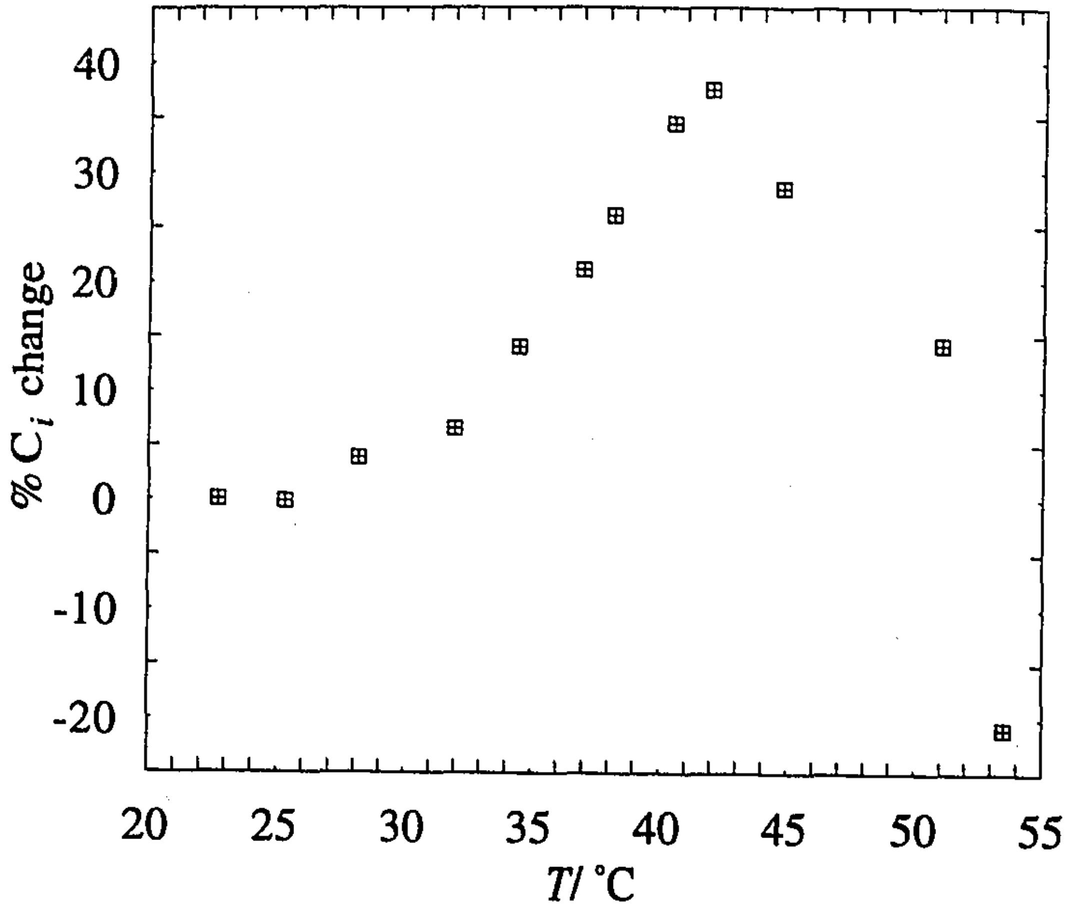

Figure 3.5. The % change in the differential capacitance (C_i) of a $C_{16}S$/Au electrode is reported as a function of the temperature. A C_i value of 1.2 µF/cm^2 was obtained at 23 °C in 0.1 M KBr solution from the charging current at -75 mV of the CV obtained at 100 mV/s from +500 mV to -100 mV.

3.3.3. Cooling Curves and Hysteresis Phenomena: Type A electrodes exhibit marked hysteresis on cooling (Figure 3.6). An important component of the hysteresis is a dependence on the rate of cooling. For example, an electrode poised above T_m^e will show a continuously decreasing current over a time scale of 0.5-2 hr. Cooling at the same slow rate as heating (*i.e.* 0.2 °C/min) has an obvious kinetic component. What is particularly significant is the fact that cooling curves exhibit neither maxima (nor minima) paralleling those seen during heating.

Reheating a Type A electrode which has undergone a heat/cool cycle leads to a type C electrode. Evidently, heating an electrode past its characteristic T_m^e value is akin to some form of annealing.

Different conditions were attempted in order to restore the T_p^e and T_m^e features to an annealed electrode. For example, re-incubation of the $C_{18}S/Au$ electrode in an RSH solution, cooling at -20 °C (for 48 hr), and maintaining it at 23 ± 2 °C for > 10 days re-establishes neither T_p^e nor T_m^e features. The only condition which has successfully restored these features is incubation in ambient atmosphere at 5 °C for 18 hr.[38] These experiments suggest that the marked hysteresis effects are linked to the kinetics of monolayer reorganization.

3.3.4. Mixed Monolayers: The thermal properties of SAMs formed from coadsorption of $C_{14}SH$ and $C_{18}SH$ or $C_{16}SH$ and $C_{18}SH$ on Au were also investigated using ferricyanide reduction. A single maximum in the Faradaic current was observed at 44 ± 3 °C (n= 5 electrodes) for the $C_{14}S/C_{18}S/Au$ mixed system (Figure 3.7A) and at 50 ± 1 °C (n= 1 electrode) for the $C_{16}S/C_{18}S/Au$ system. These temperature maxima fall between the T_m^es observed for the one-component SAMs and suggest that mixing of the 2 different chain length RSHs occurs in the monolayers. Although infrequent, phase separated SAMs have been observed for the $C_{14}S/C_{18}S/Au$ case, where current maxima were detected at ~ 35 °C and ~ 55 °C (Figure 3.7B). It is not evident at the present time what factors drive the self-assembly of different chain length alkanethiolates into phase-segregated domains.

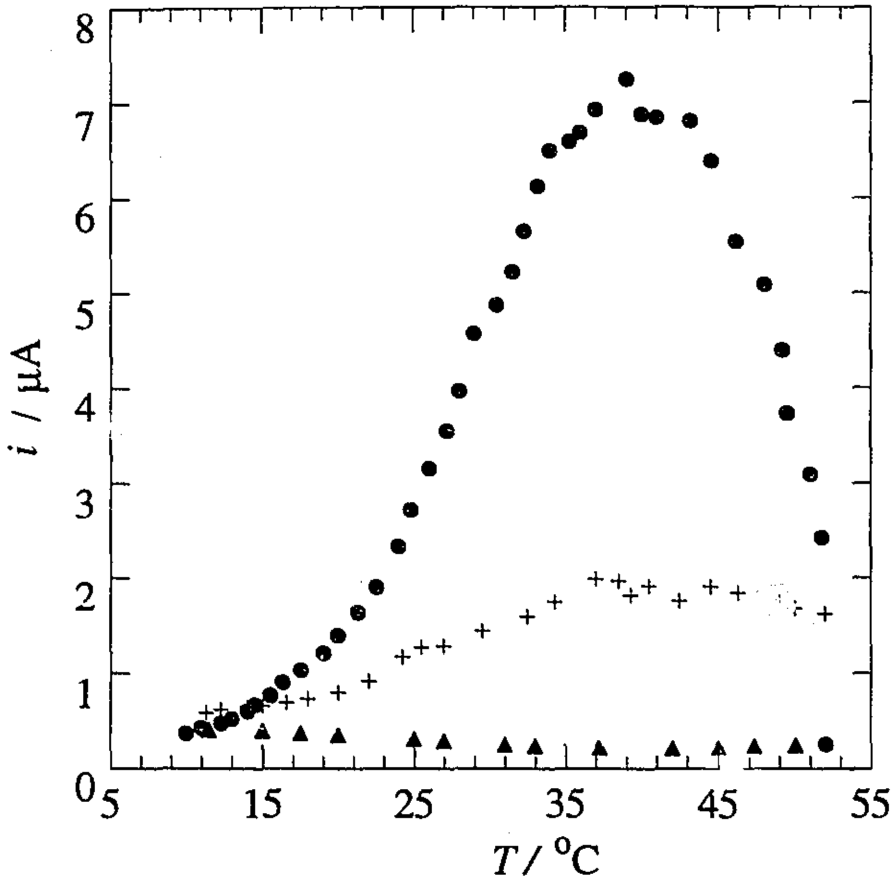

Figure 3.6. Electrochemical thermogram showing a heat-cool-reheat cycle for a $C_{16}S/Au$ electrode (Figure 2.3 in the previous chapter). The $C_{16}S/Au$ electrode was cycled as follows: (●) initial heating curve; (▲) the $C_{16}S/Au$ electrode was cooled to 15 °C and incubated in air at 5 °C for 18 hr; (+) $C_{16}S/Au$ electrode was subjected to a second heating cycle.

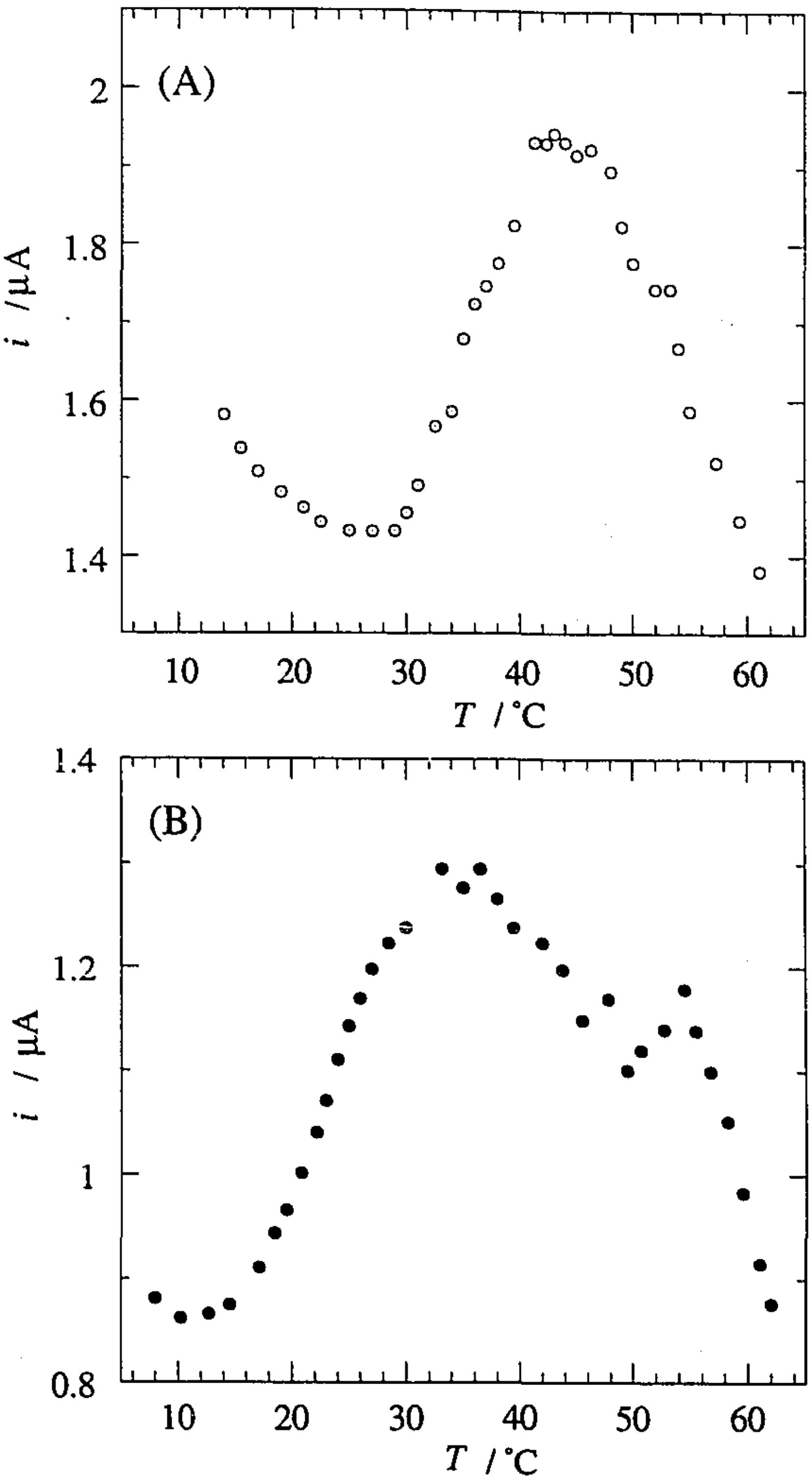

Figure 3.7. Electrochemical thermograms for $C_{14}S/C_{18}S/Au$ electrodes. (A) Mixed monolayer shows a single i maximum at $T_m^e = 44 \pm 3$ °C. (B) Mixed monolayer exhibits i maxima at $T_m^e = 35$ °C and 55 °C.

3.4. Discussion

3.4.1. Structural Features of RS/Au SAMs Probed by Electrochemistry

The current maxima observed at RS/Au monolayers are consistent with the occurrence of thermally-induced structural changes in these films which manifest increased rates of electron transfer. We have shown that the temperature phenomena reported here are not a result of the choice of probe (redox or non-redox active) or of the electrochemical technique used to study these SAMs, neither are they caused by potential-induced reorganization of the adsorbed RSH monolayer. Instead, our results clearly indicate that these current maxima occur at well-defined temperatures which are determined solely by the RSH chain length and the presence of endgroup interactions, such as hydrogen bonding.

Desorption of the RS adsorbate from the Au surface, disordering of the RS chains (*via trans-gauche* kink formation), and chain untilting transitions are all possible structural events that can occur in SAMs with increasing temperature. Whitesides *et al.* report that desorption of the RS chains (for R= *n*-alkane) from the Au surface occurs at temperatures higher than 70 °C. The rate of RS desorption was found to be dependent on the temperature, the alkyl chain length, and the ambient medium (*i.e.* organic solvent *vs.* air).[63] However, since the desorption of RS chains from the Au surface is expected to result in continually increasing current values with increasing temperature, this is not an important mechanism in aqueous solution, in the temperature region studied here. As is apparent in Figures 3.2 and 3.5, once the RSH-modified Au electrodes reach a certain temperature, defined by the RSH chain length, the Faradaic and capacitive currents decrease drastically upon further heating. Molecular dynamics simulations[33-35] predict the gradual untilting of $C_{15}S$ chains adsorbed on a Au (111) surface between 25 °C and 100 °C, followed by free molecular rotation and an increase in the density of *gauche* chain defects throughout the monolayer at higher temperature. In support of these predictions, RAIRS studies of long-chain RS molecules adsorbed onto polycrystalline[32] and Au (111)[30,31] substrates have led to the conclusion that *gauche* conformational defects gradually appear upon heating. Although these studies predict thermally-induced changes in both the chain orientation and chain conformation of RS/Au SAMs, it is not immediately evident how these changes in the monolayer film structure would manifest themselves in the properties of the monolayer as a barrier to electron transfer.

Comparison with the thermal properties of phospholipid bilayers provides insight into the physical events occurring in RS/Au SAMs upon heating. The electrochemical thermograms shown in Figure 3.2 for the RSH-modified Au electrodes in fact show striking parallels to the thermograms of diacylphospholipids of equivalent carbon chain length, where pre-transitions and gel-to-liquid crystalline transitions have been extensively characterized by calorimetric and spectroscopic techniques.[64] The excellent correspondence in the pre-transition (T_p) and main transition (T_m) temperatures between the RS/Au monolayers studied here, and *n*-diacylphosphatidylcholines dispersed in water as bilayer vesicles, suggests that there are similar mechanisms for chain reorientation/melting in these two systems. The remarkable 1:1 correlation between the T_m values (r= 0.998) and 0.7:1 correlation between the T_p values (r= 0.920)[38] of these two systems also implies that the chemisorbed monolayer has values of ΔG, associated with chain melting, which are similar to the hydrated, oriented phospholipids. We have suggested that this correlation arises because the chain packing configuration and density are very similar in the case of phospholipids packed in bilayer membranes and alkyl thiols chemisorbed at a Au surface. In the bilayer lipid membrane case, the chain packing density and orientation is dictated by the size of the phospholipid headgroup. For example, phosphatidylethanolamines (PEs), due to their smaller headgroup, have a *ca.* 20% larger chain packing density than the corresponding phosphatidylcholines (PCs).[64] The result is that PEs exhibit T_ms which are 15-20 °C higher than PCs.[64] In the RS/Au monolayers, anchoring of the thiols to the underlying Au surface and extensive lateral Van der Waals interactions are sufficient to pack the chains into an all-*trans*, extended conformation at reduced temperatures. X-ray diffraction studies have determined that the RS chain packing configuration and density is dictated by the arrangement of Au atoms on the surface.[65] Stripping of underpotential-deposited Cu[59,66,67] gives a surface roughness factor ranging from 1.1-1.5 for the bulk Au electrodes used in this study, while Pb UPD[44] reveals the surface crystalline domains to be 70% Au (110) and 30% Au (111). The areas per 2 RSH chains (*i.e.* 1 unit cell)[30,31,33,34] are therefore 47.2 $Å^2$ and 43.5 $Å^2$ for the (110) and (111) domains, respectively[65]. Furthermore, the RS chain tilt from the surface normal is ~ 30° for Au (111) and ~ 40° for Au (110).[65] By comparison, *n*-diacylphosphatidylcholines occupy an area of 43-48 $Å^2$ per molecule in their condensed phase and exhibit a chain tilt of ~ 30° from the bilayer normal.[64,68] Therefore, the phospholipid headgroup and the Au lattice serve the same purpose- to enforce a defined packing density and orientation on the alkyl chains. It is reasonable therefore that the structural film properties in these two systems are modulated by temperature in a similar manner.

Clearly, RS/Au monolayers undergo a thermally-induced order/disorder transition which leads to maxima in the $Fe(CN)_6^{3-}$ cathodic current and in the capacitive current (Type A electrodes).

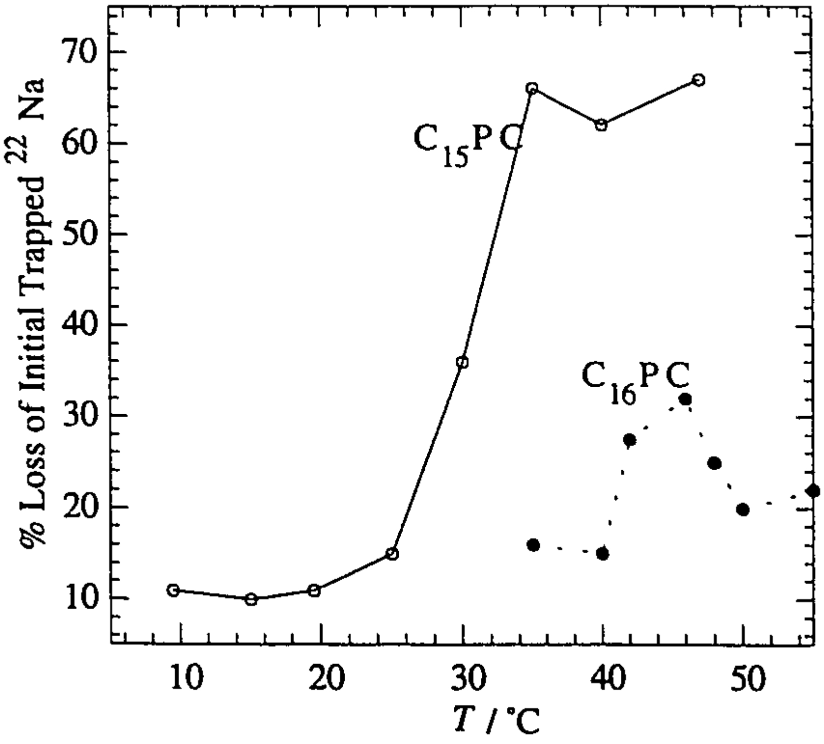

Figure 3.8. A large increase in membrane permeability is observed at $T = T_m \pm 5$ °C for *n*-diacylphosphatidylcholine lipid vesicles. This behavior is illustrated here for $C_{15}PC$ (T_m= 32 °C) and $C_{16}PC$ (T_m= 41 °C). The permeability data was obtained from reference 70.

Again, comparison with lipid bilayers is insightful given that they too experience a small increase in the transmembrane ion flux at T_p and a large flux increase at T_m (Figure 3.8).[69,70] Experimental[69,70] and theoretical studies[70,71] have established that substantial packing dislocations and grain boundary type defects arise as a result of the coexistence of gel and liquid crystalline phases at the T_m. These 'defects' are transient and are believed to correspond, in physical terms, to rapidly opening and closing pores or defect regions[69-71] capable of accommodating ions (Na^+, K^+) and water. The geometry of these "pores" is not well understood but they could be small radii cylinders and/or small width lines (stripes). A pre-transition, T_p, is also well documented for hydrated phospholipids and is associated with a tilt/untilt transition, where the phosphatidylcholine acyl chain orientation, with respect to the bilayer normal, changes from ~ 30° to ~ 0°.[68] The overall effect is a membrane *thickening* of ~ 12% as the bilayer is heated through T_p.[64,68] Related to this, molecular dynamics calculations predict an almost 11% increase in the thickness of a $C_{16}S$/Au SAM as a result of a chain untilting process.[34] In the electrochemical SAM experiment, we find that the current further increases past T_p^e, and only decreases once T_m^e has been exceeded. The post-T_m^e current decrease probably arises because the monolayer is now liquid-like and is relatively free of the permeability-mediating phase boundary defects. Thus, analogous to bilayer lipid membranes, the Faradaic current maxima observed for RSH-modified Au electrodes are believed to arise from transient regions of enhanced permeability of the monolayer to redox molecules along tilt/untilt boundaries (at $T = T_p^e$) and at coexistence boundaries between ordered and disordered alkyl chain domains (at $T = T_m^e$) (Scheme 3.1).

Gel-to-liquid crystalline phase transitions (*i.e.* at T_m) in lipid bilayers result in both a ~ 30% decrease in membrane thickness and ~ 30% increase in area, leading to a small overall volume change.[64,68] Similarly, alkanes exhibit very small density changes (*i.e.* 0.5%) on melting.[19] Disordering of the RS chains at T_m^e would also require a volume of expansion, albeit small. For the polycrystalline Au electrode surfaces, the discontinuities or grain boundaries arising between the surface domains (~250 Å in diameter)[60] could provide the volume of expansion required by the RS chains during a chain melting process. On single-crystal Au substrates, steps between the large atomically-flat crystalline terraces can act as the defect regions if perfect monolayer-substrate epitaxy is present. Grazing incidence X-ray diffraction studies[29] report that the RS domain size which acts as a co-operativity unit is quite small. More specifically, the characteristic ordered, crystalline monolayer domain size of $C_{12}S$ deposited from ethanol solution onto flame-annealed Au (111) single-crystals was measured as being only ~ 90 Å, even though the Au substrate domain size was > 1000 Å.[29]

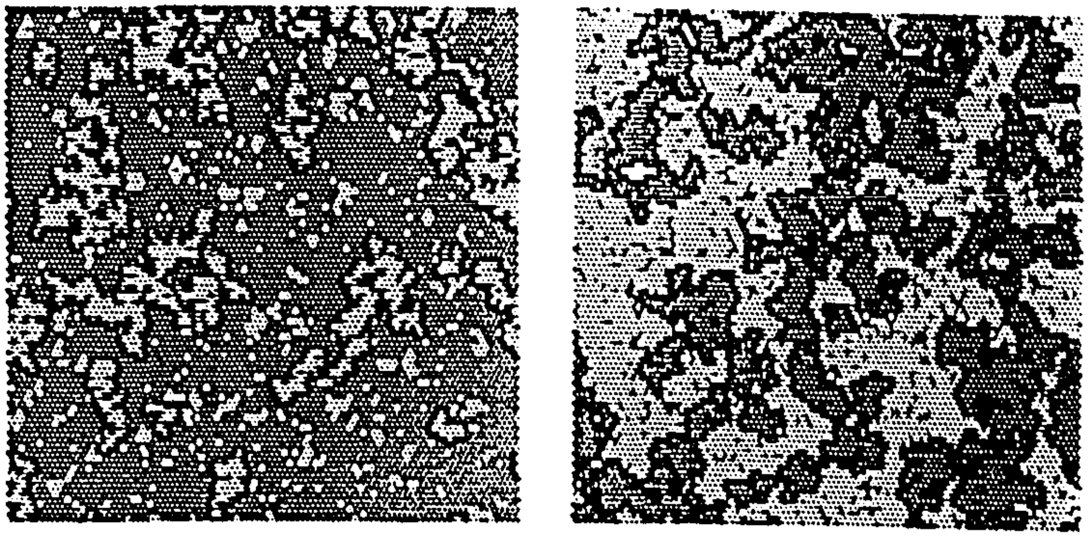

T_m^e - 1 °C

T_m^e + 1 °C

Scheme 3.1. A physical representation of the dynamic monolayer heterogeneity which is proposed to exist in a RS/Au surface near the order/disorder phase transition temperature (*i.e.* $T = T_m^e$). Ordered RS chain domains are shown by dark grey regions and disordered liquid-like domains are represented by light grey regions. Domain boundaries between the coexisting ordered and disordered regions are shown in black. This schematic representation is presented for lipid membranes in reference 70.

The crystalline RS chain domains can obviously have different dimensions from those of the underlying substrate's crystalline domains. The overall effect may be likened to a mosaic pattern of crystalline chain domains superimposed on a larger array of crystalline Au domains. Thus, in the case of the RS/Au monolayer, grain boundaries and steps in the Au surface, as well as edges existing between islands of crystalline chains, are proposed to provide the necessary area required by the expanding monolayer during melting.

Unlike phospholipid bilayers, the order/disorder transition in the RS/Au SAMs occurs over a broad temperature range (Figure 3.2). This can be due to the polycrystalline nature of the Au substrate which would produce ordered chain domains with a spectrum of differing packing densities and orientations. As a result, our electrochemical thermograms would reflect a superposition of T_m^es for the different phases. Another contributing factor to the thermogram broadness may be the direct bonding of the sulfur headgroup to the Au, which would restrict the co-operativity of the transition by restricting place exchange of the alkyl chains. Solid-supported Langmuir Blodgett (LB) monolayers of the cadmium salts of long-chain fatty acids (C_{18}, C_{20}, and C_{22}) also show broad chain disordering transitions, as reported by electron diffraction.[72] The temperature range reported for the transitions of stearic acid (C_{18}) and arachidic acid (C_{20}) is very similar to that observed electrochemically for the $C_{18}S$/Au and $C_{20}S$/Au monolayers (Figure 3.2). In stearic acid (C_{18}) LB monolayers, the onset of chain disordering is observed at 30-35 °C and the transition peaks at 55-60 °C, while disordering of the arachidic acid (C_{20}) chains starts at 50-55 °C and the transition peaks at 70-80 °C.[72] By comparison, the $C_{18}S$/Au monolayer pretransition is at 44 ± 5 °C and the main transition occurs at 53 ± 2 °C. For the $C_{20}S$/Au, the pretransition and main transition occur at 56 ± 2 °C and 63 ± 2 °C, respectively. In the fatty acid LB case, the monolayer is only physisorbed to the underlying solid support, so that the broadness of the chain disordering transition in this system cannot be attributed to a strong headgroup/substrate interaction. However, both the covalently bound RS monolayers and the physisorbed fatty acid LB films share a similar type of 2D organization, so that their broad chain order/disorder transitions may well be a manifestation of melting in two-dimensions[73]. In the fatty acid LB films, a true, chain length-independent melting of the headgroup lattice also occurs at 110 °C.[72,74] The terminally affixed alkyl chains will, in the case of the RS monolayers, prevent melting to an isotropic state, just as the polar headgroup/water interface does in the case of bilayer phospholipids.

The thermal behavior of RS/Au electrodes annealed during the self-assembly process and the marked hysteresis observed for as-deposited RS/Au monolayers during heat-cool-reheat cycles in our electrochemical experiments further suggest that chain order/disorder transitions in these SAMs are not readily reversible. Finklea *et al.* also report an irreversible decrease in both the interfacial film capacitance and the apparent rate constant for the reduction of the pendant Ru(III) group upon heating mixed $HS(CH_2)_{15}CONHCH_2pyRu(NH_3)_5^{2+}/HS(CH_2)_{15}COOH$ monolayers.[27] Chain entanglement and restricted lateral chain movement due to the covalent sulfur-Au interaction may prevent the rapid re-ordering of the RS chains (Scheme 3.2). Interestingly, an IR spectroscopic investigation of the temperature-induced structural changes in solid-supported fatty acid LB monolayers reveals that thermal annealing causes disorder in the alkyl chains which is long-lasting (*i.e.* > 6-10 hrs).[75] Swalen *et al.* point out that these results are in marked contrast to the accepted mechanism of the annealing process, whereby heating of most materials at temperatures close to the melting point improves order.[75] The observation that chain order/disorder transitions in 2D RS/Au and fatty acid LB monolayers are not readily reversible casts serious doubt on the use of a thermal annealing step to remove packing defects in these SAMs, without inducing disorder or changes in the monolayer structure.[76] In fact, STM studies of SAMs (R= C_8, C_{10}, and C_{12}), under UHV conditions have shown that thermal annealing at ~ 80-100 °C leads to partial desorption of the RS chains from the Au (111) surface, and that a reconstruction of the alkanethiolate registry from a c(4x2) supperlattice of the $(\sqrt{3} \times \sqrt{3})R30°$ unit cell to a striped p x $\sqrt{3}$ lattice overlayer results.[77,78] Thus, prolonged incubation ot the RS/Au electrode in the thiol solution at ambient temperature is a preferable alternative to thermal annealing for healing film defects.

We conclude that SAMs which have been prepared under conditions conventionally reported in the literature (*i.e.* incubation times in solution ranging from minutes to hours) and/or have been annealed (at $T > T_m^e$) may be viewed as assemblies of predominantly all-*trans* chains (as reported by RAIRS) with some degree of short range order. This short range order is however so limited that the domain sizes necessary to manifest a phase transition are not obtained. The limited order of conventionally prepared monolayers has been reported to be caused by an incomplete film reorganization in the self-assembly process.[29] Recent molecular dynamics calculations by Siepmann and McDonald support these conclusions, as they predict that there is a minimum domain size (~ 200 molecules) that must exist in order for a phase coexistence region to be manifested in long-chain RS/Au SAMs.[79] More importantly, the film phases or discontinuities that are crucial for the observation of chain order/disorder transitions are intrinsic to SAMs prepared under the experimental conditions described here. Firstly, we find that only prolonged incubation (*i.e.* days to weeks) in monolayer forming solutions produces RSH-modified Au electrodes which exhibit the current features shown in Figure 3.2. Chain ordering and crystallization has been shown to be a very slow process which occurs over a period of days[7,80], and is accompanied by both RSH-assisted reconstruction of the Au surface lattice, dissolution of Au surface features, and place-exchange of RS adsorbates at defect sites with free RSH molecules in solution[7,65,81]. Secondly, the thermal history of the monolayer and surface morphology of the electrode are important. The complex thermotropic behavior described above does not arise for all as-prepared electrodes, nor for any thermally annealed and aqua regia-etched electrodes. Chain re-ordering kinetics appear to play an important role in these systems, where the condition of the substrate (*i.e.* aqua regia-treated electrodes) is a confounding factor.

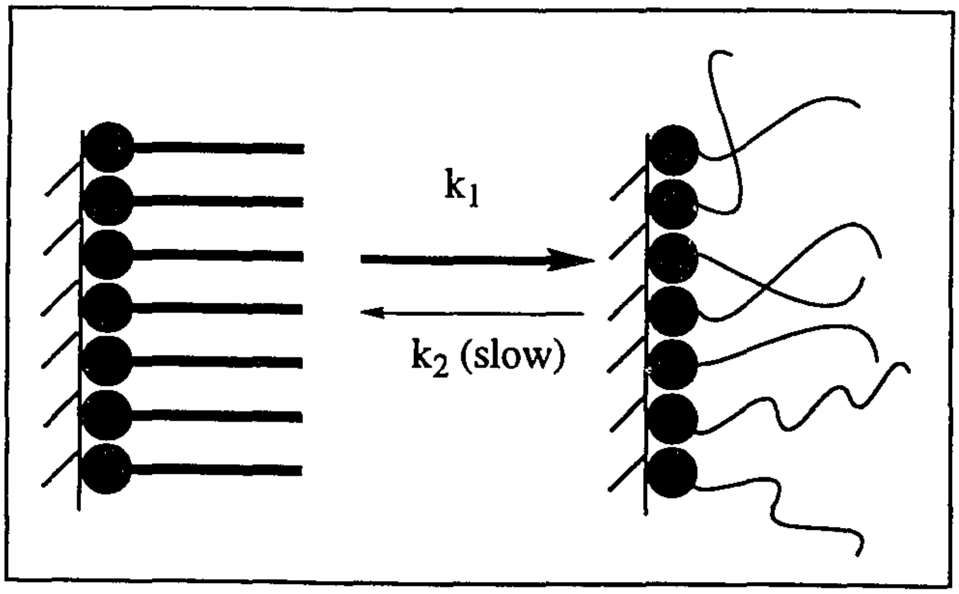

Scheme 3.2. Chain re-ordering kinetics in thermally annealed RS/Au monolayers are very slow (*ca.* 18 hr at + 5 °C). Chain entanglement and restricted lateral chain movement due to the covalent sulfur-Au interaction may prevent the rapid re-ordering of the RS chains.

3.4.2. Mechanism of Electron Transfer

Finally, we would like to note that our approach in these studies has been primarily to use a redox-active species to investigate thermally-induced film structural changes, rather than as a direct probe of the electron transfer mechanism across RS/Au SAMs. Four extreme descriptions of the electron transfer mechanism are shown in Figure 3.9. Our results require a re-evaluation of the electron transfer mechanism.

Reference to Figure 3.10A establishes that the voltammetry signatures of these electrodes is similar to many of those reported in the literature[14,17,20,21]. For example, at temperatures above and below the apparent T_m^e (*i.e.* ≤ 45 °C and > 55 °C), the *i/E* curves increase slowly with increasing negative potentials and they appear to be "dog-leg" shaped. Near the apparent T_m^e (50-55 °C), the *i/E* curves are sigmoid-shaped. Both types of curves are characteristic of monolayer-coated electrodes whose surface is pinhole-covered or whose electrode kinetics adhere to a CE or EC mechanism.[82] Previous studies of the electron transfer barrier properties of RS/Au SAMs report exponentially decreasing Faradaic currents with increasing monolayer thickness [14,16,20,43] and a curved linear free energy relationship (log *i vs. E*) or Tafel plot[14,15,21,25,26]. Defect-dominated electron transfer[21,39-42] and electron tunneling (either through-space[25] or through-bond[26,83] have been presented as the dominant mechanisms. While these descriptions are internally consistent, they are not likely to be co-incident for what is ostensibly the same system. On the other hand, the mechanistic model which is consistent with the results here, and the results (but not necessarily the analyses) reported in many other SAM electrochemical studies is an *assisted permeation* model. On the strength of the parallels noted above between RS/Au monolayers and lipid bilayer permeabilities, we propose that redox probes partition into the SAM and diffuse through the monolayer until a distance allowing for efficient electron transfer is achieved. Density fluctuations are created in the conformationally labile alkyl chain ensemble by simple thermally activated *trans-gauche* bond interconversions. These dynamic heterogeneities [70,71] in the monolayer structure facilitate partitioning and diffusion of the redox probe molecule in the monolayer. The nature of these heterogeneities is not specifically known (here or in lipid membranes), but they *need not* be water-filled pores or channels. Any localized perturbation of the surface dipole moment of the monolayer, triggered by a density fluctuation, would be sufficient to further assist the partitioning of the probe molecule into the monolayer. Parallel but uncompetitive mechanisms would include passive permeation of the redox probe and electron tunneling from a probe molecule to the Au electrode, where the probe is completely excluded from the monolayer. A number of the electrochemical features described in Figures 3.1-3.4 and 3.10, and elsewhere[14,16,17,38,43,45,46,84], are consistent with this assisted permeability mechanism. It is also important to emphasize that the film discontinuities which give rise to the current maxima described here are *not* the generic monolayer defects reported to cause film imperfection. These latter film structural defects are associated with thin patches at monolayer collapse sites, Au substrate defect structures which interrupt the adsorbate registry, monolayer grain boundaries, and regions where a co-adsorbate is clustered. The modified electrodes discussed here exhibit the properties of being thoroughly blocked. At $T < T_m{}^e$, the RS/Au electrodes show reduced capacitance values, greatly attenuated $Fe(CN)_6{}^{3-}$ reduction currents compared to bare Au electrodes, and the absence of voltammetric peaks or plateaus in the cyclic voltammograms characteristic of pinholes or bare patches in the monolayer film[82]. Cu UPD of our $C_{18}SH$-modified electrodes yields monolayer film coverages ranging from 0.990-0.998[39-42,85], indicative of a low defect density. Instead, the sites of enhanced passive diffusion responsible for the current maxima, as in Figure 3.2, are clearly under thermodynamic control. This is evident given that they exist at defined temperatures and are determined solely by the chain length of the RS adsorbate.

Moreover, we note that the electrochemical thermograms (Figure 3.2) are consistent with permeability-enhancing defects existing at temperatures considerably lower than $T_m{}^e$. Recent studies in our labs[86], using solid-state deuterium NMR and FT-IR spectroscopy, confirm that related RS SAMs formed on Au nanoparticles retain a substantial disordered component at temperatures far below the observed T_m value. For example, for $C_{18}S$/Au nanoparticles, chain disordering begins at 30 °C (FT-IR) and 80 °C (^2H NMR) below the observed T_m. These parallel studies also establish that the density of chain defects (measured as disorder in solid-state ^2H NMR spectra and the population of *gauche* bonds in FT-IR spectroscopy) greatly increases as the T_m is approached.

A permeation mechanism has been previously dismissed on the assumption that the large size and multiple charge of the redox active species will prevent partitioning into the hydrophobic region of the monolayer.[14] However, a large molecular size both decreases the Born charging energy (the energy associated with dissolving an ion in a low dielectric medium[87]) and enhances partitioning. Counterion neutralization of charge and specific solvation by water should also be considered, as both factors will decrease the redox ion's charge density considerably. Ferricyanide, for example, has been shown to exist almost exclusively in the $KFe(CN)_6{}^{2-}$ form and not as $Fe(CN)_6{}^{3-}$ in aqueous solution.[88,89] Arguments which dismiss the likelihood of ferricyanide partitioning and diffusing across a hydrocarbon monolayer on the basis of an erroneous evaluation of charge, and also neglect the role that hydration plays in reducing electrostatic energy barriers are therefore misleading. The role that solvation plays on the measured rate constants introduces further complications, given that the E° of the $Fe(CN)_6^{3-/4-}$ couple undergoes an iterative cathodic shift, totalling 1.4 V, as the extent of hydration decreases.[90] A model wherein the $Fe(CN)_6^{3-/4-}$ couple exists in a number of hydration states[90] in the monolayer could account for the observed curvature in the Tafel plot (Figure 3.10B), and could also result in a redox mediation process being set up (Figure 3.9).

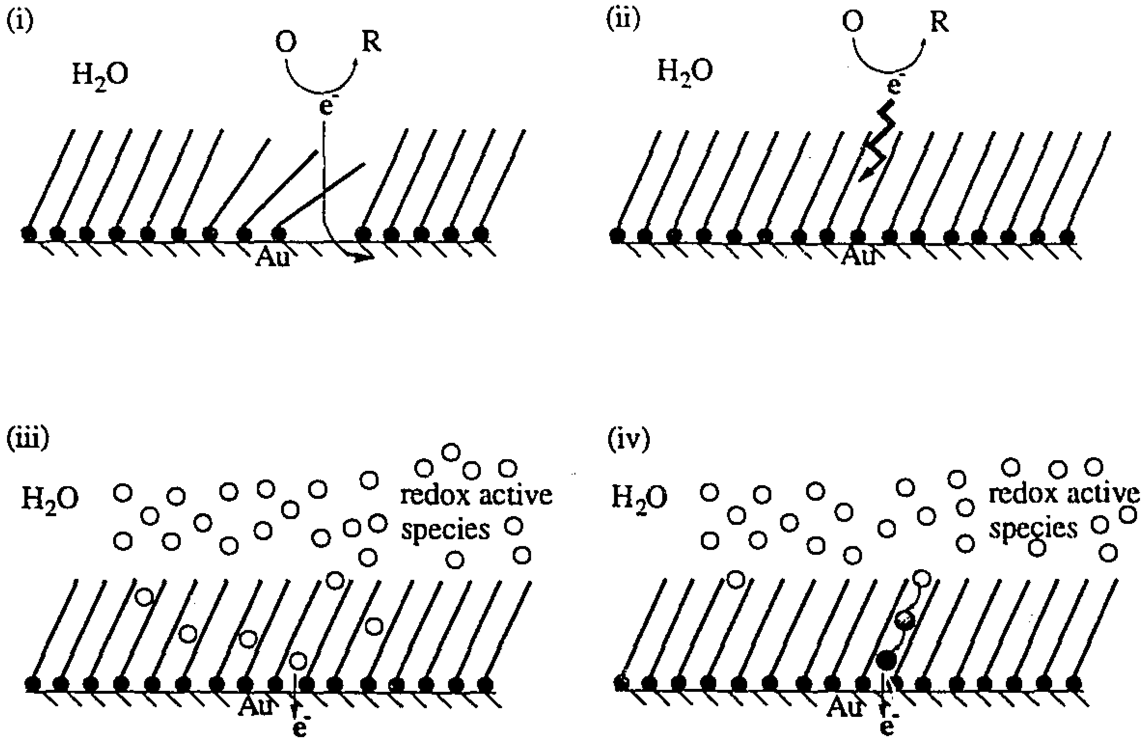

Figure 3.9. Possible mechanisms of electron transfer at RS/Au electrodes: (i) direct electron transfer at pinholes or other film defect sites; (ii) electron tunneling, either through-bond or through-space, across the full width of the film; (iii) permeation of the redox species through the monolayer and reaction at the electrode surface and (iv) redox species mediation wherein the redox couple exists in an number of hydration states that have different $E^{\circ\prime}$ values. (Figure 1.5 in Chapter 1)

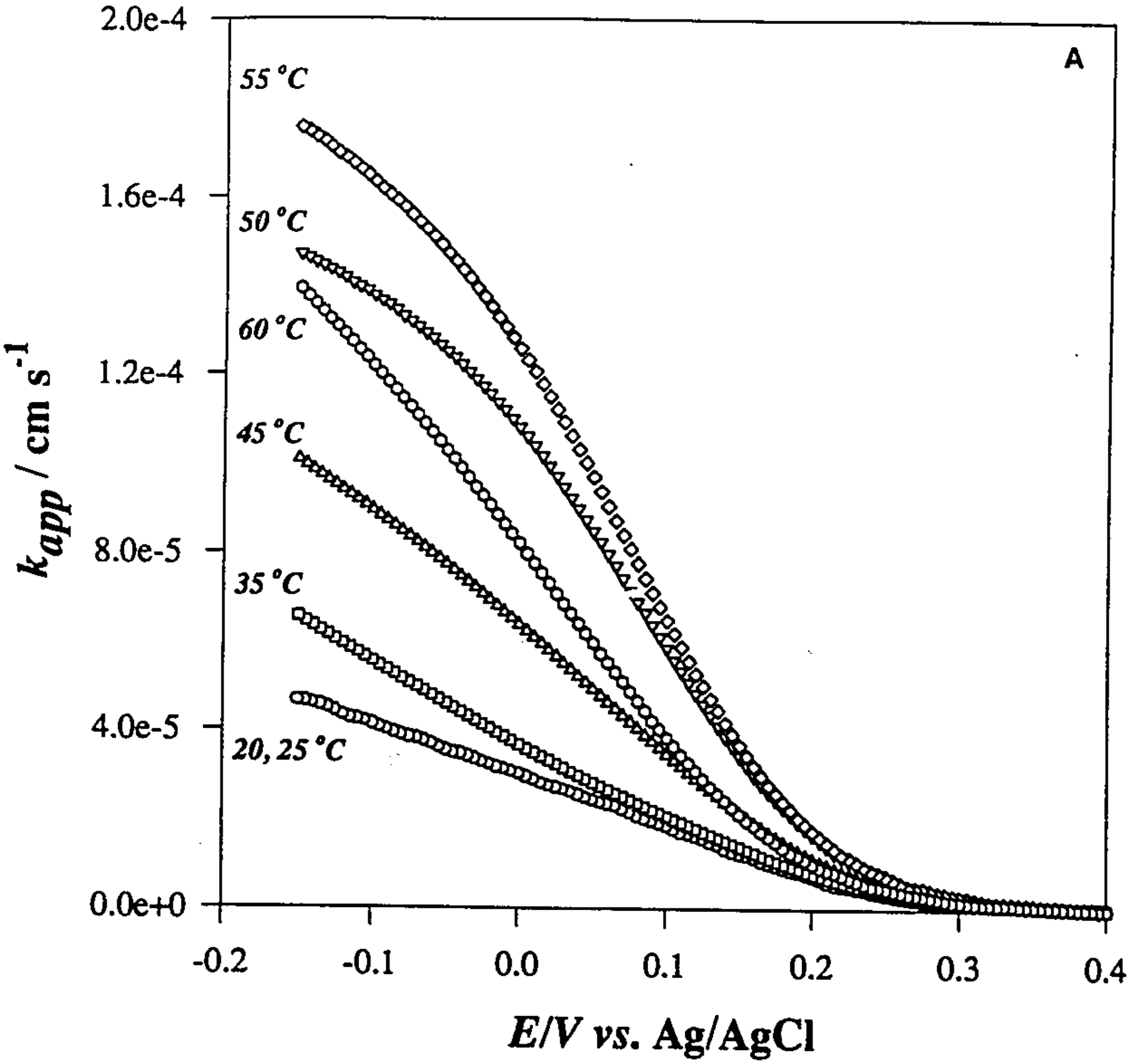

Figure 3.10. (A) k_{app}/E curves for $Fe(CN)_6^{3-}$ reduction at a Type A $C_{18}S/Au$ electrode (T_m^e = 55 °C) at T= 20, 25, 35, 45, 50, 55, and 60 °C. $k_{app} = i_c/nFAC$; where i_c is the cathodic (*i.e.* reduction) Faradaic current in amps (C/s), n= number of electrons transferred in the redox step (n=1), F is Faraday's constant (9.65 x 10^4 C/mol), A is the electrode area (0.026 cm^2), and C is the bulk $Fe(CN)_6^{3-}$ concentration (20 x 10^{-6} mol/cm^3).

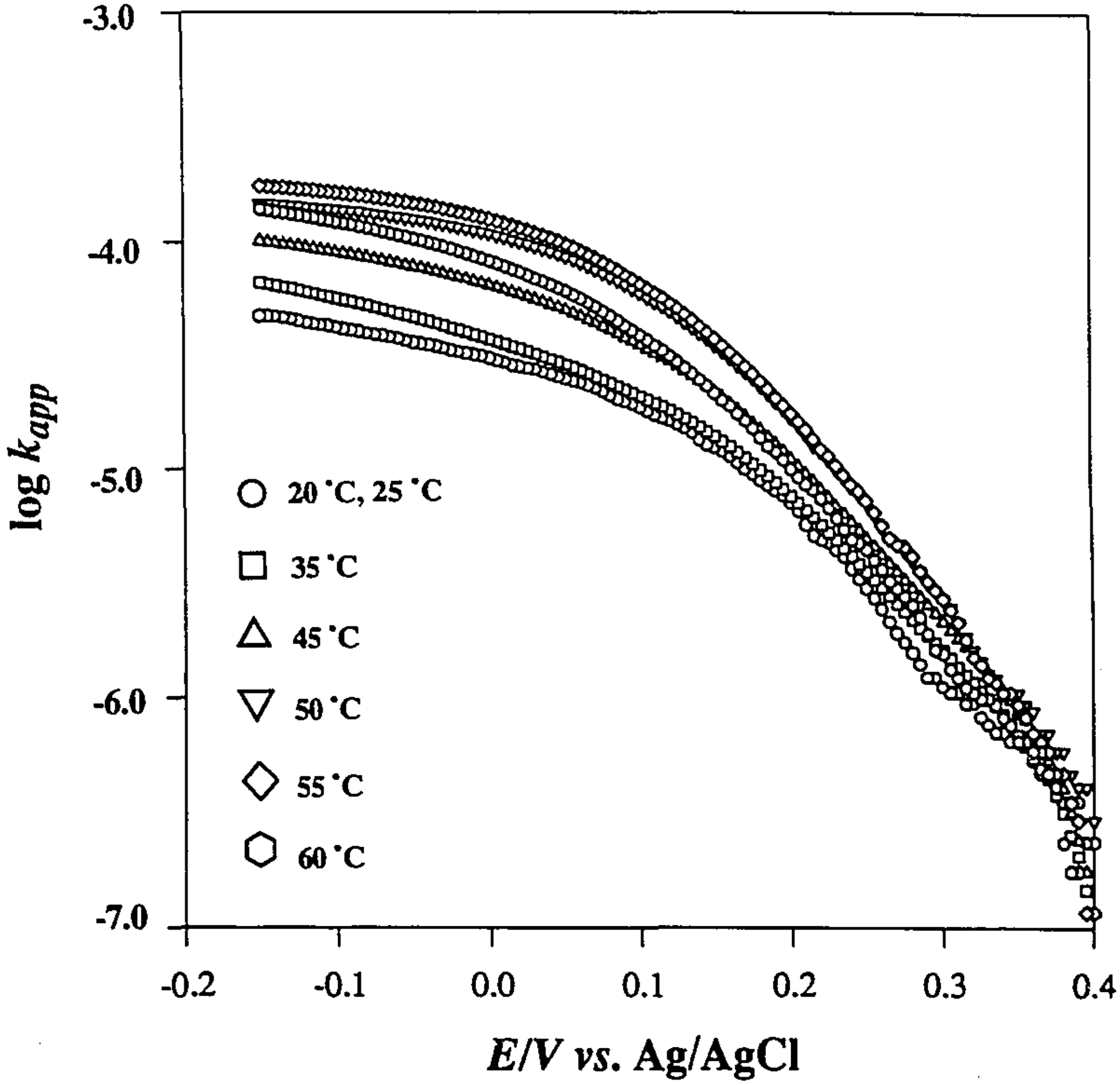

Figure 3.10. (cont'd) (B) Tafel plots (log k_{app} *vs.* E) for $Fe(CN)_6^{3-}$ reduction at a $C_{18}S$/Au electrode (T_m^e = 55 °C) at T= 20, 25, 35, 45, 50, 55, and 60 °C.

An assisted permeation mechanism is also consistent with the results from several electrochemical studies of RS/Au SAMs formed from terminally substituted RSHs (*eg.* ω-group= OH, -COOH, $-NH_2$, $-N(CH_3)_3^+$). In these studies, it has been definitively shown that the monolayer surface charge and hydrophobicity/hydrophilicity balance of the redox probes exert a dramatic effect on both the double layer capacitance[61,91] and the electron transfer rates across alkylthiol SAMs[17,22-24]. These studies establish that electron transfer proceeds through the entire thickness of the monolayer, rather than through a small number of defect sites, and that the electron transfer rates are largely determined by preconcentration (partitioning) or permeability factors.[17,22-24] The redox species is concentrated (or depleted) at the electrode surface *via* electrostatic interaction between the charged ω-substituent and the ionic redox complexes. Hydrophobic/hydrophilic interactions between the monolayer surface and the solvated redox species[17] are also affected by the change in the surface dipole moment of the monolayer assembly, even if the ω-substituent is an uncharged species[61,91]. These results clearly point to the important roles that the redox species' solvation and charge play on the permeation and facility of electron transfer at RS/Au monolayers. A tunneling mechanism tacitly assumes that the closest the redox probe can get to the electrode is defined by the monolayer thickness. These varied reports[17,22-24] clearly show that the contrary is a more common occurrence.

The assisted permeability model can also provide insight into recent results from the Majda[84] and Crooks[45,46] labs. Both groups have studied the electrochemical response at mixed monolayers composed of long-chain alkylthiols and a smaller co-adsorbate (*i.e.* ubiquinone Q50 and 1,4-hydroxythiophenol). Although both groups suggest that these rogue molecules form well-defined pinholes or channels through which redox couples can readily pass, it is also reasonable that these additives nucleate alkyl chain disordering events on a local level. In this regard, the additives would serve to melt adjacent domains of alkylthiolate chains[45,46,84] and provide regions of packing dislocations. Crooks and co-workers actually note that the most hydrophobic and least highly charged redox probes penetrate the "pores" most easily.[45,46] A hydrophobic pore structure inferred from these observations is consistent with our statement above that sites of enhanced permeability need not be structurally equivalent to aqueous channels or pores to be effective. Majda *et al.*[84] suggest in their studies that channel formation has occurred, but acknowledge that the co-adsorbate may create "defect sites" and not well-defined channels. Although Crooks[45,46], Rubinstein[40-42], and Majda[84] have fitted their voltammetry data to a microelectrode/pinhole/pore model, a CE process is kinetically equivalent to the microelectrode model[82] and is intuitively reasonable. Our assisted permeation model, of course, is nothing more than a CE process where the "chemical" step is a complex combination of partitioning/diffusion processes preceding electron transfer.

The dependence of the electron transfer rate constant on the SAM thickness and the applied voltage has been an integral element in the advocacy of a transmonolayer tunneling mechanism[14,16,19,21,43]. It is interesting to point out that ion permeability experiments performed on planar bilayer lipid membranes also yield a reasonable fit to an $i \propto \exp(-\beta d)$ relationship.[92] In this case, β (the attenuation constant) is equal to 0.45 Å^{-1} for chains from $n = C_{14}$ to C_{22}. Tunneling, on the other hand, will have a negligible to small (positive) temperature dependence over the range studied here and is not consistent with any of the three classes of *i*/*T* curves observed in all of our studies. We also observe the same *i*/*T* profile (Type A, Figure 3.1) when there is no Faradaic chemistry but only ion (*i.e.* K^+, Br^-) transport occurring. Tunneling has also been concluded based on the persistent observation of non-linear Tafel plots. Tafel plot curvature can of course have origins other than Marcus curvature within an electron tunneling formalism. A change in the rate determining step of a sequential reaction scheme (as in a CE process) can also lead to downwards curvature in a linear free energy relationship.

Clearly, determining the mechanism of electron transfer across SAMs is a difficult process given the complex interplay between all of the physical and kinetic processes occurring. Our ongoing studies in this respect are focusing on casting our experimental results in the form of a CE-partitioning mechanism so as to confirm the permeability mechanism proposed here. We are currently exploring electrochemical and interfacial chemistry approaches which provide molecular details of a monolayer permeation mechanism, being particularly aware of the role that the metal substrate plays in determining the alkyl chain surface density. Nonetheless, given the noted parallels to phospholipid membrane systems and the foregoing results, an assisted permeation mechanism is deemed to be much more important than tunneling for the RS/Au monolayers as studied.

3.5. Conclusions

Our studies show the electron transfer process from aqueous-based redox species across RS/Au SAMs to be a sensitive probe of film structure and thermodynamics. The striking correspondence between the thermotropic properties of RS/Au monolayers, lipid bilayer membranes, and solid-supported fatty acid LB monolayers demonstrate that discontinuities reminiscent of chain order/disorder transitions are indeed possible in these

SAMs, and that they are important in the control of the observed rate of electron transfer. Noted parallels to the thermodynamically controlled ion fluxes in lipid vesicles place the barrier properties of alkanethiolate SAMs into a new context, where partitioning/diffusion of the water-soluble electron transfer reagent into the thin film must be fully considered in the context of an assisted permeability mechanism. The thermal history of the monolayer is an important variable in these studies, as is an appreciation of the reactive form of the soluble redox couple. Finally, in view of these findings, it is more appropriate to consider RS/Au monolayers as dynamic structures which possess both rich thermodynamic phase properties and complex chain re-organization kinetics, rather than to view them as "well-behaved" hydrocarbon assemblies.

References

(1) Bishop, A. R.; Nuzzo, R. G. *Current Opinion in Colloid & Interface Science* **1996**, *1*, 127-136.

(2) Ulman, A. *MRS Bulletin* **6/95**, 46-51.

(3) Xu, J.; Li, H. *Journal of Colloid and Interface Science* **1995**, *176*, 138-149.

(4) Mandler, D.; Turyan, I. *Electroanalysis* **1996**, *8*, 207-213.

(5) Ulman, A. *Chem. Tech.* **3/95**, 22-28.

(6) Whitesides, G. M. *Sci. Am.* **9/95**, 146-149.

(7) Dubois, L. H.; Nuzzo, R. G. *Annu. Rev. Phys. Chem.* **1992**, *43*, 437-463.

(8) Whitesides, G. M.; Laibinis, P. E. *Langmuir* **1990**, *6*, 87-96.

(9) Bain, C. D.; Whitesides, G. M. *Angew. Chem. Int. Ed. Engl.* **1989**, *28*, 506-512.

(10) Ulman, A. *An Introduction to Ultrathin Organic Films From Langmuir-Blodgett to Self-Assembly*; Academic Press, Inc.: San Diego, CA, 1991.

(11) Laibinis, P. E.; Whitesides, G. M. *J. Am. Chem. Soc.* **1992**, *114*, 9022-9028.

(12) Yamamoto, Y.; Nishihara, H.; Aramaki, K. *J. Electrochem. Soc.* **1993**, *140*, 436-443.

(13) Volmer-Vebing, M.; Reynders, B.; Stratmann, M. *Werst. Korros.* **1991**, *140*, 19.

(14) Miller, C.; Cuendet, P.; Gratzel, M. *J. Phys. Chem.* **1991**, *95*, 877-886.

(15) Miller, C.; Gratzel, M. *J. Phys. Chem.* **1991**, *95*, 5225-5233.

(16) Becka, A. M.; Miller, C. J. *J. Phys. Chem.* **1992**, *96*, 2657-2668.

(17) Becka, A. M.; Miller, C. J. *J. Phys. Chem.* **1993**, *97*, 6233-6239.

(18) Demoz, A.; Harrison, D. J. *Langmuir* **1993**, *9*, 1046-1050.

(19) Slowinski, K.; Chamberlain II, R. V.; Bilewicz, R.; Majda, M. *J. Am. Chem. Soc.* **1996**, *118*, 4709-4710.

(20) Porter, M. D.; Bright, T. B.; Allara, D. L.; Chidsey, C. E. D. *J. Am. Chem. Soc.* **1987**, *109*, 3559-3568.

(21) Finklea, H. O.; Avery, S.; Lynch, M. *Langmuir* **1987**, *3*, 409-413.

(22) Chidsey, C. E. D.; Loiacono, D. N. *Langmuir* **1990**, *6*, 682-691.

(23) Doblhofer, J.; Figura, J.; Furhop, J.-H. *Langmuir* **1992**, *8*, 1811-1816.

(24) Takehara, K.; Takemura, H.; Ide, Y. *Electrochimica Acta* **1994**, *39*, 817-822.

(25) Chidsey, C. E. D. *Science* **1991**, *251*, 919-922.

(26) Finklea, H. O.; Hanshew, D. D. *J. Am. Chem. Soc.* **1992**, *114*, 3173-3181.

(27) Finklea, H. O.; Ravenscroft, M. S.; Snider, D. A. *Langmuir* **1993**, *9*, 223-227.

(28) Garrell, R. L.; Chadwick, J. E. *Colloids and Surfaces A: Physicochem. Eng. Aspects* **1994**, *93*, 59-72.

(29) Fenter, P.; Eisenberger, P.; Liang, K. S. *Phys. Rev. Lett.* **1993**, *70*, 2447-2450.

(30) Dubois, L. H.; Zegarski, B. R.; Nuzzo, R. G. *J. Electron Spectrosc. Relat. Phenom.* **1990**, *54/55*, 1143.

(31) Nuzzo, R. G.; Korenic, E. M.; Dubois, L. H. *J. Chem. Phys.* **1990**, *93*, 767-773.

(32) Bensebaa, F.; Ellis, T. H.; Badia, A.; Lennox, R. B. *J. Vac. Sci. Technol. A* **1995**, *13*, 1331-1336.

(33) Hautman, J.; Bareman, J. P.; Mar, W.; Klein, M. L. *J. Chem. Soc. Faraday Trans.* **1991**, *87*, 2031-2037.

(34) Hautman, J.; Klein, M. L. *J. Chem. Phys.* **1990**, *93*, 7483-7492.

(35) Mar, W.; Klein, M. L. *Langmuir* **1994**, *10*, 188-196.

(36) Evans, S. E.; Sharma, R.; Ulman, A. *Langmuir* **1991**, *7*, 156-161.

(37) Ulman, A. *Adv. Mater.* **1991**, *3*, 298-303.

(38) Badia, A.; Back, R.; Lennox, R. B. *Angew. Chem. Int. Ed. Engl.* **1994**, *33*, 2332-2335.

(39) Finklea, H. O.; Snider, D. A.; Fedyk, J. *Langmuir* **1990**, *6*, 371-376.

(40) Finklea, H. O.; Snider, D. A.; Fedyk, J.; Sabatini, E.; Gafni, Y.; Rubinstein, I. *Langmuir* **1993**, *9*, 3660-3667.

(41) Sabatani, E.; Rubinstein, I.; Maoz, R.; Sagiv, J. *J. Electroanal. Chem.* **1987**, *219*, 365-371.

(42) Sabatani, E.; Rubinstein, I. *J. Phys. Chem.* **1987**, *91*, 6663-6669.

(43) Xu, J.; Li, H.; Zhang, Y. *J. Phys. Chem.* **1993**, *97*, 11497-11500.

(44) Creager, S. E.; Hockett, L. A.; Rowe, G. K. *Langmuir* **1992**, *8*, 854-861.

(45) Chailapakul, O.; Crooks, R. M. *Langmuir* **1993**, *9*, 884-888.

(46) Chailapakul, O.; Crooks, R. M. *Langmuir* **1995**, *11*, 1329-1340.

(47) Li, T. T.-T.; Weaver, M. *J. Am. Chem. Soc.* **1984**, *106*, 6107-6108.

(48) Chidsey, C. E. D.; Bertozzi, C. R.; Putvinski, T. M.; Mujsce, A. M. *J. Am. Chem. Soc.* **1990**, *112*, 4301-4306.

(49) Collard, D. M.; Fox, M. A. *Langmuir* **1991**, *7*, 1192-1197.

(50) Creager, S. E.; Collard, D. M.; Foxe, M. A. *Langmuir* **1990**, *6*, 1617-1620.

(51) Rowe, G. K.; Creager, S. E. *Langmuir* **1991**, *7*, 2307-2312.

(52) Hickman, J. J.; Ofer, D.; Zou, C.; Wrighton, M. S.; Laibinis, P. E.; Whitesides, G. M. *J. Am. Chem. Soc.* **1991**, *113*, 1128-1132.

(53) Katz, E.; Itzhak, N.; Willner, I. *Langmuir* **1993**, *9*, 1392-1396.

(54) Closs, G. L.; Miller, J. R. *Science* **1988**, *240*, 440.

(55) Closs, G. L.; Calcaterra, L. T.; Green, N. J.; Penfield, K. W.; Miller, J. R. *J. Phys. Chem.* **1986**, *90*, 3673-3638.

(56) Paddon-Row, M. *Acc. Chem. Res.* **1994**, *27*, 18-25.

(57) Furniss, B. S.; Hannaford, A. J.; Rogers, V.; Smith, P. W. G.; Tatchell, A. R. *Vogel's Textbook of Practical Organic Chemistry;* 4th ed.; Longman Group Ltd.: Great Britain, 1978.

(58) Kim, Y.-T.; McCarley, R. L.; Bard, A. J. *Langmuir* **1993**, *9*, 1941-1944.

(59) Deakin, M. R.; Melroy, O. *J. Electroanal. Chem.* **1988**, *239*, 321-331.

(60) Widrig, C. A.; Chung, C.; Porter, M. D. *J. Electroanal. Chem.* **1991**, *310*, 335-359.

(61) Swietlow, A.; Skoog, M.; Johansson, G. *Electroanalysis* **1992**, *4*, 921-928.

(62) Stranick, S. J.; Parikh, A. N.; Allara, D. L.; Weiss, P. S. *J. Phys. Chem.* **1994**, *98*, 11136-11142.

(63) Bain, C. D.; Troughton, E. B.; Tao, Y.-T.; Evall, J.; Whitesides, G. M.; Nuzzo, R. G. *J. Am. Chem. Soc.* **1989**, *111*, 321-335.

(64) Marsh, D. *Handbook of Lipid Bilayer Membranes*; CRC Press: Boca Raton, 1991, pp 135-150.

(65) Camillone, N.; Chidsey, C. E. D.; Liu, G.; Scoles, G. *J. Chem. Phys.* **1993**, *98*, 4234-4245.

(66) Magnussen, O. M.; Hotlos, J.; Beitel, G.; Kolb, D. M.; Behm, R. J. *J. Vac. Sci. Technol. B* **1991**, *9*, 969-975.

(67) Schultze, J. W.; Dickertmann, D. *Surface Science* **1976**, *54*, 489-505.

(68) New, R. R. C. *Liposomes: A Practical Approach*; Oxford University Press: New York, 1990.

(69) Papahadjopolous, D.; Jacobson, K.; Nir, S.; Isac, T. *Biochim. Biophys. Acta* **1973**,

311, 330-348.

(70) Corvera, E.; Mouritsen, O. G.; Singer, M. A.; Zuckerman, M. J. *Biochim. Biophys. Acta* **1992**, *1107*, 261-270.

(71) Cruziero-Hansson, L.; Mouritsen, O. G. *Biochim. Biophys. Acta* **1988**, *944*, 63-72.

(72) Riegler, J. E. *J. Phys. Chem.* **1989**, *93*, 6457-6480.

(73) Bayerl, T. M.; Bloom, M. *Biophys. J.* **1990**, *58*, 357-362.

(74) Naselli, C.; Rabolt, J. F.; Swalen, J. D. *J. Chem. Phys.* **1985**, *82*, 2136-3271.

(75) Naselli, C.; Rabolt, J. F.; Swalen, J. D. *J. Chem. Phys.* **1985**, *82*, 2136-2140.

(76) Schlenoff, J. B.; Li, M.; Ly, H. *J. Am. Chem. Soc.* **1995**, *117*, 12528-12536.

(77) Camillone, N.; Eisenberger, P.; Leung, T. Y. B.; Schwartz, P.; Scoles, G.; Poirier, G. E.; Tarlov, M. J. *J. Chem. Phys.* **1994**, *101*, 11031-11036.

(78) Schonenberger, C.; Jorritsma, J.; Sondag-Huethorst, J. A. M.; Fokkink, L. G. J. *J. Phys. Chem.* **1995**, *99*, 3259-3271.

(79) Siepmann, J. I.; McDonald, I. R. *Langmuir* **1993**, *9*, 2351-2355.

(80) Hahner, G.; Woll, C.; Buck, M.; Grunze, M. *Langmuir* **1993**, *9*, 1955-1958.

(81) Edinger, K.; Golzhauser, A.; Demota, K.; Woll, C.; Grunze, M. *Langmuir* **1993**, *9*, 4-8.

(82) Amatore, C.; Saveant, J. M.; Tessier, D. *J. Electroanal. Chem.* **1983**, *147*, 39-51.

(83) Haran, A.; Waldeck, D. H.; Naaman, R.; Moons, E.; Cahen, D. *Science* **1994**, *263*, 948-950.

(84) Bilewicz, R.; Sawaguchi, T.; Chamberlain II, R. V.; Majda, M. *Langmuir* **1995**, *11*, 2256-2266.

(85) Sun, L.; Crooks, R. M. *J. Electrochem. Soc.* **1991**, *138*, L23-L25.

(86) Badia, A.; Lennox, R. B. *manuscript submitted to J. Am. Chem. Soc.* **1996**,

(87) Dorn, A. W.; Thompson, M. In *Ion-Transfer Kinetics: Principles and Applications*; J. R. Sandifer, Ed.; VCH Publishers, Inc.: New York, 1995; pp 55-69.

(88) Eaton, W. A.; George, P.; Hanania, G. I. H. *J. Phys. Chem.* **1967**, *71*, 2016-2021.

(89) Peter, L. M.; Durr, W.; Bindra, P.; Gerischer, H. *J. Electroanal. Chem.* **1976**, *71*, 31-50.

(90) Noftle, R. E.; Pletcher, D. *J. Electroanal. Chem.* **1990**, *293*, 373.

(91) Sondag-Huethorst, J. A. M.; Fokkink, L. G. J. *Langmuir* **1995**, *11*, 2237-2241.

(92) Vodyanoy, I.; Hall, J. E. *Biophys. J.* **1984**, *46*, 187-194.

Chapter Four

SELF-ASSEMBLED MONOLAYERS ON GOLD NANOPARTICLES*

4.1. Introduction

The properties of organic molecules adsorbed on metal surfaces are of particular interest due to the central role adsorbates play in catalysis, corrosion, and electrode processes. A number of studies, for example, have dealt with the structure and dynamics of monolayer (or sub-monolayer) coverage situations where the adsorbate is an aromatic heterocycle or *n*-alkylthiol.[1-3] To date, little is known about the organizational state of chains in self-assembled monolayers (SAMs) of the otherwise much-studied *n*-alkylthiols chemisorbed on gold (RS/Au). The conformational lability of the alkyl chains introduces the possibility that order-disorder transitions may arise which are analogous to the gel-to-liquid crystalline phase transitions observed in ordered lipid assemblies. A complex melting process which occurs within RS/Au SAMs has in fact been recently inferred using both electrochemical and synchrotron X-ray diffraction as reporting techniques.[4, 5] Of note in the former are the striking parallels observed between temperature dependent ion fluxes in RS/Au SAMs and the phase transition behaviour of biomimetic lipid vesicles.[4]

In the following, we describe a characterization of the thermal properties of RSH-derivatized gold nanoparticles.[6] This system was chosen because of its obvious potential to serve as a high surface area analogue to SAMs formed on planar metal surfaces. Sensitivity restrictions imposed by monolayer coverage greatly hinder the application of techniques such as calorimetry and NMR to the study of planar SAMs. As a result, issues

---

* This chapter is almost a *verbatim* copy of the text of the paper *Chem. Eur. J.* **1996**, *2*, 359-363. Slight modifications have been made here for clarity and continuity.

such as chain dynamics, adsorbate phase diagrams, and relaxation processes remain open and ill-defined at the present time. We are especially interested in chain ordering and disordering in these monolayers, and how this interplay manifests itself as grain boundaries and defect sites. If SAMs are to be ultimately used in molecular electronic and optoelectronic devices, then their structural integrity must be thoroughly understood, in both kinetic and thermodynamic terms. To this end, we have characterized the thermal properties of RSH monolayer-coated gold nanoparticles in macroscopic (*via* calorimetry and NMR spectroscopy) and microscopic (*via* infrared and transmission electron microscopy) terms. The result is the discovery that these SAMs show strong parallels to monolayers formed at planar surfaces, but also distinct differences become apparent due to the large curvature of these spherical gold particles.

4.2. Experimental Section

4.2.1. Materials: The preparation and purification of C_{12}-, C_{14}-, C_{16}-, C_{18}-, and $C_{20}SH$ were as previously described (Chapter 3). Hydrogen tetrachloroaurate trihydrate, sodium borohydride (99%), and tetraoctylammonium bromide (98%) were obtained from Aldrich and used as received.

4.2.2. Synthesis: Gold nanoparticles derivatized with alkylthiols of chain lengths of 12, 14, 16, 18, and 20 carbons were prepared following the method of Brust *et al.*[6a] This procedure involves two phases (toluene/water), where $Au(III)Cl_4^-$ is transferred to the toluene layer using $(C_8H_{17})_4NBr$ as a phase transfer reagent, and then reduced by $NaBH_4$ in the presence of the thiol surfactant at the toluene/water interface. The reactions were carried out under ambient atmosphere typically using 1.8 mmoles of $HAuCl_4 \cdot 3H_2O$ and mole ratios of $NaBH_4$: $(C_8H_{17})_4NBr$: $HAuCl_4$: RSH of 12: 4.8: 1.1: 1.

Rigorous purification of the RS/Au colloid was found to be necessary as both the original preparation and the recrystallized sample showed large amounts of residual thiol and disulfide. Exhaustive washing/extraction of the colloid preparation with ethanol served to quantitatively remove unbound species. Complete removal of residual thiol and disulfide was verified by TLC using hexane as the mobile phase and iodine as the indicator. The final purified material used in calorimetry and spectroscopy experiments is a finely divided, crystalline (for $n \geq 16$) or waxy ($n \leq 14$) brown-black powder which remains as a solid pellet in water, yet disperses to yield a colloidal solution in solvents such as hexane, benzene, toluene, and chloroform.[6a]

Two samples of RSH-derivatized gold were subjected to elemental analysis (Galbraith Laboratories, Knoxville, USA). $C_{14}H_{29}S/Au$ nanoparticles yield 75.67% Au, 3.40% S, 18.30% C, and 3.03% H, while the $C_{18}H_{37}SH$-derivatized Au nanoparticles yield 69.32% Au (by difference), 3.33% S, 23.49% C, and 3.86% H.

4.2.3. Transmission electron microscopy: Samples for TEM were prepared by dipping standard carbon-coated (200-300Å) Formvar copper grids (200 mesh) into a dilute hexane solution of the RS/Au nanoparticles for several seconds. The TEM grids were withdrawn from the solution and allowed to dry under ambient atmosphere for a few minutes. Phase contrast images of the particles were obtained using a top-entry Phillips EM 410 electron microscope operated at an accelerating voltage of 80 keV. Micrographs were obtained at magnifications of 52 000X and 92 000X. The size distributions of the various RS/Au nanoparticles were determined from the diameters of at least 100 particles located in a representative region of the 17X enlarged micrographs using a video image analysis software program (JAVA, Jandel Scientific).

4.2.4. NMR spectroscopy: Solution state NMR experiments were performed on a JEOL ECLIPSE-270 spectrometer at 25 °C, on samples prepared by dispersion of 30-40 mg of the RSH-derivatized Au colloid in 0.7 mL of d_6-benzene. Variable temperature ^{13}C NMR of the $C_{14}S/Au$ and $C_{18}S/Au$ powders were carried out on a Varian Unity 500 NMR spectrometer using a D_2O coaxial insert as a field/frequency lock. ^{13}C NMR measurements were performed under conditions of broadband ^1H decoupling. The proton and the ^{13}C resonances are reported in ppm *vs.* TMS.

4.2.5. Infrared Spectroscopy: The RS/Au colloidal particles were deposited dropwise onto a NaCl disc from a concentrated hexane solution. Except for the $C_{20}H_{41}S/Au$ case, evaporation of the solvent resulted in a uniform film. Infrared spectroscopy was carried out using a Perkin-Elmer FT-IR Microscope Model 16PC with a MCT detector. Spectra were collected in the transmission mode with an unpolarized beam, at a resolution of 2 cm^{-1} using 32 scans, and a spectral window from 4000 to 600 cm^{-1}. The FT-IR microscope was equipped with a Mettler FP52 hot stage for variable temperature experiments (5 - 100 °C). The sample was purged continuously with dry nitrogen and maintained at each temperature for 30 min before a spectrum was acquired. Background spectra of the clean NaCl disc were collected at the same temperatures and subtracted from the sample spectra.

4.2.6. Differential Scanning Calorimetry: DSC experiments were conducted using a Perkin-Elmer DSC-7 instrument calibrated for temperature and peak area using indium and octadecane standards. Thermograms were run using samples of 2-8 mg of a

RS/Au colloid in sealed aluminum pans under a nitrogen atmosphere at heat/cool rates of 2 °C/min or 5 °C/min.

4.3. Results and Discussion

Investigation of the phase properties of monolayer films requires particular precautions to ensure the purity of their preparation. After the initial synthesis, thin layer chromatography (TLC) of the "recrystallized" colloidal particles shows the presence of free disulfide. Extensive washing with ethanol to remove unbound disulfide surfactant leads to a disulfide-free ^1H NMR spectrum of the RSH-derivatized gold, and TLC shows no trace of either labile thiol and/or disulfide. The ^1H and ^{13}C NMR resonances of the powders dispersed in solvent are considerably broadened for the RS/Au nanoparticles as compared to those of free RSH. This linebroadening observed in the solution NMR spectra of the thiol-derivatized gold nanoparticles is consistent with the alkyl chains being bound to the colloidal gold surface.[7] For example, in the ^1H NMR spectrum of $C_{18}S$/Au colloid (Figure 4.1A) the α, β , and γ methylene proton signals are noticeably absent, whereas the resonances associated with the C_4-C_{17} methylene hydrogens and the terminal methyl hydrogens are observed as broad signals. In the ^{13}C NMR spectrum (Figure 4.1B), only the signals due to the carbons at positions 15-18 are clearly resolved, and the α, β , and γ carbons (*i.e.* the carbons closest to the gold surface) are not apparent. These signals may be buried under the broad peak at ~ 30 ppm (assigned to the interior methylene carbons of the alkylthiol chain), shifted by virtue of their binding to the metal, or more likely, broadened because of the "solid-like" nature of these carbons in the immobilized alkylthiol, as suggested elsewhere.[8]

TEM images (Figure 4.2), in conjunction with elemental analyses, can be used to estimate the median coverage of thiols on the gold nanoparticles.[9] The synthetic procedure of Brust *et al.*,[6a] combined with our purification process, yields a coverage (assuming the particles to be spherical) at the gold surface corresponding to 17.2 ± 0.4 Å^2 and 15.2 ± 0.4 Å^2 per alkylthiol molecule for the $C_{14}SH$ and $C_{18}SH$-derivatized Au colloids, respectively. A maximum packing density of these chains on a planar gold surface would require an area of 17.8 Å^2 to 23.6 Å^2 per chain,[10] depending on the adsorption site (hollow or on-atom site) and the surface crystallography of the gold particle. Although this data is consistent with complete coverage by RSH, the ratio of the particle size to chain length precludes close packing of the chains along their entire length.[11] This restriction, imposed by the substantial curvature of the gold particle surface, leads to interesting particle-particle interactions, which in turn manifest themselves in the temperature dependence studies described below.

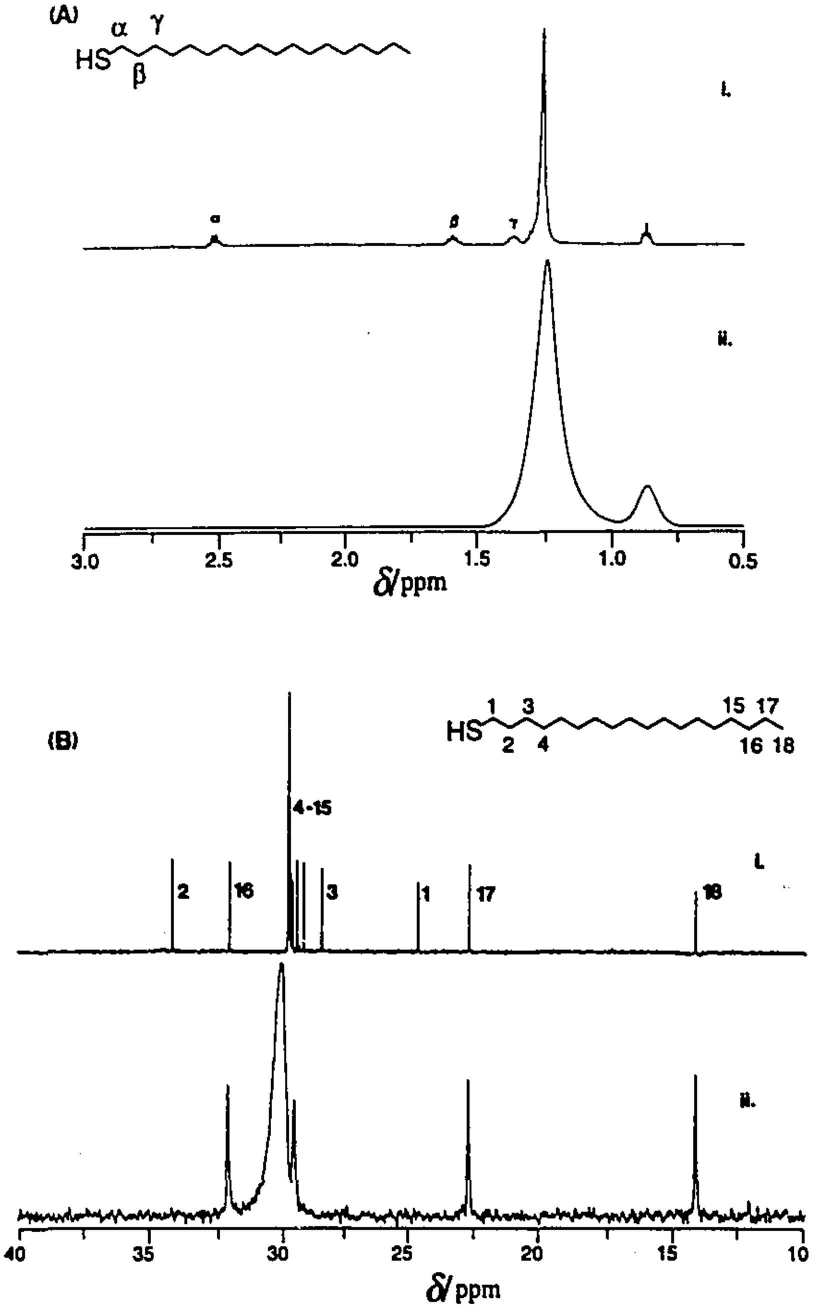

Figure 4.1. (A) Solution-state ^{1}H NMR spectra (270 MHz) of (i) bulk n-$C_{18}H_{37}SH$ in d-chloroform, 64 transients and (ii) $C_{18}H_{37}S/Au$ colloid in d_6-benzene, 128 transients. (B) Solution-state ^{13}C NMR spectra (67.9 MHz) of (i) bulk n-$C_{18}H_{37}SH$ in d-chloroform, 1024 transients and (ii) $C_{18}H_{37}S/Au$ colloid in d_6-benzene, 13 000 transients.

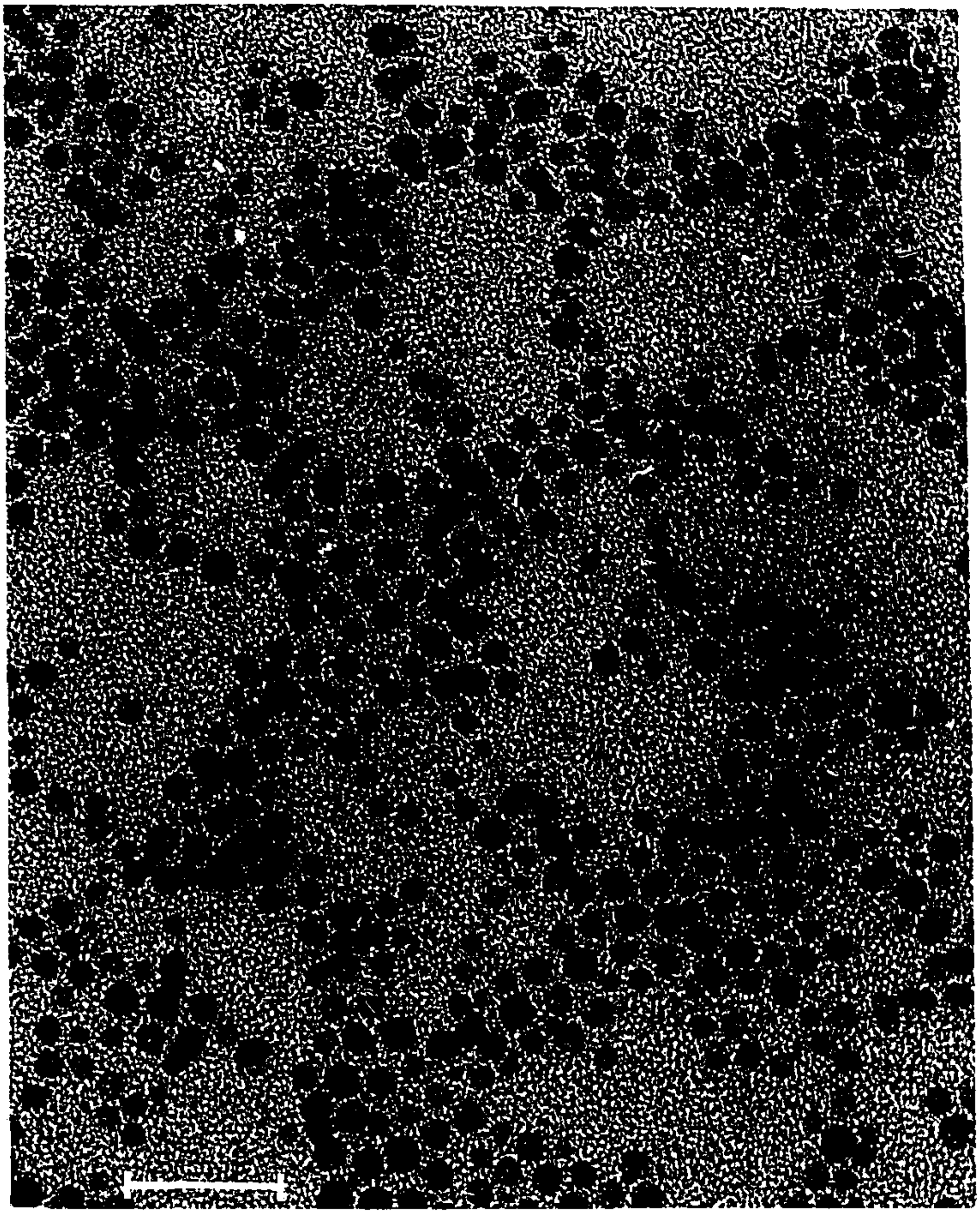

Figure 4.2. (A) Representative TEM image of $C_{18}SH$ derivatized-Au nanoparticles. The scale bar is 100 Å. The TEM images of the $C_{12}S/Au$, $C_{14}S/Au$, $C_{16}S/Au$, and $C_{20}S/Au$ samples were similar to $C_{18}S/Au$.

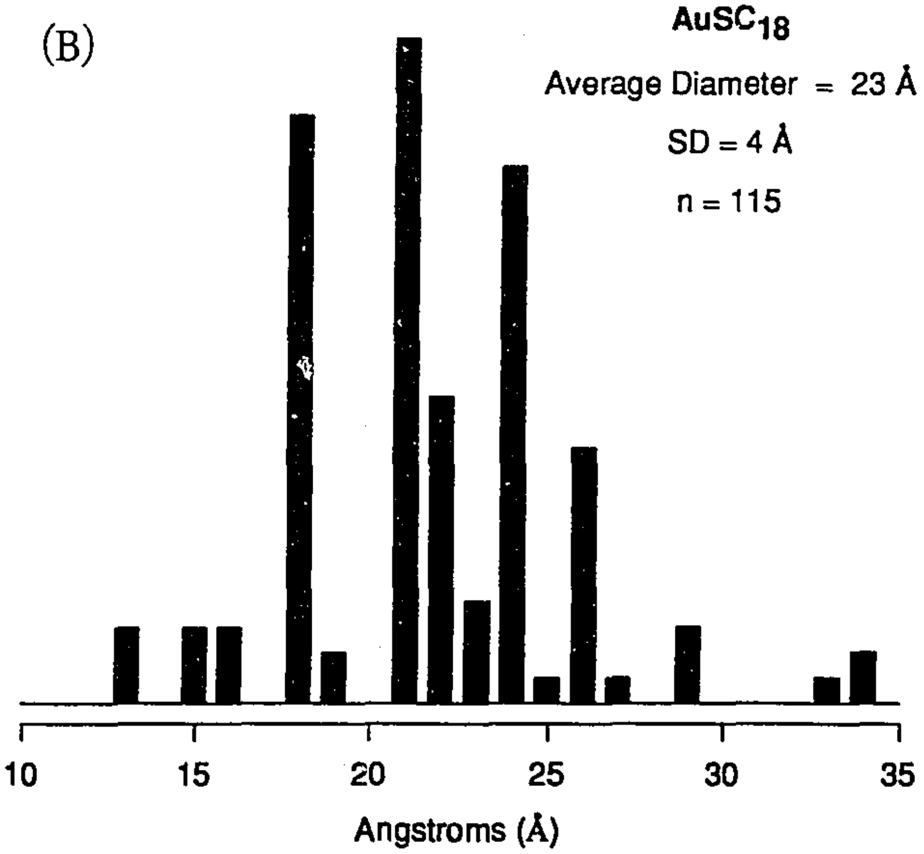

Figure 4.2. (B) Histogram of particle diameters observed in (A). Mean particle diameters, standard deviations, and the particle population size (n) are reported for each chainlength. Median diameters are given in parentheses. C_{12}: 19 ± 5 Å, n = 103 (18.5 Å); C_{14}: 20 ± 8 Å, n = 126 (21.4 Å); C_{16}: 29 ± 6 Å, n = 108 (28.0 Å), C_{18}: 23 ± 4 Å, n = 115 (22.4 Å), and C_{20}: 41 ± 14 Å, n = 103 (35.8 Å).

Variable temperature NMR spectra of the dry powder samples, obtained using a liquid spectrometer, suggest that these alkylated nanoparticles undergo some form of melting transition. For instance, the ^{13}C NMR spectrum of the $C_{18}S/Au$ powder shows a broad weak signal between 20-40 ppm at 25 °C (Figure 4.3B). Between 55 °C and 65 °C a distinct peak (~ 30 ppm), assigned to the interior methylenes of the alkyl chain, appears and becomes relatively sharp. A signal consistent with the terminal methyl (~ 15 ppm) also becomes apparent at elevated temperatures. Furthermore, for the $C_{14}S/Au$ nanoparticles, the methylene signal is already apparent at 25 °C, and becomes substantially sharper (as per Figure 4.3A) as the coated nanoparticles are heated to 45 °C. It is notable nonetheless, that there is a discernible population of mobile chains even at temperatures below the apparent phase transition temperature of these samples.[12] A detailed variable temperature solid-state ^{13}C NMR examination of these samples has found a gradual change in the population of *trans* to *gauche* conformers, consistent with the temperature-dependent data presented here.[8]

Differential scanning calorimetry (DSC) of $C_{12}SH$-, $C_{14}SH$-, $C_{16}SH$-, $C_{18}SH$-, and $C_{20}SH$-derivatized gold nanoparticles *quantifies* the temperature dependence of the changes qualitatively observed by NMR. Each sample exhibits a broad endotherm (or a set of overlapping endotherms) in the heat cycle (Figure 4.4A). The peak maximum temperature is clearly chain length dependent and the ΔH associated with this transition increases with increasing chain length. This trend parallels that seen in materials undergoing gel-to-liquid crystalline transitions, given that an increasing chain length affords more extensive Van der Waals interactions and resulting enthalpic contributions. On cooling, a sharp exotherm is observed at ~ 7 °C below the endotherm (Figure 4.4B). Although this hysteresis behavior is observed with all the RS/Au samples studied here, the thermal processes are evidently reversible given that the $\Delta H_{endo} = \Delta H_{exo}$. Upon reheating the cooled nanoparticles, a sharper endotherm results due to annealing of the alkylated particles. However, the enthalpies and peak maximum temperatures remain the same (*i.e.* $\Delta H_{heat} = \Delta H_{reheat}$, $\Delta T \approx 2$ °C), indicating that the DSC-detected transition is reversible. Clearly, since the thermograms are reversible, thiol desorption does not compete with the thermal properties of the alkylated particles at temperatures ≤ 95 °C.[13] The DSC thermograms clearly show that these RS/Au particles, in the solid-state, undergo distinct phase transitions in a chain length dependent manner. The transition temperature associated with each chain closely parallels those found in both electrochemical SAM studies,[4] and in classic studies of phospholipid (PC) bilayer membranes.[14]

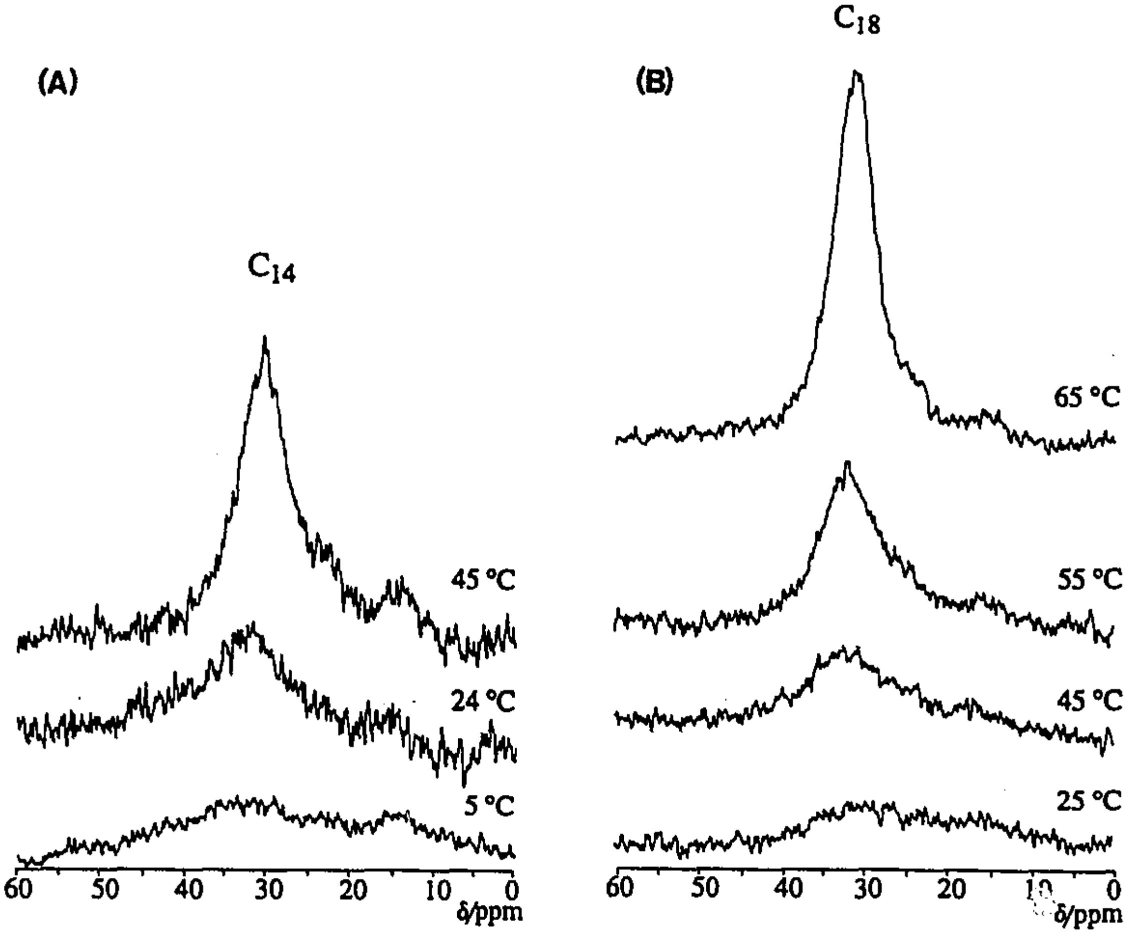

Figure 4.3. Variable temperature ^{13}C NMR (125 MHz) spectra of (A) $C_{14}S/Au$ powder and (B) $C_{18}S/Au$ powder; internal D_2O lock, 8400 transients.

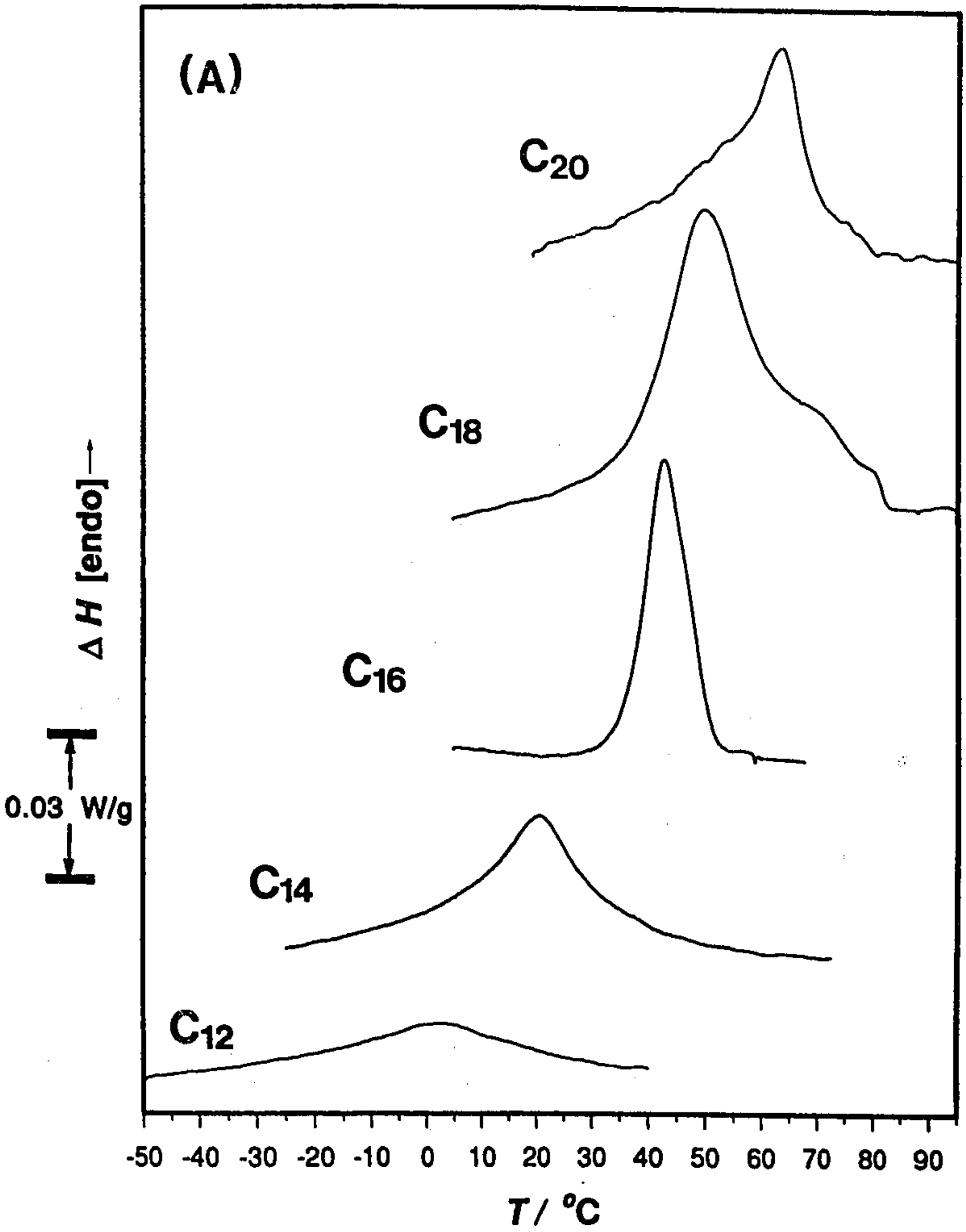

Figure 4.4. (A) Differential scanning calorimetry endotherms of RS/Au powders. Heat cycle scan rate is 5 °C·min^{-1}, except for C_{20}S/Au where the scan rate is 2 °C·min^{-1}.

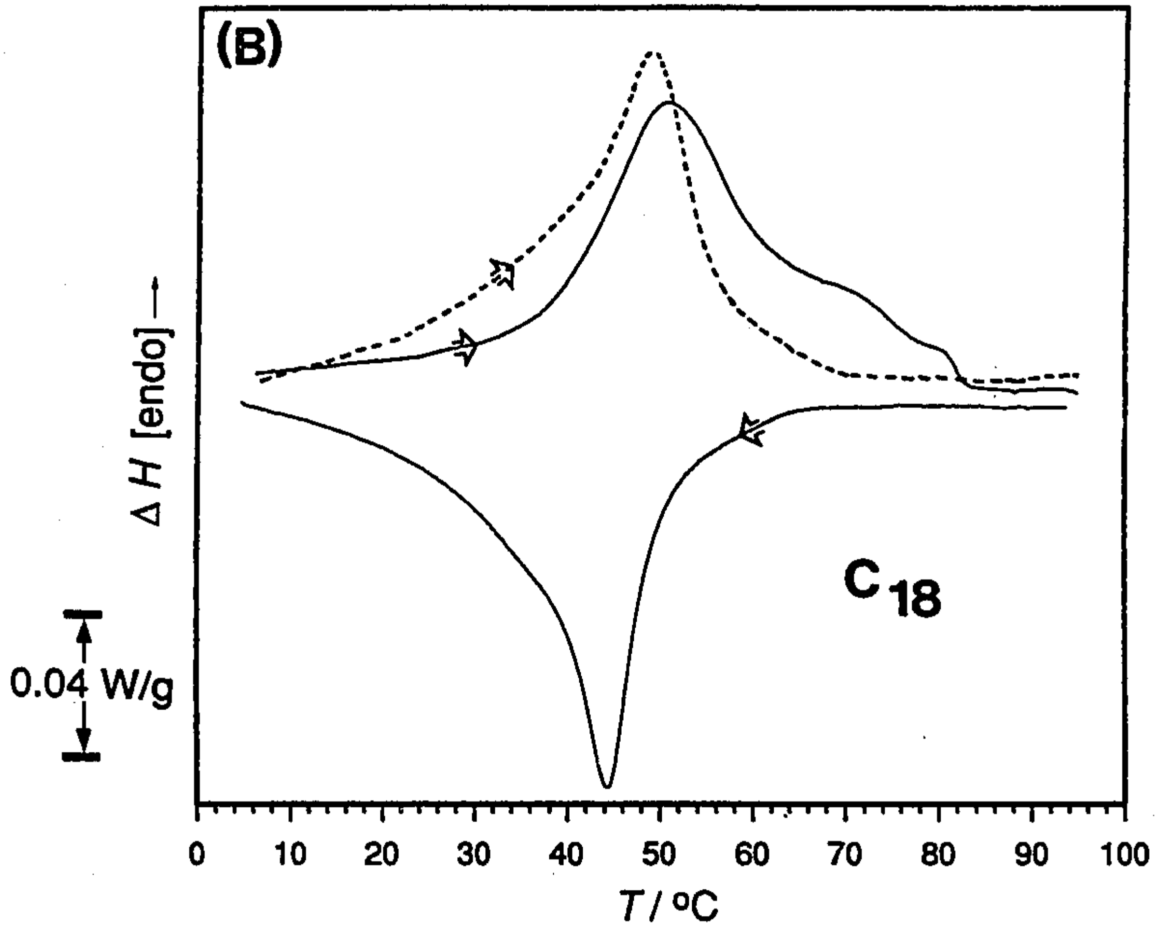

Figure 4.4. (B) Heat, (—⇨—), cool (—⇦—), reheat (-⇨-) cycling of $C_{18}S/Au$ sample.

FT-IR spectroscopy used in conjunction with NMR and DSC provides information concerning the conformation of chains adsorbed onto surfaces. For example, surface infrared spectroscopy (*i.e.* reflection absorption infrared spectroscopy, RAIRS) has been used to probe the chain conformation and orientation in thiol SAMs on planar gold.[15] However, the dispersed nature of the gold nanoparticle system allows us to use conventional transmission FT-IR, with the sample deposited as a thin film on an inert substrate. For example, Figure 4.5 tracks the CH_2 symmetric (d^+: 2850 cm^{-1}) and antisymmetric (d^-: 2920 cm^{-1}) stretches of $C_{18}S/Au$ as a function of temperature. Figure 4.6 thus shows that upon heating, the $C_{14}S/Au$, $C_{16}S/Au$, and $C_{18}S/Au$ samples undergo a transition from a highly chain-ordered state to a chain-disordered state, where the CH_2 symmetric (d^+: 2850 cm^{-1}) and antisymmetric (d^-: 2920 cm^{-1}) stretches are used as markers of ***trans*** and ***gauche*** bond populations in the chains.[2,16] Although this process occurs over a relatively broad temperature range (~ 25 °C), as is the case in the NMR and calorimetry experiments (Figures 4.3 and 4.4), the apparent transition temperatures are similar to those found using the other techniques reported here. Also notable is the observation that the population of *gauche* bonds at 25 °C follows the trend of $C_{14} > C_{16} > C_{18}$. This is consistent with a differing extent of chain disordering in the samples when they are observed near to, or distant from, the DSC-determined phase transition temperature. These data are especially noteworthy in that several studies using RAIRS of RS monolayers on planar gold substrates in UHV conditions have failed to detect phase transitions *via* the temperature dependence of either the (d^+) or (d^-) CH_2 stretching peaks, which would otherwise be indicative of order-disorder transitions.[16]

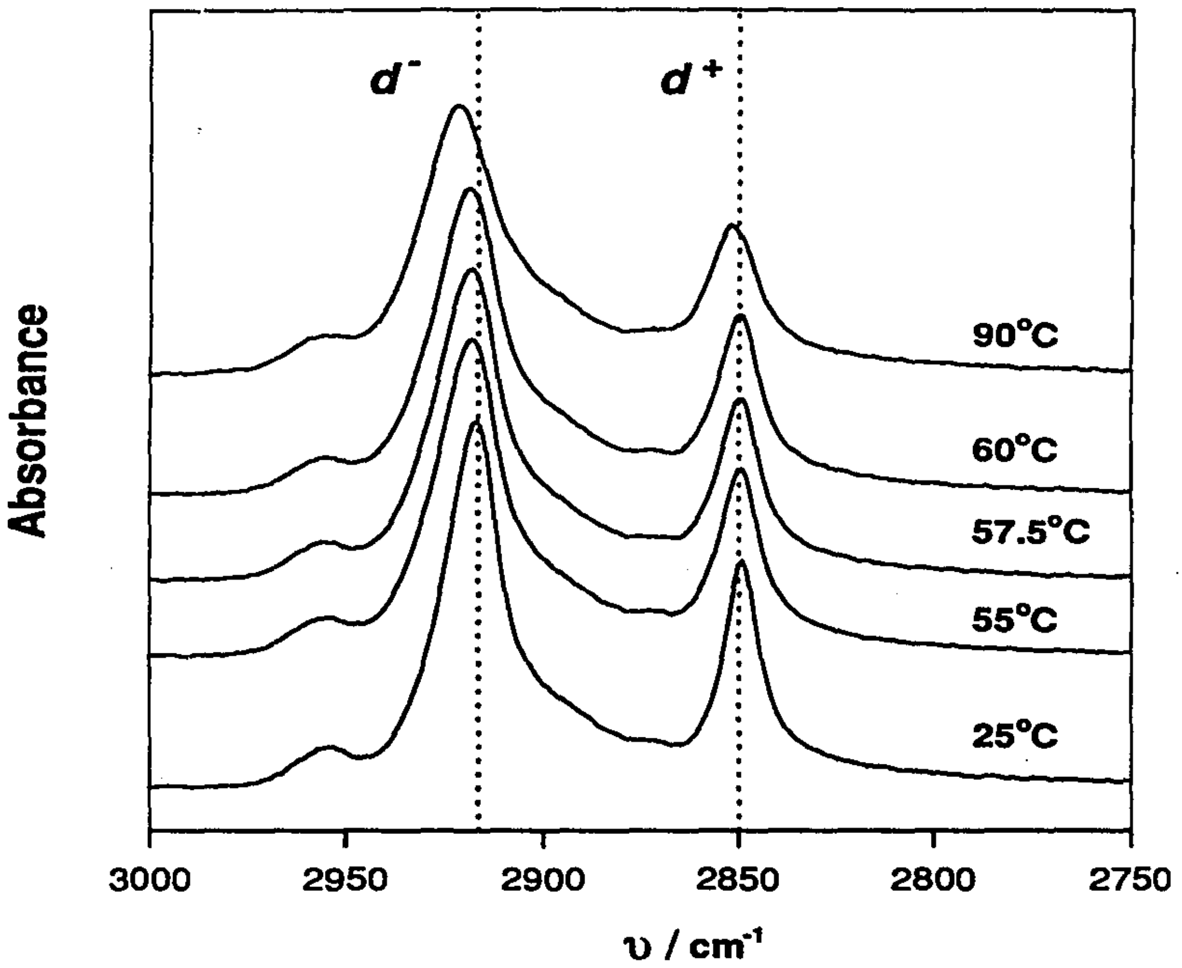

Figure 4.5. Variable temperature transmission FT-IR spectra of the CH_2 stretching region (2750-3000 cm^{-1}) for $C_{18}S/Au$ particles. The dotted lines at 2917 cm^{-1} and 2850 cm^{-1} are visual aids.

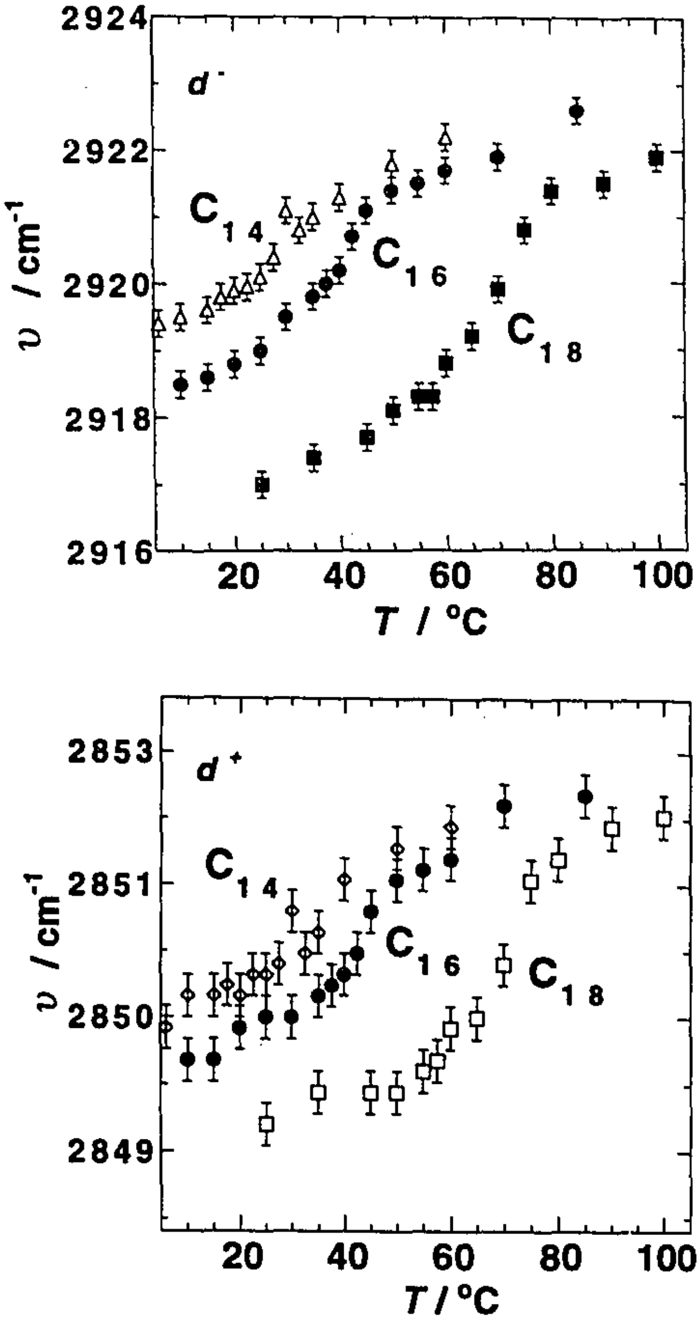

Figure 4.6. Peak position of the antisymmetric (*d*-) and symmetric (*d*+) CH_2 stretches as a function of temperature for thin films of $C_{14}S/Au$, $C_{16}S/Au$, and $C_{18}S/Au$ nanoparticles deposited on a NaCl crystal.

The DSC and FT-IR experiments establish that a cooperative chain melting process occurs in these alkylated metal colloids, the mechanism of which is not immediately evident given the relationship between the extended chain conformation and the gold nanoparticle geometry. Extensive chain-chain interactions may arise in two ways assuming a variation in density of the adsorbed surfactant. Chains may collectively tilt to form close-packed domains. Detailed diffraction studies established that RS chains chemisorbed on planar Au(111) are tilted ~ 30° with respect to the surface normal so as to maximize Van der Waals interactions.[10] While this may in fact occur in the thiol-modified nanoparticles, close examination of TEM micrographs suggests that chain ordering arises from the interdigitation of chain *domains* between neighbouring particles (Scheme 4.1). Given that TEM images the gold nanoparticle, and not the organic adsorbate, the distances between the edges of many pairs of adjacent particles (Figure 4.2) clearly are substantially less than twice an all-*trans* extended chain length, and indeed, are closer to being one chain in length (*i.e.* ~ 20 Å). Recent powder X-ray diffraction studies confirm that adjacent Au particles are separated by approximately one chain length.[17,18,19]

An interdigitated state is interesting in that the void-filling process leads to a bilayer-like configuration of chains. Phase transition temperatures (T_ms) reflect the extent of Van der Waals interactions, which depend on the chain packing density. Thus, the agreement between the T_m values of planar RS/Au SAMs (determined electrochemically)[4], phospholipid bilayers[14], fatty acid Langmuir-Blodgett monolayer films[20], and RS/Au nanoparticles (Table 4.1) suggests that these order/disorder processes are structurally related. Changes in chain ordering could lead to broadening of the phase transitions and may cause shifts in the observed T_m values. The RS/Au nanoparticle T_m would also be influenced by the packing state of the RS chains in the modified gold nanoparticles. In a related system, a C_{12}-derivatized C_{60} fullerene (d = 11.3 Å) exhibits a phase transition at ~ 24 °C (measured by DSC). In this particular case, an interdigitated phase was determined by X-ray diffraction, and is thought to be the source of the observed phase transition.[21]

Despite many similarities in the thermal properties of the RS/Au nanoparticles and planar RS/Au SAMs, the order/disorder phase transition in the RS/Au particle system is reversible while the RS/Au monolayer shows a marked hysteresis. The origins of these differences in the hysteresis behavior is not well understood at the present time. The reversibility of the phase transition in the RS/Au nanoparticles is most probably due to transverse motion and/or tumbling of the entire Au nanoparticle above the T_m. In fact, calorimetry studies of mechanical mixtures of $C_{14}S$/Au and $C_{18}S$/Au nanoparticles show two distinct endotherms (peak maxima at 20 °C and 50 °C) in the first heating trace and only one endotherm (peak maximum at 34 °C) upon reheating.

Table 4.1. A Comparison of the Thermal Properties of Self-Assembled Films

Chain	RS/Au nanoparticles			planar RS/Au	di-PC lipids		$Cd(RCO_2)$ LB
length	T_m^{DSC}(a)	ΔH(b)	T_m^{IR}(c)	T_m^{e}(d)	T_m(e)	ΔH	monolayer(f)
C_{12}	3 °C	(5 Jg^{-1})	-	-	-1.1 ± 0.4 °C	-	-
C_{14}	22 °C	10 $kJmol^{-1}$ (11 Jg^{-1})	24 °C	-	23.5 ± 0.4 °C	12.8 ± 1.4 $kJmol^{-1}$	-
C_{16}	41 °C	(12 Jg^{-1})	42 °C	39.3 ± 0.6 °C	41.4 ± 0.5 °C	-	-
C_{18}	51 °C	21 $kJmol^{-1}$ (23 Jg^{-1})	66 °C	53.3 ± 2.4 °C	55.1 ± 1.5 °C	21.2 ± 1.8 $kJmol^{-1}$	55 - 60 °C
C_{20}	64 °C	(30 Jg^{-1})	-	62.8 ± 1.8 °C	64.5 ± 0.5 °C	-	70 - 80 °C

(a) T_m^{DSC} refers to the peak maximum temperature of the endotherm in the first heat cycle. (b) ΔH is reported in Jg^{-1} of RS/Au powder and in $kJmol^{-1}$ of alkylthiol for the samples subjected to elemental analyses. (c) Inflection points of these plots were determined by taking the second derivative of the best fit polynomial in each case, and are used as apparent T_m values reported by FT-IR spectroscopy. (d) T_m^{e} values determined electrochemically for alkylthiols adsorbed on planar gold[4]. (e) T_m values of *n*-diacylphosphatidylcholine lipids determined by DSC[14]. The ΔH value reported is per acyl chain. (f) Chain melting pretransitions determined by electron diffraction for solid-supported Langmuir-Blodgett (LB) monolayers of the cadmium salts of long-chain fatty acids[20].

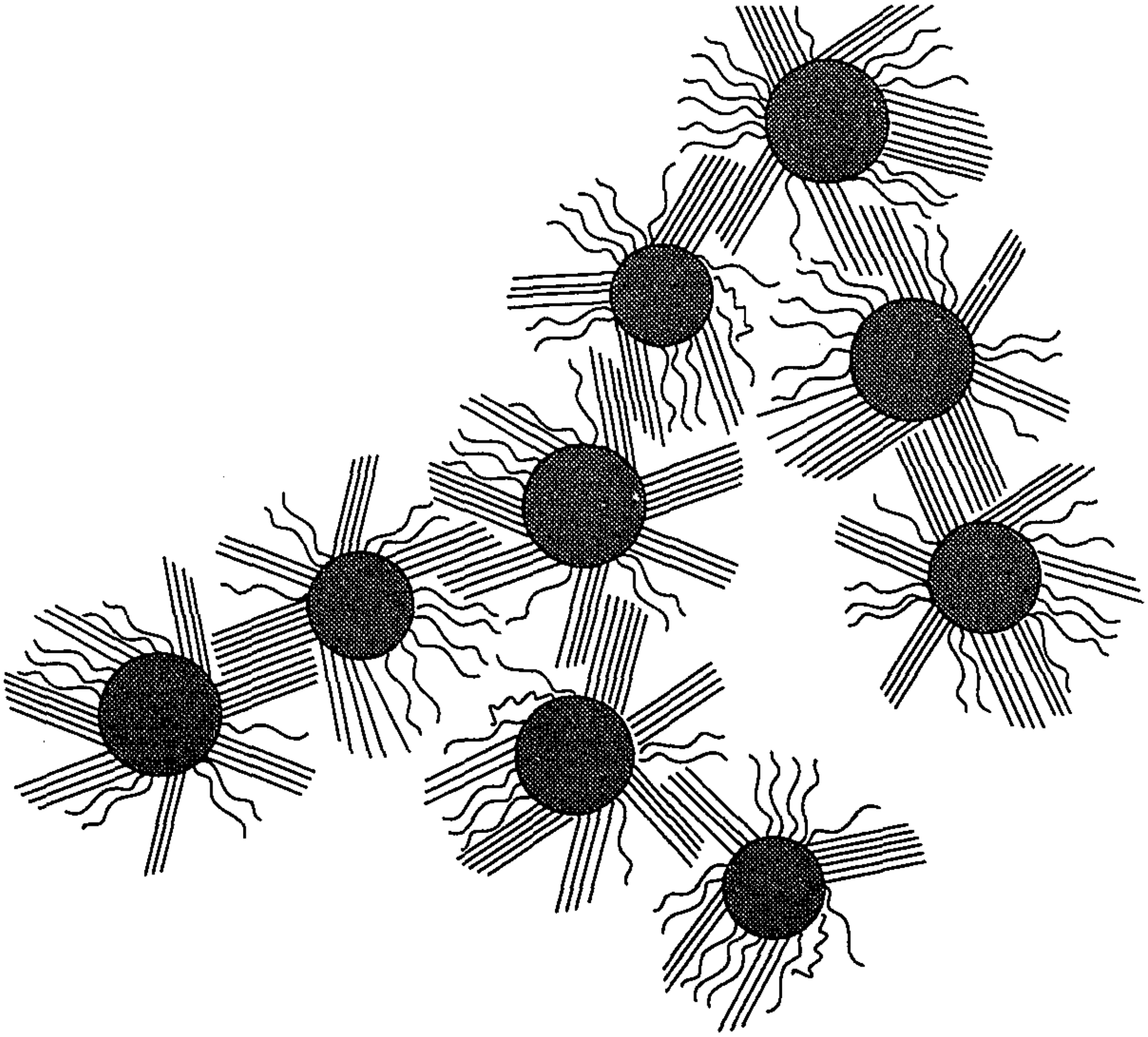

Scheme 4.1. A schematic two-dimensional representation of the RS/Au nanoparticles in the solid state, as suggested by the data shown in Figures 4.1-4.6. In this description, a number of chain domains on a given gold particle will interdigitate into the chain *domains* of neighboring particles in order to compensate for the substantial decrease in the chain density which occurs towards the methyl chain end. Chains with large populations of *gauche* bonds may arise from (i) those which occupy *interstitial* regions in the particle lattice and cannot efficiently overlap with adjacent chains or from (ii) chains residing at domain boundaries. An alternative packing configuration, involving the interdigitation of individual chains from neighboring particles, is not likely given the large chain end to surface area ratio.[11]

This suggests that at temperatures above the T_m, the $C_{14}S$ chain domains can interdigitate with $C_{18}S$ chain domains on neighboring particles to form mixed chain assemblies. We believe that this behavior would only be possible if diffusion/and or tumbling of the entire Au particle occurs once the alkyl chains are melted. However, we cannot rule out the possibility that chain re-ordering in the RS/Au nanoparticles is assisted by RS chain diffusion at the particle surface above the T_m. RS chain diffusion may be more facile at the colloidal Au surface because the physical state of the surface Au atoms (caused by surface curvature or surface faceting)[6b,17,18] is different from that of planar Au surfaces.

4.4. Conclusions

These studies show that RS/Au nanoparticles can be prepared with monolayer coverage of the gold particles, rendering them the same physical and chemical properties of thiol monolayers. An order-disorder transition is readily monitored using FT-IR spectroscopy and NMR spectroscopy[8], and this transition correlates with DSC-detected endotherms. This thermally-induced transition is associated with structural changes in the organic monolayer coating, given the distinct chain length dependence of the phenomenon. Distinct phase transitions are detectable in these organic films, suggesting that the RS/Au nanoparticle can be considered to be a highly dispersed, large surface area analogue to the much-studied self-assembled thiol monolayers on planar gold. It is important to note that neither calorimetry nor NMR experiments can be performed, at present, on SAMs supported on planar surfaces. The research presented here paves the way for the extension of biomimetic and optical applications, now undertaken with RS/Au SAMs, to these readily prepared colloidal systems.

References

(1) A. Ulman, *An Introduction to Ultrathin Organic Films from Langmuir-Blodgett to Self-Assembly*, Academic Press, San Diego, CA, **1991**; C. D. Bain, G. M. Whitesides, *Angew. Chem. Adv. Mater.* **1989**, *101*, 522; *Angew. Chem. Int. Ed. Engl. Adv. Mater.* **1989**, *28*, 506, and references therein.

(2) L. H. Dubois, R. G. Nuzzo, *Annu. Rev. Phys. Chem.* **1992**, *43*, 437, and references

therein.

(3) J. Lipkowski in *Modern Aspects of Electrochemistry, vol. 11*, Plenum, N.Y., USA.

(4) A. Badia, R. Back, R. B. Lennox, *Angew. Chem.* **1994**, *106*, 2429; *Angew. Chem. Int. Ed. Engl.* **1994**, *33*, 2332.

(5) P. Fenter, P. Eisenberger, K.S. Liang, *Phys. Rev. Lett.* **1993**, *70*, 2447.

(6) a) M. Brust, M. Walker, D. Bethell, D. J. Schriffin, R. Whyman, *J. Chem. Soc., Chem. Commun.* **1994**, 802; b) D. V. Leff, P. C. Ohara, J. R. Heath, W. M. Gelbart, *J. Phys. Chem.* **1995**, *99*, 7036.

(7) E. Söderlind, P. Stilbs, *Langmuir* **1993**, *9*, 1678.

(8) A. Badia, W. Gao, S. Singh, L. Demers, L. Cuccia, L. Reven, *Langmuir* **1996**, *12*, 262-1269.

(9) Elemental analyses, in conjuction with the median diameters of the gold nanoparticles were used to determine the thiol coverage. The median diameter rather than the mean diameter was used since it more accurately reflects the size of an idealized particle, as seen in Figure 4.2. However, the median and mean diameters were found to be similar. The $C_{14}S/Au$ colloid of 21.4 Å diameter resulted in a coverage of 84 ± 2 $C_{14}S$ chains per Au nanoparticle, and a corresponding area per chain of 17.2 ± 0.4 Å^2. $C_{18}S/Au$, of particle diameter 22.4 Å, gave a coverage of 104 ± 3 $C_{18}S$ chains per Au nanoparticle, and an area per chain of 15.2 ± 0.4 Å^2, which is comparable to the Van der Waals' area per chain of ~ 15.9 Å^2. These coverages correspond to a surface Au to thiol ratio of ~ 2.5:1 (C_{14}) and 2.2:1 (C_{18}). Heath *et al.* calculated a ratio of ~ 2:1 surface Au to thiol for $C_{12}SH$-derivatized Au nanoparticles of 20 Å diameter.[6b]

(10) N. Camillone, C. E. D. Chidsey, G. Liu, G. Scoles, *J. Chem. Phys.* **1991**, *94*, 8493, and references therein.

(11) For example, a colloid (d = 22 Å) whose $C_{18}H_{37}SH$ area is 18 Å^2 and all-*trans* extended chain length is 29.8 Å would provide an area per chain end which is 14-fold greater.

(12) Dispersion of the nanoparticles in a good solvent (*i.e.* benzene, toluene, $CHCl_3$) leads to a disordering or solubilization of the chains on the particle. This is evident in solution-state NMR studies, where the spectra become relatively well-resolved and narrow-lined, indicative of a highly mobile state. Any solvent which provides for an isolation of the RS/Au particles in solution will most likely also solvate the alkyl chains and disrupt chain-chain interactions; the net result is an absence of any phase transition behavior in the temperature region probed in Figures 4.3 and 4.4.

(13) Temperature-programmed desorption studies of a hexadecanethiol monolayer

chemisorbed on a Au(111) single-crystal surface show that desorption of the thiol occurs at temperatures ≥ 227 °C.[15a]

(14) D. Marsh, *Handbook of Lipid Bilayer Membranes*, CRC, Boca Raton, FL, **1991.**

(15) a) R. G. Nuzzo, L. H. Dubois, D. L. Allara, *J. Am. Chem. Soc.* **1990**, *112*, 558; b) P. E. Laibinis, G. M. Whitesides, D. L. Allara, Y.-T. Tao, A. N. Parikh, R. G. Nuzzo, *ibid. 1991*, *113*, 7167; c) M. D. Porter, T. B. Bright, D. L. Allara, C. E. D. Chidsey, *ibid.* **1987**, *109*, 3559.

(16) a) L. H. Dubois, B. R. Zegarski, R. G. Nuzzo, *J. Electron Spectrosc. Relat. Phenom.***1990**, *54/55,* 1143; b) R. G. Nuzzo, E. M. Korenic, L. H. Dubois, *J. Chem. Phys.* **1990**, *93*, 767; c) F. Bensebaa, T. H. Ellis, A. Badia, R. B. Lennox, *J. Vac. Sci. Technol. A* **1995,** *13 (3)*, 1331, and references therein.

(17) R.H. Terrill, A. Postlethwaite, C.-h. Chen, C.-D. Poon, A. Terzis, A. Chen, J.E. Hutchison, M.R. Clark, G. Wignall, J.D. Londono, R. Superfine, M. Falvo, C.S. Johnson Jr., E.T. Samulski, R.W. Murray, *J. Am. Chem. Soc.* **1995,** *117*, 12537-12548.

(18) a) R.L. Whetten, J.T. Khoury, M.M. Alvarez, S. Murthy, I. Vezmar, Z.L. Wang, C.L. Cleveland, W.D. Luedtke, U. Landman in *Proceedings of the NATO Advanced Research Workshop on "The Chemical Physics of Fullerenes 10 (and 5) Years Later"*, (Ed: Andreoni), Kluwer Academic Publishers, Varenna Italy, 1995; pp. 475-490; b) R.L. Whetten, J.T. Khoury, M.M. Alvarez, S. Murthy, I. Vezmar, Z.L. Wang, P.W. Stephens, C.L. Cleveland, W.D. Luedtke, U. Landman, *Adv. Mater.* **1996**, *8*, 428-433.

(19) A. Lebuis, Department of Chemistry, McGill University, Nov. 1995, personal communication.

(20) J.E. Riegler, *J. Phys. Chem.* **1989**, *93*, 6457-6480.

(21) K. Levon, D. Weng, J. Mao, H. K. Lee, J. M. Tour, W. A. Schrivens, *Mat. Res. Soc. Symp. Proc.* **1994**, *349*, 127.

Chapter 5

Structure and Dynamics in SAMs: A DSC, IR, and Deuterium NMR Study*

5.1. Introduction

The phase properties of self-assembled alkanethiolate monolayers on metal surfaces have been addressed *via* the synthesis of alkanethiol-stabilized gold metal clusters of 20-30 Å diameter.[1,2] This system was chosen because of its unique potential to serve as a large surface area analogue to SAMs formed on planar metal surfaces. These alkylated nanoparticles have enabled the *quasi*-2D monolayer film structure to be probed by conventional methodologies such as NMR spectroscopy, calorimetry, and transmission FT-IR spectroscopy.[1,2] We find that SAMs on Au nanoparticles show strong parallels to the monolayers formed at planar surfaces. Differences do arise however due to the high radius of curvature of the surface and possible faceting of the particles[3-6].

The CH stretching vibrations in the FT-IR spectra of RS/Au nanoparticles (where R= C_8-C_{20}) indicate that for R $\geq C_{16}$, the alkyl chain exists predominantly in an extended, all-*trans* conformation at 25 °C.[1,7] Solid-state ^{13}C NMR spectroscopy further reveals the coexistence of motionally restricted all-*trans* chains with a smaller population of liquid-like conformationally disordered chains in $C_{18}S/Au$ at 25 °C.[2] More importantly, calorimetry[1,5], variable temperature FT-IR spectroscopy[1] and solid-state ^{13}C NMR studies[1,2] have established that a chain melting transition occurs in these alkylated metal colloids. The transition temperature associated with each chain (for R= C_{12}-C_{20}) closely parallels those found in electrochemical studies of planar RS/Au SAMs[8], X-ray diffraction studies of fatty acid Langmuir-Blodgett monolayer films[9], and in calorimetry studies of phospholipid bilayer membranes[10]. Melting transitions are highly sensitive to the degree of chain organization. Given that the thermotropic behavior of the RS/Au nanoparticles is

---

* Manuscript submitted to the *Journal of the Americal Chemical Society*, June 1996.

very similar to that of highly ordered, 2D self-assembled systems, there is surprisingly a high degree of chain conformational order in these colloids. How chain ordering arises is not immediately apparent, given the relation between the extended chain conformation and the curved geometry of these particles. Recent molecular dynamics (MD) simulations of butanethiol and dodecanethiol derivatized Au clusters reveal that the butanethiolate chains uniformly coat the colloid surface, while the longer dodecanethiolate chains exist (at low temperature) in ordered clusters or "bundles".[6] Transmission electron microscopy[1] and powder X-ray diffraction[5,6,11] reveal that adjacent Au particles are separated by approximately one chain length and not by the expected two chain lengths. This strongly suggests that chain ordering arises from an interdigitation of *chain domains* on neighboring particles.[1] An alternative packing configuration, involving the interdigitation of individual chains[5], is not likely given the large ratio of chain end area to Au-S headgroup area of 14:1.[1]

In this chapter, variable-temperature solid-state deuterium NMR spectroscopy is used, in conjunction with FT-IR spectroscopy and differential scanning calorimetry (DSC), to study both perdeuterated and specifically deuterated $C_{18}S/Au$ samples to gain insight into chain ordering and dynamics. Solid-state ^2H NMR has been extensively used to probe conformational order and molecular motion in lipid membranes[12-15], spherical supported lipid bilayers[16,17], rigid-rod polymers with alkyl side-groups[18-20], alkylammonium layer-structure compounds[21], and in alkylsilyl-modified silica gel chromatographic stationary phases[22,23]. Solid-state ^2H NMR spectroscopy offers distinct advantages over ^{13}C and ^1H NMR for probing the structure and dynamics of ordered systems. The peaks observed in ^2H NMR originate from the nuclear quadrupole coupling of the deuteron with the electric field gradient of the C-^2H σ-bond. An axially symmetric quadrupolar interaction dominates the ^2H NMR spectrum so that the line shapes are simple and solely dependent upon the amplitude and symmetry of the molecular motions. The peak shapes reflect intramolecular dynamics and there are no complex contributions from the chemical shift anisotropy and heteronuclear dipolar interactions which greatly increase the complexity of ^{13}C and ^1H NMR spectra in regards to analyzing motional phenomena. Furthermore, since the relaxation of the ^2H nucleus is dominated by the quadrupolar interaction, there is no need to establish relaxation mechanisms.[14,23-25] More importantly, the low natural abundance of deuterium (*i.e.* 0.015%) eliminates background contributions from unlabeled material so that the dynamics of a single position can be exclusively observed in selectively labeled molecules.

Quadrupolar splitting in ^2H NMR is especially sensitive to motions and orientations at different positions in a molecule. For the ^2H nucleus with spin $I = 1$ and an asymmetry parameter $\eta = 0$ for the C-^{2}H bond, the allowed energy transitions are $-1\leftrightarrow 0$ and $0\leftrightarrow 1$, giving rise to a doublet in the NMR spectrum with a peak separation given by

$$\Delta \upsilon_Q = 3/4\ (e^2qQ/h)(3\cos^2\theta - 1) \qquad (1);$$

where $\Delta \upsilon_Q$ is the quadrupolar splitting or peak separation in frequency units, (e^2qQ/h) is the quadrupolar coupling constant (168 kHz for an aliphatic sp^3 C-^{2}H bond), θ is the angle between the principal axis of the electric field tensor of the ^{2}H nucleus and the magnetic field, H_0.[14,25] For a rigid polycrystalline solid, all values of θ are possible and a so-called rigid powder pattern or Pake pattern is obtained (Scheme 5.1A). In this case, the separation between the peak maxima ($\theta = 90°$) is *ca.* 130 kHz and the separation between the steps at the wings ($\theta = 0°$) is twice this value.[14,25] In the case of lipid membranes, organic thin films, and rigid-rod polymers with flexible side chains, there is considerable motion of the C-^{2}H bond due to such processes as methyl group rotation, *gauche-trans* bond isomerization in an alkyl chain, rotation of a molecule about its long axis or flipping of a phenyl ring about its C_2 axis. Molecular motions that have correlation times of *ca.* 10^{-7}-10^{-4} s[14,24] can be studied by ^{2}H NMR, a much longer time scale than most other spectroscopic techniques. Motions that are slow on the NMR timescale are expected to have a negligible influence on the ^{2}H NMR spectrum. Fast motions ($t \ll 10^{-6}$ s), on the other hand, cause the $(3\cos^2\theta - 1)$ term in equation 1 to be averaged with time, resulting in a decrease of the quadrupolar splitting and/or changes in the peak line shape (Scheme 5.1B and C).[14,25] Thus, in most cases, the ^{2}H NMR spectral line shapes and the spin-lattice (T_1) relaxation times provide incisive information on molecular orientation as well as on the type and the rate of motion that a particular ^{2}H-labeled site is undergoing.[14,25] For this reason, FT-IR and ^{2}H NMR spectroscopy can give complementary information on the structure and dynamics of ^{2}H-labeled systems, given that FT-IR spectroscopy probes a timescale which is less than 10^{-10} s.[26]

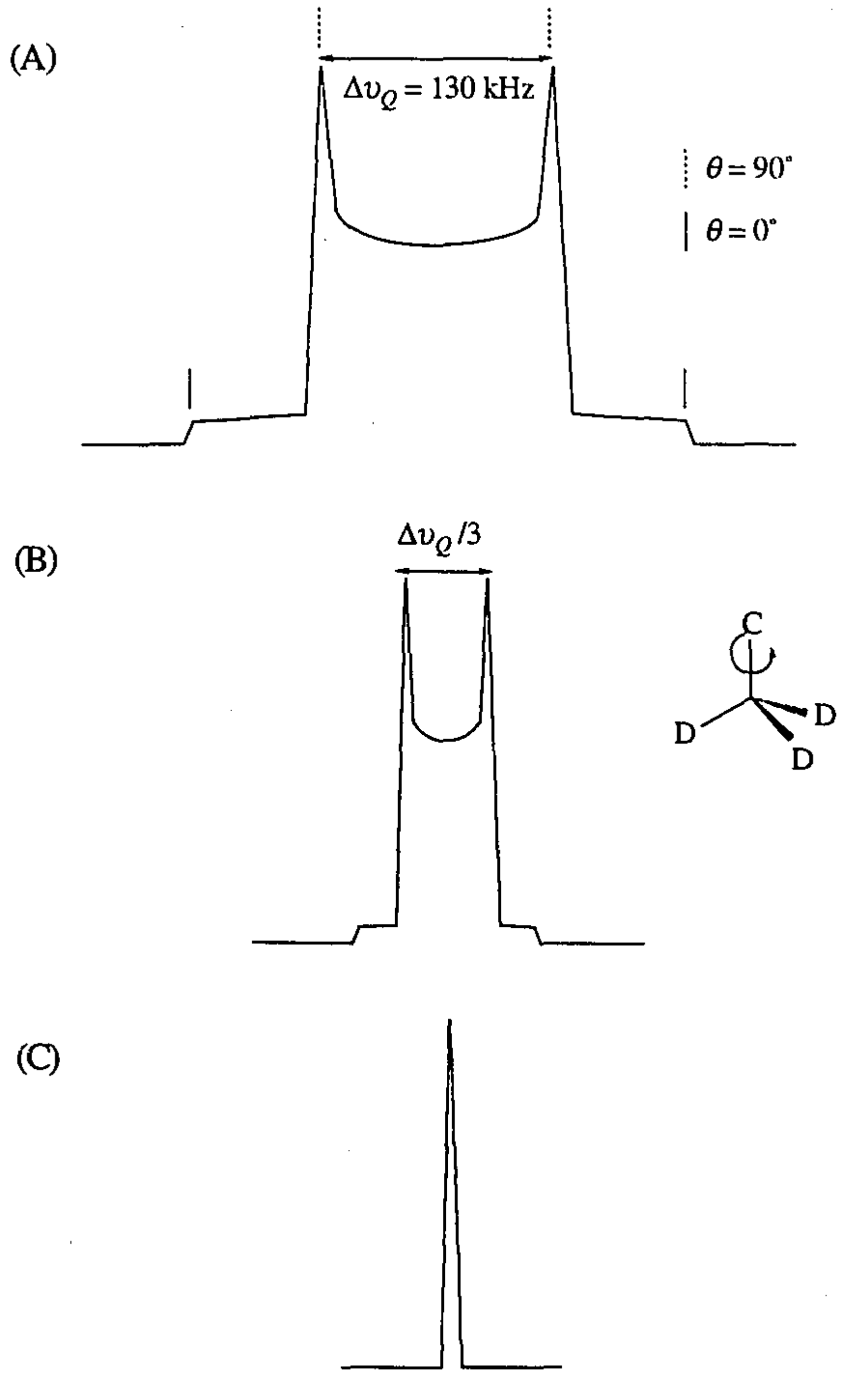

Scheme 5.1. Theoretical ^{2}H NMR spectral line shapes for (A) a rigid polycrystalline solid (Pake pattern), (B) a methyl group rotating about a C_3 axis, and (C) isotropic motion.

In this study, *n*-octadecanethiols deuterated at different positions along the alkyl chain were synthesized and used to prepare $C_{18}SH$-derivatized Au nanoparticles for variable temperature solid-state ^2H NMR studies. The materials studied include:

$CD_3(CD_2)_{16}CH_2SH$	(positions 2-18 deuterated)
$CH_3(CH_2)_{16}CD_2SH$	(position 1 deuterated)
$CH_3(CH_2)_4CD_2CD_2CD_2CD_2(CH_2)_9SH$	(positions 10-13 deuterated)

In conjunction with DSC and FT-IR spectroscopy, solid-state ^2H NMR is used to resolve outstanding structural and dynamic issues concerning the chain order and phase behavior of these alkylated Au nanoparticles.

5.2. Experimental Section

5.2.1. Materials: d_{35}-Stearic acid (98 atom % D) and deuterium gas (99.99%) were purchased from Cambridge Isotope Laboratories, Inc. (Andover, MA). 10, 12-Octadecadiynoic acid was obtained from Farchan Laboratories, Inc. (Gainesville, FL). Stearic acid (lab-grade), from Anachemia Chemicals Ltd. (Montreal, Canada), was recrystallized from hexanes before use. *n*-Octadecanethiol (98%, Aldrich Chemical Co., Milwaukee, WI) was recrystallized three times from ethanol. Tris(triphenylphosphine)rhodium(I)chloride (Wilkinson's catalyst), lithium aluminum hydride, lithium aluminum deuteride (98 atom % D), hydrogen tetrachloroaurate(III) trihydrate, and tetraoctylammonium bromide were all purchased from Aldrich. Sodium thiosulfate was from A&C American Chemicals Ltd. (Montreal, Canada) and 48% HBr was from Fluka Corp. (Ronkonkoma, NY).

5.2.2. d_{35}-Octadecanethiol: d_{35}-Stearic acid (1.10 g, 3.45 mmol) was dissolved in 60 mL of dry THF. This solution was added *via* a dropping funnel to a three-neck round bottom flask, equipped with a reflux condenser and a calcium carbonate drying tube, and containing $LiAlH_4$ (1.04 g, 27.5 mmol) dissolved in 125 mL of dry THF. The reaction mixture was refluxed for *ca.* 12 hr. The reaction vessel was cooled in an ice bath and distilled water was carefully added dropwise to the reaction mixture to destroy the residual $LiAlH_4$. A 4 mL aliquot of 6 N HCl solution was added and reflux was continued for an additional 12 hr. Hexanes (100 mL) were added with stirring to the cooled reaction mixture. The remaining white precipitate was removed by filtration at this stage and the mixture poured into a separatory funnel. The organic layer was separated from the aqueous layer. The aqueous phase was further extracted with 2 x 50 mL of hexanes. The combined organic extracts were washed with 2 x 100 mL of distilled water and then dried over anhydrous magnesium sulfate. The solvent was removed by rotary evaporation to yield 0.980 g (93%) of d_{35}-octadecanol (*i.e.* $CD_3(CD_2)_{16}CH_2OH$).

The perdeuterated octadecanol (0.980 g, 3.21 mmol) was added to a mixture of 50 mL of 48% HBr and 100 μL of concentrated H_2SO_4. The mixture was refluxed for 8 hr. The HBr mixture was diluted with 25 mL of distilled water and 50 mL of hexanes were added with stirring. The hexanes phase was separated from the aqueous HBr phase, and then the HBr phase was further extracted with 2 x 50 mL of hexanes. The hexanes extracts were pooled together, washed with 2 x 75 mL of water, and dried over anhydrous magnesium sulfate. The solvent was removed by rotary evaporation and the residue purified by column chromatography (silica gel, *n*-hexane) to yield 0.986 g (84%) of d_{35}-octadecyl bromide.

The octadecyl bromide (0.980 g, 2.66 mmol) was dispersed in 50 mL of absolute ethanol. A solution of $Na_2S_20_3 \cdot 5H_20$ (0.660 g, 2.66 mmol) in 10 mL of water was added to the octadecyl bromide and the reaction was refluxed for 6 hr. The resulting Bunte salt was hydrolyzed with HCl (9.0 mL of 6 N HCl) by refluxing for 4 hr. The cooled reaction mixture was poured with stirring into a two-phase mixture of 10 mL of distilled water and 25 mL of hexanes. The organic layer was separated from the aqueous layer, and the aqueous phase was then further extracted with 2 x 25 mL of hexanes. The combined hexanes extracts were washed with 2 x 35 mL of water and dried over anhydrous magnesium sulfate. The solvent was removed by rotary evaporation and the residue was recrystallized from ethanol to yield pure d_{35}-octadecanethiol (0.768 g, 90%). TLC (silica gel, *n*-hexane): $R_f = 0.7$; ^1H NMR (499.84 MHz, $CDCl_3$): δ 2.52 (s, CH_2SH); ^2H NMR (76.73 MHz, $CHCl_3$); δ 0.83 (s, 3D, CD_3), 1.19 (s, 30D, $CD_3(CD_2)_{15}$), 1.53 (s, 2D CD_2CH_2SH). MS (EI): m/z 321 $[M]^{\cdot+}$.

5.2.3. 1-d_2-Octadecanethiol: Stearic acid (2.00 g, 7.03 mmol) was converted to 1-d_2-octadecanol (1.78 g, 93%) by reduction with $LiAlD_4$ as described above. Bromination followed by Bunte salt formation and hydrolysis using the procedures previously described yielded 1-d_2-octadecanethiol (1.36 g, 67% with respect to stearic acid). TLC (silica gel, *n*-hexane): $R_f = 0.7$; ^1H NMR (499.84 MHz, $CDCl_3$): δ 1.59 (t, 2H, CH_2CD_2SH), 1.37 (m, 2H, $CH_2CH_2CD_2SH$), 1.26 (s, 28H, $CH_3(CH_2)_{14}$), 0.88 (t, 3H, CH_3); ^2H NMR (76.73 MHz, $CHCl_3$); δ 2.49 (s, CD_2SH); MS (EI): m/z 288 $[M]^{\cdot+}$.

5.2.4. 10,11,12,13-d_8-Octadecanethiol: 10, 12-Octadecadiynoic acid (1.00 g, 3.62 mmol) was dissolved in 10 mL of freshly distilled, argon saturated THF. 100 mg of Wilkinson's catalyst were added and the reactor was evacuated and flushed with argon three times. The reactor was then flushed with D_2 gas and filled to a pressure of 1 PSI. The reaction mixture was stirred for ~ 19 hr after which the reactor was refilled with additional D_2 gas. The reaction mixture was stirred for an additional 3 days. The solvent was removed by rotary evaporation and the residue chromatographed (silica gel, 80:20 v/v hexanes:ethyl acetate). Recrystallization from hexanes yielded pure 10,11,12,13-d_8-octadecanoic acid (0.495 g, 47%). mp 67-69 °C; ^{1}H NMR (499.84 MHz, $CDCl_3$): δ 2.35 (t, 2H, CH_2COOH), 1.63 (m, 2H, CH_2CH_2COOH), 1.25 (s, 20H, $CH_3(CH_2)_4(CD_2)_4(CH_2)_6CH_2CH_2COOH$), 0.88 (t, 3H, CH_3); ^{2}H NMR (76.73 MHz, $CHCl_3$); δ 0.93 (s, $(CD_2)_4$).

10,11,12,13-d_8-Octadecanoic acid (0.485 g, 1.66 mmol) was reduced to the alcohol (0.364 g, 79%) using $LiAlH_4$ as described previously. Bromination with 48% HBr followed by Bunte salt formation and hydrolysis yielded 10, 11, 12, 13-d_8-octadecanethiol (0.268 g, 70% with respect to d_8-octadecanol). TLC (silica gel, *n*-hexane): $R_f = 0.7$; ^{1}H NMR (499.84 MHz, $CDCl_3$): δ 2.51 (t, 2H, CH_2SH), 1.59 (m, 2H, CH_2CH_2SH), 1.37 (m, 2H, $CH_2CH_2CH_2SH$), 1.25 (s, 20H, $CH_3(CH_2)_4(CD_2)_4(CH_2)_6CH_2CH_2CH_2SH$), 0.88 (t, 3H, CH_3); MS (EI): m/z 294 $[M]^{\cdot+}$.

5.2.5. C_{18}SH-Derivatized Gold Nanoparticles: Gold nanoparticles derivatized with 10, 11, 12, 13-d_8-octadecanethiol, 1-d_2-octadecanethiol, and d_{35}-octadecanethiol were prepared following the method of Brust *et al.*[1,27]. The syntheses were carried out using 1.8 mmol of $HAuCl_4 \cdot 3H_2O$ and a modified $AuCl_4^-$:$C_{18}SH$ mole ratio of 3:1, instead of 1:1[27]. The 3:1 $AuCl_4^-$:RSH ratio was used because it produces fully covered Au nanoparticles (~ 30 Å in diameter) and eliminates the exhaustive (and exhausting!) washing/extraction process required to remove the large amounts of residual thiol and disulfide present in the original preparation.[1,28] For the synthesis of Au nanoparticles coated with 10, 11, 12, 13-d_8-octadecanethiol, only one-third of the octadecanethiol surfactant molecules were deuterated. For the other syntheses, the deuterated octadecanethiols were used undiluted. The C_{18}S/Au colloids were purified as described in Chapter 4 and dried under vacuum.[1] Complete removal of unbound thiol was verified by TLC (silica gel, *n*-hexane) and by ^{1}H NMR (499.84 MHz) and/or ^{13}C NMR (125.70 MHz) spectroscopy (*i.e.* 30-40 mg of C_{18}S/Au colloid in 0.7 mL of d_6-benzene).[1] With 1.8 mmol of $AuCl_4^-$ as the starting material, 350-380 mg of purified C_{18}S/Au powder was obtained.

5.2.6. Transmission Electron Microscopy: Samples for TEM were prepared by dipping standard carbon-coated grids (200-300 Å) Formvar copper grids (200 mesh) into a dilute hexane solution of the RS/Au nanoparticles for several seconds. The TEM grids were withdrawn from the solution and allowed to dry under ambient atmosphere for 5 min. Phase contrast images were obtained with a top-entry Phillips EM 410T electron microscope operated at an accelerating voltage of 80 keV. Micrographs were obtained at $6{\cdot}10^4$X and $8{\cdot}10^4$X. The size distributions of the $C_{18}S/Au$ nanoparticles were determined from the diameters of at least 250 particles located in a representative region of the micrographs using a video image analysis software program (SigmaScan Pro3, Jandel Scientific). The particle sizes obtained are the following: 1-d_2-$C_{18}S/Au$ 27 ± 8 Å; 10,11,12,13-d_8-$C_{18}S/Au$ 29 ± 8 Å; d_{35}-$C_{18}S/Au$ 27 ± 6 Å.

5.2.7. Infared Spectroscopy: The $C_{18}S/Au$ colloidal particles were deposited dropwise onto a KBr disc from a concentrated hexane solution. Evaporation of the solvent resulted in a uniform film. Infrared spectra were acquired on a Perkin-Elmer FT-IR Microscope Model 16PC (MCT detector) equipped with a Mettler FP 52 hot stage for variable temperature experiments (10-100 °C). Spectra were collected in the transmission mode with an unpolarized beam, at a resolution of 2 cm^{-1} with 128 scans, and a spectral window of 4000-600 cm^{-1}. The IR sample was purged continuously with dry nitrogen and maintained at each temperature for 20 min before a spectrum was acquired. Background spectra of the clean KBr disc were collected at the same temperatures and subtracted from the sample spectra.

5.2.8. Differential Scanning Calorimetry: DSC experiments were conducted with a Perkin-Elmer DSC-7 instrument calibrated for temperature and peak area by means of indium and octadecane standards for the -40 °C to 100 °C temperature range or indium and cyclohexane for runs of -100 °C to 100 °C. Thermograms were run on samples of ~ 10 mg of $C_{18}S/Au$ particles in sealed aluminum pans under a purging atmosphere of either nitrogen (-40 °C to 100 °C) or helium (-100 °C to 100 °C) gas at heat-cool rates of 5 °C/min or 10 °C/min.

5.2.9. Solid-State Deuterium NMR spectroscopy: Samples for ^{2}H NMR were prepared by packing a shortened 5 mm NMR tube with 150-180 mg of dry ^{2}H-labeled $C_{18}S/Au$ powder and covering the tube with teflon tape. ^{2}H NMR spectra were recorded on a Chemagnetics 300 MHz spectrometer operating at a frequency of 46.045 MHz. A quadrupole echo sequence $(90°_{\pm x} - \tau_1 - 90°_y - \tau_2)^{29}$ with transmitter blanking was employed and a 500 kHz spectral window was scanned. τ_1 and τ_2 were 40 μs and 20 μs, respectively. Spectra were acquired at both low and high temperature with pulse delays ranging from 0.5 s to 5 s. Since the longer pulse delay times produced spectra that were identical to the ones acquired using short delays, all spectra were acquired with a pulse delay of 0.5 s to shorten the acquisition time. Depending on the signal-to-noise ratio, between 512 - 29 000 transients were accumulated. After data accumulation, the FID was left-shifted by the correct number of points so that for each spectrum, the FID was Fourier transformed starting at the echo maximum. Heating and cooling of the NMR sample was accomplished using air, cooled by passage through an acetone/dry ice bath, and a calibrated temperature control unit (Bruker Instruments, Inc.). A 30 min sample equilibration time was allowed at each temperature before the start of spectral acquisition. For each ^{2}H-labeled $C_{18}S/Au$ sample, an initial spectrum was acquired at 25 °C and then spectra were collected at progressively lower temperatures. The cooled sample was then gradually reheated past 25 °C and spectra were collected at higher temperatures. After heating past the melting transition, the sample was cooled to 25 °C and a spectrum was acquired to check if any thermally-induced changes had occurred.

5.3. Results and Discussion

5.3.1. DSC Measurements: The phase behavior of thiol-derivatized Au nanoparticles has been characterized by DSC in terms of the temperature and the enthalpy of the phase transition.[1] The DSC thermograms clearly show that the RS/Au particles (where R= C_{12}-C_{20}), in the solid state, undergo distinct phase transitions which can be associated with reversible disordering of the alkyl chains. Both the peak maximum temperature and the enthalpy associated with the DSC transition was found to increase with increasing chain length.[1] This trend strongly parallels that seen in other materials undergoing gel-to-liquid crystalline transitions, such as diacyl phospholipids.

Figure 5.1 shows the DSC endotherms of the various deuterated $C_{18}S/Au$ samples. The peak maximum temperature for both the 1-d_2-$C_{18}S/Au$ and d_{35}-$C_{18}S/Au$ is 48 °C, while the peak maximum temperature for the 10,11,12,13-d_8-$C_{18}S/Au$ is 52 °C. A peak maximum temperature of 51 °C was previously reported for the fully hydrogenated $C_{18}S/Au$.[1] The main phase transition temperatures of perdeuterated phospholipids[17] are depressed by ~ 4 - 5 °C compared to the fully hydrogenated analogue. Such a strong conclusion cannot be made in our case for the d_{35}-$C_{18}S/Au$ because the peak maximum temperature observed by DSC varies by 2 - 3 °C from one $C_{18}S/Au$ preparation to another.

It is important to note that unlike the gel-to-liquid crystalline transitions in lipid bilayer membranes, the transition for the RS/Au colloidal system is relatively broad and occurs over a *ca.* 30 °C temperature range for each sample. Furthermore, the DSC peaks of the deuterated $C_{18}S/Au$ samples are preceded by a sloping or curved baseline extending down to -100 °C, which is best seen in the endotherm of d_{35}-$C_{18}S/Au$ (Figure 5.1). This may reflect either the existence of a disordered liquid-like chain population or the occurrence of chain motional processes which accompany the phase transition.

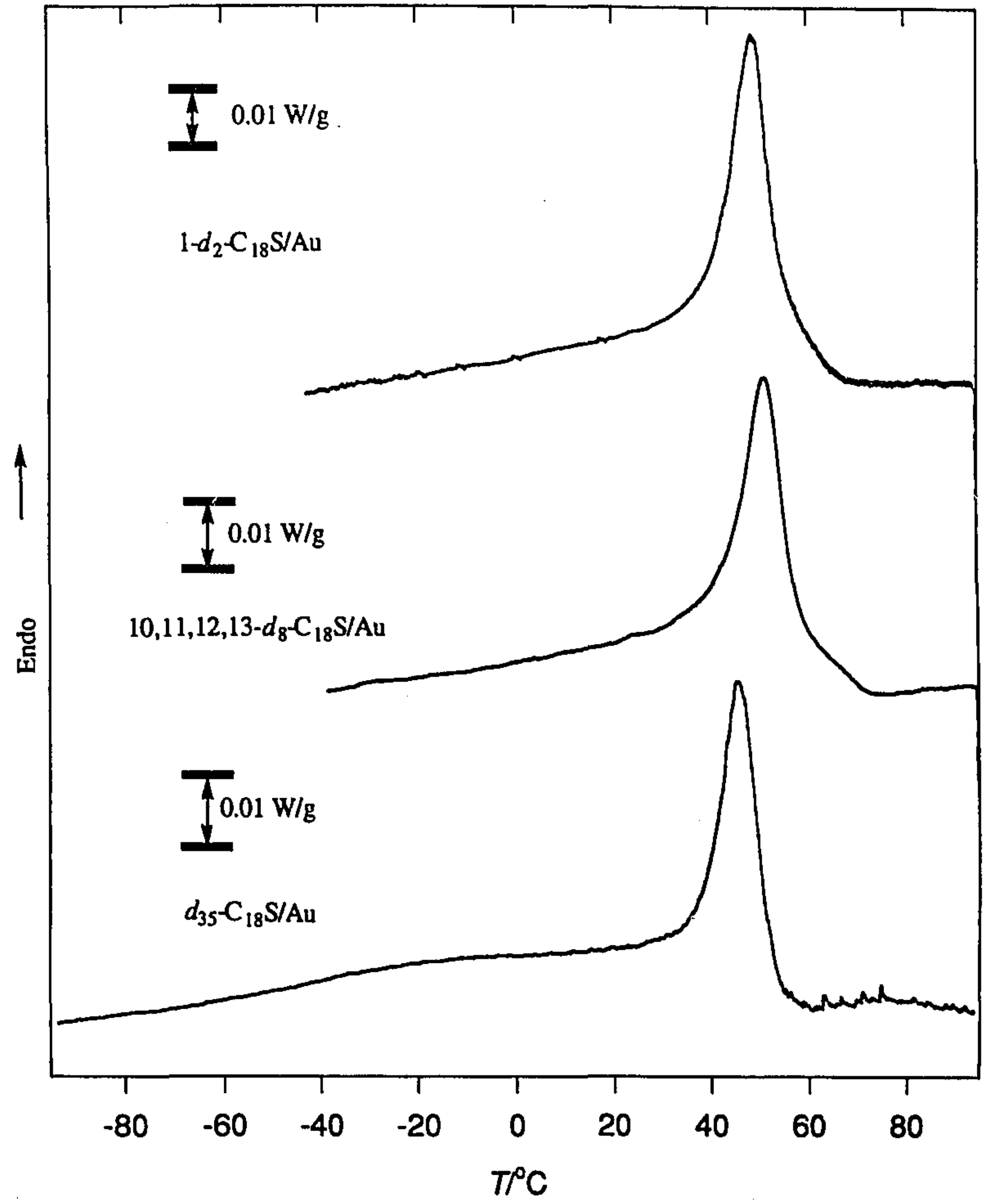

Figure 5.1. DSC endotherms of 1-d_2-C_{18}S/Au, 10,11,12,13-d_8-C_{18}S/Au, and d_{35}-C_{18}S/Au powders. Scan rate is 5 °C·min^{-1} for 1-d_2-C_{18}S/Au and 10,11,12,13-d_8-C_{18}S/Au and 10 °C·min^{-1} for d_{35}-C_{18}S/Au.

As suggested earlier, the broadness of the transition may be caused by poor bulk crystallization of the RS/Au nanoparticles.[1,2] Recrystallization and thermal annealing do not however significantly sharpen the DSC peak. The broad transition may also be due to the fairly large particle size distribution which can affect the alkyl chain packing. While these factors may contribute somewhat to the peak broadening, comparison with the thermotropic behavior of model polymer lipid membranes[30] and planar RS/Au SAMs[8] suggests that covalent bonding of the sulfur headgroup to the gold may restrict the cooperative nature of the transition, resulting in a broad peak.

In recent years, model polymer membranes have been designed to obtain lipid bilayers which exhibit thermal stabilities superior to those of biomembranes.[30-32] Such stable membranes are of interest for studies of cell-cell interaction and as drug carriers. For this purpose, a C_{18} diacyl lipid analogue has been synthesized with a polymerizable methacryloylic moiety attached to the quaternary ammonium headgroup.[30-32] Polymerization restricts the lateral mobility of the lipid headgroup in the bilayer and is reported to significantly reduce the cooperativity of the gel-to-liquid crystalline phase transition. This restricted headgroup mobility caused the polymer membrane to exhibit a broader gel-to-liquid crystalline transition than the monomer membrane (*i.e.* the peak width at half maximum is 0.7 °C for the monomer membrane and 2.1 °C for the polymer membrane).[30] Furthermore, the peak maximum temperature is depressed by 20 °C and the enthalpy is reduced by a factor of 2 compared to the monomer bilayer.[30] The enthalpy measured earlier for the DSC transition of $C_{14}S/Au$ (10 kJ/mol) and $C_{18}S/Au$ (21 kJ/mol) is however close to that of the main transition enthalpies for *n*-diacylphosphatidylcholines of equivalent chain length[10].[1] Thus, even though these lipid molecules have relatively unrestricted lateral mobility whereas pinning of the sulfur to the Au is expected to restrict the alkanethiolate chain mobility, there is no effect manifested in terms of either the RS/Au transition temperature or enthalpy. Melting of the RS/Au nanoparticles also introduces the possibility that rotational and/or lateral motion of the entire particle sets in. The onset of an isotropic peak in the ^2H NMR spectra at higher temperatures (*vide infra*) may suggest rotational motion of the Au particle. This rotation can be formally equivalent to the 2D diffusion available to lipid molecules on melting. If this were the case, then the DSC peak broadness may be a manifestation of the particle size distribution in an indirect way. That is, the particle tumbling rates may be size dependent. The alkyl chains (in this model) must melt before the tumbling (or entropy) issue becomes important. The width of the RS/Au DSC peak and the similarity in the enthalpy values of the RS/Au nanoparticles and *n*-diacylphosphatidylcholine multilamellar vesicles are sensitive indicators of the cooperative nature of the order-disorder process[33]. As such, the broad transitions observed for both planar and colloidal RS/Au SAMs are most probably due to the complex inter-relationship between the metal surface and RS chain domain sizes and their polydispersities.

Bloom and Bayerl also report significant differences in the DSC phase behavior of single lipid bilayers supported on glass microspheres (SSVs) as compared to multilamellar lipid vesicles (MLVs).[17] For instance, the SSV does not exhibit a chain tilt/untilt pretransition, the main transition temperature is lowered by 2 °C over that of the MLV, the half-width of the main transition peak is a factor of four broader for the SSV than for the MLV, the enthalpy of the main transition is 25% lower for the SSV, and the hysteresis observed between the melting and crystallization temperature values is larger.[17] Bloom and Bayerl attribute these changes to *quasi*-2D melting phenomena. In MLVs, interbilayer interactions also increase the cooperativity of the phase transition. This is interesting because fatty acid Langmuir-Blodgett (LB) monolayers on silicon wafers also show broad chain disordering transitions as detected by electron diffraction.[9] The gradual chain disordering occurs over a *ca.* 20 °C temperature range and the temperatures are very similar to those of equivalent chain length RS/Au SAMs[1]. Since the fatty acid chains are only physisorbed to the underlying silicon, the gradual chain melting process observed for these LB monolayer films cannot be a manifestation of restricted chain mobility due to strong headgroup-substrate interaction. Thus, it may well be that the broad chain order-disorder phase transitions observed for self-assembled alkylthiol monolayers on planar and colloidal Au surfaces are due to melting in *quasi*-2D systems.

5.3.2. FT-IR Spectroscopy: DSC establishes that a phase transition occurs in alkylthiol monolayers self-assembled at colloidal Au surfaces. Although the transition can be characterized in terms of temperature, enthalpy, and cooperativity, no direct information can be obtained from DSC about the conformational state of the alkyl chains. FT-IR spectroscopy is a powerful technique for probing the conformation and orientation of alkyl chains adsorbed to surfaces.[34-40] In particular, the frequencies of the methylene symmetric and antisymmetric vibrational stretches are related to the population of *trans* and *gauche* conformers.[16,35,36,38,41] Variable temperature transmission FT-IR spectroscopic studies show that these alkylated nanoparticles undergo a transition from a highly chain-ordered state to a chain-disordered state at the phase transition temperatures measured by DSC.[1] However, no insight was gained concerning where the disordering starts in the alkyl chain and how far along the chain the disorder propagates. FT-IR studies of deuterated lipids in multilamellar vesicles[41] and supported on spherical microbeads[16] have shown that the temperature dependence of the symmetric CD_2 stretching vibration depends on the average number of *gauche* conformers per lipid acyl chain. The symmetric CD_2 stretching frequency (~ 2090 cm^{-1}) increases by ~ 5 cm^{-1} during the gel-to-liquid crystalline phase transition.[16] The antisymmetric CD_2 stretch (~ 2190 cm^{-1}) also increases with temperature, but the shift is less pronounced.[41] By deuterating the $C_{18}SH$ molecule at specific sites along the chain, the thermally-induced onset of local disorder can be monitored *via* the CD_2 stretching vibrations.

Figure 5.2 tracks the CD_2 symmetric ($\upsilon_{sym}(CD_2)$) and antisymmetric ($\upsilon_{asym}(CD_2)$) stretches of the deuterated $C_{18}S/Au$ samples as a function of temperature. In Figure 5.3A, the peak position of $\upsilon_{sym}(CD_2)$ is plotted as a function of temperature for d_{35}-$C_{18}S/Au$ and 10,11,12,13-d_8-$C_{18}S/Au$. The value of the $\upsilon_{sym}(CD_2)$ peak frequency for the 10,11,12,13-d_8-$C_{18}S/Au$ nanoparticles exhibits a sharp discontinuity at the DSC detected phase transition temperature, ~ 50 °C. By contrast, the d_{35}-$C_{18}S/Au$ sample shows only a gradual chain disordering transition. A similar trend is observed for the $\upsilon_{asym}(CD_2)$ peak. Furthermore at 10-15 °C, $\upsilon_{sym}(CD_2)$ for 10,11,12,13-d_8-$C_{18}S/Au$ occurs at ~ 2084 cm^{-1}, while $\upsilon_{sym}(CD_2)$ for d_{35}-$C_{18}S/Au$ is ~ 2088 cm^{-1}. This clearly indicates that at 10-15 °C, the population of *gauche* conformers is larger in the perdeuterated $C_{18}S/Au$ material than for 10,11,12,13-d_8-$C_{18}S/Au$. Obviously, in d_{35}-$C_{18}S/Au$, there are contributions from *gauche* CD_2s located in the C_{14}-C_{17} region, even 35 °C below the DSC-detected phase transition temperature. Helium diffraction[42,43] and surface IR studies[35,36] of long chain alkylthiol SAMs on planar Au confirm that *gauche* conformational defects are concentrated at the chain termini at temperatures below 27 °C. These chain end *gauche* defects persist even at -70 °C.[35,36] Thus, the *ca.* 4 cm^{-1} shift in peak frequency of the symmetric CD_2 stretch (υ_{sym}) of d_{35}-$C_{18}S/Au$ relative to that of 10,11,12,13-d_8-$C_{18}S/Au$ is definitely a result of the disordered state of the chain ends. Since only a gradual shift in $\upsilon_{sym}(CD_2)$ is observed for d_{35}-$C_{18}S/Au$ with increasing temperature, it is most probable that a weighted average of the *trans* and *gauche* bond populations along the *entire* chain length is reported in this experiment. In variable temperature surface IR studies of planar alkylthiol monolayers, Dubois and Nuzzo[35,36] observed the gradual appearance of *gauche* conformational chain defects upon heating, instead of the dramatic population increase expected from first-order melting processes. By contrast, the shift in $\upsilon_{sym}(CD_2)$ for d_8-$C_{18}S/Au$ shown in Figure 5.3A specifically reflects the temperature dependence of the *trans* and *gauche* bond population at positions 10-13 (*i.e.* in the middle of the alkyl chain) and a sharp transition is observed. Molecular dynamics simulations of $C_{15}S$ chains absorbed onto a Au(111) surface predict that at 27 °C, the percentage *gauche* defect concentration is approximately 4.4% and **all** of the *gauche* defects are located at the chain termini.[44]

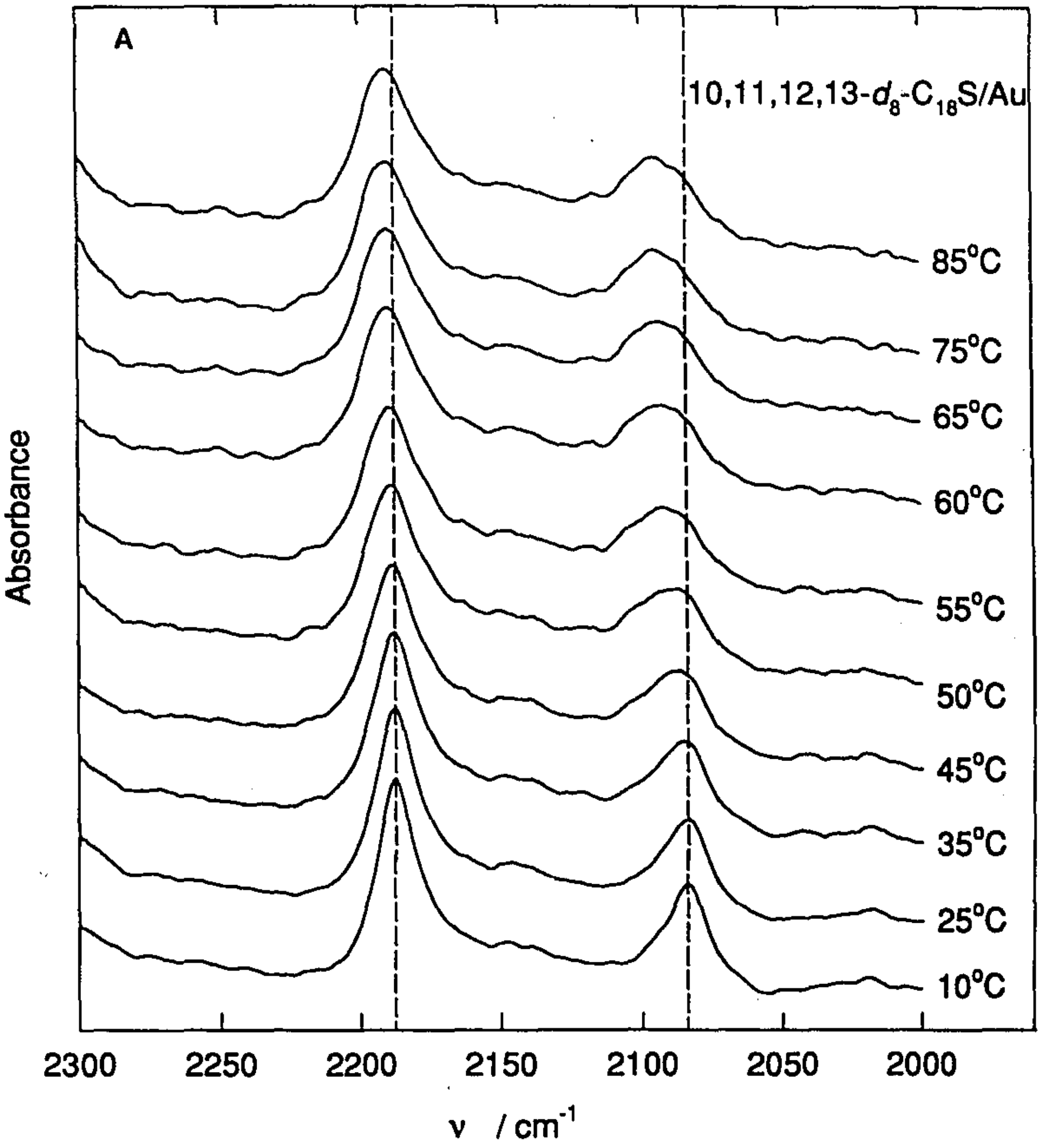

Figure 5.2. Variable temperature transmission FT-IR spectra of the CD_2 stretching region (2300-2000 cm^{-1}) for the deuterated C_{18}S/Au particles. The dotted lines are visual aids. (A) FT-IR spectra of 10,11,12,13-d_8-C_{18}S/Au.

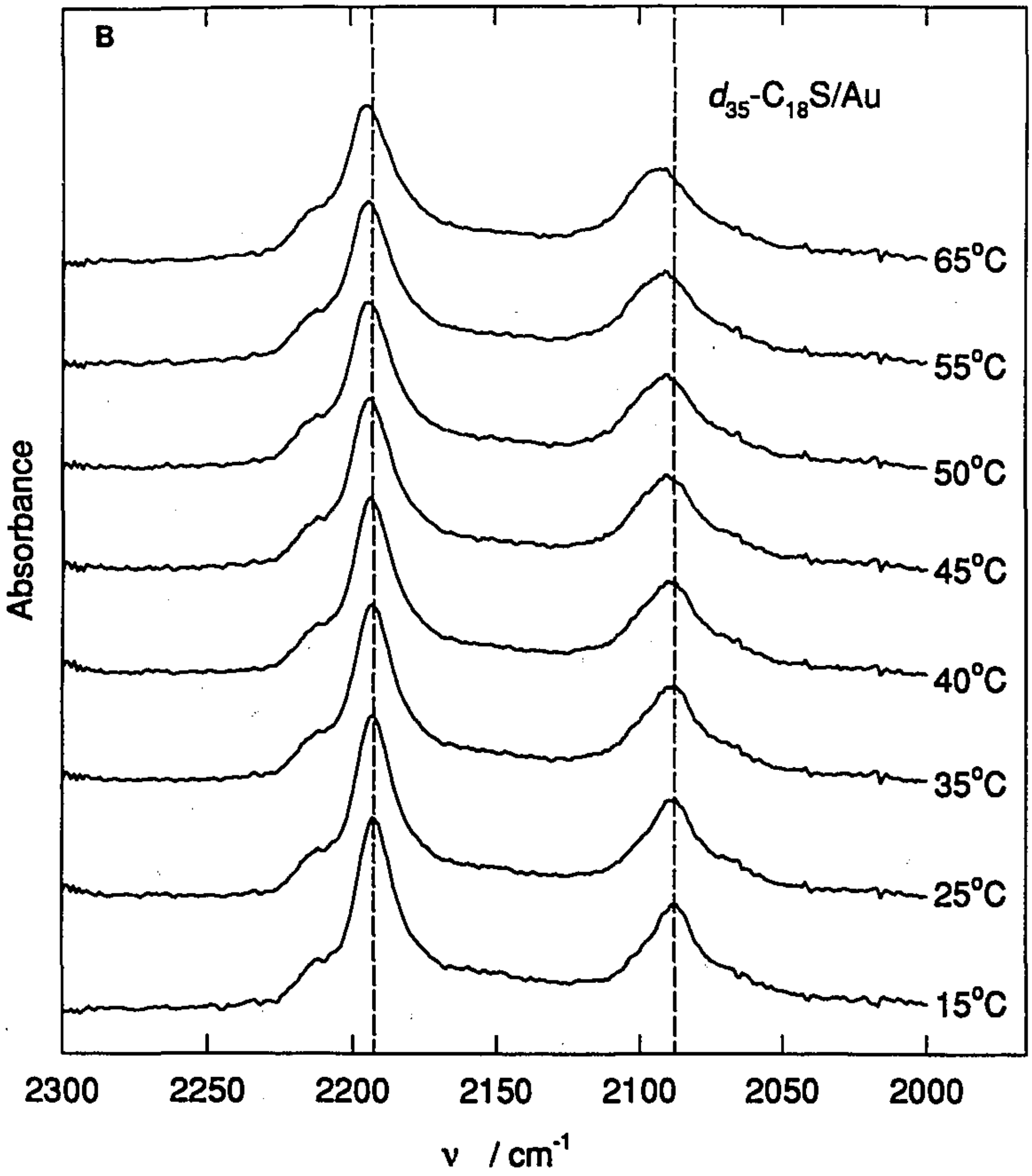

Figure 5.2. (cont'd) (B) FT-IR spectra of d_{35}-C_{18}S/Au.

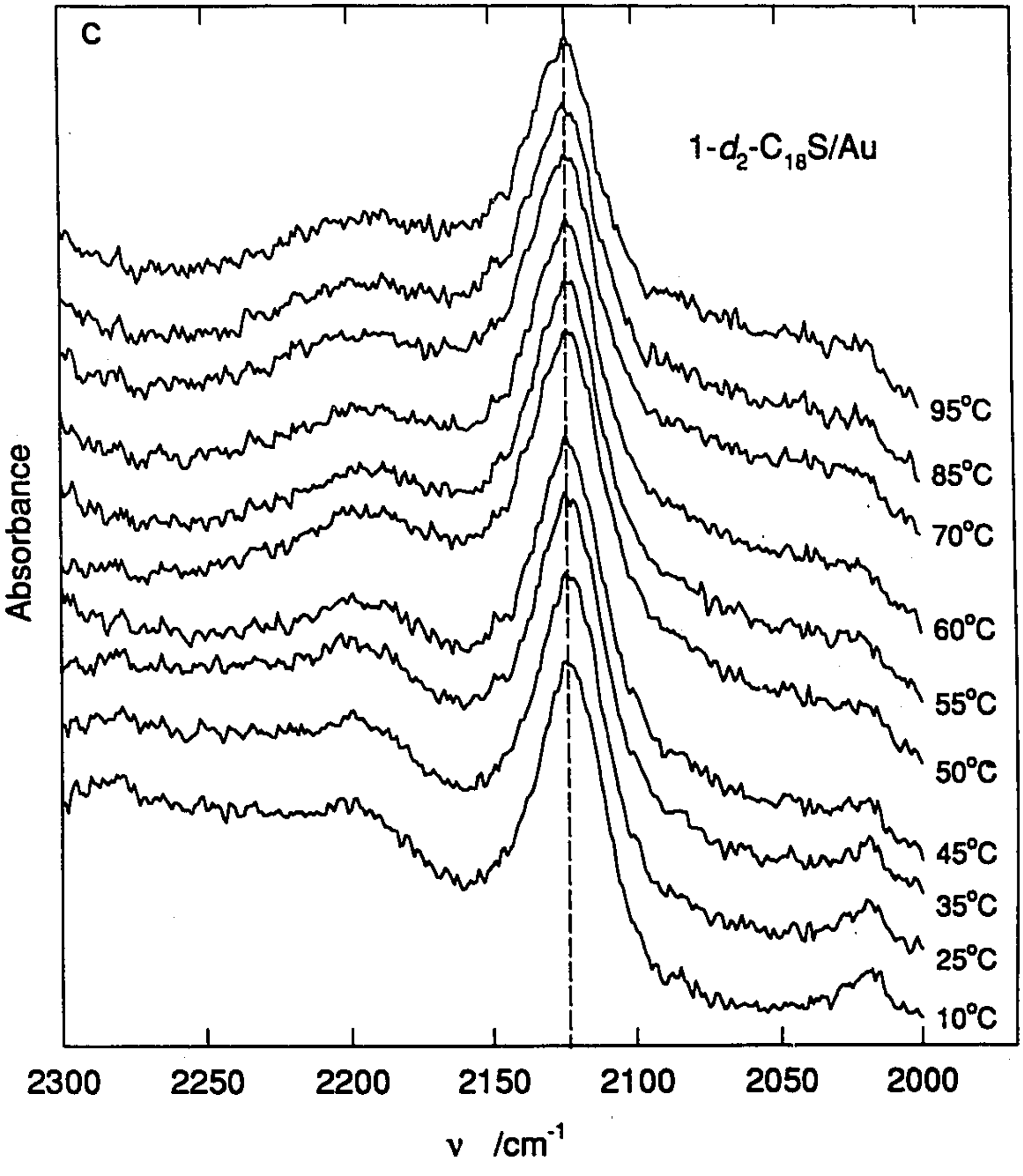

Figure 5.2. (cont'd) (C) FT-IR spectra of 1-d_2-C_{18}S/Au.

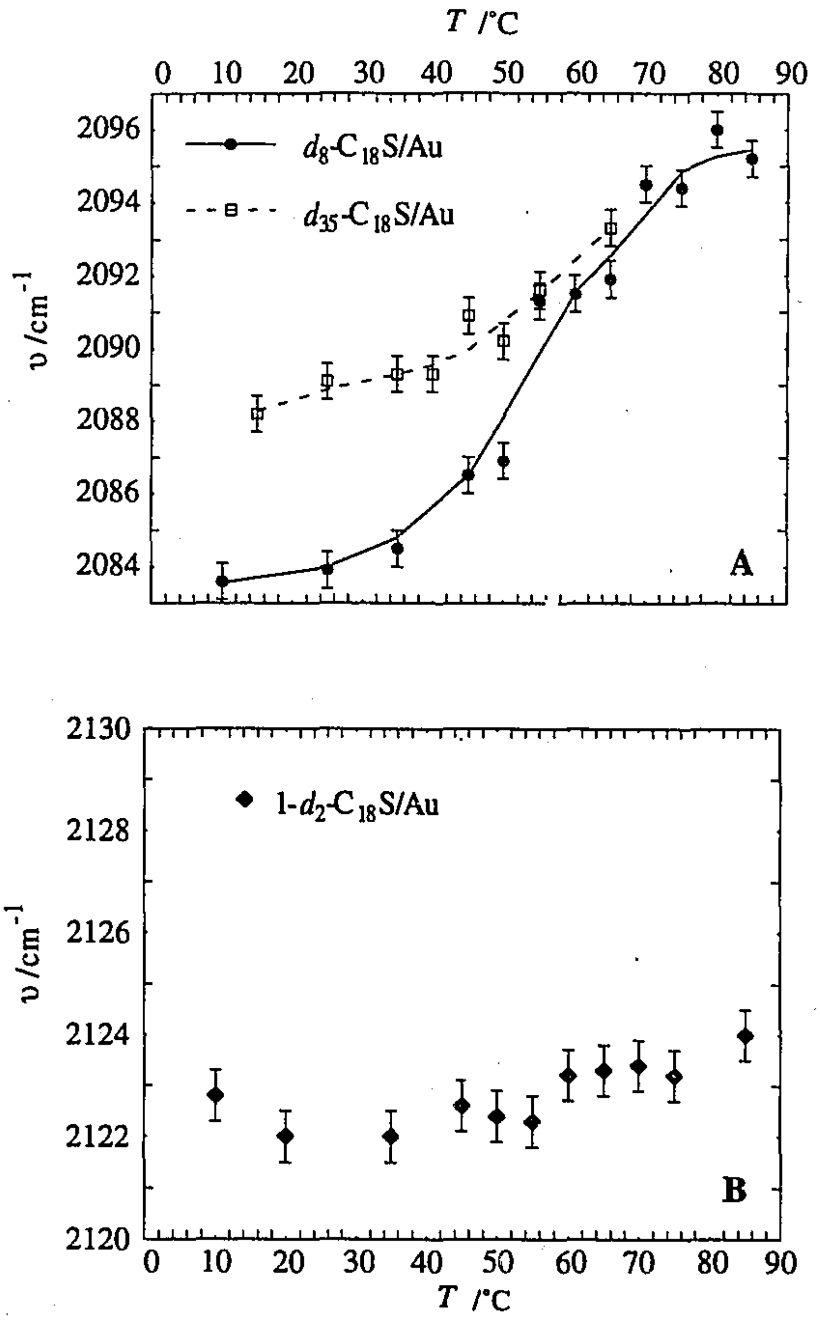

Figure 5.3. Peak position of the symmetric CD_2 stretch as a function of temperature for (A) 10,11,12,13-d_8-$C_{18}S/Au$ and d_{35}-$C_{18}S/Au$ and (B) 1-d_2-$C_{18}S/Au$. The error bars represent a 0.5 cm^{-1} uncertainty in the peak position values.

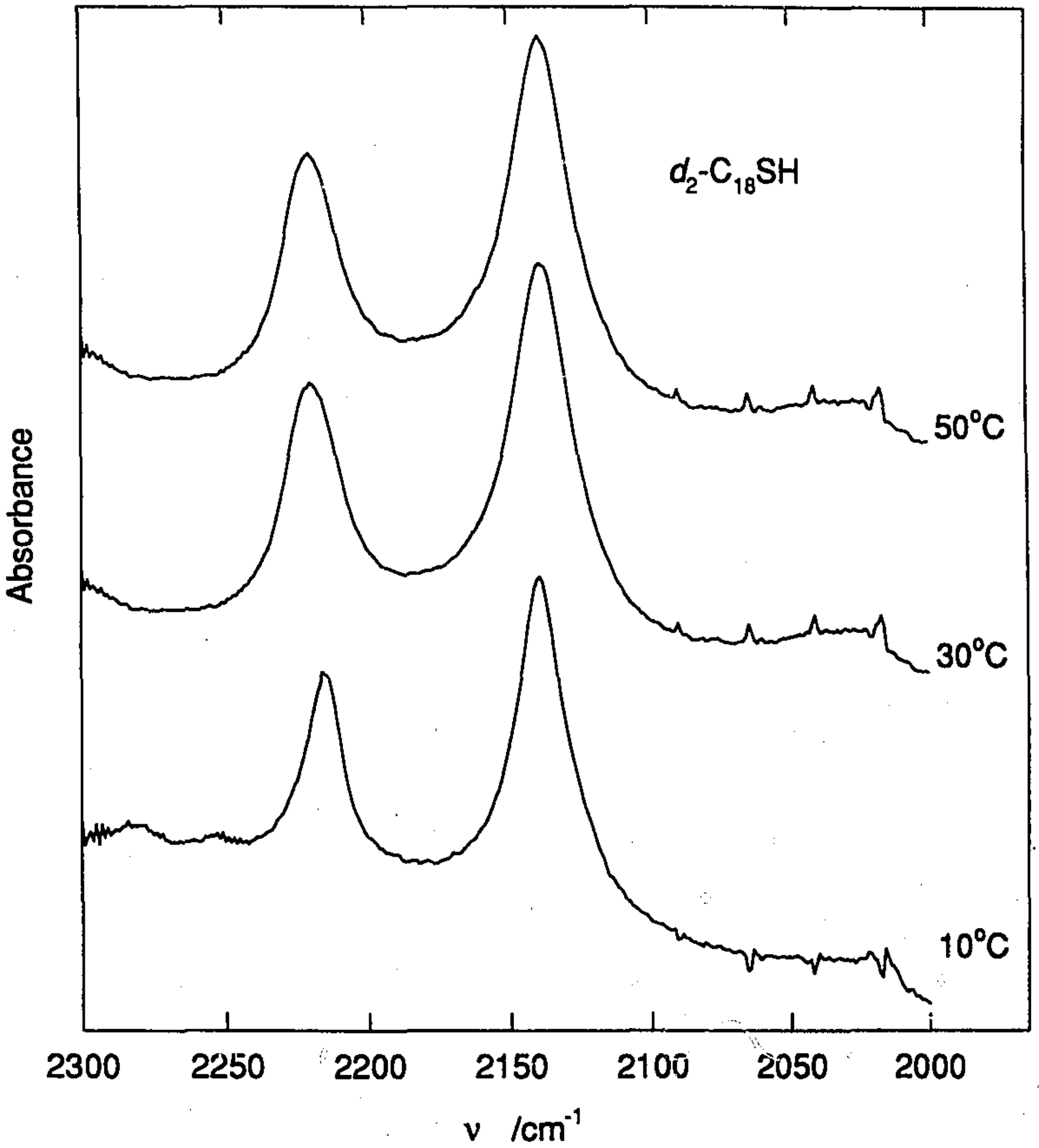

Figure 5.4. Variable temperature transmission FT-IR spectra of bulk 1-d_2-$C_{18}H_{37}SH$. The melting point of 1-d_2-$C_{18}H_{37}SH$ is 28-30 °C.

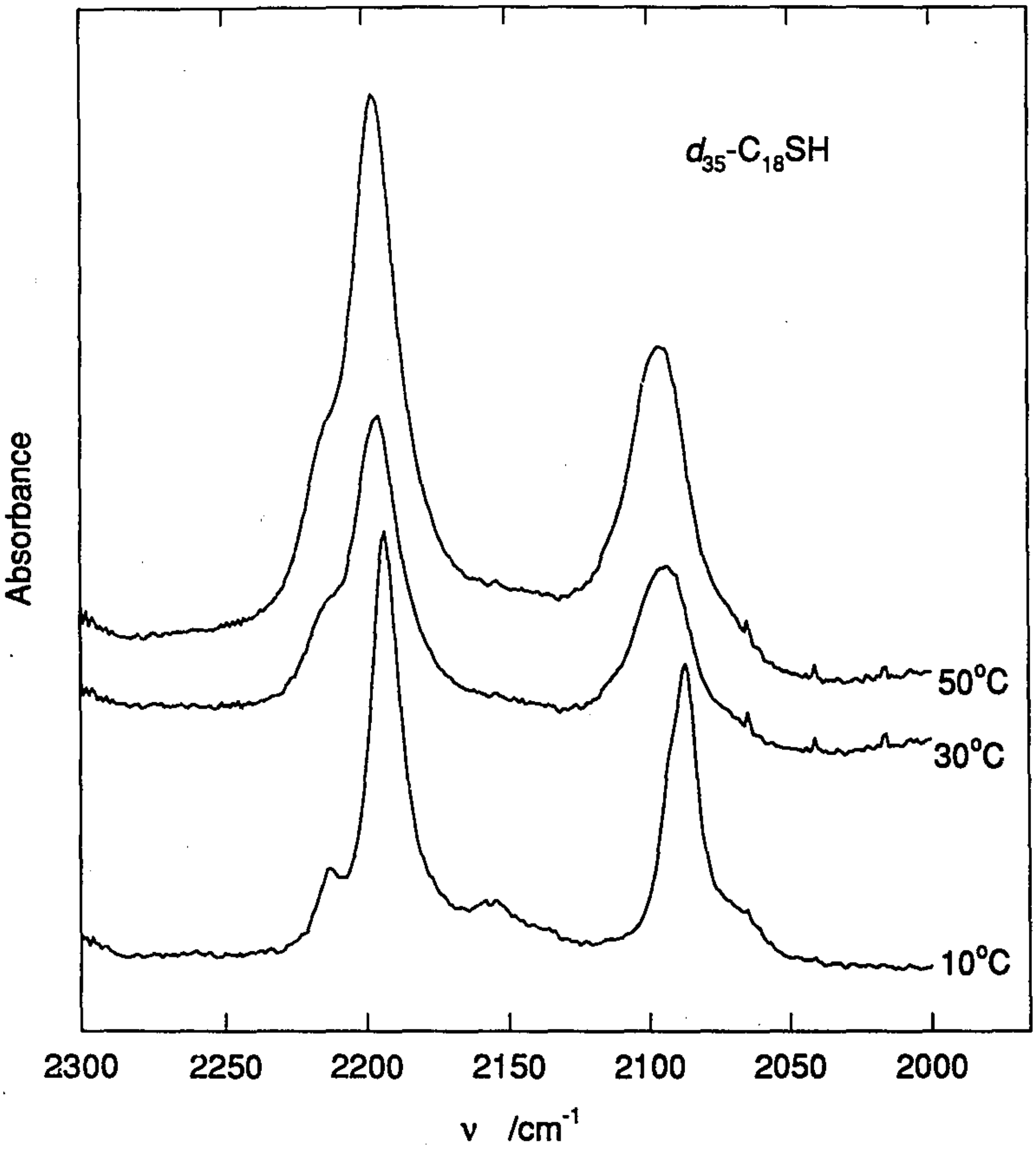

Figure 5.4. (cont'd) Variable temperature transmission FT-IR spectra of bulk d_{35}-$C_{18}H_{37}SH$. The melting point of d_{35}-$C_{18}H_{37}SH$ is 27-28 °C.

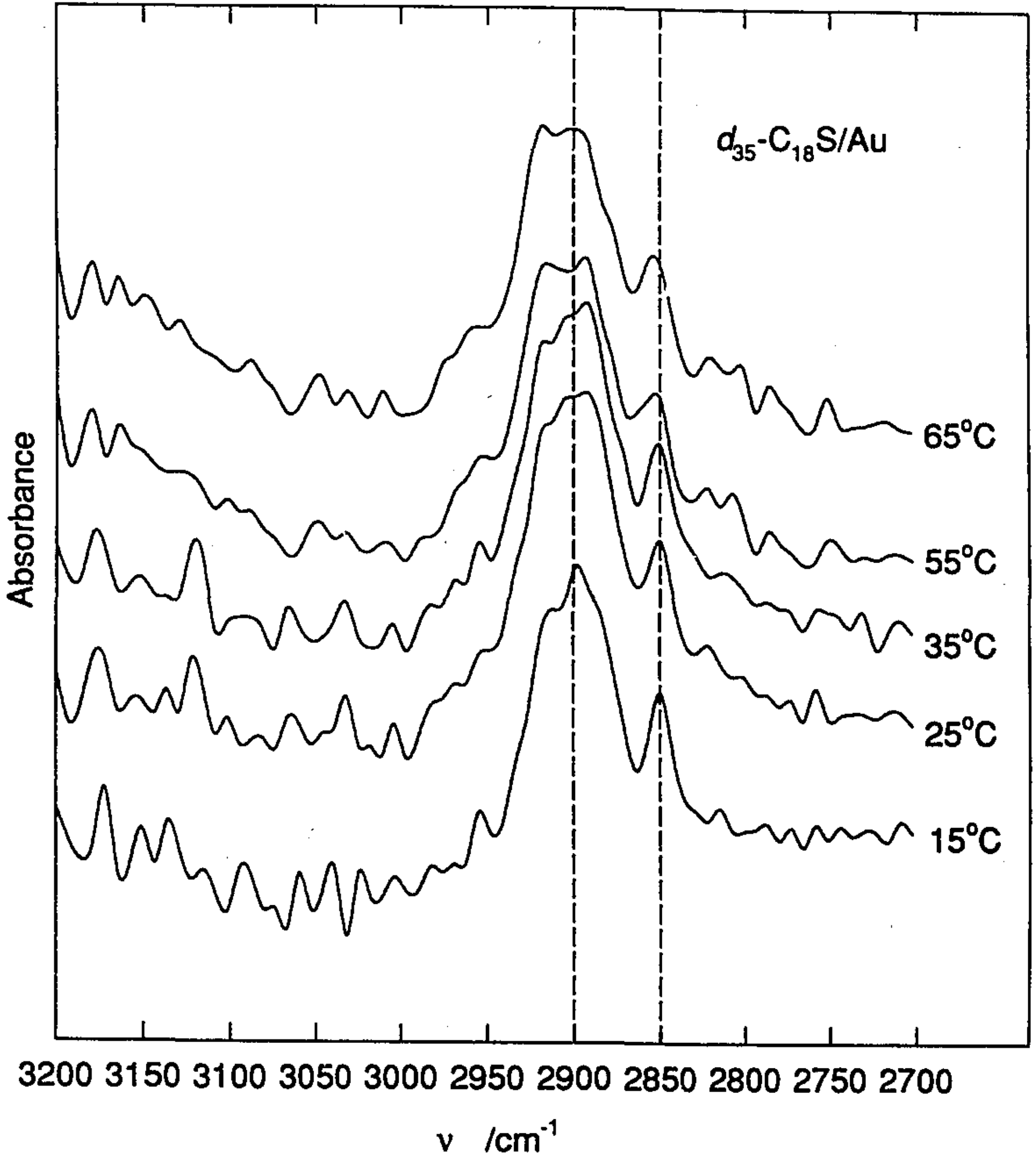

Figure 5.5. Variable temperature FT-IR spectra of the CH_2 stretching region (3200-2700 cm^{-1}) for 1-d_{35}-C_{18}S/Au. The dotted lines at 2900 cm^{-1} and 2850 cm^{-1} are visual aids.

At this temperature, the middle of the chain is essentially defect free. The FT-IR results described here for 10,11,12,13-d_8-$C_{18}S/Au$ and d_{35}-$C_{18}S/Au$ confirm this prediction. Furthermore, as the temperature is raised past 27 °C in the MD calculations, the development of *gauche* bonds is concentrated to the middle of the $C_{15}S$ chains and a low *gauche* defect population is observed near the sulfur headgroup.[44] These predictions are, again, in excellent agreement with the thermal behavior observed here for 10,11,12,13-d_8-$C_{18}S/Au$ and 1-d_2-$C_{18}S/Au$.

The variable temperature FT-IR spectra of 1-d_2-$C_{18}S/Au$ nanoparticles (Figure 5.2C) show a $\upsilon_{sym}(CD_2)$ peak (~ 2123 cm^{-1}) which is shifted by ~ 15 cm^{-1} compared to the bulk thiol (~ 2139 cm^{-1}). A weak, broad $\upsilon_{asym}(CD_2)$ peak at *ca.* 2200 cm^{-1} is also observed. It is noteworthy that for the bulk 1-d_2-$C_{18}SH$ (Figure 5.4), the $\upsilon_{asym}(CD_2)$ peak is less intense than the $\upsilon_{sym}(CD_2)$ peak, while in d_{35}-$C_{18}SH$, the $\upsilon_{asym}(CD_2)$ peak exhibits a greater intensity than the $\upsilon_{sym}(CD_2)$ peak. The assignment of the 2120 cm^{-1} peak to $\upsilon_{sym}(CD_2)$ is reasonable given that (i) there are no interfering C-H or C-C vibrations in the 2000-2300 cm^{-1} region, (ii) deuteration is at a single position in 1-d_2-$C_{18}S/Au$, and (iii) the values of the relative intensities of the symmetric and antisymmetric CD_2 stretches in bulk 1-d_2-$C_{18}SH$. The complementary $\upsilon(CH_2)$ data for d_{35}-$C_{18}S/Au$ (*i.e.* hydrogenated at carbon 1) at 25 °C reveals a υ_{asym} at ~ 2900 cm^{-1} and υ_{sym} at ~ 2851 cm^{-1} (Figure 5.5). In this case, the $\upsilon_{asym}(CH_2)$ peak is shifted by *ca.* 18 cm^{-1} from that measured for fully hydrogenated $C_{18}S/Au$ at 25 °C.[1] This is not surprising given that the $\upsilon_{asym}(CH_2)$ peak position is more sensitive to bond conformation than the $\upsilon_{sym}(CH_2)$ peak position but the CD_2 stretching vibrations follow the opposite trend. Interestingly, SERS[45] studies of planar RS/Au SAMs report a *ca.* 20 cm^{-1} decrease in the υ(C-S) frequency upon bonding of the thiol to the Au surface. Besides the *ca.* 15 cm^{-1} shift in the $\upsilon_{sym}(CD_2)$ peak observed for the carbon alpha to the sulfur headgroup, it is important to note that its position does not shift over the temperature range of 10-90 °C (Figure 5.3B). This strongly suggests that local order is maintained at the carbon closest to the Au surface during the chain disordering transition described above.

Transmission FT-IR spectroscopy thus definitively establishes that the DSC-detected phase transition arises from an alkyl chain disordering process which increases the number of *gauche* conformers in the chain. One can envisage that deuteration of different positions along the length of the alkylthiol chain will allow one to study the onset of chain disordering at specific regions in an assembly of alkyl chains.

5.3.3. ^{2}H NMR Spectroscopy: IR spectroscopy probes molecular vibrations occurring on a timescale shorter than 10^{-10} s, so that the IR measurement is essentially a "snapshot" of the different bond conformations existing at a given instant averaged out over the area of irradiation.[26] IR spectroscopy thus reveals the equilibrium *trans* and *gauche* bond populations as a function of temperature, but does not provide any insight into the motional processes which accompany chain disordering. For this reason, the long timescale probed by ^{2}H NMR (typically 10^{-6} - 10^{-4} s)[26] has been exploited to study the temperature dependence of the alkanethiolate chain dynamics.

The variable temperature ^{2}H NMR spectra of 10,11,12,13-d_8-C_{18}S/Au are displayed in Figure 5.6. At -55 °C, a static Pake pattern with a quadrupolar splitting of 118 kHz (*i.e.* $\theta = 90°$) is observed, clearly indicating that there is little motion of the C-^{2}H bonds at positions 10-13 of the C_{18}S chain. As the 10,11,12,13-d_8-C_{18}S/Au sample is heated, the ^{2}H NMR spectra exhibit motional averaging of the line shape. At -30 °C, the ^{2}H resonance appears as a "flat-topped" peak, a line shape which has been attributed to a slow, restricted *trans-gauche* bond isomerization.[24,46,47] Figure 5.6 shows that with further increases in temperature, a number of the C_{18}S chains exhibit motion that is characterized by rounded triangular patterns such as that observed in the ^{2}H NMR spectrum at 0 °C. In the temperature range of *ca.* 0 °C to 50 °C, the spectral line shapes consist of a narrower triangular component superimposed on a much broader component. The "de-Paked" spectrum at 25 °C (Figure 5.7), for example, clearly shows that the complex lineshape of the powder pattern actually consists of two sets of two peaks. The outer set of peaks has a static quadrupolar splitting of ~ 240 kHz (*i.e.* $\theta = 0°$) and the inner set has a quadrupolar splitting of ~ 40 kHz. The inner set of peaks reflects disordered RS chains that are not subject to true isotropic motion because they are tethered to the Au surface. More importantly, with increasing temperature, the relative contribution of the triangular peak in the powder pattern increases. The full width at half height (FWHH) of the broad spectral component in the powder pattern is plotted as a function of temperature in Figure 5.8. The graph reveals that from -55 °C to 45 °C, the FWHH remains fairly constant (110-130 kHz). Near the phase transition temperature of 50 °C, the broad component abruptly disappears and the de-Paked spectrum (not shown) consists of only a pair of peaks with a small quadrupolar splitting (*ca.* 40 kHz). The absence of both a narrow isotropic peak and a pair of rigid peaks establishes that neither surface diffusion of the RS chains or tumbling of the entire Au particle is important at this temperature (50 °C). The ^{2}H NMR spectra at 55 °C and 65 °C exhibit solely a narrow isotropic peak. The *gauche* conformer population largely determines the width of the broad spectral component in the powder pattern.[30] More precisely, when the *gauche* bond population equals the *trans* population, no quadrupole splitting remains.[30]

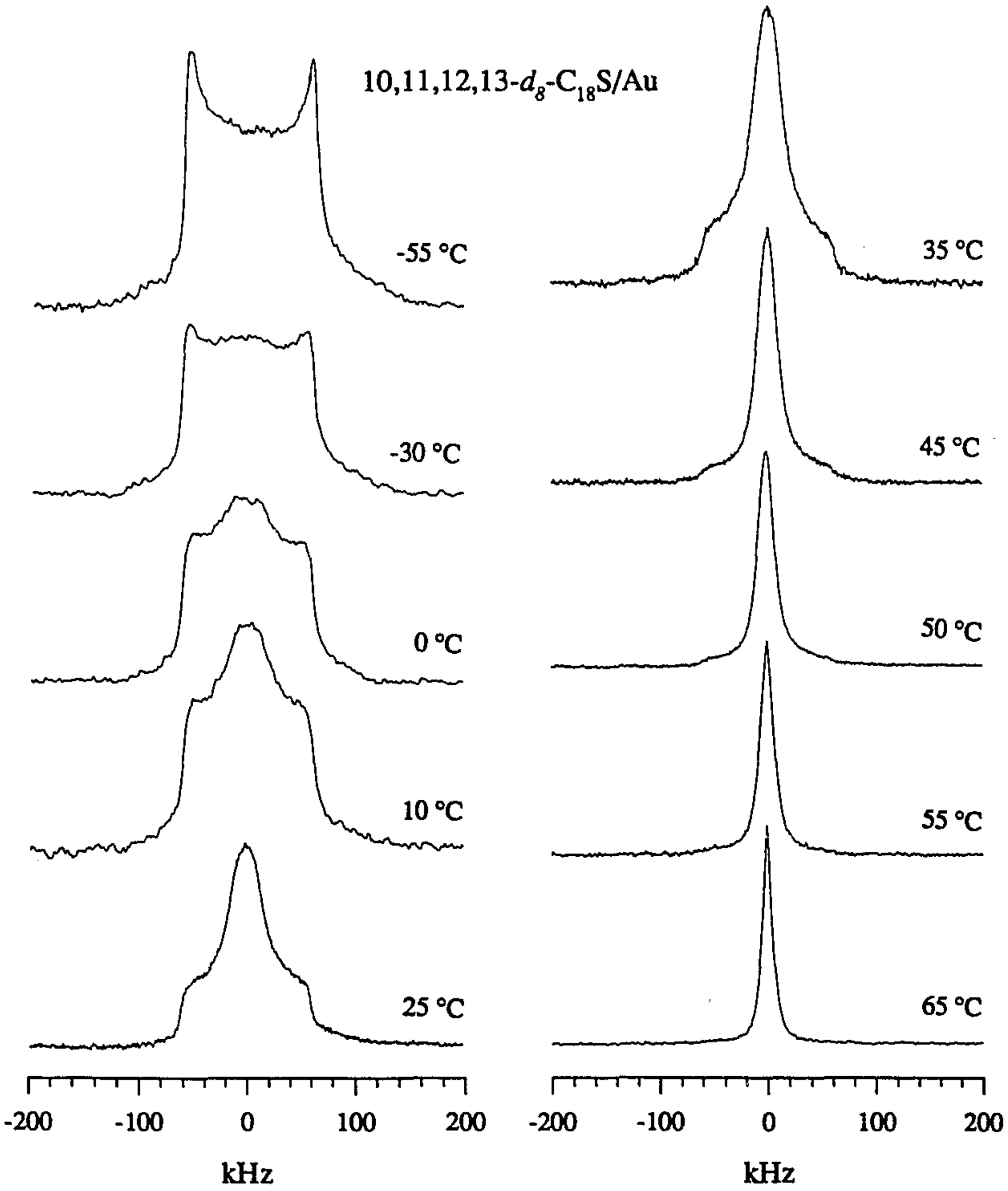

Figure 5.6. ^{2}H NMR spectra of 10,11,12,13-d_8-C_{18}S/Au.

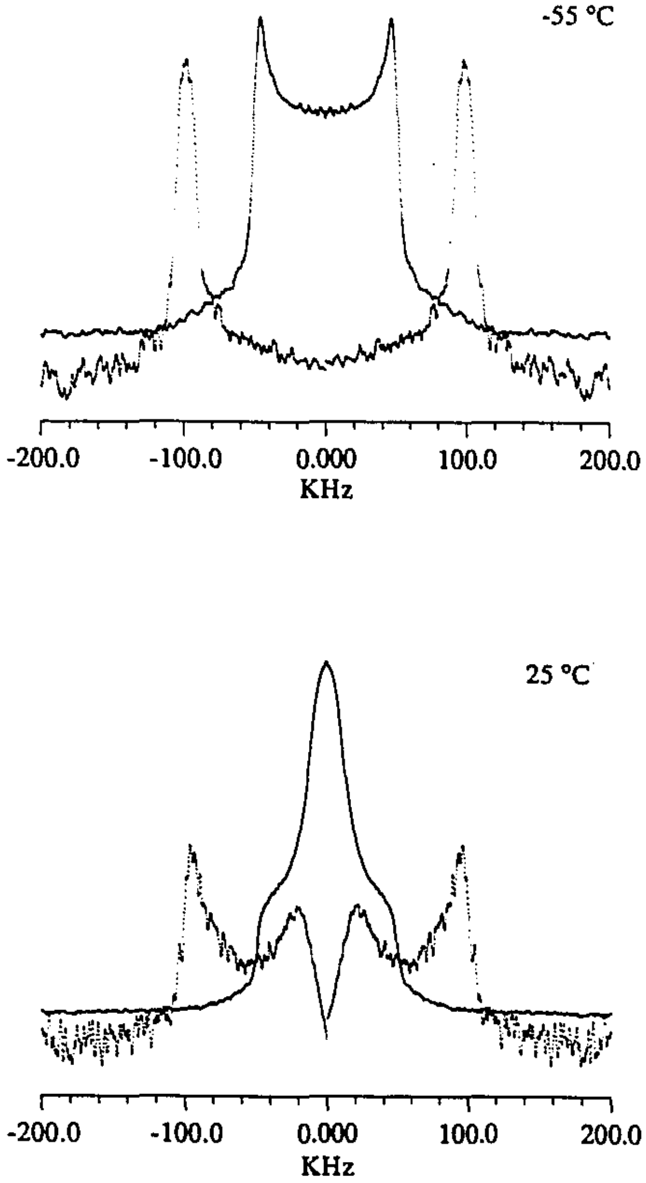

Figure 5.7. Computationally "de-Paked" spectra overlaid on the ^{2}H NMR powder patterns obtained at -55 °C and 25 °C for 10,11,12,13-d_8-$C_{18}S$/Au. The "de-Paking" process filters out all but the 0° orientation from the powder pattern.[12,13,17]

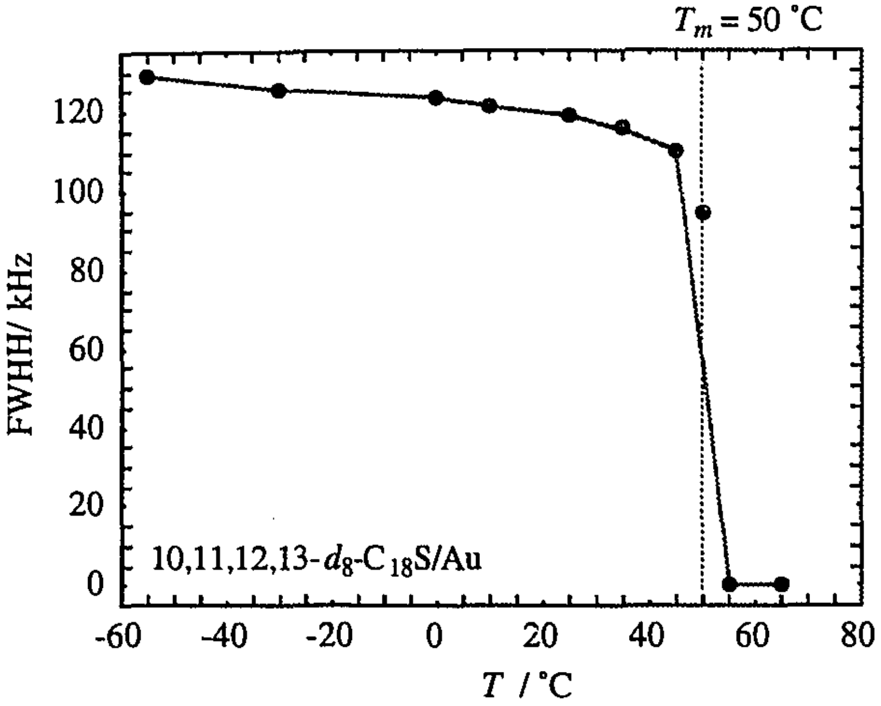

Figure 5.8. Plot of the full width at half height (FWHH) of the broad spectral component in the powder pattern of 10,11,12,13-d_8-C_{18}S/Au *vs.* temperature (T). T_m refers to the DSC peak maximum temperature.

This detail clearly explains the disappearance of the broad spectral component in the ^{2}H NMR spectrum between 50 °C and 55 °C. (Figure 5.7). The absence of a narrow isotropic peak at temperatures below the phase transition temperature supports our previous hypothesis that the chains exist in ordered clusters or bundles and that the Au particles close-pack *via* the interdigitation of these ordered chain clusters[1]. The interdigitation of individual chains on adjacent Au particles would not be sufficient to fill the void volume created by the 14:1 ratio of chain end area to Au-S headgroup area imposed by the curvature of the nanoparticle. Individually interdigitated chains would be disordered far below the observed phase transition temperature. The $\upsilon(CD_2)$ peak positions (Figures 5.2 and 5.3A) observed for 10,11,12,13-d_8-C_{18}S/Au at *ca.* 35 °C below the phase transition temperature also point to the existence of ordered chain domains.

Both the flat-topped and triangular peak shapes observed in the ^{2}H NMR spectra of 10,11,12,13-d_8-C_{18}S/Au have been observed in studies of amorphous polymers[24,46,47], liquid crystals[48], lipid bilayers[12], polymer model membranes[30-32], and alkylsilyl-modified silica gel[23]. This line shape is associated with conformational exchanges of alkyl chains between two unequally populated *trans* and *gauche* sites through reorientations of individual C-^{2}H bonds around the tetrahedral angle (109.5°). These bond reorientation processes have been modeled using both two-site and six-site "jump" models[23,24,30,46,48], and the resulting simulated lineshapes (*i.e.* flat-topped *vs.* triangular peak) are reported to be dependent upon both the relative *trans* and *gauche* bond populations *and* the conformational exchange or jump rates. For the RS/Au nanoparticles, the population of *trans* and *gauche* conformers is controlled by the temperature. By analogy to the chain dynamics reported for similar tethered alkyl chain systems[23,30], a motional model emerges for the RS chains involving both *trans-gauche* bond isomerization and axial chain rotation (Scheme 5.2).

In this model, the chains are densely packed at temperatures far below the phase transition temperature. Less space is available for molecular reorientations and *trans-gauche* bond isomerization is restricted. This results in a slow conformational exchange rate and the resulting flat-topped spectral line shapes should be describable by a simple two-site jump model.[23,30] A low *gauche* conformer population is expected at these temperatures and the overall orientation of the chains can be maintained by the formation of kinks and jogs[30]. As the number of chain *gauche* conformers increases with temperature, the chain free volume should increase. This causes a pseudo-rotational motion of individual chain segments about the long axis of the RS molecule.[30] Thus, at higher temperatures, the motional behavior of the RS chain segments is expected to include both axial rotation and rapid bond isomerization, such that the complex, rounded triangular line shapes should be able to be adequately described by a six-site jump model.[23,30] In fact, molecular dynamics simulations by Mar and Klein[44] reveal that the formation of internal *gauche* defects for densely packed $C_{15}S$ chains is coupled to the onset of axial chain rotation.[44]

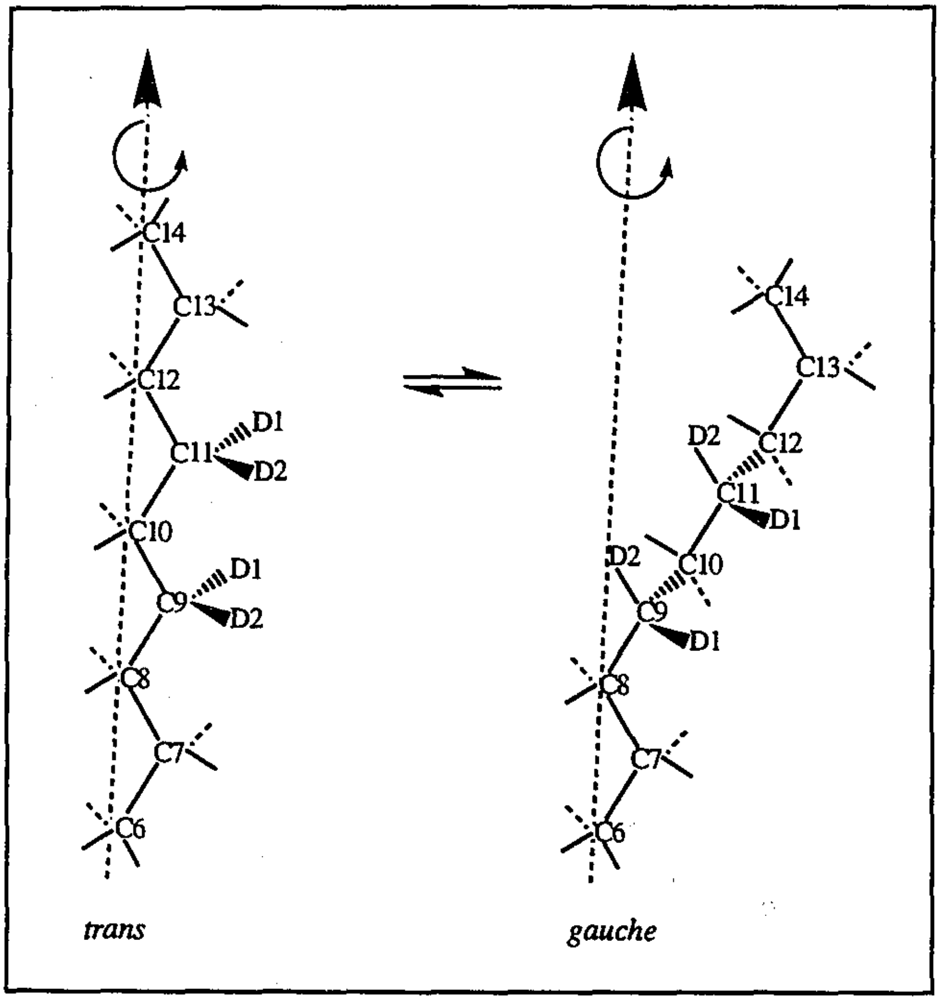

Scheme 5.2. The possible types of chain dynamic processes in RS/Au nanoparticles involve *trans-gauche* bond isomerization and pseudo-rotational motion of individual chain segments about the long axis of the RS molecule.

The narrow isotropic peak observed at temperatures above 50 °C for 10,11,12,13-d_8-$C_{18}S/Au$ and d_{35}-$C_{18}S/Au$ (see below) can also be associated with tumbling or rotation of the entire Au particle within the ensemble of Au particles. Since the diameter of our Au colloids is the same length as the RS chains, Au particle tumbling would presumably be accessible once the alkyl chains have melted, but would not be observable by FT-IR spectroscopy. Although these qualitative comparisons with the spectral line shapes of other tethered chain systems is insightful, detailed line shape simulations of the ^2H NMR spectra of 10,11,12,13-d_8-$C_{18}S/Au$ are presently underway to more precisely define the types and rates of chain motion.

The fact that a rounded triangular peak component is already observed in 10,11,12,13-d_8-$C_{18}S/Au$ at 0 °C (Figure 5.6) suggests that there exists a significant population of $C_{18}S$ molecules with a large number of *gauche* defects in the middle of the chain below 25 °C. This likely arises from a distribution of chain geometries where large *gauche* bond populations exist in chains which occupy interstitial regions in the particle lattice.[1] These chains cannot efficiently interdigitate or bundle with adjacent chains to form ordered domains. Chains residing at domain boundaries are also expected to be disordered at these low temperatures.[1] In fact, Reven and coworkers have shown through ^{13}C spin-lattice relaxation measurements of $C_{18}S/Au$ that at 25 °C, a population (74%) of motionally restricted all-*trans* chains coexists with a smaller population (26%) of liquid-like disordered chains.[2] In addition, the ^{13}C chemical shift of the interior methylene carbons and the reduced methylene ^1H proton linewidths observed in two-dimensional wideline separation (WISE) NMR experiments[49,50], suggest that the conformationally ordered $C_{18}S$ chains are undergoing large-amplitude motions about their long axis at room temperature.[2]

The temperature dependent behavior of the ^2H NMR spectra of d_{35}-$C_{18}S/Au$ (Figure 5.9) is distinctly different from that of 10,11,12,13-d_8-$C_{18}S/Au$, but the spectral line shapes are similar. This suggests that the chain motions are the same but that the onset of these motions occurs at different temperatures for specific regions of the chain. For instance, the spectral line shape of d_{35}-$C_{18}S/Au$ exhibits a rounded triangular peak in the center of the static Pake pattern at -55 °C (Figure 5.9). Since 10,11,12,13-d_8-$C_{18}S/Au$ shows only a rigid Pake pattern at this temperature (Figure 5.6), the triangular peak must arise from C-^2H bond motions at positions 14-18 along the chain. This behavior is expected given that ^{13}C spin-lattice relaxation measurements[2] indicate that molecular mobility increases toward the untethered chain ends which have a higher population of *gauche* conformers.[35,36,42,43] Moreover, it is in accord with the FT-IR correlations discussed above.

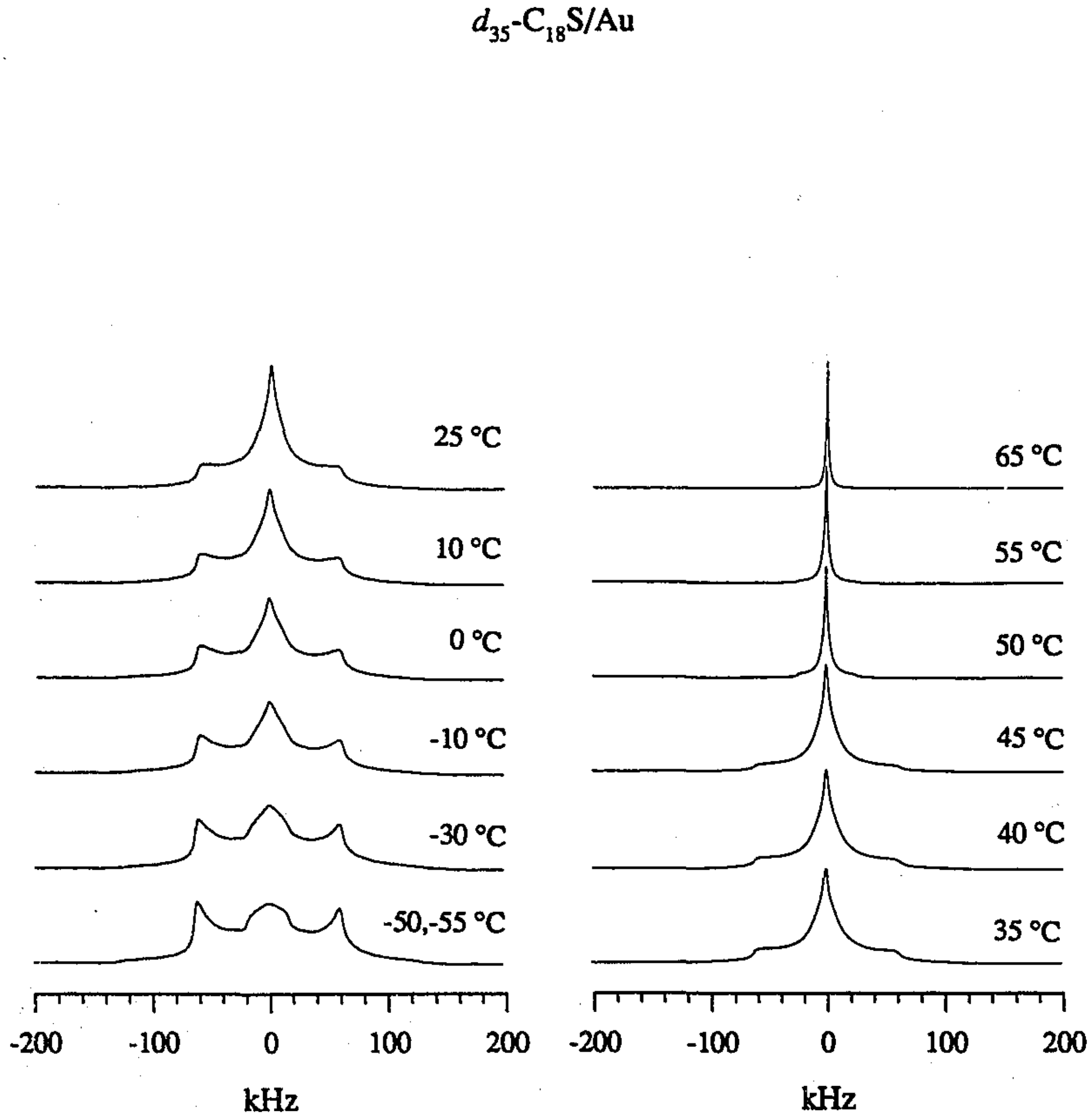

Figure 5.9. ^{2}H NMR spectra of d_{35}-C_{18}S/Au.

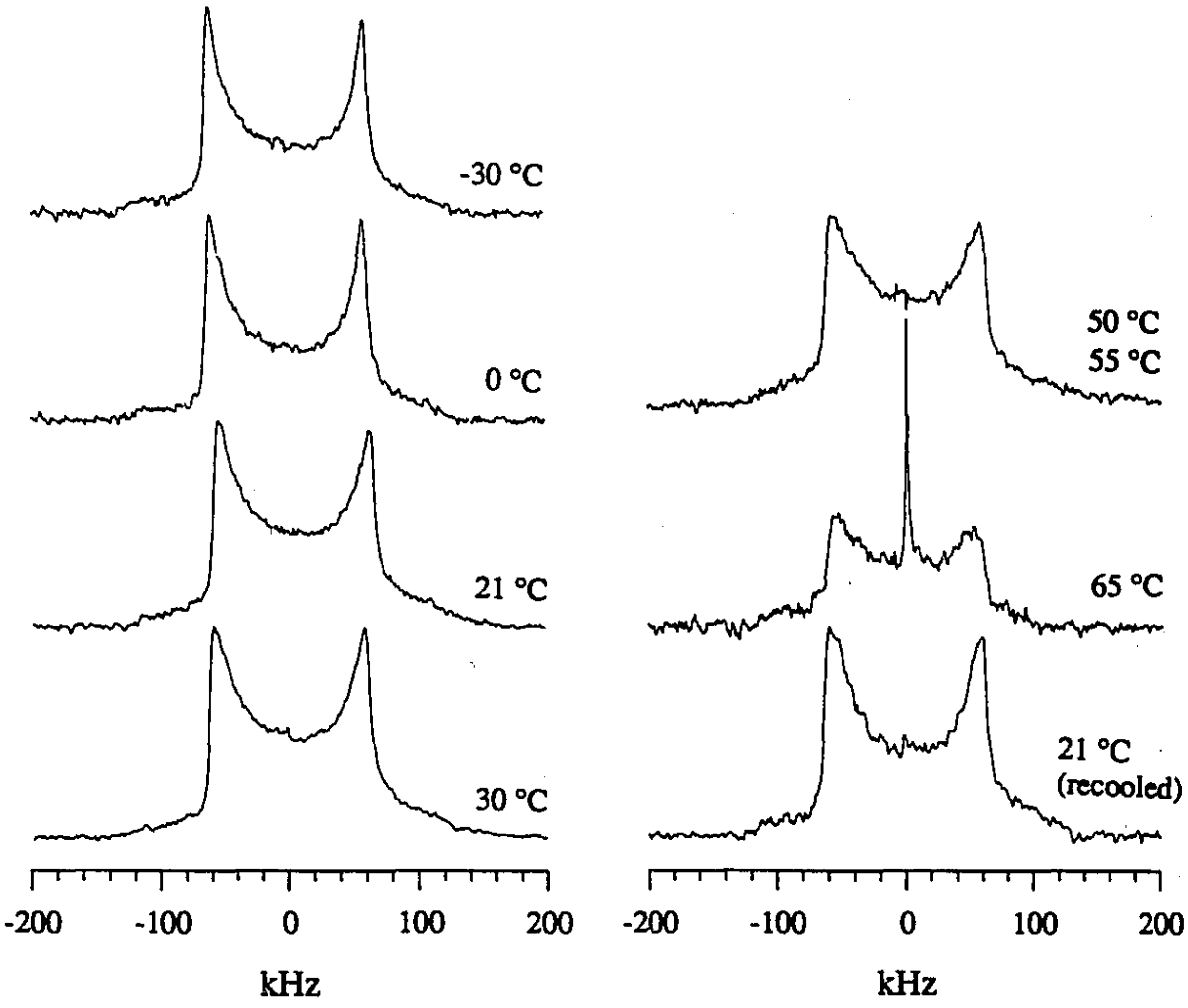
1-d_2-C_{18}S/Au

Figure 5.10. ^{2}H NMR spectra of 1-d_2-C_{18}S/Au.

It is particularly noteworthy that by contrast to the ^{2}H NMR spectra obtained for multilamellar vesicles of perdeuterated lipids[12,17,29], distinct quadrupolar splittings from individual methylene and methyl resonances are not observed for d_{35}-C$_{18}$S/Au. The different splittings observed for the perdeuterated lipids arise from the existence of a flexibility gradient along the lipid chain which changes the characteristics of the molecular motions.[12,13] However, Bayerl and Bloom have shown that as the surface curvature increases for lipid bilayers supported on micron-sized beads (SSVs), the powder spectrum is broadened and the individual methylene quadrupolar splittings become indistinguishable.[17] The RS/Au nanoparticle would be an extreme case of surface curvature (*i.e.* a radius of 15 Å *vs.* 2500 Å in the Bayerl and Bloom SSVs), so that the powder patterns obtained for d_{35}-C$_{18}$S/Au most likely reflect the extended chain geometry and high radius of curvature of the metal particle.

Finally, the ^{2}H NMR spectra of 1-d_2-C$_{18}$S/Au are shown in Figure 5.10. Unlike, the spectra of 10,11,12,13-d_8-C$_{18}$S/Au and d_{35}-C$_{18}$S/Au, those of 1-d_2-C$_{18}$S/Au are rigid Pake patterns with a quadrupolar splitting of 120 kHz at temperatures up to 65 °C. This establishes that, at least on the microsecond timescale probed by ^{2}H NMR spectroscopy: (i) the C1-C2 bonds do not experience a measurable degree of *trans-gauche* bond isomerization, (ii) it is unlikely that the RS chain undergoes axial rotation about the C-S bond, and (iii) there is no diffusion of the RS-Au species on the Au particle surface. The surface migration of thiolate-Au species has in fact been observed in UHV-STM studies [51-53] over periods of minutes to hours. The rigid Pake patterns observed here for 1-d_2-C$_{18}$S/Au do not conclusively reveal whether two-dimensional diffusion of the RS chains, with or without attached Au atoms, occurs on the particle surface. At 65 °C, a narrow isotropic peak is observed in the center of the rigid Pake pattern, whose contribution to the total spectrum is ~10 %. The intensity/contribution of this peak does not change with a further increase in temperature. We believe this isotropic peak is due to melting of free or loosely bound thiol.

At the present time, we are focused on the broader, qualitative information derived from the temperature dependence of the ^{2}H NMR spectra, and not on more refined kinetic information. The latter requires a detailed analysis of the chain conformation kinetics and evolves into issues of model evaluation.

5.4. Conclusions

RS/Au nanoparticles present themselves as an interesting class of materials given their parallels to planar SAMs and the fact that their physical properties are strongly dependent upon the structure and properties of the RS chains. We have demonstrated in the foregoing that the DSC-detected phase transition is in fact a thermally induced chain melting process. The chain melting begins at the chain terminus region and propagates towards the center of the chain as the temperature increases. FT-IR spectroscopy of specifically deuterated samples establishes that the chain termini are highly disordered, even at 35 °C below the calorimetrically-determined phase transition temperature. ^{2}H NMR spectroscopy, as a powerful probe of chain order and dynamics, establishes that chain melting arises from an increased frequency of *gauche* bonds in the Au-tethered alkylthiol chains. Finally, a narrow isotropic ^{2}H NMR peak at temperatures higher than the phase transition temperature may correspond to the onset of rapid Au particle tumbling within the solid matrix.

References

(1) Badia, A.; Singh, S.; Demers, L.; Cuccia, L.; Brown, G. R.; Lennox, R. B. *Chem. Eur. J.* **1996**, *2*, 359-363.

(2) Badia, A.; Gao, W.; Singh, S.; Demers, L.; Cuccia, L.; Reven, L. *Langmuir* **1996**, *12*, 1262-1269.

(3) Leff, D. V.; Ohara, P. C.; Heath, J. R.; Gelbart, W. M. *J. Phys. Chem.* **1995**, *99*, 7036-7041.

(4) Brust, M.; Fink, J.; Bethell, D.; Schiffrin, D. J.; Kiely, C. *J. Chem. Soc., Chem. Commun.* **1995**, 1655-1656.

(5) Terrill, R. H.; Postlethwaite, A.; Chen, C.-h.; Poon, C.-D.; Terzis, A.; Chen, A.; Hutchison, J. E.; Clark, M. R.; Wignall, G.; Londono, J. D.; Superfine, R.; Falvo, M.; Johnson Jr., C. S.; Samulski, E. T.; Murray, R. W. *J. Am. Chem. Soc.* **1995**, *117*, 12537-12548.

(6) Whetten, R. L.; Khoury, J. T.; Alvarez, M. M.; Murthy, S.; Vezmar, I.; Wang, Z. L.; Cleveland, C. L.; Luedtke, W. D.; Landman, U. In *Proceedings of the NATO Advanced Research Workshop on "The Chemical Physics of Fullerenes 10 (and 5) Years Later"*; Kluwer Academic Publishers: Varenna, Italy, 1995; pp 475-490;

Whetten, R. L.; Khoury, J. T.; Alvarez, M. M.; Murthy, S.; Vezmar, I.; Wang, Z. L.; Stephens, P. W.; Cleveland, C. L.; Luedtke, W. D.; Landman, U. *Adv. Mater.* **1996**, *8*, 428-433.

(7) Demers, L.; Badia, A.; Lennox, R. B. "The Synthesis and Characterization of Thiol-Capped Gold Nanoparticles," poster presentation, McGill University, 1995.

(8) Badia, A.; Back, R.; Lennox, R. B. *Angew. Chem. Int. Ed. Engl.* **1994**, *33*, 2332-2335.

(9) Riegler, J. E. *J. Phys. Chem.* **1989**, *93*, 6457-6480.

(10) Marsh, D. *Handbook of Lipid Bilayer Membranes*; CRC Press: Boca Raton, 1991, pp. 135-150.

(11) Lebuis, A. M., Department of Chemistry, McGill University, Nov. 1995, personal communication.

(12) Griffin, R. G. *Methods Enzymol.* **1981**, *72*, 108.

(13) Davis, J. H. *Biochim. Biophys. Acta* **1983**, *737*,

(14) Smith, R. L.; Oldfield, E. *Science* **1984**, *225*, 280-288.

(15) Blume, A.; Hubner, W.; Muller, M.; Bauerle, H. D. *Ber. Bunsenges. Phys. Chem.* **1989**, *93*, 964-973.

(16) Naumann, C.; Brumm, T.; Bayerl, T. M. *Biophys. J.* **1992**, *1314-1319*,

(17) Bayerl, T. M.; Bloom, M. *Biophys. J.* **1990**, *58*, 357-362.

(18) Spiess, H. W. *Ber. Bunsenges. Phys. Chem.* **1993**, *97*, 1294-1305.

(19) Kricheldorf, H. R.; Wutz, C.; Probst, N.; Domschke, A.; Gurau, M. In *Multidimensional Spectroscopy of Polymers: Vibrational, NMR, and Fluorescence Techniques*; M. W. Urban and T. Provder, Ed.; American Chemical Society: Washington, D.C., 1995; pp. 311-332.

(20) van Genderen, M. H. P.; Pfaadt, M.; Moller, C.; Valiyaveettil, S.; Spiess, H. W. *J. Am. Chem. Soc.* **1996**, *118*, 3661-3665.

(21) Jurga, S.; Macho, V.; Huser, B.; Spiess, H. W. *Z. Phys. B- Condensed Matter* **1991**, *84*, 43-49.

(22) Kelusky, E. C.; Fyfe, C. A. *J. Am. Chem. Soc.* **1986**, *108*, 1746-1749.

(23) Ziegler, R. C., Maciel, G. E. *J. Am. Chem. Soc.* **1991**, *113*, 6349-6358.

(24) Jelinski, L. W.; Dumais, J. J.; Engel, A. K. *Macromolecules* **1983**, *16*, 492-496.

(25) Fyfe, C. A. In *Solid State NMR for Chemists* C.F.C. Press: Guelph, ONT, Canada, 1983; pp 73-137.

(26) Bloom, M.; Thewalt, J. *Chem. Phys. Lipids* **1994**, *73*, 27-38.

(27) Brust, M.; Walker, M.; Bethell, D.; Schiffrin, D. J.; Whyman, R. *J. Chem. Soc., Chem. Commun.* **1994**, 801-802.

(28) Schmidt, H., B.Sc. Honours Thesis, McGill University, 1996.

(29) Davis, J. H.; Jeffrey, K. R.; Bloom, M.; Valic, M. I. *Chem. Phys. Lett.* **1976**, *42*, 390-394.

(30) Ebelhauser, R.; Spiess, H. W. *Ber. Bunsenges. Phys. Chem.* **1985**, *89*, 1208-1214.

(31) Ebelhauser, R. *Makromol. Chem., Rapid Commun.* **1984**, *5*, 403-411.

(32) Ebelhauser, R.; Spiess, H. W. *Makromol. Chem.* **1987**, *188*, 2935-2949.

(33) Blume, A. *Biochemistry* **1980**, *19*, 4908-4913.

(34) Porter, M. D.; Bright, T. B.; Allara, D. L.; Chidsey, C. E. D. *J. Am. Chem. Soc.* **1987**, *109*, 3559-3568.

(35) Nuzzo, R. G.; Korenic, E. M.; Dubois, L. H. *J. Chem. Phys.* **1990**, *93*, 767-773.

(36) Dubois, L. H.; Zegarski, B. R.; Nuzzo, R. G. *J. Electron Spectrosc. Relat. Phenom.* **1990**, *54/55*, 1143.

(37) Nuzzo, R. G.; Dubois, L. H.; Allara, D. L. *J. Am. Chem. Soc.* **1990**, *112*, 558-569.

(38) Bensebaa, F.; Ellis, T. H.; Badia, A.; Lennox, R. B. *J. Vac. Sci. Technol. A* **1995**, *13*, 1331-1336.

(39) Ulman, A. *Adv. Mater.* **1991**, *3*, 298-303.

(40) Naselli, C.; Rabolt, J. F.; Swalen, J. D. *J. Chem. Phys.* **1985**, *82*, 2136-2140.

(41) Mendelsohn, R.; Davies, M. A.; Brauner, J. W.; Schuster, H. F.; Dluhy, R. A. *Biochemistry* **1989**, *28*, 8934-8939.

(42) Chidsey, C. E. D.; Liu, G.; Rowntree, P.; Scoles, G. *J. Chem. Phys.* **1989**, *91*, 4421-4423.

(43) Camillone, N.; Chidsey, C. E. D.; Liu, G.; Putvinski, T. M.; Scoles, G. *J. Chem. Phys.* **1991**, *94*, 8493-8502.

(44) Mar, W.; Klein, M. L. *Langmuir* **1994**, *10*, 188-196.

(45) Bryant, M. E.; Pemberton, J. E. *J. Am. Chem. Soc.* **1991**, *113*, 8284-8293.

(46) Huang, T. H.; Skarjune, R. P.; Witterbort, R. J.; Griffin, R. G.; Oldfield, E. *J. Am. Chem. Soc.* **1980**, *102*, 7377-7379.

(47) Hentschel, D.; Sillescu, H.; Spiess, H. W. *Macromolecules* **1981**, *14*, 1605-1607.

(48) Liesen, J.; Boeffel, C.; Spiess, H. W.; Yoon, D. Y.; Sherwood, M. H.; Kawasumi, M.; Percec, V. *Macromolecules* **1995**, *28*, 6937-6941.

(49) Chin, Y.-H.; Kaplan, S. *Magn. Reson. Chem.* **1994**, S53.

Chapter Six

CONCLUSIONS, CONTRIBUTIONS TO ORIGINAL KNOWLEDGE, AND IDEAS FOR CONTINUED RESEARCH

6.1. Overview and Conclusions

The phase properties of self-assembled alkylthiol monolayer films at Au surfaces have been investigated through (i) interfacial electron transfer at thiol-modified Au electrodes and (ii) structure and thermotropic behavior of thiol-derivatized Au nanoparticles. The effects of temperature, alkyl chain length, end group interactions, and chain packing geometry on the structure/property/activity relationship have been elucidated.

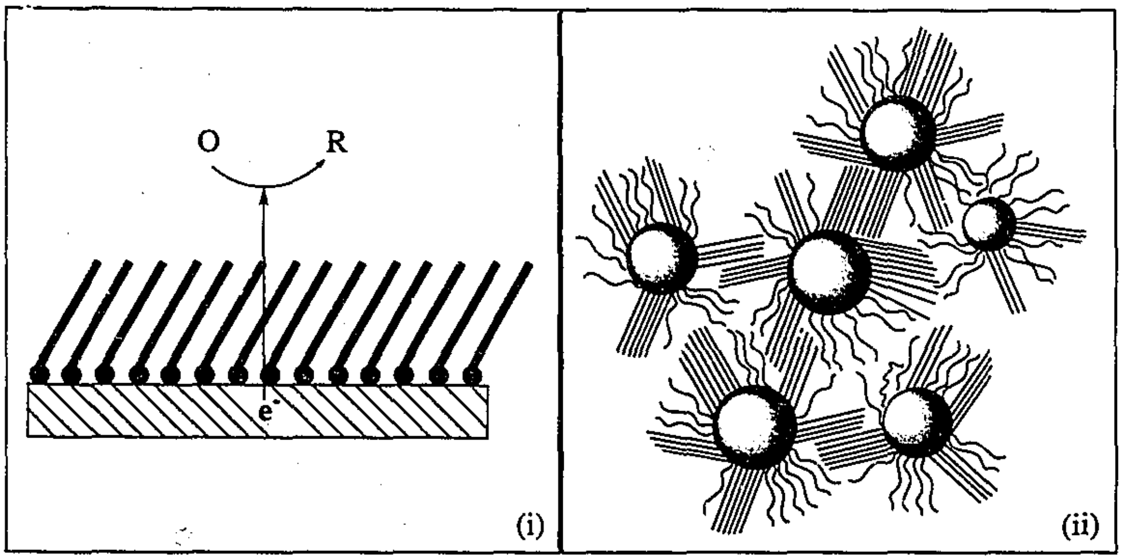

The organizational state of RS/Au SAMs has been addressed in Chapters 2 and 3 by using the electron transfer process between a water-soluble redox species, $Fe(CN)_6^{3-}$, and a thiol-coated Au electrode as a probe of the monolayer film structure. The transmonolayer and a thiol-coated Au electrode as a probe of the monolayer film structure. The transmonolayer redox ion current flux at RS/Au electrodes (where R = n-$C_{16}H_{33}$-$C_{20}H_{41}$ and $HO(CH_2)_{16}$) exhibits maxima at well defined temperatures which are determined solely by the thiol alkyl chain length and the presence of stabilizing end group interactions, such as hydrogen bonding. This behavior closely parallels the enhanced permeability of phospholipid bilayer vesicles to ions at their chain order/disorder phase transition temperatures. The 1:1 correlation between the pre-transition (T_p) and main transition (T_m) temperatures of the RS/Au monolayers studied here and n-diacylphosphatidylcholines of equivalent chain length suggests that there are similar mechanisms for chain melting and reorientation in these two systems. This correlation arises because the chain packing configuration and density, as dictated by the Au lattice and the phospholipid headgroup, are very similar in the two cases. Analogous to bilayer lipid membranes, the complex, thermally-induced Faradaic current maxima observed in self-assembled RS/Au monolayers are proposed to arise from transient regions of enhanced permeability to redox species along boundaries between domains of tilted and untilted chains (at $T = T_p$) and at discontinuities between coexisting crystalline and melted chain domains (at $T = T_m$). More importantly, the noted parallels with phospholipid membrane systems and the complex temperature dependence of the differential capacitance and $Fe(CN)_6^{3-}$ reduction current observed here strongly indicates that permeation, and not electron tunneling, is the dominant electron transfer process at RS/Au electrodes.

The monolayer preparation conditions and thermal history have been found to be important variables in the study of planar 2D RS/Au SAMs. The film phases that are crucial for the observation of the current features which are associated with chain order/disorder transitions are intrinsic to SAMs prepared by prolonged incubation in monolayer-forming solutions. Chain ordering and crystallization kinetics appear to play an important role in these systems. Furthermore, the thermal behavior of RS/Au electrodes annealed during the self-assembly process and the marked hysteresis observed during thermal cycling of as-deposited RS/Au monolayers in the electrochemical experiment suggest that chain order/disorder transitions in SAMs are not readily reversible. Chain entanglement and restricted lateral chain movement due to the covalent tethering of the sulfur to the Au surface likely prevent the rapid re-ordering of the monolayer. It is thus concluded that SAMs which have been prepared under conventional conditions (*i.e.* incubation times in solution ranging from minutes to hours) and/or have been annealed are assemblies of disordered chains with some degree of short range order, but limited in the extent of order necessary to be manifested as a phase transition.

While the current maxima observed at RS/Au electrodes are consistent with thermally induced film structural changes and a chain order/disorder process is thereby inferred, the electrochemistry/SAM experiment does not provide *direct* information about the conformational state of the RS chains. Since previous studies of the phase behavior of RS/Au monolayers using signal enhancement characterization techniques reported conflicting results, a highly dispersed analogue to SAMs formed at planar surfaces was chosen. For this reason, the chain order and thermal properties of thiol-derivatized Au nanoparticles of 20-30Å diameter have been investigated in Chapters 3 and 4. The large surface area of these nanoparticles have enabled the *quasi*-2D monolayer film structure to be uniquely probed by techniques conventionally used for bulk materials, such as NMR spectroscopy, transmission FT-IR spectroscopy, and calorimetry. These combined techniques are particularly powerful in terms of defining the chain conformation and orientation in ordered systems such as lipid membranes.

Characterization studies reveal that despite the large surface curvature of the spherical Au nanoparticles, these SAMs possess similar physical and chemical properties as monolayers formed at planar surfaces. The CH_2 antisymmetric and symmetric stretching vibrations in FT-IR spectroscopic studies of RS/Au nanoparticle films reveal that for long-chain thiols ($\geq C_{16}$), the alkyl chains exist predominantly in an extended, all-*trans* ordered conformation at 25 °C. Furthermore, differential scanning calorimetry (DSC), variable temperature FT-IR spectroscopy, and solid-state ^{13}C NMR studies establish that a cooperative chain melting process occurs in these alkylated metal colloids. The DSC-measured thermograms clearly show that the RS/Au particles, in the solid state, undergo distinct phase transitions in a chain length dependent manner. FT-IR spectroscopy qualifies that this DSC phase transition arises from an increased population of *gauche* chain conformers. More importantly, the transition temperatures measured here closely parallels those found in the electrochemical RS/Au SAM studies (Chapters 2 and 3). This conclusively shows that thermally induced film structural changes which give rise to increased Faradaic currents at RS/Au electrodes *are* associated with RS chain disordering. As both the DSC phase transition temperatures and enthalpies for $C_{14}S/Au$ and $C_{18}S/Au$ are identical to the values obtained for equivalent chain length *n*-diacylphosphatidylcholine lipids, similar chain melting/reorientation processes probably occur in these two systems. How this cooperative chain melting process arises is not immediately evident given the relationship between the extended chain conformation and the geometry of the spherical nanoparticles. Transmission electron microscopy and powder X-ray diffraction show an interparticle separation distance of only one chain length, suggesting that chain ordering arises from the interdigitation of *domains* of chains between neighboring particles. As such, the broad phase transitions observed for both planar and colloidal RS/Au SAMs are most probably a manifestation of the complex inter-relationship between the particle, the RS chain domain sizes, and their polydispersities.

A concurrent solid-state ^{13}C NMR study revealed that 26% of the alkyl chains in $C_{18}S/Au$ have *gauche* defects in the chain interior (*i.e.* C4-C15) at 25 °C below the phase transition temperature, while the IR spectrum reports only highly ordered chains at this temperature. This is attributed to the short timescale (10^{-10} s) and signal averaging nature of FT-IR spectroscopy. The longer timescale probed by ^{2}H NMR spectroscopy (10^{-6}-10^{-4} s) was exploited to study the chain packing structure and local disordering phenomena in perdeuterated and selectively deuterated $C_{18}S/Au$ samples. By FT-IR, the CD_2 stretching vibrations indicate that at 35 °C below the phase transition temperature, the population of *gauche* conformers is much larger in perdeuterated $C_{18}S/Au$ than in 10,11,12,13-d_8-$C_{18}S/Au$. This is due to contributions from the disordered chain termini in d_{35}-$C_{18}S/Au$. ^{2}H NMR spectroscopy further reveals that the chain ends are disordered even at -55 °C, in full support of the conclusions drawn by other research groups from surface IR spectroscopy, He diffraction, and molecular dynamics simulations of planar RS/Au SAMs. A sharp order/disorder transition is observed by FT-IR spectroscopy for 10,11,12,13-d_8-$C_{18}S/Au$, whereas d_{35}-$C_{18}S/Au$ shows only the gradual appearance of *gauche* conformational defects, as observed previously for planar RS/Au SAMs. This strongly suggests that specific ^{2}H-labeling is the key to observing distinct phase transitions by FT-IR spectroscopy. ^{2}H NMR indicates that chain mobility is greatly restricted at the sulfur headgroup and increases towards the chain ends. Thus, chain melting starts at the chain termini and propagates towards the middle of the chains as the temperature increases. Furthermore, the variable temperature FT-IR spectra of 1-d_2-$C_{18}S/Au$ clearly show that the chain disorder does not propagate as far down as the sulfur headgroup. The temperature dependence of the ^{2}H NMR lineshapes establish that rapid *trans-gauche* isomerization and axial rotation of the C-C bonds accompany chain melting. A narrow isotropic peak at $T > T_m$ may correspond to the onset of rapid particle tumbling within the solid matrix. The absence of such a peak in the ^{2}H NMR spectra of 10,11,12,13-d_8-$C_{18}S/Au$ at temperatures below the phase transition temperature confirms that the chains exist in ordered clusters or bundles and that the particles close-pack *via* the interdigitation of these ordered domains. The $\upsilon(CD_2)$ peak positions for 10,11,12,13-d_8-$C_{18}S/Au$ at *ca.* 35 °C below the phase transition temperature also point to the existence of ordered chain clusters. However, the ^{2}H NMR line shape of 10,11,12,13-d_8-$C_{18}S/Au$ reveals that at 25 °C below the phase transition temperature, a significant population of the $C_{18}S$ chains are already undergoing rapid *trans-gauche* isomerization and axial rotation of the C-C bonds near the middle of the alkyl chain. This likely arises from a distribution of chain geometries where large *gauche* bond populations exist in chains which occupy interstitial regions in the particle lattice.

This thesis establishes that self-assembled alkylthiolate monolayers at Au surfaces are dynamic structures with both rich phase properties and complex reorganization kinetics. The strong parallels noted between RS/Au nanoparticles and SAMs at planar surfaces make these readily prepared colloidal systems amenable to a number of biomimetic and optical applications already underway with conventional RS/Au SAMs.

6.2. Contributions to Original Knowledge

The thermal triggering of ion permeability as a probe of the monolayer film structure constitutes a novel approach to the study of self-assembled alkylthiol SAMs at metal surfaces. This thesis establishes that order/disorder transitions do in fact occur in RS/Au SAMs and that film preparation conditions play an important role in their observation. This is the first report on the existence of cooperative phase transitions and order/disorder processes in these systems. Strong parallels to the phase behavior of phospholipid vesicles have been noted. These studies demonstrate that the Au-S epitaxy and the resulting chain packing density establish RS/Au SAMs as model biomimetic surfaces.

The characterization studies of thiol derivatized Au nanoparticles presented in this thesis are some of the first to realize the potential of this readily prepared colloidal system to serve as a large surface area analogue to SAMs formed on planar metal surfaces. Through the RS/Au nanoparticles, the film structure, Au-S interaction, and thermal properties of SAMs have been uniquely characterized by transmission FT-IR spectroscopy, ^{13}C and ^{1}H NMR spectroscopy, and differential scanning calorimetry. A cooperative chain melting process has been found to occur in these alkylated metal colloids at temperatures which parallel those of planar RS/Au SAMs, phospholipid bilayer membranes, and fatty acid Langmuir Blodgett monolayer films. The physical properties of SAMs at colloidal surfaces have been found to exhibit a remarkable similarity to those of conventional SAMs at planar surfaces. It has been established that these alkylated nanoparticles are excellent functional models of the much-studied planar SAMs. This important observation paves the way for the study of the chain dynamics, adsorbate phase diagrams, and relaxation processes by techniques used to characterize bulk materials.

This thesis contains the first study of the chain dynamics and phase behavior of RS/Au SAMs by solid-state ^{2}H NMR spectroscopy. *Trans-gauche* isomerization and C-C bond axial rotation have been observed to be the dominant motional processes in the tethered RS chains. Chain melting is observed to start at the chain termini and propagate towards the middle of the chains. The C-C bond next to the sulfur headgroup was found to be motionally restricted. Selective chain deuteration has been established as a key factor in the observation of sharp order/disorder transitions by FT-IR spectroscopy.

Finally, this thesis is the first to draw parallels between chain melting and reorientation processes in self-assembled monolayers at metal surfaces, lipid bilayer membranes, and Langmuir Blodgett monolayer films.

6.3. Ideas for Continued Research

i. X-ray diffraction studies of thiol SAMs at Au single crystal surfaces have established that the chain packing density is determined by the Au-S epitaxy. For example, the RS/Au(110) monolayer has an 8% less dense surface chain packing than RS/Au(111). By contrast, the RS chain packing density on a Au(100) surface is 20% tighter than for RS/Au(111) monolayers. Since the chain packing density affects the chain order/disorder phase transition temperatures in phospholipid membranes, a similar behavior is expected for SAMs at single-crystal surfaces. A tighter packing density will increase the T_m value if this analysis is correct. Thus, the temperature dependence of the Faradaic current at alkylthiol monolayers on Au(111), Au(110), and Au(100) surfaces should be investigated. For a given chain length, the T_m is expected to increase in the order *i.e.* Au(110) < Au(111) < Au(100). These experiments will serve to establish the effect of the chain packing structure on the nature of the phase transition and will show whether Au polycrystallinity is a contributing factor to the broad electrochemical transition observed previously.

ii. The temperature dependence of the interfacial capacitance at RS/Au monolayers should be studied in more detail to establish a permeability-linked origin.

iii. The $Fe(CN)_6^{3-/4-}$ redox probe used in the electrochemical studies is hydrophilic and is not expected to readily partition into the hydrophobic methyl-terminated alkythiol monolayer. It would be interesting to use a hydrophobic redox probe which can easily partition into the hydrocarbon monolayer to study changes in the Faradaic current at RS/Au electrodes as a function of temperature.

iv. Alkylthiol monolayers with pendant redox centers are particularly attractive systems since tethered redox probes eliminate background contributions from electron transfer at film defect sites. An electron tunneling mechanism, either through-bond or through-space, has been proposed for these systems. A study of the temperature dependence of the electron transfer kinetics in RS/Au SAMs with tethered redox centers could provide insight into the effect of temperature and chain conformation on the electron tunneling process. The efficiency of through-bond electron coupling has been predicted to be significantly decreased as the number of *gauche* bond conformers increase.

v. Reflection absorption infrared spectroscopic studies of planar RS/Au SAMs with selectively deuterated chains are recommended. Based on similar studies with RS/Au nanoparticles, a sharp order/disorder transition is predicted for the middle of the RS chains, as opposed to the gradual chain disordering observed previously with hydrogenated alkythiols.

vi. The synthesis and thiol derivatization of Au nanoparticles of *ca.* 30 nm diameter is recommended. This particle diameter would result in a chain end area to Au-S area ratio of 1.2:1, instead of the 14:1 ratio for 2 nm Au particles. This would result in a dispersed Au surface which more approximates planar metal surfaces. The characterization of the 2D monolayer film structure and thermotropic properties of these larger RS/Au particles should be carried out by transmission FT-IR spectroscopy, NMR (^{13}C, ^{1}H, and ^{2}H) spectroscopy, transmission electron miscroscopy, and calorimetry. A comparison with the physical properties of the 2-3 nm particles would then be possible. This can provide possible insight into the relationship between film order and the geometries of the metal surface and RS chains.

vii. Finally, the large surface area and highly dispersed nature of the RS/Au colloidal system offer possible access to such a wide range of experiments (*eg.* NMR, IR, Raman, calorimetry etc.) that its use in novel technological and biosensor applications is only limited by the imagination. In this case, *small truly is beautiful*!

APPENDIX

"Probing the different phases of self-assembled monolayers on metal surfaces: Temperature dependence of the C-H stretching modes"
(Reprinted with permission from F. Bensebaa, T.H. Ellis, A. Badia, and R.B. Lennox, *J. Vac. Sci. Technol. A* **1995**, *13 (3)*, May/June, 1331-1336. Copyright 1995 American Institute of Physics)

"Structure and Chain Dynamics of Alkanethiol-Capped Gold Colloids"
(Reprinted with permission from A. Badia, W. Gao, S. Singh, L. Demers, L. Cuccia, and L. Reven, *Langmuir* **1996**, *12*, 1262-1269. Copyright 1996 American Chemical Society)

Probing the different phases of self-assembled monolayers on metal surfaces: Temperature dependence of the C–H stretching modes

F. Bensebaa and T. H. Ellis
Département de Chimie, Université de Montréal, Montréal, Québec H3C 3J7, Canada

A. Badia and R. B. Lennox
Department of Chemistry, McGill University, Montréal, Québec H3A 2K6, Canada

(Received 25 October 1994; accepted 13 March 1995)

Reflection-absorption infrared spectroscopy at near grazing incidence is used to investigate the thermal stability of self-assembled monolayers of alkyl thiols, HS–$(CH_2)_{n-1}$-R, adsorbed on polycrystalline metal surfaces. The spectral features of the C–H stretching region have been carefully analyzed in the temperature range from 150 to 450 K. These features are highly sensitive to chain orientation and chain conformation. On gold, the chains are found to gradually untilt but remain largely all-*trans* up to about 350 K. Above this temperature, a broad, irreversible transition to a liquidlike phase is observed, and which is characterized by a large number of *gauche* conformational defects. This overall behavior did not depend upon the chain length or terminal group for the systems studied. In contrast, significant differences were observed on a silver substrate. © *1995 American Vacuum Society.*

I. INTRODUCTION

Self-assembled monolayers (SAMs) of alkyl thiols, HS–$(CH_2)_{n-1}-R$, tightly bonded to gold surfaces have been characterized by a number of techniques.[1,2] Well ordered and densely packed films with different chain lengths (referred to as C_n where n is the total number of carbons per chain) and different chain ends (where R can be CH_3, COOH, OH,...) are easily synthesized. At room temperature and below, the linear polymethylene chains tightly bonded to the substrate are mostly linear (i.e., all-*trans*), and they are tilted with respect to the substrate normal in order to optimize the chain–chain packing. The situation at higher temperature is quite different. Several phenomena have been observed by numerous techniques. The appearance of *gauche* conformational defects upon heating was proposed by Dubois *et al.*[1] based on Fourier transform infrared (FTIR) studies. Heat treatment is also suggested to induce orientational and rotational disordering based on molecular dynamic (MD) calculations.[3] Specifically, a gradual untilting followed by free molecular rotation and gauche defect formations at high temperature was predicted. Thermal disordering has also been studied with diffraction[4,5] and direct imaging[6,7] techniques. Using grazing incident x-ray diffraction, Fenter *et al.*[5] observed a phase transition in a C_{14} film around 340 K from a hexagonal two-dimensional (2D) structure that is commensurate with the substrate to an incommensurate phase. By 370 K, a reversible transition to a liquidlike state was observed. A recent scanning tunnel microscopy (STM) study suggested that short-chain thiols (C_4 and C_6) are liquidlike even at room temperature.[6] For longer chains, STM data[7] showed the presence of vacancy islands that heal upon annealing at 350 K. At these high temperatures, we have to take into account the effects of partial monolayer desorption. Early studies[8] suggested the onset of desorption and/or decomposition of the alkyl chains at temperatures above 340 K.

The ability of vibrational techniques to characterize the nature of the order–disorder occurring in organic thin films (SAM and Langmuir–Blodgett), lipid bilayers, and bulk alkanes has been demonstrated.[9–13] The peak frequency, the integrated intensity, and the linewidth of the spectral features are sensitive to various structural parameters. For example, Katayama *et al.*[12] found that the critical temperature at which the linewidth changes is below the onset of the frequency shift which is observed upon melting in Langmuir–Blodgett films. This was offered as proof that the onset of chain movement precedes the growth of conformational defects.

Although the thermal stability of SAM films is critical for any technological application, only a few investigations of their thermotropic behavior on a molecular level have been reported so far.[3–10] The main focus of the present work was to correlate temperature dependent variations in infrared (IR) spectral features to changes in the structural properties of the films. We have found a high sensitivity to chain tilt and chain conformation. Specifically, thiols, adsorbed on two different noble metals, were studied by reflection absorption infrared spectroscopy (RAIRS) in a wide temperature range. Dubois and co-workers previously reported the temperature dependence of the peak height and frequency position of the stretching modes of some alkyl chains (n = 16, 17, and 22) on gold.[9] We have reproduced their data and extended the higher temperature limit. Furthermore, we followed the temperature dependence of the linewidth. To understand the effect of the substrate and the role of other intermolecular interactions (such as hydrogen bonding) on the thermotropic properties, two variations were introduced. First, we varied the substrate (gold versus silver). Second, the terminal methyl group was replaced by a carboxyl group.

II. EXPERIMENT SECTION

RAIRS measurements were performed on a Research series FTIR spectrometer from Mattson Instruments (RS-1 FTIR) equipped with a water cooled globar source. A midrange (~500–4000 cm^{-1}) liquid nitrogen cooled mercury cadmium telluride (MCT) detector set to 4 cm^{-1} resolution, was used. Details of the setup have been given elsewhere.[13] After the different sample spectra were recorded, typically three cycles of annealing-sputtering of 6 min with 600 eV Ar ions and a sample temperature around 700 K were carried out to remove the thin thiol layer film in order to expose the clean gold substrate. A background spectrum was then recorded on this clean substrate.

For determination of the position, linewidth, and area of the vibrational peaks, Grams Software (Galactic Industries, Salem, NH) was used. The trapezoidal rule was used for the determination of the peak area (experimental uncertainty +/−0.0015 a.u., where a.u. are arbitrary units of peak area used in Figs. 2, 5, and 8(a) and the linewidth is represented by the full width at half-maximum (FWHM) of the peak (+/−0.6 cm^{-1}). Since the peaks are overlapping, the integration is limited to a frequency range of ~4 times the FWHM. For example, the antisymmetric CH_2 stretch is integrated between 2950 and 2900 cm^{-1}. The center of mass of each peak was used for the position (+/−0.3 cm^{-1}). This value is typically within 0.5 cm^{-1} of the position of the peak maximum.

The gold substrates obtained from Evaporated Metal Films, Inc. (Ithaca, NY) are 1000 Å of Au evaporated onto $3\times1\times0.2\ cm^3$ glass plates precoated with a 50 Å titanium layer. Before thiol adsorption, the substrate is chemically cleaned, and typically 1 mM thiol concentration in ethanol and an incubation time of at least 24 h were used.

A pure silver substrate (99.9985%) purchased from Johnson-Matthey (Ward Hill, MA) was cleaned by two cycles of Ar sputtering before insertion in a 1 mM solution of the C_{18} thiol in ethanol for less than 3 h. Ambient atmosphere exposure of the silver substrate between the end of Ar^+ sputtering and thiol adsorption was less than 5 min.

III. RESULTS

Displayed in Fig. 1 are RAIRS spectra of $SH-(CH_2)_{21}-CH_3$ adsorbed on a polycrystalline gold surface at four representative temperatures. The assignment of the different CH stretching peaks is based on previous works.[9,14] Around 155 K, the peak assigned to the symmetric methylene stretch mode (d^-) is narrow (FWHM~10 cm^{-1}) and its position (2917 cm^{-1}) reflects a certain degree of crystalline order. With increasing temperature the peak height decreases and the peak broadens. The symmetric methylene stretch (d^+) behaves similarly. The shoulder on the d^- peak which appears around 2935 cm^{-1} was previously attributed[4,15] to a Fermi resonance interaction between the symmetric stretching mode of the methyl group (2948 cm^{-1}) with the overtone of the methylene scissoring mode ($2\times1467=2934$ cm^{-1}). This assignment is questionable because the same shoulder appears in our spectra of a COOH terminated thiol SAM. Since the intensity of both d^- and d^+ show identical behavior as a function of temperature, we conclude that this shoulder does not perturb our analysis. The broad shape of the vibrational peaks at 411 K is consistent with an isotropic state. Furthermore, all the peak positions of the C–H stretches are similar to those found in thiols and bulk alkanes in the liquid state.[14–16] Based on previous studies of bulk alkanes,[15,16] Langmuir–Blodgett films[10–12] and SAMs,[5,6] we conclude that there has been a transition from a polycrystalline phase towards a liquidlike phase. Figures 2–5 give details of the temperature dependencies of the different stretching modes for the same sample (C_{22}) and provide insight into the nature of this transition.

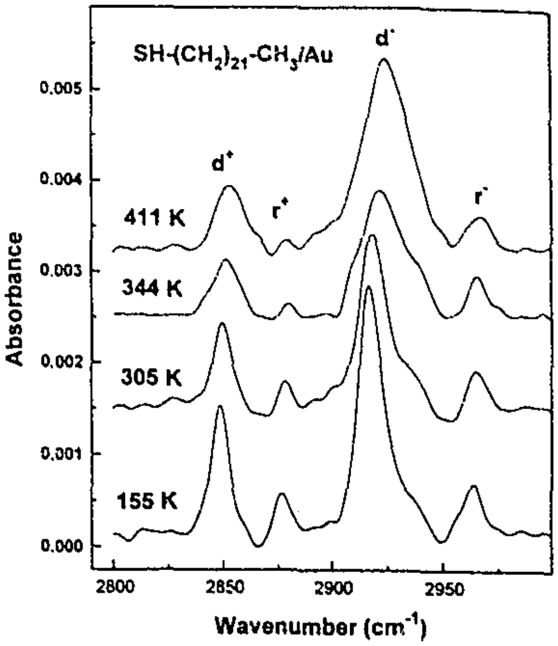

FIG. 1. RAIRS spectra in the C–H stretching region of $SH-(CH_2)_{21}-CH_3$ adsorbed on polycrystalline gold at four representative temperatures. A linear baseline correction is performed on each spectra. For reasons of clarity, curves are offset along the *Y* axis.

The temperature dependence of the integrated intensity of the d^- peak mode consists of at least three stages [Fig. 2(a)]. The first is between 150 and 350 K, where the intensity decreases to about 50% of the initial intensity. The intensity increases between 350 and 400 K before starting to decrease again ~410 K. The minimum around 350 K is also observed for other chain lengths from C_{15} up to C_{22} without any significant shift in temperature.[13] Similar trends are found for the d^+ peak [Fig. 2(b)]. Not included in Fig. 2(b) is the last point at 435 K because the d^+ peak is at the noise level, confirming the decrease in the intensity at high temperature. After heating to these high temperatures, the spectral features do not return to their initial state upon cooling. This irreversible behavior indicates that significant desorption and/or decomposition has occurred.

The peak frequency of the d^- mode increases slightly between 150 and 350 K by less than 1 cm^{-1} [Fig. 3(a)], in contrast with the d^+ mode which shows a nearly 2.5 cm^{-1} upward shift over the same temperature range [Fig. 3(b)]. For the d^- mode, an increase of more than 6 cm^{-1} is observed over an interval of 50° starting at the critical temperature 350 K [Fig. 3(a)]. The peak frequency of the d^+ mode also increases rapidly above 350 K, but the magnitude of the shift is only about 2 cm^{-1}. Values of peak frequency of ~2918 (2848) and 2926 (2854) cm^{-1} were observed for the $d^-(d^+)$ mode in bulk alkane in the crystalline and liquid state, respectively.[14] This again indicates a transition to a liquidlike state when the sample is heated above 350 K. However, unlike the phase transition in lipid bilayers,[17]

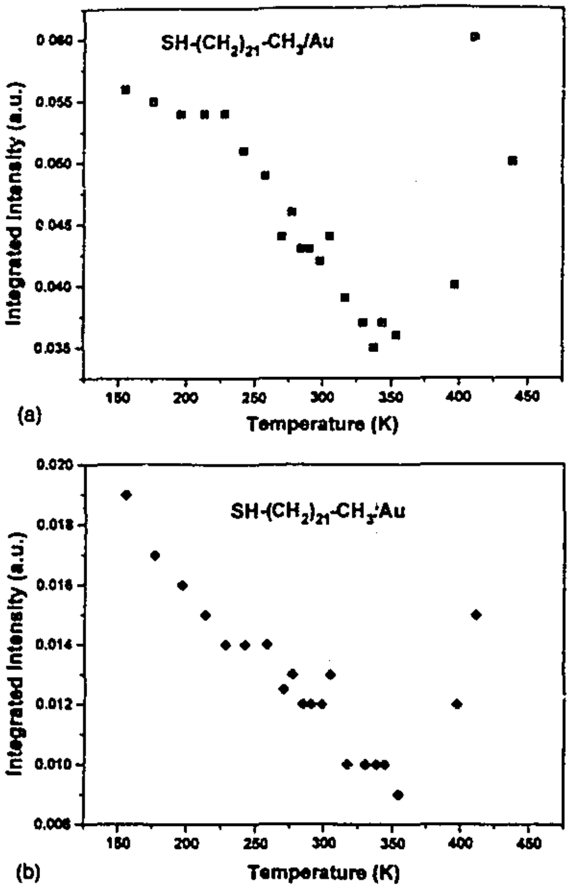

FIG. 2. Temperature dependence of the integrated intensity of (a) the antisymmetric (d^-) and (b) symmetric (d^+) methylene stretching modes for the same sample as in Fig. 1.

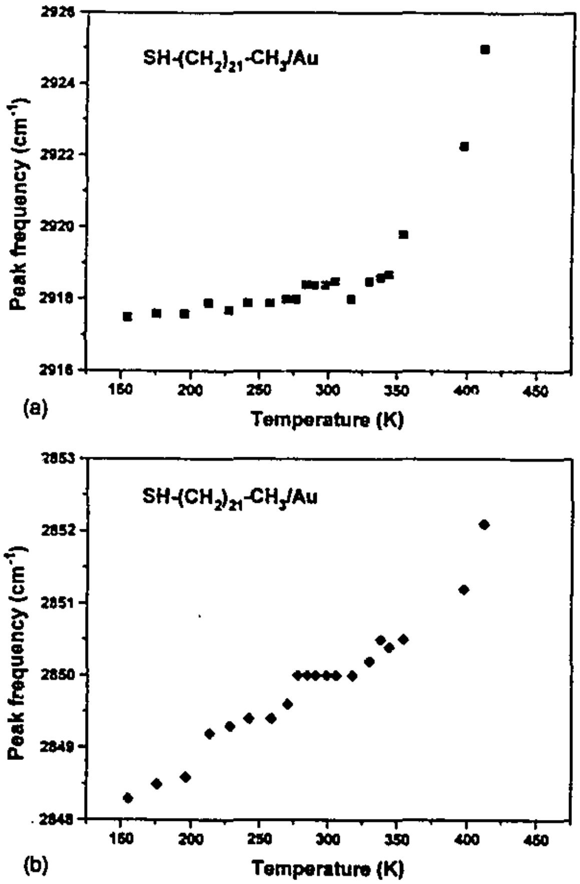

FIG. 3. Temperature dependence of the peak frequency of (a) the antisymmetric (d^-) and (b) symmetric (d^+) methylene stretching modes for the same sample as in Fig. 1.

which occurs sharply over a range of only a few degrees, the transition to a liquidlike state in these SAMs is very gradual.

The temperature dependence of the linewidth (FWHM) shows two different stages, below and above 300 K (Fig. 4). It is relatively constant up to ~300 K and thereafter it increases linearly. This lower temperature threshold, when compared to the peak frequency one, was used as evidence of an onset of chain movement before the appearance of bulk conformation defects in Langmuir–Blodgett films.[12]

The integrated intensities of the symmetric methyl stretching peaks exhibit a different behavior when compared to the methylene modes (Fig. 5). The intensity of the r^+ peak decreases between 145 and 435 K with a plateaulike peak around 350 K. The slope of the intensity decrease seems even greater above ~350 K. At 435 K, the peak is below the noise level and is not included in Fig. 5. The peak frequency stays relatively constant over the entire temperature range, increasing by less than 1.5 cm^{-1}.

Figure 6 shows the effect of a series of heat treatments on an alkyl thiol with a different terminal group SH–(CH$_2$)$_{15}$–COOH. As expected, only the methylene stretching modes were observed in the 2800–3000 cm^{-1} range. When heated to 315 K (first cycle), the original spectrum (low temperature) is completely recovered, as shown with the peak frequency of the d^- mode. Heating to 344 K (second cycle) shows a consistent positive but weak shift of the position of the d^- peak. An irreversibility effect is clearly observed when the same sample is heated to 393 K. The upward shift of nearly 4 cm^{-1} suggests the presence of a sizable amount of *gauche* defects at low temperature. Overall, the results were similar to those obtained with methyl

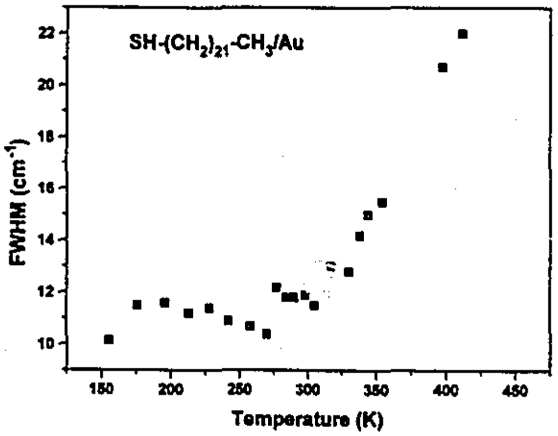

FIG. 4. Temperature dependence of the full width at half-maximum (FWHM) of the antisymmetric methylene stretching modes (d^-) for the same sample as in Fig. 1.

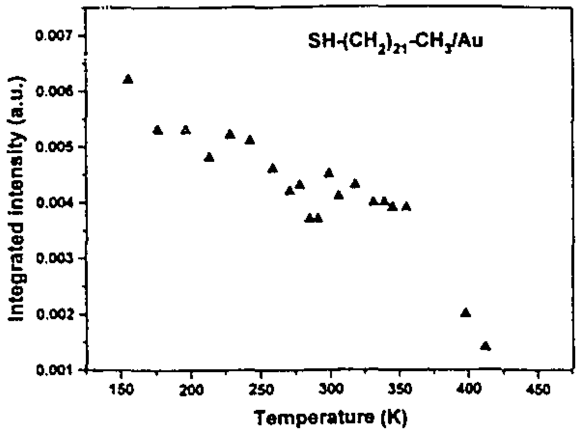

FIG. 5. Temperature dependence of the integrated intensity of the symmetric methyl stretching mode (r^+) on the same sample as in Fig. 1.

terminated thiols, where the onset of significant irreversibility was also found above 350 K.

No studies of the thermotropic properties of thiols adsorbed on substrates other than gold have been reported, so we have undertaken a study on polycrystalline silver. Contrary to the data of Laibinis *et al.*,[18] the low temperature RAIRS spectra of C_{18} on silver shown in Fig. 7 are qualitatively similar to those on gold substrates. However, the intensity of the methylene stretching bands of the thiol adsorbed on Ag are ~30% higher than on gold. This is at odds with the lower tilt angle suggested for thiols adsorbed on silver (~15°).[18,19] The temperature dependence of $SH-(CH_2)_{17}-CH_3$ on silver shows large differences to what has been observed so far on gold samples (Fig. 8). The methylene intensities do not significantly change up to 350 K, and there is only a decrease in the intensity above this temperature [Fig. 8(a)]. Peak frequency [Fig. 8(b)] and peak linewidth [Fig. 8(c)] show a sharp increase above 300 K. Laibinis *et al.*[18] suggested that a long incubation time of thiols on silver substrates leads to multilayer formation. Even though we used a short incubation time, we cannot completely rule out the possibility of multilayer formation. The sharp change in the peak position and linewidth of the d^- mode are similar to those reported for a lipid bilayer.[17]

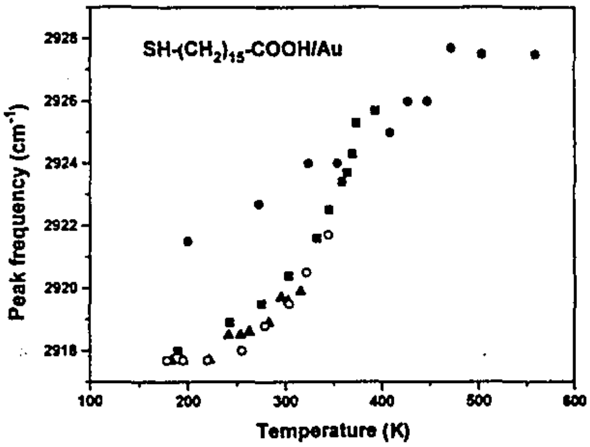

FIG. 6. Heat treatment effect on the peak frequency of the antisymmetric CH_2 stretching mode (d^-) for $SH-(CH_2)_{15}-COOH$ adsorbed on polycrystalline gold. Thermal cycles up to 315 (▲), 344 (○), 393 (■), and 450 K (●) are shown.

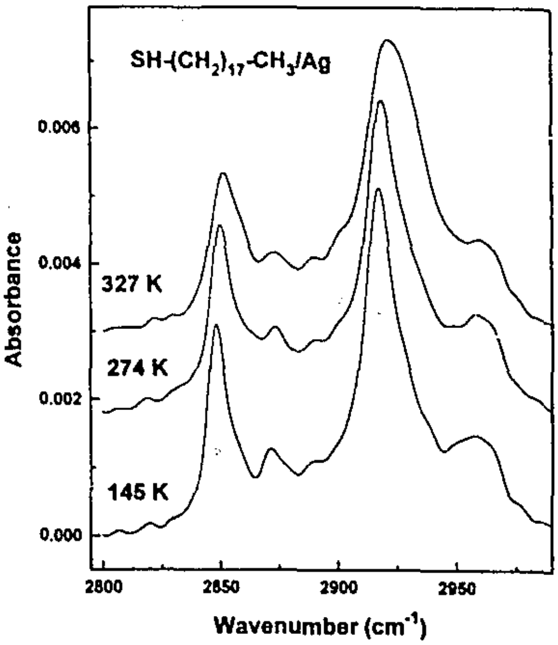

FIG. 7. RAIRS spectra in the C–H stretching region of $SH-(CH_2)_{17}-CH_3$ adsorbed on polycrystalline silver at three representative temperatures. A linear base line correction is performed on each spectra. For reasons of clarity, curves are offset along the Y axis.

IV. DISCUSSION

Several techniques have been used to investigate the thermally induced changes in SAMs. Except for STM and atomic force microscopy (AFM) measurements, most surface techniques probe the average properties of the material. Diffraction techniques[4,5] are sensitive to long-range order and are complementary to IR spectroscopy. Recent investigations have shown that heating induces changes in the orientational, conformational, and positional order parameters.[3–7,9,10,19–21] In this discussion we address two questions. (i) To which of these parameters are the peak position, integrated intensity, and linewidth most sensitive? (ii) To what extent can one correlate the RAIRS results to those from other complementary techniques?

Starting at around 350 K, alkyl thiol monolayers on gold go through a gradual structural transformation with increasing disorder. Based on the absolute values of the positions of the CH_2 stretching modes, this can be described as a gradual transformation of the film from a polycrystalline state to a liquidlike state. This temperature induced solid-liquid phase transition is not conventional and is, furthermore, irreversible. This transition region is also quite large (>50 K) compared to, for example, lipid bilayers,[17] where the transition is very abrupt. It is possible that both liquidlike and polycrystallinelike states coexist in a wide temperature range.

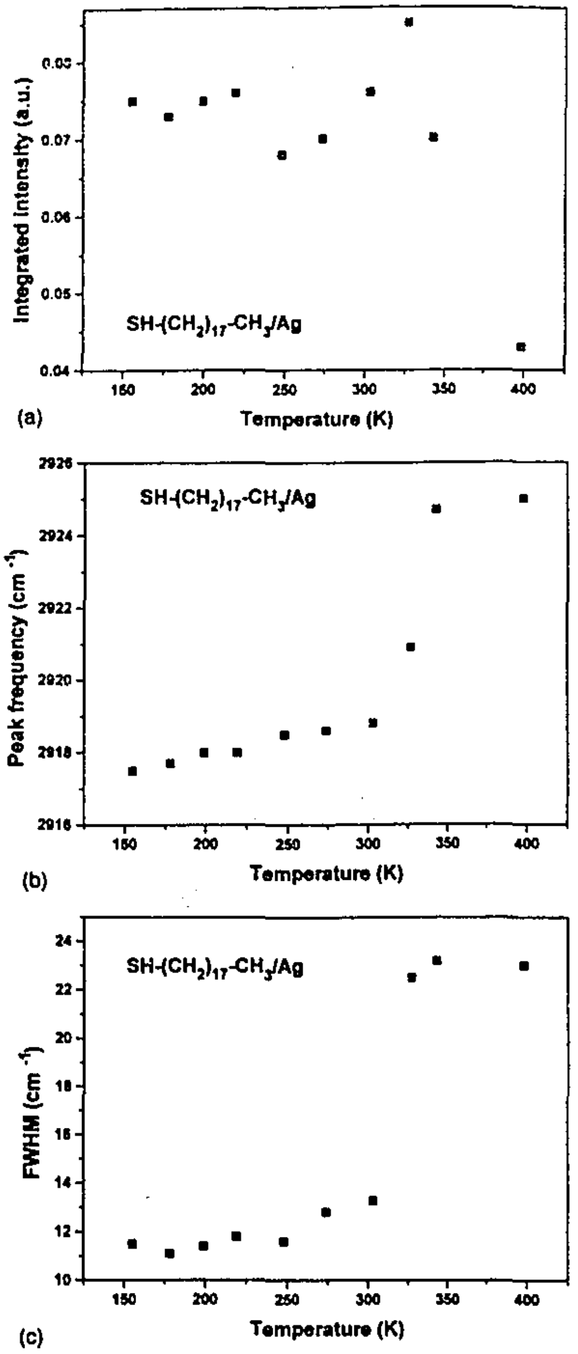

FIG. 8. Temperature dependence of (a) integrated intensity, (b) peak frequency, and (c) FWHM for the antisymmetric stretching mode (d^-) of SH-(CH$_2$)$_{17}$-CH$_3$ adsorbed on polycrystalline silver.

From many previous studies,[1,9-17] it was inferred that the position of the d^- peak is directly related to the amount of *gauche* conformations in an alkyl chain. The large increase in frequency above ~350 K [Fig. 3(a)] is therefore attributed to the appearance of *gauche* conformational defects throughout the chain. Single and double *gauche* conformations[15] are most likely to appear at the surface below 350 K. Above 350 K kink defects[16] are the stable *gauche* conformation. These latter *gauche* defects remain even if the sample is cooled down. Chain entanglement and strong interaction of the sulfur to the substrate may prevent a quick return of the chain to its thermodynamic equilibrium state. However, it is not excluded that chains return to the *trans* conformation after an extended time. Klein *et al.*[3] proposed that *gauche* conformations diffuse to the middle of the chains because of the freed volume from chain untilting. Thus, at low temperature, defects are mainly concentrated at chain ends, and bulk diffusion of these surface defects occurs when the temperature is raised above 350 K.

Due to a combination of the surface IR selection rule and the initial alignment of the chains, *gauche* defects are expected to induce an increase in the peak intensity, whereas untilting has an opposite effect. Around 200 K, MD calculations[3] indicate that the tilt angle is approximately 30°. It decreases by nearly 10° at 350 K. Parikh and Allara[21] calculated that changing the chain tilt from 31° to 23° induces a decrease in the d^- peak intensity by a factor of 2. Above 350 K the presence of bulk gauche defects randomizes the orientation of the C–H groups, leading to an increase in intensity with respect to the aligned, all-*trans* chains. This is similar to the intensity increase observed during the melting of Langmuir–Blodgett films.[11]

Phase transitions were recently observed in solution for long chain alkyl thiols adsorbed on polycrystalline gold.[20] The electrochemical thermogram showed a maximum of current through the films at temperatures 20–30 °C higher than the melting point of the corresponding bulk alkane. The current maximum is believed to arise from facilitated diffusion of the redox species at coexistence boundaries between ordered and disordered alkyl chain domains. Based on these IR studies, the increase of ionic current as a result of chain untilting followed by a decrease of the current due to chain entanglement must be considered as important microscopic factors.

STM data[7] show an increase in the ordered domain size when heating from room temperature to 350 K. In this temperature range an increase in the ordered domain size from ~90 Å to more than 1000 Å was observed by Fenter *et al.*[5] after a first annealing cycle (360 K) of $n=12$ thiol. In contrast, RAIRS seems to show a partial irreversible effect when heating around this temperature for chains with $n>15$.

The final decrease in intensity above 420 K (Fig. 2) corresponds to the partial desorption of alkyl chain thiol as supported by temperature programmed desorption (TPD) data,[8] which showed that a partial desorption of the alkyl chain starts around 343 K.

In general, RAIRS detects, with high sensitivity, changes in chain orientation and chain conformation. Both of these effects occur upon heating alkyl thiol monolayers on gold. On the other hand, some of the changes in long-range order that have been detected using other techniques are not clearly manifested in the C–H stretching region of the spectrum (such as the commensurate–incommensurate transition). However, in almost all studies performed to date, there are large, irreversible changes that occur when *as deposited* layers are heated in the range of 350–400 K. This has now been observed for a wide range of chain lengths, different chain ends, and different gold substrates. It is not possible at present to precisely identify all the processes that occur at this point, but almost certainly there is a decrease in film density, which allows room for the conformational defects that are observed in RAIRS. The important question that now must be addressed is whether this comes about from lateral chain movement, partial chain decomposition, partial chain desorption, or a combination of these.

Finally, there are clear differences in the temperature dependence of alkyl thiol films on silver substrates. Much less characterization of layers on this substrate has been done by complementary techniques, and this limits the ability to interpret the results at present. It seems clear that the preparation of well-defined films on silver is much more delicate than on gold, as manifested by different results obtained from one laboratory to another.

V. CONCLUSION

Significant temperature-induced changes in the structure of alkyl thiol monolayers have been observed by RAIRS. The methylene C–H stretching modes are highly sensitive to the orientation of the alkyl chain and the presence of conformational defects. The temperature induced dependence of the peak positions, linewidth, and integrated intensity can be explained by the following order of events. From low temperature up to about 350 K the chains gradually untilt and there are a limited number of *gauche* defects that begin to occur near the top surface. These effects are reversible. A broad transition to a liquidlike state, which starts near 350 K, introduces a large number of *gauche* conformational defects within the chains, and this effect is not reversible. Although partial desorption may occur starting at 350 K, significant desorption of the film does not occur until 400 K. This overall behavior is not very sensitive to either chain length (at least above C_{14}), or to whether the terminal group is CH_3 or COOH. Significant differences were observed when the substrate was changed from gold to silver, but further characterization of this system is needed.

ACKNOWLEDGMENTS

This research was supported by the Natural Sciences and Engineering Council of Canada, and the Centers of Excellence for Molecular and Interfacial Dynamics.

[1] L. H. Dubois, R. G. Nuzzo, Annu. Rev. Phys. Chem. **43**, 437 (1992).

[2] A. Ulman, in *An Introduction to Ultrathin Organic Films* (Academic, Boston, 1991).

[3] J. Hautman and M. L. Klein, J. Chem. Phys. 93, 7483 (1990); W. Mar and M. L. Klein, Langmuir **10**, 188 (1994).

[4] N. Camillone III, C. E. D. Chidsey, T. M. Putvinski, and G. Scoles, J. Chem. Phys. 94, 8493 (1991); N. Camillone III, C. E. D. Chidsey, G. Liu, and G. Scoles, J. Chem. Phys. 98, 3503 (1993).

[5] P. Fenter, P. Eisenberger, and K. S. Liang, Phys. Rev. Lett. **70**, 2447 (1993); P. Fenter, A. Rberhardt, and P. Eisenberg, Science **266**, 1216 (1994).

[6] G. E. Poirier, M. J. Tarlov, and H. E. Rushmeier, Langmuir **10**, 3383 (1994).

[7] J.-P. Boucher, L. Santesson, and K. Kern, Langmuir **10**, 979 (1994).

[8] C. D. Bain, E. B. Troughton, Y.-T. Tao, J. Evall, G. M. Whitesides, R. G. Nuzzo, J. Am. Chem. Soc. **111**, 321 (1989).

[9] L. H. Dubois, B. Zegarski, and R. G. Nuzzo, J. Electron Spectrosc. Relat. Phenom. 54/55, 1143 (1990); R. G. Nuzzo, E. M. Korenic, and L. H. Dubois, J. Chem. Phys. 93, 767 (1990).

[10] A. Ulman, Adv. Mater. 3, 298 (1991).

[11] G. N. Naseli, J. F. Rabolt, and J. D. Swallen, J. Chem. Phys. **82**, 2136 (1985).

[12] N. Katayama, S. Enomoto, T. Sato, Y. Ozaki, and N. Kuramoto, J. Phys. Chem. 97, 6880 (1993).

[13] F. Bensebaa, T. H. Ellis, A. Badia, and R. B. Lennox, J. Chem. Phys. (submitted).

[14] M. D. Porter, T. B. Bright, D. L. Allara, and C. E. D. Chidsey, J. Am. Chem. Soc. **109**, 3559 (1987).

[15] R. G. Snyder, H. L. Strauss, and C. A. Ellinger, J. Chem. Phys. **86**, 5145 (1982); R. A. McPhail, R. G. Snyder, H. L. Strauss, and C. A. Ellinger, J. Phys. Chem. **88**, 334 (1984).

[16] M. Maroncelli, S. P. Qi, H. L. Strauss, and R. G. Snyder, J. Am. Chem. Soc. **104**, 6237 (1982); R. G. Snyder, M. Maroncelli, H. L. Strauss, and V. M. Hallmark, J. Phys. Chem. **90**, 5623 (1986).

[17] R. Mendelsohn, M. A. Davies, J. W. Brauner, H. F. Schuster, and R. A. Dluhy, Biochemistry 28, 8934 (1989); G. Cameron, H. L. Casal, and H. H. Mantsch, Biochemistry 19, 3665 (1980).

[18] P. E. Laibinis, G. M. Whitesides, D. L. Allara, Y.–T. Tao, A. N. Parikh, and R. G. Nuzzo, J. Am. Chem. Soc. **113**, 7152 (1993).

[19] H. Sellers, A. Ulman, Y. Shnidman, and J. E. Eilers, J. Am. Chem. Soc. **115**, 9389 (1993).

[20] A. Badia, R. Back, and R. B. Lennox, Angew. Chem. Int. Ed. Engl. 33, 2332 (1994).

[21] A. N. Parikh and D. L. Allara, J. Chem. Phys. 96, 927 (1992).

Structure and Chain Dynamics of Alkanethiol-Capped Gold Colloids

A. Badia, W. Gao, S. Singh, L. Demers, L. Cuccia, and L. Reven*

*Department of Chemistry, McGill University, 801 Sherbrooke St. W.,
Montreal, Quebec, Canada H3A 2K6*

Received November 17, 1995§

The structure and dynamical behavior of short and long chain alkanethiols, $CH_3(CH_2)_7SH$ and $CH_3(CH)_{17}SH$, and of a hydroxyalkanethiol, $HO(CH_2)_{16}SH$, adsorbed onto gold nanoparticles were studied by variable temperature solid-state ^{13}C NMR spectroscopy. In both the solution and solid state, the resonances of the first three carbons next to the sulfur headgroup disappear upon binding to the gold, indicating a strong interaction with the surface. A ^{13}C-enriched sample, $CH_3(CH_2)_{12}{}^*CH_2SH$/gold, displays a broad resonance centered at 42 ppm for the carbon next to the sulfur headgroup. Whereas the solid-state ^{13}C shifts of $CH_3(CH_2)_7SH$/gold are essentially the same as in solution, the methylene carbons of $CH_3(CH_2)_{17}SH$ and $HO(CH_2)_{16}SH$/gold shift downfield by 4.5 ppm in the solid state, indicating that the chains crystallize into an extended all-trans conformation. The high conformational order, along with reduced methylene proton line widths in the $CH_3(CH)_{17}SH$/gold sample, indicates that the chains are undergoing large-amplitude motions about their long axes. Molecular mobility increases toward the unbound ends which have a higher population of gauche conformers. Relaxation measurements show the coexistence of motionally restricted all-trans chains and a smaller population of liquid-like conformationally disordered chains in $CH_3(CH_2)_{17}SH$/gold at room temperature. The two types of chains are proposed to arise from close packing of the gold colloidal spheres, resulting in interstitial spaces and regions where chains of neighboring colloids can interdigitate to produce ordered domains. Phase transitions of the thiol-capped gold nanocrystals, which are detected by differential scanning calorimetry, are shown to involve a reversible disordering of the alkyl chains.

1. Introduction

The synthesis and physical properties of nanometer-scaled semiconductor and metal colloids are currently very active areas of research due to their potential applications in optoelectronics,[1] thin film growth,[2] and catalysis.[3] Syntheses employing surfactants to stabilize the size and shape of these crystallites have successfully produced single-sized semiconductor[4] and noble metal clusters.[3] Recently, a novel surfactant-mediated synthesis of gold colloids was reported by Brust and co-workers.[5] This system is particularly interesting because the surfactant used, dodecanethiol, is well-known to form self-assembled monolayers (SAMs) on planar gold.[6] Leff and co-workers have further demonstrated that control of the gold particle size in this system is achieved by varying the gold-to-thiol ratio and applied a model in which the role of the thiol is analogous to that of the surfactant in water-in-oil microemulsions.[7]

Since the nature of the surfactant chain structure in the alkanethiol-capped gold nanoparticles has not been reported, we have used NMR spectroscopy to study the surfactant molecules directly. In spite of the poor sensitivity of NMR spectroscopy, recent ^{13}C and ^2H NMR studies have demonstrated its unique ability to probe the dynamic and conformational behavior of long-chained ionic surfactants on metal oxides[8] and latex particles.[9] In the case of noble metal colloids, ^{13}C NMR provided evidence that surfactant-stabilized platinum nanoparticles are protected by the direct adsorption of the hydrophobic segment of the surfactant onto the metal surface.[10] In most of these studies, high-resolution solid-state NMR techniques were not used despite the fact that the surfactant may become immobilized to the point that some of the carbon sites would not be observable under conventional solution NMR conditions.

Self-assembled monolayers, which form ordered, tightly bonded films to metal surfaces, are the extreme example of immobilization of adsorbed molecules. We have recently shown solid-state NMR to be highly useful for structural and dynamic studies of self-assembled monolayers of alkylsilanes and metal alkylphosphonates.[11] Although alkanethiols on gold are the most intensively studied self-assembled monolayers, molecular level understanding of their dynamic properties is relatively limited. Variable temperature infrared,[12] X-ray diffraction,[13] and electrochemical[14] studies, as well as molecular dynamic simulations,[15] indicate that the dynamic behavior of the thiol monolayers involves a complex structural phase diagram which depends on variables such as the chain length and terminal functional groups. Although the surface cur-

---

§ Abstract published in *Advance ACS Abstracts*, February 15, 1996.

(1) (a) Wang, Y.; Herron, N. *J. Phys. Chem.* 1991, *95*, 525. (b) Colvin, V. L.; Schlamp, M. C.; Alvisatos, A. P. *Nature* 1994, *370*, 354.

(2) Heath, J. R.; Gates, S. M.; Chesc, C. A. *Appl. Phys. Lett.* 1994, *64*, 3569.

(3) Schmid, G. *Chem. Rev.* 1992, *92*, 1709.

(4) Herron, N.; Calabrese, J. C.; Farneth, W. E.; Wang, Y. *Science* 1993, *259*, 1426.

(5) Brust, M.; Walker, M.; Bethell, D.; Schriffin, D. J.; Whyman, R. *J. Chem. Soc., Chem. Commun.* 1994, 802.

(6) Dubois, L. H.; Nuzzo, R. G. *Annu. Rev. Phys. Chem.* 1992, *63*, 437.

(7) Leff, D. V.; Ohara, P. C.; Heath, J. R.; Gelbart, W. M. *J. Phys. Chem.* 1995, *99*, 7036.

(8) (a) Söderlind, E.; Stilbs, E. *J. Colloid Interface Sci.* 1991, *143*, 586. (b) Söderlind, E.; Blum, F. D. *J. Colloid Interface Sci.* 1993, *157*, 172. (c) Söderlind, E.; Stilbs, E. *Langmuir* 1993, *9*, 2024.

(9) (a) Macdonald, P. M.; Yue, Y.; Rydall, J. R. *Langmuir* 1992, *8*, 164. (b) Yue, Y.; Rydall, J. R.; MacDonald, P. M. *Langmuir* 1992, *8*, 390. (c) Kuebler, S. C.; Macdonald, P. M. *Langmuir* 1992, *8*, 397.

(10) Yonezawa, T.; Gotoh, Y.; Toshima, N. *React. Polym.* 1994, *23*, 43.

(11) Gao, W.; Reven, L. *Langmuir* 1995, *11*, 1860.

(12) (a) Nuzzo, R. G.; Korenic, E. M.; Dubois, L. H. *J. Chem. Phys.* 1990, *93*, 767. (b) Dubois, L. H.; Zegarski, B. R.; Nuzzo, R. G. *J. Electron Spectrosc. Relat. Phenom.* 1990, *54/55*, 1143.

(13) Fenter, P.; Eisenberger, P.; Liang, K. S. *Phys. Rev. Lett.* 1993, *70*, 2447.

(14) Badia, A.; Back, R.; Lennox, R. B. *Angew. Chem., Int. Ed. Engl.* 1994, *33*, 2332.

(15) (a) Hauptman, J.; Klein, M. L. *J. Chem. Phys.* 1990, *93*, 7483. (b) Hauptman, J.; Bareman, J. P.; Mar, W.; Klein, M. L. *J. Chem. Soc., Faraday Trans.* 1991, *87*, 2031. (c) Siepmann, J. I.; McDonald, I. R. *Langmuir* 1993, *9*, 2351.

0743-7463/96/2412-1262$12.00/0

vature of the colloidal gold used here may limit direct comparison with alkanethiols on planar gold, the synthesis of the thiol-capped gold colloids provides an opportunity to examine the chain dynamics of covalently bound alkanethiols by NMR spectroscopy.

In this study, we report ^{13}C chemical shift, relaxation, and line shape data which reveal that in the case of long chains ($n = 16, 18$), the alkanethiol surfactant on the gold is in a semicrystalline state. At room temperature, domains of all-trans chains coexist with a smaller population of more mobile chains containing gauche conformers. The high curvature of the surface of the very small gold particles (diameter ~2 nm) prevents efficient packing of neighboring chains as in the case of alkanethiol monolayers on planar gold. Instead, the spacing between the colloids, as measured by transmission electron microscopy (TEM) and X-ray diffraction,[16] suggests that intercalation of the chains of neighboring gold particles allows crystallization into an extended all-trans conformation. The chain termini, however, display mobilities comparable to the short chain ($n = 8$) alkanethiol on the gold which is completely conformationally disordered at room temperature.

A concurrent TEM, transmission FTIR, and differential scanning calorimetry (DSC) study of the alkanethiol-capped gold nanoparticles of varying chain lengths demonstrates that an order/disorder transition occurs in the same temperature range as in analogous lipid bilayers.[16] A similar trend has also been observed for self-assembled monolayers of alkanethiols on planar gold by variable temperature electrochemical measurements.[14] The solid-state NMR spectra of the alkanethiol-capped gold nanoparticles show that as the temperature is raised, a gradual growth of the population of disordered chains occurs up to the DSC transition temperature, and above this temperature all of the chains are in a liquid-like state. Interestingly, when the gold colloids are capped with C_{16} hydroxyl-terminated thiols, the disordering of the chains occurs in a higher temperature range than in the case of the C_{18} methyl-terminated thiols. This is proposed to be due to the presence of hydrogen bonding between the terminal OH groups of neighboring chains, on the same or neighboring colloid, which both introduces some order and increases the thermal stability of the alkane chain ordering.

2. Experimental Section

Syntheses. Gold colloids derivatized with octanethiol (C_8H_{17}-SH), octadecanethiol ($C_{18}H_{37}SH$), and 16-hydroxyhexadecanethiol ($HOC_{16}H_{32}SH$) were prepared following the procedure of Brust and co-workers,[5] and the detailed conditions will be reported elsewhere.[16] Briefly, this involves a two-phase (toluene/water) synthesis and $(C_8H_{17})_4NBr$ as the phase transfer reagent. $Au^{III}Cl_4^-$ is transferred to the toluene layer from the water layer, and then reduced by $NaBH_4$ in the presence of the thiol surfactant at the toluene/water interface. Reactions were carried out using mole ratios of 1.1:1 $HAuCl_4$/RSH, 4.4:1 $(C_8H_{17})_4NBr/HAuCl_4$, and 11:1 $NaBH_4/HAuCl_4$. *n*-Octadecanethiol was purchased from Aldrich (98%) and was recrystallized three times from ethanol. *n*-Octanethiol (Aldrich, 98%) was purified by passage through a silica gel column before use. 16-Hydroxyhexadecanethiol was synthesized from the corresponding *n*-hexadecanediol (Fluka, >98%) following the method of Miller *et al.*[17] The purity of the bulk thiol surfactants was verified by ^1H NMR (500 MHz, $CDCl_3$), ^{13}C NMR (125 MHz, $CDCl_3$), TLC (silica gel, *n*-hexane), and melting point determination using DSC. The elemental analyses were consistent with 100% coverage of the colloids by the alkanethiols.[16]

NMR Instrumental Conditions. Solution-state ^{13}C NMR spectra for the bulk thiols and thiol-derivatized gold colloids were acquired at 125 MHz with broadband ^1H decoupling on a Varian Unity 500 NMR spectrometer. The solid-state 67.92 MHz ^{13}C CP MAS spectra were run on a Chemagnetics CMX-270 NMR spectrometer with a 7 mm double-tuned fast-MAS Doty probe. For $^1H-^{13}C$ cross polarization, the carbon and proton power levels were adjusted to achieve the Hartmann–Hahn match at 60 kHz. The ^1H 90° pulse widths were between 3.5 and 4.5 μs, and contact times of 3 ms were used. The samples were typically spun at 2.5–3.5 kHz, and an average of 400–1000 scans were taken with delay times of five times the longest proton T_1 value. For the variable temperature CP MAS experiments, the sample temperature was controlled to within ±2 °C by a Chemagnetics temperature controller.

For the proton T_1 measurements, an inversion–recovery pulse sequence with ^{13}C CP MAS detection was used. In this sequence, the proton spins are inverted with a 180° pulse, and after a variable decay period the remaining proton magnetization is transferred to the carbon spins by cross polarization. The carbon T_1 values were measured using the Freeman–Hill modified inversion–recovery sequence[18] with the initial ^{13}C magnetization generated by cross polarization. T_{CH} and $T_{1\rho}$ were determined by fitting the variable contact time data to the appropriate equation describing the decay of the proton spin-locked magnetization.[19]

The dipolar dephasing times, T_{dd}, were measured with an interrupted decoupling pulse sequence.[20] After cross polarization, the proton decoupler is turned off for a variable delay during which the carbon spins rapidly dephase due to heteronuclear dipolar interactions, and the resulting signal is detected with high-power proton decoupling. A 180° pulse is inserted halfway through the delay to remove linear phase distortions and refocus long-term chemical shift spin order. In the case of weak dipolar interactions due to molecular motion, the data was fit to a first-order (Lorentzian) decay, $I_L = I_{0L} \exp(-\tau/T_{2L})$, where τ is the delay time and T_{2L} is the Lorentzian decay constant. For rigid solids, the fast decays are often best fit by a second-order (Gaussian) decay, $I_G = I_{0G} \exp(-\tau^2/2T_{2G}^2)$, where T_{2G} is the Gaussian decay constant. In the case of the gold–thiol colloids, the faster decaying carbons were found to be best fit by a two-component Gaussian–Lorenztian decay, $I = I_{0G} \exp(-\tau^2/2T_{2G}^2) + I_{0L} \exp(-\tau/2T_{2L})$.[20]

In the 2D wide-line separation pulse sequence (WISE),[21] a ^1H 90° pulse was followed by a proton evolution period, t_1, consisting of 32 increments of 2 μs. After each t_1 period, cross polarization, followed by carbon detection with proton decoupling, gives a carbon spectrum which is modulated as a function of t_1 by the free induction decay of the associated protons. A second Fourier transform gives a 2D spectrum with high-resolution ^{13}C CP MAS spectra along the first dimension and the wide-line proton spectra associated with each carbon along the second axis.

3. Results

(i) NMR Chemical Shifts. In Figures 1–3, the solution- and solid-state ^{13}C NMR spectra of three alkanethiols alone and bound to gold nanoparticles are displayed along with the carbon site assignments. The ^{13}C chemical shifts of these samples and a ^{13}C-labeled sample are listed in Table 1. The $HOC_{16}S-Au$ colloid was not soluble in common organic solvents, and the solid-state NMR spectrum of the pure surfactant is shown instead in Figure 3b. Upon bonding to the gold, the resonances of the C_8 and C_{18} thiols broaden and the carbon sites closest to the sulfur headgroup, C1 and C2 at 24.5 and 33.9 ppm, appear to vanish completely. The C3 peak, which at 28.2 ppm is only slightly shifted from the interior

---

(16) Badia, A.; Singh, S.; Demers, L. M.; Cuccia, L. A.; Brown, G. R.; Lennox, R. B. *Chem.-Eur. J.* **1996**, *2*, 205.

(17) Miller, C. J.; Becka, A. M. *J. Phys. Chem.* **1992**, *96*, 2657.

(18) Torchia, D. A. *J. Magn. Reson.* **1978**, *30*, 613.

(19) Garroway, A. N.; Moniz, W. B.; Resing, H. A. *ACS Symp. Ser.* **1979**, *No. 103*, 67.

(20) Alemany, L. B.; Grant, D. M.; Alger, T. D.; Pugmire, R. J. *J. Am. Chem. Soc.* **1983**, *105*, 6697.

(21) (a) Chin, Y.-H.; Kaplan, S. *Magn. Reson. Chem.* **1994**, S53. (b) Clauss, J.; Schmidt-Rohr, K.; Adam, A.; Boeffel, C.; Spiess, H. W. *Macromolecules* **1992**, *25*, 5208.

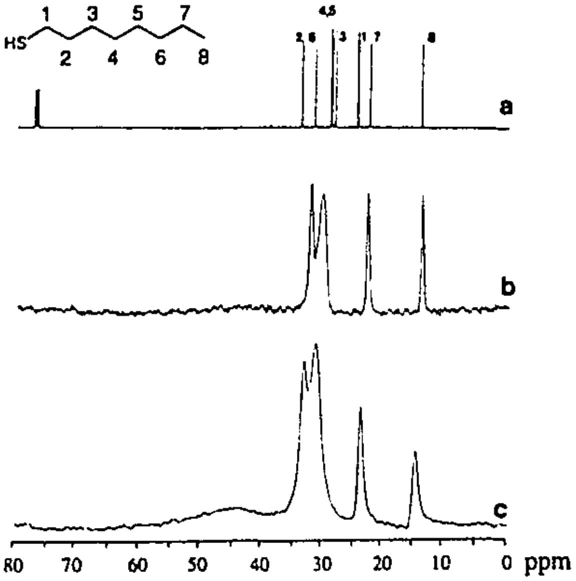

Figure 1. ^{13}C NMR spectra of $CH_3(CH_2)_7SH$ (a) in $CDCl_3$, (b) on colloidal gold in benzene-d_6, and (c) on colloidal gold in the solid state. The triplet at 77 ppm in (a) is due to the solvent. The solid-state ^{13}C CP MAS NMR spectrum of $CH_3(CH_2)_7SH$ on colloidal gold was obtained with a 3 ms contact time, a 3 s recycle time, and a 3 kHz sample rotation frequency.

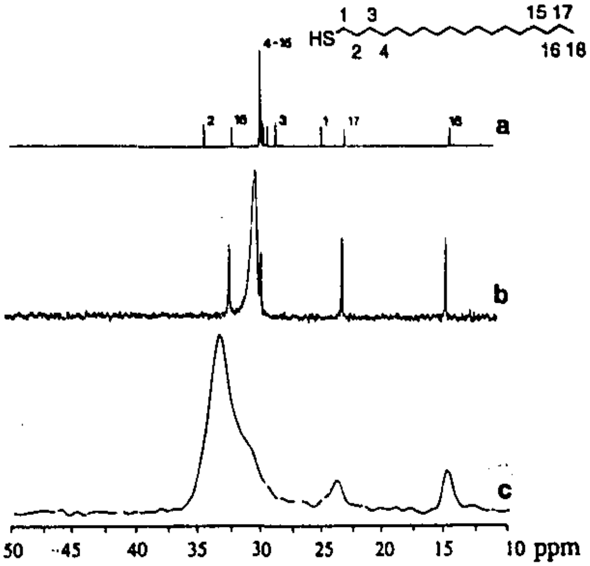

Figure 2. ^{13}C NMR spectra of $CH_3(CH_2)_{17}SH$ (a) in $CDCl_3$, (b) on colloidal gold in benzene-d_6, and (c) on colloidal gold in the solid state.

methylenes at 29.9 ppm, may also be absent or has shifted underneath the broad resonance of the interior methylenes. The same changes were observed in the ^1H NMR solution spectra (not shown); that is, the resonances of the protons attached to the first two carbons closest to the sulfur headgroup are not visible in the alkanethiol-capped gold. A similar phenomena was observed in the case of the alkane chain part of poly(ethylene glycol), when this surfactant was used to stabilize platinum nanoparticles.[10] The disappearance of some of the solution state carbon signals with increasing concentration of the platinum cluster was attributed to solidification of the hydrophobic part of the surfactant, which contains the metal cluster. In the solid-state ^{13}C NMR spectrum of the $C_8S{-}Au$ in Figure 1c, a broad resonance centered at ~45 ppm is present, which is due to one or more of the carbons closest to the gold surface. As discussed below, this short chain thiol does not crystallize at room temperature, and the greater mobility of the C_8 chains must sufficiently average the effects of the gold to make this broad resonance visible. This assignment of the broad resonance was confirmed by a sample which was isotopically labeled at the carbon

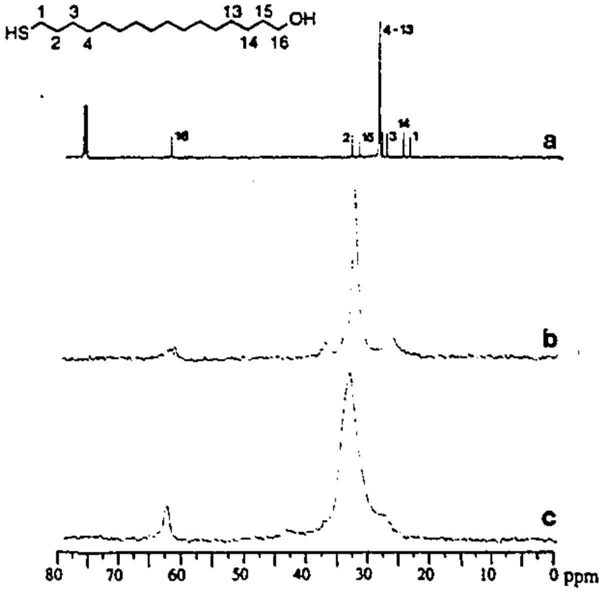

Figure 3. ^{13}C NMR spectra of $HO(CH_2)_{16}SH$ (a) in $CDCl_3$, (b) in the solid state, and (c) on colloidal gold in the solid state. The triplet at 77 ppm in (a) is due to the solvent. The $HO(CH_2)_{16}SH$ on colloidal gold was not soluble in common organic solvents.

Table 1. Chemical Shifts of Alkanethiols Alone and Adsorbed onto Gold Colloids

	thiol solution[a]	thiol/gold solution	thiol/gold solid state[b]
$HS(CH_2)_7CH_3$			
C1	24.5		
C2	33.9		
C3	28.2		
C4,C5	28.9, 29.0	30.8	31.1
C6	31.6	32.8	33.1
C7	22.5	23.3	23.8
C8	13.9	14.4	14.9
$HS^*CH_2(CH_2)_{12}CH_3$			
C1	24.5	42.5	42.5
C2	33.9		
C3	28.2		
C4–C11	28.9–29.6	30.2–29.5	33.2, 31.3
C12	31.8	31.9	d
C13	22.5	22.7	23.8
C14	13.9	13.9	15.0
$HS(CH_2)_{17}CH_3$			
C1	24.5		
C2	33.9		
C3	28.2		
C4–C15	28.9–29.6	30.9–29.5	33.8
C16	31.8	31.9	*d*
C17	22.5	22.7	24.2
C18	13.9	13.9	15.1
$HS(CH_2)_{16}OH$[c]			
C1	24.5		
C2	33.9		
C3	28.2		
C4–C13	28.8		33.5
C14	25.6		27.9
C15	32.6		d
C16	62.9		62.7

[a] The bulk thiol and thiol-capped gold colloid solution NMR spectra were run in $CDCl_3$ and benzene-d_6, respectively, and are referenced to TMS. [b] ^{13}C solid-state NMR spectra are referenced to hexamethylbenzene at 17.45 ppm from TMS. [c] The $HS(CH_2)_{16}OH$-capped gold colloids were not soluble in common NMR solvents. [d] Not resolvable in the solid state.

next to the sulfur, $CH_3(CH_2)_{12}{}^*CH_2S-Au$. Integration of the relative intensities shows that the broad resonance, centered at 42.5 ppm (fwhh = 1440 Hz), accounts for all of the labeled ^{13}C intensity and is not due to a minor species.

The downfield shifts of the ^{13}C resonances in the solid-state NMR spectra shown in Figures 2c and 3c indicate that the long chain alkanethiols on the gold colloids are conformationally ordered. The chemical shift of the interior methylenes of $C_{18}S-Au$ (C4–C15) and $HOC_{16}S-Au$ (C4–C13) changes from 29.0–29.5 ppm in organic solvents to 33.5–33.8 ppm in the solid state. For bulk *n*-alkanes, these carbons resonate at 29–30 ppm in solution where there are equilibrium populations of trans and gauche conformations, but in the crystalline state, they shift downfield to 33–34 ppm for an all-trans conformation.[22] This chemical shift difference has been used to characterize the chain conformations of ionic surfactants[23] and self-assembled monolayers on silica.[11] When the C_{18}-gold was placed in D_2O, and its signal collected using solution-NMR techniques, a broad resonance centered at 33 ppm was observed, indicating that the chains had solidified. When the temperature was raised to 55 °C, this resonance narrowed considerably and increased in intensity. As shown later by variable temperature solid-state NMR, this is the temperature at which the chains disorder. This observation correlates with electrochemical studies of thiols on gold electrodes where the alkanethiol self-assembled monolayers suppress Faradaic currents of redox couples in aqueous solutions, but not in organic solvents where the chains are solvated.[24]

The downfield shift for the α-CH_2 of $C_{18}S-Au$, C17, is less than that observed for solid alkanes. Normally this carbon shifts from 22.6 in the liquid state to 25.0 ppm for a crystalline all-trans conformation.[22a] In the case of the C_{18} thiol, the shift changes from 22.5 in solution to only 24.2 ppm in the solid state, reflecting a higher population of gauche defects at the chain end. The solution and the solid-state chemical shifts of C_8S-Au differ only slightly, indicating that in this case, the surfactant has not crystallized. This liquid-like state is to be expected for thiols of chain lengths less than 12 since they are known not to form ordered phases on planar gold.[13]

(ii) Relaxation Studies. (a) Spin–Lattice Relaxation. A relaxation study was carried out in order to compare the chain dynamics of the alkanethiol-capped gold with highly ordered and disordered systems: crystalline organic solids and monodispersed alkylsilyl chains grafted onto silica.[25] The proton and carbon spin–lattice relaxation times, T_1^H and T_1^C, probe molecular motions in the vicinity of the Larmor frequencies of the two nuclei, 270 and 68 MHz, respectively. Inspection of Table 2 shows that there is little variation in the proton spin–lattice relaxation times associated with the various carbon sites. This homogeneity of T_1^H is typical of organic solids where $^1H-^1H$ spin diffusion tends to equalize the spin–lattice relaxation times among the proton sites. The primary source of proton relaxation is the modulation of the dipolar interaction by the rapidly rotating methyl group. In contrast, the pure surfactant, $HS(CH_2)_{16}OH$ (a crystalline solid at room temperature), was found to have a relatively long T_1^H (10.7 s) since the terminal carbons are immobilized by hydrogen bonding.

Table 2. Solid-State Relaxation Parameters for Alkanethiol-Capped Gold Colloids and Related Systems

	T_1^H (s)	T_1^C (s)	T_{CH} (ms)	$T_{1\rho}^H$ (ms)	T_{DD} (μs)[a]
$AuS(CH_2)_7CH_3$					
C4–C5	0.45	0.45	0.17	6.6	114
C6	0.46	0.50	0.18	7.6	134
C7	0.45	0.61	0.45	9.9	213
C8	0.44	1.6	0.84	12.1	242
$AuS(CH_2)_{17}CH_3$					
C4–C16	0.65	12	0.053	8.2	16[b]
C17		1.28			94
C18		1.82			190
$AuS(CH_2)_{16}OH$					
C4–C15		37	0.052	7.6	17[b]
C16		0.2	0.19	9.3	102
$HS(CH_2)_{16}OH$					
C1, C15		243			
C2, C14		217			
C3–C13	10.5	250			
C16		102			
C_{18}–silica[c]					
C1	0.52	0.32	0.09	20	
C3	0.47	0.27	0.17	24	
C4–C15	0.48	0.33	0.17	54	
C16	0.51	0.81	0.25	95	
C2+C17	0.49	0.89	0.28	>100	
C18	0.43	1.8	1.31	>100	

[a] All of the values listed are T_{2L} derived from a fit to a single-exponential decay curve except for the inner CH_2's of $C_{18}S-Au$ and $HOC_{16}-Au$. [b] T_{2G} values were derived from a fit to a two-component Gaussian–Lorenztian decay curve as described in the Experimental Section. [c] Data from ref 25.

Carbon spin–lattice relaxation times are a more selective probe of molecular motion due to the absence of spin diffusion. In rigid organic solids, the carbon T_1 values can be quite long, on the order of many minutes, as in the case of highly crystalline polyethylene. The relaxation times of all the carbon sites of C_8S-Au, as well as the terminal carbons of the long chain samples, were on the order of a few seconds or less. In contrast, the 33 ppm peak assigned to the all-trans interior methylenes of $HOC_{16}S-$ and $C_{18}S-Au$ relaxed much more slowly, and the decay did not fit a single-exponential curve. This behavior is expected in the case of varying mobilities along the chain. In addition, as discussed below, there will be a contribution from the small resonance at 31 ppm due to the disordered chains. The decay of the 33 ppm component in the C_{18} sample was found to be biexponential, with a short decay time of 0.92 s, presumably associated with the more mobile carbons near the chain termini and the disordered chains, and a longer decay time of 12 s, arising from the interior methylenes closer to the bound end. A somewhat longer value of 37 s was measured for the long T_1^C decay component of $HOC_{16}S-Au$.

The shorter T_1^C values of the more mobile unbound chain ends in $C_{18}S-Au$ (C17 and C18), compared to the motionally restricted carbons near the bound end, may be explained by an increasing amplitude and/or rate of motion. However, since T_1^C of the internal methylene carbons decreases with field strength ($T_1^C \sim 8$ s at 25 °C, $\omega_L = 25$ MHz) and temperature ($T_1^C \sim 9$ s at 55 °C, $\omega_L = 68$ MHz), we can assume that some of the chain motions are slow on the NMR time scale with a rate of reorientation less than ω_L. The longer T_1^C value of 37 s measured for $HOC_{16}S-Au$ shows that the methylene chain motion is more restricted than in the methyl-terminated $C_{18}S-Au$. However, these T_1^C values are still considerably smaller than those of rigid organic solids, as demonstrated by the 250 s value measured for the interior methylene resonance of the pure surfactant, $HO(CH_2)_{16}SH$. The monodispersed

---

[22] (a) Earl, W. L.; VanderHart, D. L. *Macromolecules* **1979**, *12*, 762. (b) Tonelli, A. E.; Schilling, F. C. *Acc. Chem. Res.* **1981**, 223.

[23] Söderlind, E.; Stilbs, P. *Langmuir* **1993**, *9*, 1678.

[24] (a) Sandroff, C. J.; Garoff, S.; Leung, K. P. *Chem. Phys. Lett.* **1983**, *96*, 547. (b) Finklea, H. O.; Avery, S.; Lynch, M.; Furtsch, T. *Langmuir* **1987**, *3*, 409.

[25] Zeigler, R. C.; Maciel, G. E. *J. Phys. Chem.* **1991**, *95*, 7345.

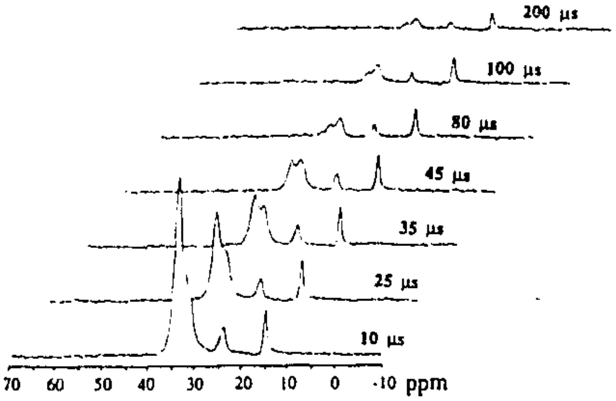

Figure 4. Selected dipolar dephasing spectra of $CH_3(CH_2)_{17}$-SH on colloidal gold. The small peak at 31 ppm, which is resolvable at delay times greater than 40 μs, is assigned to conformationally disordered chains.

chains of C_{18}−silica display the opposite trend; the T_1^C values of the chain ends are larger than those of the interior methylenes, and were assumed to be in the motional-narrowing limit. However, the T_1^C values of C_{18}−silica were found to be field dependent, so the motional frequencies must be close to the Larmor frequency (50 MHz) in this system.[25] The T_1^C values of C_8S−Au are slightly smaller than those of C_{18}−silica and show the same trend, with the values increasing toward the unbound end. The motional frequencies of the C_8S−Au chains, which are also conformationally disordered, are probably close to those of the monodispersed chains, that is, between 10 and 50 MHz. The cross polarization parameters, also listed in Table 1, are consistent with these trends in chain mobility.

(b) Dipolar Dephasing. $^{13}C-^{1}H$ heteronuclear dipolar dephasing experiments are highly useful for spectral editing and detection of relative molecular mobilities.[20] After the contact time in the cross polarization experiment, a delay without dipolar decoupling is inserted before data acquisition. During this time the signal will decay with a time constant T_2 which depends on the strength of the $^{13}C-^{1}H$ heteronuclear dipolar interaction, molecular motion, and to some extent, the sample spinning speed. Short decays due to a strong heteronuclear dipolar interaction are characterized by a Gaussian decay, whereas weaker coupling, in the presence of molecular motion, can be fit to an exponential (Lorentzian) decay. In rigid solids, the decay times for methylene and methyl carbons are in the range of 10−30 and 50−100 μs, respectively,[20] since the methyl groups are normally undergoing rapid rotation at room temperature. The intensities of all of the C_8S−Au, carbons and terminal [illegible]ps of $C_{18}S$− and $HOC_{16}S$−Au under dipolar dephasing, could be fit to first-order exponential decay curves, yielding $T_{2L} \geq 100$ μs. In contrast, the interior methylene carbons of the two long chain samples exhibit a two-component Gaussian−Lorentzian decay. The short Gaussian component ($T_{2G} \sim 8$ μs), which dominates the decay, is due to the carbons which are in a more motionally restricted environment, whereas the small exponential component ($T_{2L} \sim 80$ μs) presumably arises from mobile carbons toward the chain ends and disordered chains. In Figure 4, examination of the dipolar dephasing spectra of the C_{18} thiol sample reveals that a small peak centered at 31 ppm becomes visible at longer delay times (>40 μs), after the 33 ppm peak has mostly decayed away. This more slowly decaying component, which has the same shift as the interior methylenes of the gold colloids in solution, is assigned to highly mobile, conformationally disordered chains.

(iii) Integrated Intensities. As revealed by the dipolar dephasing experiments, the shoulder at 31 ppm in the room temperature solid-state ^{13}C NMR spectrum of $C_{18}S$−Au in Figure 2c is due to more mobile chains containing a larger number of gauche conformers. The amount of transoid and gauchoid chain segments can be derived from the integrated intensities of the respective signals at 33.5 and 31 ppm. The integrated intensities of these signals, corrected for the different cross polarization efficiencies, yield 74% transoid and 26% gauchoid chain segments in the $C_{18}S$−Au sample at 25 °C.

(iv) 2D WISE NMR. The degree of crystallinity was investigated by two-dimensional wideline separation (WISE) NMR experiments, which are useful for determining morphology and local dynamics in complex systems.[21] In crystalline solids, the proton line widths are greatly increased due to strong dipolar interactions among the abundant proton spins. This interaction will be reduced by molecular motion, making proton line widths a sensitive probe of local dynamics. However, due to a limited chemical shift range, distinguishing the proton signals from different domains (crystalline versus amorphous) is difficult, and a variety of experiments have been devised to separate the individual components. In the WISE experiment, the high-resolution ^{13}C CP MAS spectrum is along one dimension and the proton spectrum is along the second, which allows measurement of the proton line width associated with individual carbon sites. The room temperature 2D WISE spectrum of $C_{18}S$−Au showed that the peak at 31 ppm, visible as a small shoulder in the 1D ^{13}C CP MAS spectrum, has a proton line width of ~20 kHz, whereas the 33 ppm component has a larger proton line width of ~35 kHz, somewhat less than the values for rigid crystalline organic solids (50−60 kHz). Very similar 1D carbon and 2D WISE spectra were observed by Spiess and co-workers for a polyester with C_{16} alkyl side chains (PPTE-A), which has a layer-type packing structure.[21b] In this polymer, the large reduction of the proton line width to 40 kHz, with retention of the extended-trans character of the chains, was taken as evidence for a large-amplitude motion effective around the side-chain axes.[21b] A similar anisotropic motion of the chains must be taking place in $C_{18}S$−Au. TEM images and X-ray diffraction indicate that the average interparticle distance in the 2 nm gold colloid samples is equal to one alkyl chain length, suggesting that close packing of the alkane chains into an all-trans conformation is achieved by intercalation or interpenetration of individual chains or domains of chains of neighboring gold particles. A similar structure has been reported for dodecylated C_{60}, in which paraffinic crystallites are formed by interdigitation of the side chains.[26] The component at 31.0 ppm is assigned to chains which are not intercalated, either due to thermal disordering or because they are chains which are too far from the chains of neighboring particles to interpenetrate. In other words, these chains would be located in the interstitial regions arising whenever spheres are close-packed, as illustrated in Figure 5, which shows a possible packing arrangement along with a TEM image of $C_{18}S$−Au. The reduced proton line width of the transoid component indicates that these intercalated chains are loosely packed, with sufficient free volume to allow considerable motion and disorder at the chain ends.

In the case of $HOC_{16}S$−Au, the interior methylene peak at 33 ppm in the 1D ^{13}C CP MAS spectrum is broader than that of $C_{18}S$−Au. Although its room temperature 2D WISE spectrum does not show a distinct 31 ppm

---

(26) Levon, K.; Weng, D.; Mao, J.; Lee, H. K.; Tour, J. M.; Schrivens, W. A. *Mater. Res. Soc. Symp. Proc.* **1994**, *349*, 127.

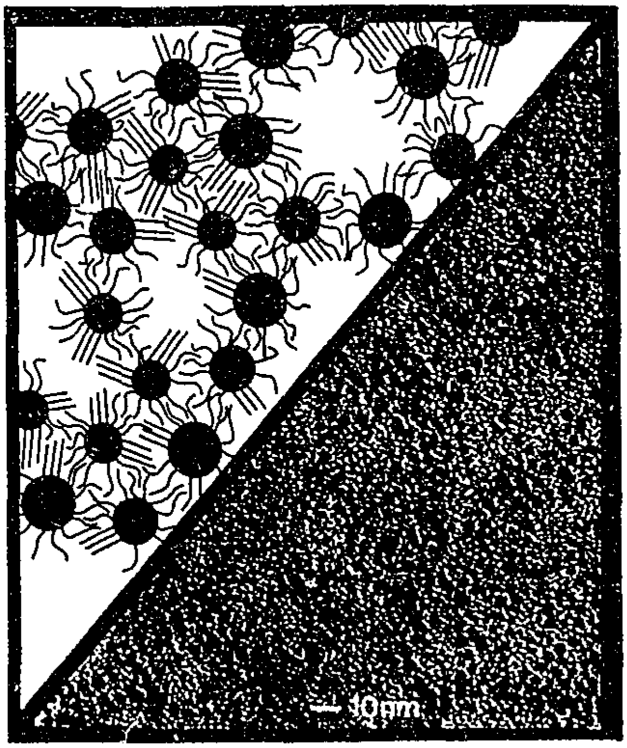

Figure 5. TEM image and an idealized representation of the two types of chains arising from close packing of the gold colloids in $C_{16}S-Au$. Conformationally ordered, intercalated chains (straight lines) are shown along with mobile, isolated chains located at interstitial regions between the colloids. The intercalated chains are loosely packed compared to rigid crystalline systems, with enough free volume for conformational disorder at the chain ends.

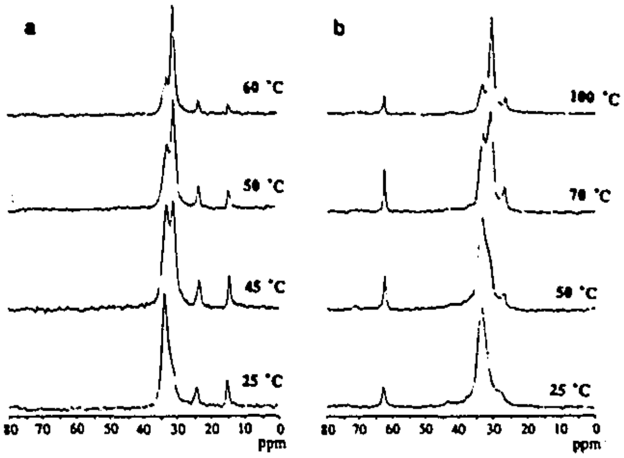

Figure 6. Variable temperature ^{13}C CP MAS spectra of (a) $CH_3(CH_2)_{17}SH$ and (b) $HO(CH_2)_{16}SH$ on colloidal gold. The spectra returned to their original state upon cooling.

component, the line width of the protons associated with the interior methylenes is also significantly reduced to 30 kHz.

(v) Variable Temperature ^{13}C CP MAS NMR. The variable temperature ^{13}C CP MAS NMR spectra of the C_{18} methyl-terminated and C_{16} hydroxyl-terminated gold particles are displayed in Figure 6. DSC measurements show that the methyl-terminated gold colloids, $AuS(CH_2)_nCH_3$ (for $n = 11, 13, 15, 17, 19$), have transitions in the same range as the gel-to-liquid crystalline transitions of *n*-diacylphosphadityIcholine bilayers of the same chain lengths.[16] In the ^{13}C NMR spectra, this transition is manifested as a gradual increase in the component at 31 ppm, assigned to conformationally disordered chains, and a diminishing of the all-trans component at 33 ppm. Above 55 °C, only the conformationally disordered component remains for $C_{16}S-Au$. The signals of C17 and the methyl group sharpen and then diminish at higher temperatures, since the mobility of the chain terminus has increasesd to the point that cross polarization is no longer efficient. This thermal disordering is reversible, and the ^{13}C NMR spectrum returns to its original state upon cooling.

In the case of $HOC_{16}S-Au$, as shown in Figure 6b, disordering of the chains is not complete until above 100 °C. As the mobility increases, the chain end carbons (C14 and C15), which have solution shifts of 25.6 and 32.6 ppm, narrow and become visible in the solid-state spectrum. Although the increased thermal stability of the hydroxyl-functionalized thiol on gold may be expected due to the presence of hydrogen bonding, its terminal carbon appears to be quite mobile compared to the unbound thiol. As shown in Figure 3b,c, the C16 peak of $HS(CH_2)_{16}OH$ narrows, and its T_1^C decreases from 102 to 0.2 s after attachment to the gold colloid. However, neither dipolar dephasing, nor the 2D WISE experiment, revealed a distinct component at 31 ppm for disordered chains in $HOC_{16}S-Au$. The interior methylenes are evidently less mobile than the methyl-terminated C_{18} thiol gold colloids. In contrast to the long chain samples, when the C_8S-Au sample was heated to 50 °C, the only changes observed were a slight narrowing and a small upfield shift of the four resolvable carbon peaks, confirming that the short chains are already in a liquid-like state at 25 °C.

4. Discussion

The ^{13}C and ^1H NMR spectra demonstrate that the alkanethiols are strongly chemisorbed to the gold colloids and are not present as free surfactant. Our preparation conditions suggest that this would be the case, as we have taken considerable care in washing free thiol surfactant from the samples.[16] Broadening of the NMR resonances, due to immobilization of the surfactant, as well as the apparent disappearance of the signals of the carbons closest to the sulfur headgroup point to a strong interaction with the metal surface. The solid-state NMR spectrum of the ^{13}C-labeled sample, $CH_3(CH_2)_{12}{}^*CH_2S-Au$, further confirms this, with the C1 carbon next to the sulfur headgroup inhomogeneously broadened and shifted downfield by 18 ppm, compared to the bulk thiol. Inhomogeneous broadening of adsorbates on metallic particles, which is not eliminated by magic-angle spinning, can arise from heterogeneity of adsorption sites and/or a dispersion of susceptibilities or Knight shifts, which will mirror the particle size distribution. Typically, the ^{13}C resonances of molecules chemisorbed onto Pd and Pt clusters are severely broadened by demagnetization fields arising from the large magnetic susceptibilities of these metals.[27] A study of ethylene adsorbed on supported Pt and Ag clusters compared the relative demagnetization fields of open and closed d-block metals and found no problems with magnetic susceptibility in the case of silver.[28] In contrast, the near ferromagnetic character of the platinum metal interferes with $^1H-^{13}C$ cross polarization by creating large off-resonance shifts of the proton signals, resulting in a large loss of signal intensity. However, like silver, gold has a filled d-level, so the magnetic susceptibility should not be a large source of broadening. Another possibility is a distribution of Knight shifts which arise from the conduction electrons of the gold metal particles. Mössbauer spectra of $Au_{55}(PPH_3)_{12}Cl_6$ clusters show separate con-

---

(27) Ansermet, J.-Ph.; Slichter, C. P.; Sinfelt, J. H. *Progr. Nucl. Magn. Reson. Spectrosc.* **1990**, *22*, 401.

(28) Chin, Y. H.; Ellis, P. D. *J. Am. Chem. Soc.* **1993**, *115*, 204.

tributions from the surface atoms and the inner core of 13 gold atoms, which has a Mössbauer shift close to bulk metallic gold.[29] Since the thiol-capped gold clusters in this study contain ~400 gold atoms, they should also be metallic. Whether a carbon atom which is not directly bonded to a metal surface will have a Knight shift has not been explored, but presumably the metallic contribution will rapidly decrease as one moves along the alkyl chain, away from the surface.[27] Relaxation measurements and studies of model gold thiolate complexes are underway to determine the contributions to the shift of the C1 resonance in $CH_3(CH_2)_{12}{}^*CH_2S-Au$, and thus gain insight into the nature of the bonding of the alkanethiol to the gold.[30]

The ^{13}C chemical shifts in this study, together with a concurrent FTIR study (which show narrow peaks at 2918 cm^{-1} (fwhh of 16 cm^{-1}) and 2850 cm^{-1} (fwhh of 9.5 cm^{-1}) for the methylene antisymmetric and symmetric stretching modes),[16] suggest that the $C_{18}S-Au$ chains are crystallized into an all-trans extended conformation. The hydroxyl-terminated thiol on gold likewise displays an infrared spectrum characteristic of an all-trans conformation (2918 cm^{-1} (fwhh of 19 cm^{-1}) and 2848 cm^{-1} (fwhh of 10 cm^{-1}) for the methylene antisymmetric and symmetric stretching modes). The sharpness and low frequencies of the CH_2 stretches in these samples match those measured for the highly ordered planar self-assembled monolayers that have also been characterized by contact angle, ellipsometry,[31] and helium diffraction measurements.[32] However, the NMR spectra of $C_{18}S-Au$ reveal a significant population of mobile, conformationally disordered chains at 25 °C. We have also detected disordered chains by ^{13}C NMR in a metal phosphonate self-assembled monolayer, while the infrared spectrum indicated only highly ordered chains.[11] Infrared spectroscopy is a signal-averaging technique, and these results demonstrate that the infrared spectra alone cannot be used to assume a high degree of order in self-assembled monolayers or in related long chain systems. In any case, the existence of disordered chains in the thiol-capped gold is not surprising since recent STM studies support the presence of a significant number of conformational defects, even in the most carefully prepared thiol self-assembled monolayers.[33]

The shift of C17 in $C_{18}S-Au$ is more upfield than that observed for bulk alkanes, reflecting that the gauche defects are concentrated at the chain ends, as is the case for thiol SAMs on planar substrates.[6] The contrast between the mobility of the chain ends versus the more motionally restricted interior methylenes is most evident in the dipolar dephasing experiment, where the latter exhibit rapid Gaussian decays rather than liquid-like Lorentzian decays. This thermal disordering of the chain ends is consistent with infrared studies of alkanethiol monolayers on planar gold, showing that gauche defects at the chain termini persist down to 200 K.[12b] ^{13}C spin–lattice relaxation measurements demonstrate that the reorientation rate of the gold-bound methylene chains is far slower than in the case of dispersed grafted alkyl chains, but still exceeds that of highly crystalline solids due to the motional freedom of the unbound chain ends. The fact that the methylene proton line widths are relatively narrow (35 kHz) compared to rigid crystalline chains (75 kHz in low-density polyethylene[21b]), combined with the high degree of conformational order, indicates that large amplitude motions are taking place about the chain axes. This type of anisotropic motion occurs also in the rotator phases of n-alkanes immediately preceding the melting point. ^2H NMR studies of selectively labeled samples are underway to identify the chain motions taking place.

The coexistence of covalent anchoring of the thiols on the gold colloids with lateral van der Waals interactions, sufficient to pack the chains into an all-trans conformation, are properties in common with SAMs on planar gold. The fact that TEM images and X-ray diffraction measurements suggest that this dense packing is achieved *via* the intercalation of chains of neighboring colloids limits comparisons of the dynamical properties between the two systems. However, similarities in the thermal properties can be identified. Both the variable temperature electrochemical measurements[14] and X-ray diffraction studies[13] of $CH_3(CH_2)_nSH$ self-assembled on planar gold show that chain length dependent phase transitions occur in carefully prepared samples. The transition temperatures detected by the electrochemical measurements carried out in aqueous solutions,[14] which match those detected by DSC in the gold colloids,[16] are lower than those found in the X-ray diffraction studies in ultrahigh-vacuum conditions.[13] This may be attributable to the common presence of water overlayers in both the aqueous electrochemistry and the DSC measurements in air. Our NMR spectra reveal that while the C_{18} chains on gold are solid-like in water, they become mobile upon heating to 55 °C. This coincides with the transition temperature determined by DSC.[16]

The variable temperature ^{13}C solid-state NMR spectra demonstrate conclusively that these transitions are due to reversible disordering of the chains. In the same C_{18}–gold colloid sample examined by solid-state NMR, the DSC transition was somewhat broad, and in the NMR spectra this is manifested as the 31 ppm peak growing in at temperatures below the peak maximum temperature of the endotherm. The broad transitions displaying gradual disordering may be partly due to poor bulk crystallization. Some C_n–gold samples, not studied by solid-state NMR, were found to have sharper DSC transitions after recrystallization and thermal annealing.[16] Likewise, in the case of self-assembled monolayers, sharp discontinuities were only observed in electrochemical thermograms when the thiol-modified gold electrodes had been carefully annealed for prolonged periods.[14] Even in these best samples, the temperature range of the transition is still broad compared to lipid bilayers. This may be due to the fact that the sulfur headgroup is covalently bonded to the gold, restricting the cooperative nature of the transition. Fatty acid Langmuir–Blodgett (LB) monolayers on silicon wafers also show broad transitions as detected by electron diffraction studies.[34] For example, in stearic acid LB films, a pretransitional disordering of the chains starts at ~35 °C and peaks at 50–55 °C. This transitional temperature range is very similar to that observed by DSC for $C_{18}S-Au$ in this study: onset temperature at 39 °C and a peak maximum temperature of 51 °C.[16] In the stearic acid LB film, a main melting transition also occurs at 110 °C, due to an irreversible disruption of the headgroup lattice.[34] However, this type of isotropic state, which defines a true melting transition, is not observed for the alkanethiols covalently bound to the gold colloids at temperatures up to 100 °C.

The variable temperature NMR spectra of thiol-capped

---

[29] Kappes, M. *Chem. Rev.* **1988**, *88*, 369.

[30] Badia, A.; Reven, L. Manuscript in preparation.

[31] (a) Porter, M. D.; Bright, T. B.; Allara, D. L.; Chidsey, C. E. D. *J. Am. Chem. Soc.* **1987**, *109*, 3559.

[32] Camillone, N., III; Chidsey, C. E. D.; Liu, G.-Y.; Putvinski, T. M.; Scoles, G. *J. Chem. Phys.* **1991**, *94*, 8493.

[33] Delamarche, E.; Michel, B.; Gerber, Ch.; Anselmetti, D.; Güntherodt, H. J.; Wolf, H.; Ringsdorf, H. *Langmuir* **1994**, *10*, 2869.

[34] Reigler, J. *J. Phys. Chem.* **1989**, *93*, 6475 and references therein.

gold colloids are very similar in appearance to our recent study of octadecylsiloxane self-assembled monolayers on silica, with the main difference being the temperature range of interest.[11] Although these samples were more disordered than the thiols, complete thermal disordering occurs at much higher temperatures (>115 °C). The increased thermal stability in these monolayers is due to cross-linking at the monolayer/substrate interface. Similar thermal stability has also been recently observed for more highly ordered metal phosphonate monolayers, which like the alkylsiloxanes, are linked together by a strong inorganic network at the substrate interface.[35]

The degree of conformational order depends on a number of variables besides chain length. These factors include the gold particle size and the nature of the terminal group, as both will affect the extent of intercalation of chains between colloid particles. The hydroxyl-terminated thiol was found to have a higher chain-disordering temperature. Moreover, a resolved peak associated with disordered chains was not detected at 25 °C. Unlike the methyl-terminated thiols, the $HOC_{16}S-Au$ flocculates in both polar and nonpolar solvents. Both NMR and FTIR spectra indicate a structure with extended all-trans chains. The reduced proton line width of 30 kHz shows that large amplitude motions are also taking place about the chain axes. However, the longer T_1^C value of the interior methylene carbons indicates that the introduction of a hydroxyl terminal group results in a decrease in the rate of the high-frequency motions compared to the methyl-terminated samples. While the terminal group of the alcohol thiol becomes more mobile upon binding to the gold, the infrared spectrum still shows a broad absorption band at 3300 cm^{-1}, indicating that hydrogen-bonded OH groups are present. The higher mobility of the terminal group indicates that the hydrogen bonding in $HOC_{16}S-Au$ is weaker than in the pure surfactant. Partial hydrogen bonding between the chain ends of neighboring colloids would introduce order and also account for the reduced chain mobility and increased thermal stability. Molecular dynamics calculations for OH-terminated thiols on planar gold predict structures which are more rigid than the methyl-terminated thiol monolayers, with both free and hydrogen-bonded OH groups being present.[15b]

Monte Carlo studies indicate that some structural and dynamic features of monolayers critically depend on the system size. The formation of domains of varying conformations which have been detected by scanning tunneling and atomic force microscopies can be accurately simulated only for systems larger than 200 molecules.[15c] A 2 nm gold colloid used in this study can only accommodate approximately 80 thiol chains on its surface, so this system is too small to manifest the structural and dynamic properties arising from longer range order, even if the large surface curvature was disregarded. This limitation is apparently circumvented by the tendency of the chains on adjacent colloidal particles to interpenetrate. We are presently synthesizing much larger gold colloids which will more closely approximate the environment of self-assembled monolayers on planar gold. Future work will also include ^2H-labeled thiols to determine the geometry of the chain motion through line shape studies.

Conclusion

The surfactant in C_{18} thiol-capped gold colloids exists in an extended conformation and is strongly bound to the surface by the sulfur headgroup. In the solid state, a semicrystalline structure forms with the all-trans chains densely packed by intercalation with chains of neighboring colloids. The chains displaying a high degree of conformational order are not rigid, but instead are undergoing a dynamic process involving large-amplitude motion about the chain axes. Although transmission FTIR spectroscopy indicates an ordered all-trans extended chain conformation, NMR spectra show that conformationally disordered chains are also present on the C_{18} thiol-capped gold colloids. Phase transitions determined by DSC are revealed by NMR to be attributable to a simple, reversible disordering of the chains. The fact that this disordering occurs at temperatures identical to the discontinuities observed in the electrochemical thermograms of thiol-modified planar electrodes points toward similar order/disorder phase transitions occurring in self-assembled monolayers.

Note Added in Proof. A recent solution ^{13}C NMR study of the alkylthiol–gold colloid system (Terrill; et al. *J. Am. Chem. Soc.* **1995**, *117*, 12537) attributes the disappearance of the C1–C3 resonances primarily to residual heteronuclear (C–H) dipolar broadening. However, we note that these resonances remain greatly broadened in the ^{13}C solid-state NMR spectra under high-power proton decoupling. In addition, their calculated shift for C1 of 27 ppm, a 190 Hz shift from the unbound monomer calculated by assuming a magnetic susceptibility contribution only, is inconsistent with the observed value of 42 ppm reported here for the ^{13}C-labeled sample. The solid-state NMR spectra show that additional contributions to the shift and line width of the C1 resonance are present.

Acknowledgment. The authors are grateful to Professor R. B. Lennox for useful discussions and a critical reading of the manuscript. Support for this research from the Natural Sciences and Engineering Research Council of Canada (NSERC) and the FCAR Nouveaux Chercheurs programme of Quebec is gratefully acknowledged.

LA9510487

---

(35) Gao, W.; Grozinger, C.; Reven, L. Unpublished results.